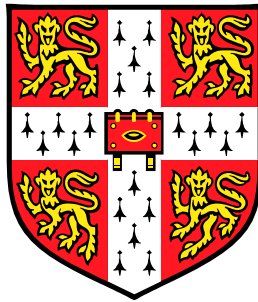


The development of magnetic tunnel junction fabrication techniques

Clifford Alastair Elwell

Darwin College, Cambridge.



A dissertation submitted for the degree of Doctor of Philosophy at
the University of Cambridge

July 2002

The development of magnetic tunnel junction fabrication techniques

The discovery of large, room temperature magnetoresistance (MR) in magnetic tunnel junctions in 1995 sparked great interest in these devices. Their potential applications include hard disk read head sensors and magnetic random access memory (MRAM). However, the fabrication of repeatable, high quality magnetic tunnel junctions is still problematic. This thesis investigates methods to improve and quantify the quality of tunnel junction fabrication.

Superconductor-insulator-superconductor (SIS) and superconductor-insulator-ferromagnet (SIF) tunnel junctions were used to develop the fabrication route, due to the ease of identifying their faults. The effect on SIF device quality of interchanging the top and bottom electrodes was monitored. The relationship between the superconducting and normal state characteristics of SIS junctions was investigated. Criteria were formulated to identify devices in which tunneling is not the principal conduction mechanism in normal metal-insulator-normal metal junctions.

Magnetic tunnel junctions (MTJs) were produced on the basis of the fabrication route developed with SIS and SIF devices. MTJs in which tunneling is the principal conduction mechanism do not necessarily demonstrate high MR, due to effects such as magnetic coupling between the electrodes and spin scattering. Transmission electron microscope images were used to study magnetic tunnel junction structure, revealing an amorphous barrier and crystalline electrodes.

The decoration of pinholes and weak-links by copper electrodeposition was investigated. A new technique is presented to identify the number of copper deposits present in a thin insulating film. The effect of roughness, aluminium thickness and voltage on the number of pinholes and weak-links per unit area was studied.

High frequency testing of read heads at wafer level was performed with a network analyser. Design implications for read head geometry were investigated, independent of magnetic performance. This technique has great potential to aid the rapid development of read and write heads whilst improving understanding of the system.

Preface

This dissertation, which is submitted for the degree of Doctor of Philosophy at the University of Cambridge, describes work carried out from October 1998 to July 2002 in the Department of Materials Science and Metallurgy, University of Cambridge. Except where specific reference is made, this is entirely the result of my own work and includes nothing that is the outcome of work done in collaboration. No part of this work has been or is being submitted for any other qualification at this or any other university.

Clifford Alastair Elwell

Device Materials Group, Dept. Materials Science, University of Cambridge

July, 2002.

Acknowledgements

This work would not have been possible without the support of a number of people. I would firstly like to thank my supervisor, Dr Mark Blamire for all his help, support, generosity and ideas over the years. I would also like to thank the head of the research group, Prof. Jan Evetts for use of the research facilities and some useful discussion. Dr Zoe Barber has provided practical help and discussion with sputtering. Dr Gavin Burnell deserves particular mention, due to the generous time he has spent with me over the last four years. His programming skills, practical help and proof reading have been invaluable.

I would like to thank Seagate Technology for providing the CASE award and the EPSRC for my studentship. Thanks to Dr Alan Johnston for a great deal of help and support during the 3 months I spent in Londonderry. I'd also like to thank Paul Scullion, Robert Lamberton, William O'Kane, and Adrian Marsh, for their help. Thanks to everybody in Springtown for the craic, in addition to the above, Peter, Niru, Declan, Colin and Dennis.

I was also grateful to receive wafers for testing, courtesy of Seagate and, in particular, Patrick Doherty.

All my proof readers have been great: Frances Gibson, Karen Yates, Mike Gibson, Angus Bryant, Angela MacKay, Gemma France, Mike Elwell and John Durrell. In the words of Socrates: “The unexamined life is not worth living.”

I’d like to thank everyone in the lab for their help and company over the last four years. In particular, thanks to Richard Moseley and Wilfred Booij for a great deal of help in the cleanroom when I arrived in the lab. Thanks also to Noel Rutter, Phil McBrien, Neil Todd, Robert Kinsey, Jose Prieto, Nadia Stelmashenko and John Durrell for general assistance. Thanks to Chris Bell for the FIB work and Stephen Lloyd for TEM images. My office-mates for three years deserve mention for their stimulating discussion... Mike Hogg, Ashish Garg, Yee Cheng and Moon-Ho Jo.

Needless to say, my friends and family have provided immeasurable support over the last 4 years. Sincere thanks to all of you – this PhD would not have been possible without you. Particular thanks to Frances who has experienced all the highs and lows of my PhD and given unstinting support. Thanks to my parents for everything – they could not have been better.

**To Frances
and
to my parents.**

Table of Contents

Chapter 1:	1
Introduction	1
1.1 Motivation for MTJ development	2
1.1.1 Read head principles and technology.....	3
1.1.2 Motivation for this thesis.....	6
1.2 The form of this thesis	6
Chapter 2:	8
Theoretical introduction	8
2.1 Tunneling	9
2.1.1 One dimensional rectangular barrier	9
2.1.2 Normal metal - insulator - normal metal junctions	14
2.1.3 Superconductivity – a brief review.....	16
2.1.4 Superconductor-insulator-ferromagnet.....	19
2.1.5 Superconductor-insulator-superconductor	26
2.2 Magnetism	27
2.2.1 Basic magnetism reviewed	27
2.2.2 Ferromagnetism	28
2.2.3 Magnetic tunnel junctions.....	36
2.3 Summary	39
Chapter 3:	40
Experimental methods	40
3.1 Substrate choice and preparation	41
3.2 Deposition of thin films	42
3.2.1 Deposition system.....	42
3.2.2 Evacuation of the system.....	44
3.2.3 Gas pressure	45
3.2.4 Deposition rate calibration.....	46
3.3 Processing	46
3.3.1 Photoresist	48
3.3.2 Optical lithography.....	48
3.3.3 Ion milling.....	51
3.3.4 Silica deposition.....	52
3.3.5 Contact pad deposition	53
3.4 Testing	54
3.4.1 Film characterisation.....	55
3.4.2 Device characterisation	57
3.5 Nomenclature	62
3.6 Summary	62
Chapter 4:	63
The use of SIS and SIF junctions to optimise device fabrication	63
4.1 Previous work	64
4.1.1 SIS junctions.....	64
4.1.2 SIF junctions	70
4.2 The fabrication of SIS and SIF tunnel junctions	75
4.2.1 Deposition of films	75
4.2.2 Fabrication of devices.....	78

4.2.3	Variation in the fabrication route	79
4.3	Results	79
4.3.1	SIS tunnel junctions.....	79
4.4	SIF tunnel junctions.....	86
4.4.1	Superconducting bottom electrode.....	86
4.4.2	SIF, ferromagnet bottom electrode	90
4.4.3	Al/Al ₂ O ₃ /Al/Co/Nb tunnel junctions.....	90
4.5	Conclusions.....	92
Chapter 5:		94
High frequency testing of read heads and capacitors		94
5.1	Introduction to high frequency testing	95
5.1.1	Transmission lines.....	95
5.1.2	Basic network analyser theory.....	98
5.1.3	Errors and limitations	100
5.2	High frequency response of read heads	101
5.2.1	Roll-off frequency	104
5.2.2	Experimental procedures	104
5.2.3	Results and discussion	109
5.2.4	Subsequent literature	120
5.2.5	Implications for read head design	122
5.3	The high frequency performance of insulators	123
5.3.1	Capacitors at high frequency.....	123
5.3.2	The dielectric properties of insulators	123
5.3.3	Experimental Procedure	126
5.3.4	Results and Discussion.....	127
5.4	Conclusions.....	129
Chapter 6:		131
Magnetic tunnel junctions.....		131
6.1	Literature review	132
6.1.1	The definition of magnetoresistance	133
6.1.2	Ferromagnetic electrodes	134
6.1.3	Exchange bias.....	134
6.1.4	Angular dependence of MR	136
6.1.5	MR dependence on voltage	137
6.1.6	MR dependence on temperature	139
6.1.7	Problems of magnetic tunnel junction fabrication	140
6.2	Fabrication and testing of magnetic tunnel junctions	153
6.2.1	Film deposition.....	154
6.2.2	Device fabrication	155
6.3	Results	158
6.3.1	The effect of bottom electrode	158
6.3.2	Device and TEM characterisation.....	164
6.4	Conclusions.....	167
Chapter 7:		170
Copper decoration of pinholes and weak-links.....		170
7.1	Introduction to electrodeposition	171
7.1.1	Electrochemical cells.....	172
7.1.2	Electrodeposition	174
7.1.3	Electrodeposition apparatus	177

7.2	Previous work.....	178
7.2.1	Copper decoration of pinholes.....	178
7.2.2	Dielectric breakdown.....	180
7.3	Experimental technique.....	185
7.3.1	Deposition of thin films.....	185
7.3.2	Electrodeposition	185
7.3.3	Analysis of electrodeposited films	187
7.4	Results of initial experimental investigations	187
7.4.1	Feature identification	187
7.4.2	Effect of roughness.....	189
7.4.3	The effect of voltage.....	191
7.4.4	The effect of oxidation technique	192
7.4.5	Problems with the technique.....	192
7.5	New experimental technique.....	193
7.5.1	Film deposition.....	193
7.5.2	Lithography and film preparation	195
7.5.3	Apparatus and electrodeposition technique	196
7.5.4	Analysis of the films.....	197
7.6	Results	198
7.6.1	Effect of roughness.....	198
7.6.2	The effect of aluminium thickness on pinhole density.....	200
7.6.3	The relationship between current and pinhole density	202
7.7	Conclusions.....	205
Chapter 8:		207
Conclusions		207
8.1	Device fabrication	208
8.2	Copper decoration of pinholes.....	209
8.3	High frequency testing of read heads.....	210
Publications		212
Bibliography		213

Chapter 1:

Introduction

It is a good morning exercise for a research student to discard a pet hypothesis every day before breakfast. It keeps him young.

- Konrad Lorenz (zoologist)

Jullière first demonstrated spin polarized tunneling between two ferromagnets separated by an insulator in 1975 [Jullière, 1975]. He reported a variation in conductance of 14% at 4.2 K on application of a magnetic field sweep for Fe/Ge/Co devices. He defined the variation in conductance as the maximum difference in conductance over the maximum recorded conductance during the field sweep. Such devices are termed magnetic tunnel junctions (MTJs). Recently, a great deal of interest has been taken in MTJs due to the large magnetoresistance of 18% at room temperature first demonstrated by Miyazaki *et al.* [Miyazaki, 1995]. Magnetoresistance (MR), the change of resistance on application of a magnetic field, may be defined according to either of two conventions. Equation (1.1) shows the definition of MR used in this thesis.

$$\text{MR} = \frac{R_{\max} - R_{\min}}{R_{\min}}, \quad (1.1)$$

where R_{\max} and R_{\min} are the maximum and minimum resistance respectively, recorded as the magnetic field changes. The interest in magnetic tunnel junctions displayed by the magnetic recording industry is discussed below, followed by the motivation for the specific work undertaken during this study. The structure of the thesis is then presented.

1.1 Motivation for MTJ development

Research into the development of magnetic tunnel junctions has been driven by the magnetic data storage industry. The fierce competition between companies to produce faster, cheaper computers with higher data storage capacity has led to the rapid development of magnetic storage media. Two principle applications have been suggested for MTJs: as read head sensors for hard disks and as magnetic random access memory (MRAM). Hard disk manufacturers Seagate Technology sponsored this work, and therefore this thesis concentrates on read head applications of MTJs. However, MRAM has received a great deal of interest as a fast, non-volatile replacement for the current random access memory. MRAM's key advantage is its ability to store data with no applied power.

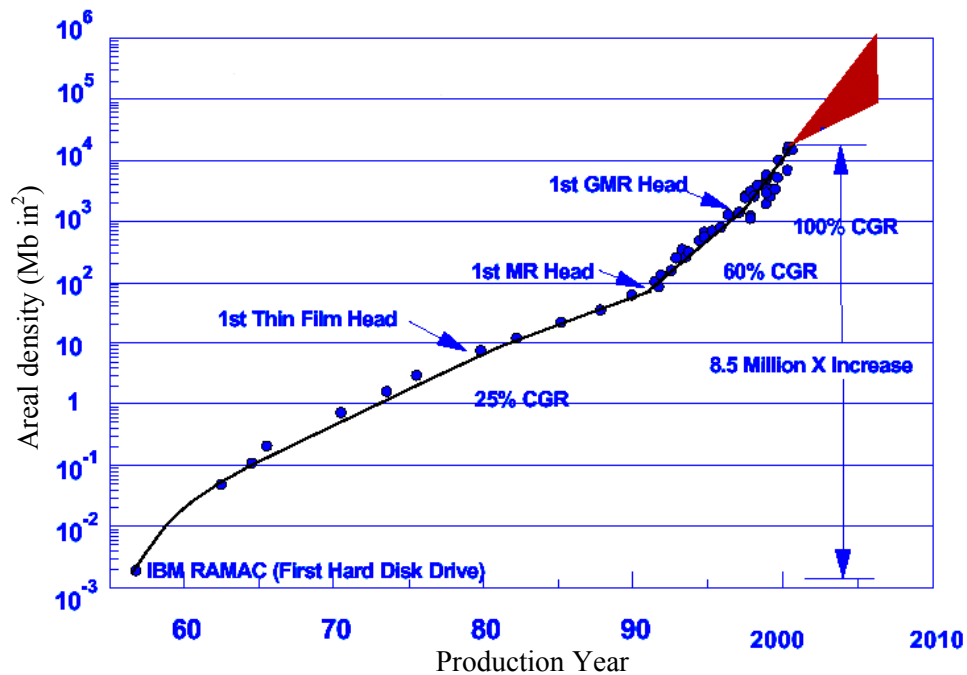


Figure 1.1: Increase in areal density for hard disks over the last 45 years. CGR is compound growth rate. GMR is giant magnetoresistance. Adapted from IBM website

Figure 1.1 shows the huge increase in hard disk areal density achieved over the last forty years. Areal density is defined as the number of bits of memory stored per unit area and is generally measured in megabytes per square inch. Areal density has increased by 60% per year between 1991 and 1997, and has since increased by 100% per year. However, the price per megabyte has decreased by 40-50% per year, whilst the internal data transition rate (measured in megabytes per second) increased by 40% per year [IBM, 2002]. In order to appreciate the pace of development of this industry, it is valuable to understand the principles of read head technology.

1.1.1 Read head principles and technology

A hard disk comprises a recording medium (the disk itself), a write head to transfer data to the disk, and a read head to recover data from the disk. Figure 1.2 is a schematic diagram of a hard disk. The disk spins at high speed; 5000 rpm to 7000 rpm is common. Binary data is stored on the disk as the direction of magnetisation within the bit. The read and write heads are scanned extremely close to the disk surface by an actuator; recent laboratory demonstrations have been performed at a height of just 10 nm

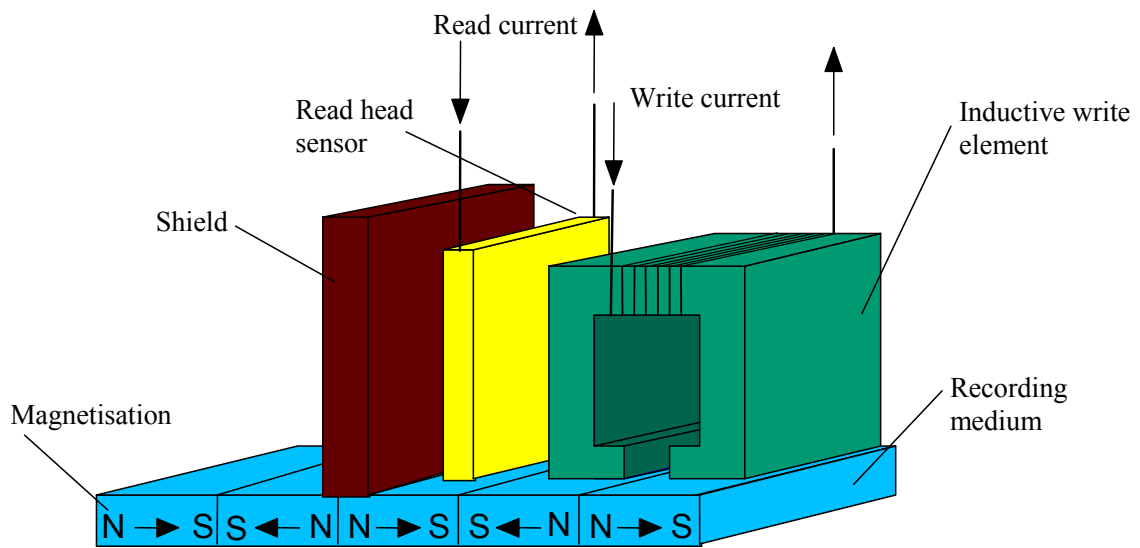


Figure 1.2: Schematic diagram of a hard disk. The shield between read head and writer has been omitted for clarity.

[Thompson, 2000]. Areal density is increased by reducing the size of each magnetic bit on a disk, as shown by Figure 1.3. Read and write head dimensions must therefore decrease correspondingly.

Initially, inductive read heads were used, consisting of tightly wound coils around a central magnetic core. Changes in magnetisation as the coils are scanned across the disk surface induce a voltage, V , in the coils, according to Faraday's law:

$$V = \oint \mathbf{E} \cdot d\mathbf{l} = -N \frac{d\Phi}{dt}, \quad (1.2)$$

where $\oint \mathbf{E} \cdot d\mathbf{l}$ is the line integral of the electric field, \mathbf{E} , around the circuit, N is the number of turns of the coil, and $\frac{d\Phi}{dt}$ is the rate of change of magnetic flux, Φ . The sign of the induced voltage indicates the direction of magnetisation in a bit. It is not practical to fabricate inductive read heads sufficiently small and sensitive for modern, high areal density disks. Thin film magnetic sensors were developed to replace inductive heads, where the presence of a magnetic field induces resistance changes in the film. The first magnetoresistive read head was introduced in 1991 by IBM. Permalloy films achieved an MR of $\approx 2.5\%$ in read heads. Reduced bit size requires increased reader sensitivity, leading to the introduction of giant magnetoresistance (GMR) read heads in 1997. GMR

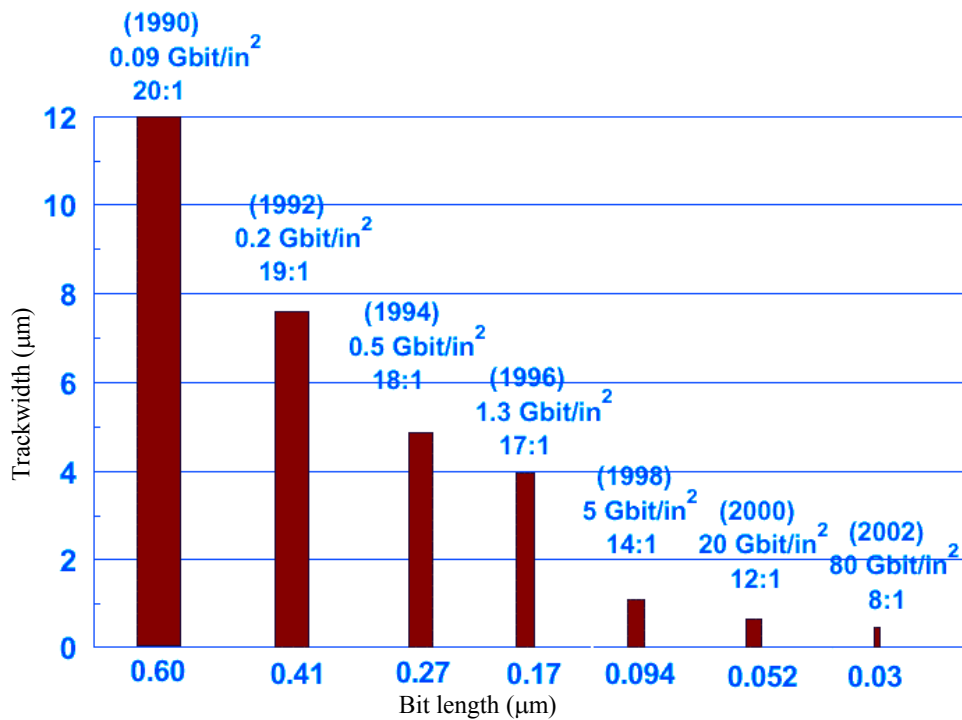


Figure 1.3: Decrease in bit size over the last twelve years. Trackwidth represents the difference in inner and outer diameter of the concentric rings of bits on a hard disk. Bit length is the size of the bit in the concentric direction. Adapted from IBM website.

read heads have been demonstrated with a room temperature MR of around 25% in low magnetic fields [IBM, 2002]. In the future, magnetic tunnel junctions may replace GMR read heads, due to the high MR of MTJ devices of over 30% in very low fields.

The requirements placed on magnetic tunnel junctions for read head applications are stringent. The junctions must be thermally stable at operating temperatures, which may exceed 250°C. The effect of grain size, shape, voltage bias, temperature, layer thickness and roughness should be understood and controllable, in order to produce reproducible junctions. The most problematic requirement has been that of low resistance. Magnetic tunnel junctions are intrinsically high resistance, due to the presence of an insulating barrier, and smaller sensors increase the resistance of the read head. Resistances of the order of 1 kΩ have been suggested in order to facilitate high data rate operation, as discussed in Chapter 6.

1.1.2 Motivation for this thesis

One of the key problems experienced by many workers on magnetic tunnel junctions is that, whilst the requirements on device fabrication are high, results of resistance against magnetic field indicate only whether the magnetic sensor is good or bad. Non-optimal performance of magnetic tunnel junctions can result from a wide range of faults which can be difficult to diagnose, such as barrier inhomogeneity and pinhole formation. The aim of the work described in this thesis was to improve the techniques to analyse magnetic tunnel junction quality. Quantitative tests for junction and barrier quality were investigated and developed.

Seagate Technology sponsored this project as a CASE partnership, as a consequence of which three months research work was undertaken on site in Londonderry. This relationship presented the opportunity to research an exciting new technique to assess the effect of material and device parameters on the high frequency response of read heads using a network analyser. This highly successful investigation gave insight into the parameters of importance to read head frequency response, in particular the requirement of low resistance.

1.2 The form of this thesis

Tunnel junction theory is introduced in Chapter 2, together with the concepts of superconductivity and magnetism required to understand different junction types. Normal metal-insulator-normal metal (NIN), superconductor-insulator-ferromagnet (SIF) and superconductor-insulator-superconductor (SIS) tunnel junctions are discussed. Magnetism, with emphasis on ferromagnetism, is then reviewed, followed by an introduction to magnetic tunnel junctions. The practical techniques of film deposition, lithography and processing are considered in Chapter 3.

The relationship between the normal state and superconducting characteristics of SIS and SIF tunnel junctions was investigated in Chapter 4. A high quality tunnel junction fabrication route was developed. The ratio of the superconducting state to the normal state resistance is a convenient measure of junction leakage, termed the figure-of-merit (FOM). The relationship between the FOM and NIN characteristics was investigated.

Criteria were formulated to identify devices in which tunneling is not the principal conduction mechanism in normal metal-insulator-normal metal junctions.

High frequency testing of read heads with a network analyser is presented in Chapter 5. The principles of high frequency testing and network analysers are introduced, facilitating the interpretation of a series of measurements on read heads. The effect of sensor length, width, insulator thickness, shield size and type are investigated. A simple electrical model of read heads at high frequency is developed. Design implications of the results to the development of read heads for high data transmission rate applications are then considered.

Magnetic tunnel junctions are discussed in Chapter 6. Developments in the experimental and theoretical study of MTJs are reviewed. Results are presented for magnetic tunnel junctions fabricated during this study. The effect of lower electrode roughness on magnetic tunnel junction performance is investigated. Transmission electron microscope images indicate the structure of the films produced.

The use of copper decoration by electrodeposition, to identify pinholes and weak-links in the insulating barrier, is presented Chapter 7. The experimental apparatus and technique are investigated, and the alterations and improvements to the method discussed. The effect of lower electrode roughness, deposition voltage, and aluminium thickness, on number of copper deposits per unit area and electrodeposition current are presented.

Finally, the conclusions and implications of this work are discussed in Chapter 8. The complexity of high quality magnetic tunnel junction fabrication is reviewed in relation to the techniques developed over the course of this study.

Chapter 2:

Theoretical introduction

“Anyone who is not shocked by quantum theory has not understood it.”

-Niels Bohr

This work covers a wide range of topics, however this chapter concentrates on the main theme of the thesis: electron tunneling and magnetism. The development of techniques to monitor and improve the quality of magnetic tunnel junctions for hard disk read head applications is better understood with an appreciation of background theory. Firstly, the mechanisms for tunneling between metals separated by an insulator are considered, before building more complicated systems and introducing different electrodes. A brief summary of the concepts of superconductivity required to identify the key features of superconductor-insulator-superconductor (SIS) and superconductor-insulator-ferromagnet metal (SIF) tunnel junctions is also presented. Magnetism is discussed, with particular attention to the theory of ferromagnetism and polarisation. Finally the basics of magnetic tunnel junctions are introduced, a more detailed literature survey is presented in Chapter 6.

2.1 Tunneling

Classical physics cannot explain the transmission of electrons through a potential barrier when the barrier potential energy is greater than the electron kinetic energy. However, such transmission of electrons does occur and quantum mechanics is used to explain the observed effects. Firstly, a simple model of electron tunneling through an idealised rectangular barrier is presented; it is then extended to derive expressions for the current density. Two extremely important models of tunneling in metallic junctions are considered, Simmons' and Stratton's theories, followed by the effect of the image force on these models. Specific examples of tunneling are discussed starting with the normal metal-insulator-normal metal (NIN) junction. The behaviour of SIF and SIS junctions is then considered, after the concepts of superconductivity required to describe such junctions are introduced.

2.1.1 One dimensional rectangular barrier

A simple representation of quantum mechanical tunneling applies to electron transport through a barrier consisting of two free electron metals separated by an insulator. A number of assumptions simplify the problem, which are that the metals are identical, the interface perfect, image potentials negligible and interactions elastic. Figure 2.1

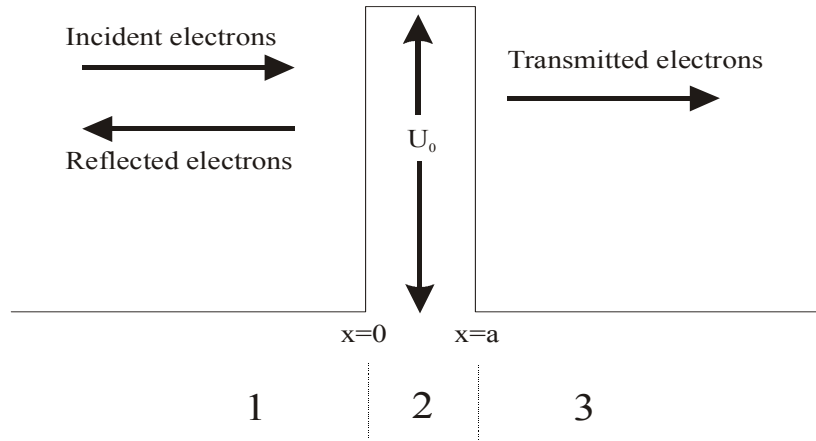


Figure 2.1: The rectangular tunnel barrier.

represents the rectangular barrier describing this situation. Additionally, free electron metals can be considered to have potential energy, $U(x) = 0$, and the barrier has a potential $U(x) = U_0 > 0$ acting over the region $0 \leq x \leq a$. When the particle energy, E , is such that $E < U_0$, the wave function $\psi(x)$ may be obtained by solving the time independent, one dimensional Schrödinger equation:

$$E\psi(x) = \left[-\frac{\hbar^2}{2m} \nabla^2 + U_0 \right] \psi(x). \quad (2.1)$$

Where $\hbar = h/2\pi$, h is Planck's constant and m the mass of the particle. The general solutions to the Schrödinger equation are:

$$\psi(x) = \begin{cases} A \exp(ik_1x) + B \exp(-ik_1x) & x \leq 0 \\ C \exp(ik_2x) + D \exp(-ik_2x) & 0 \leq x \leq a \\ F \exp(ik_1x) & a \leq x, \end{cases} \quad (2.2)$$

with wave numbers, k_1 and k_2 :

$$k_1 = \frac{\sqrt{2mE}}{\hbar} \quad \text{and} \quad k_2 = \frac{\sqrt{2m(U_0 - E)}}{\hbar}. \quad (2.3)$$

At the boundaries of the potential barrier both the wave functions and their differentials must be continuous. Solving Equation (2.2), the constants B , C , D and F are found in terms of A . The transmission coefficient, T , which is defined as the ratio of the

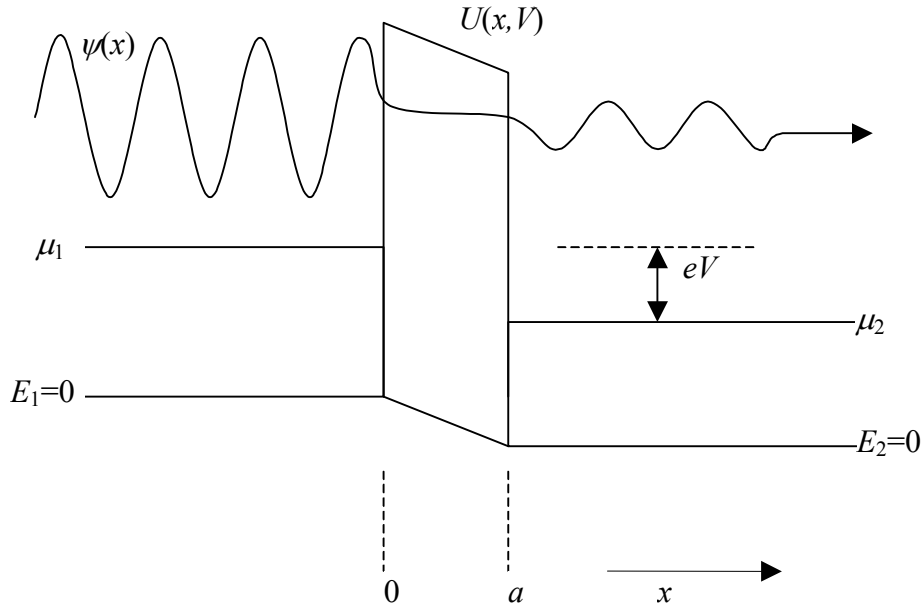


Figure 2.2: The trapezoidal barrier.

transmitted probability current density to the incident probability current density, can now be calculated:

$$T = \frac{v_1 F^* F}{v_3 A^* A} = \left[1 + \frac{\sinh^2(k_2 a)}{4 \frac{E}{U_0} (1 - \frac{E}{U_0})} \right]^{-1} \approx 16 \frac{E}{U_0} \left(1 - \frac{E}{U_0} \right) \exp(-2k_2 a), \quad (2.4)$$

where v_1 and v_3 are the group velocities in regions 1 and 3 respectively. The wave number in regions 1 and 3 (Figure 2.1) are the same, thus after tunneling the momentum and effective mass of the electron are unchanged, so $v_1 = v_3$. Despite the barrier potential exceeding the energy of the incident electron, it can be transmitted, the probability of which decreases exponentially as barrier thickness increases.

2.1.1.1 Extending the simple model

Consider the case when metal electrodes are not similar, resulting in an asymmetric barrier. This trapezoidal barrier is simply represented in Figure 2.2. The time invariant, one-dimensional Schrödinger Equation (2.1) is used with the same assumptions as above. However, the potential energy, $U(x, V)$, is now a function of both distance, x , and the applied potential, V . The Wentzel-Kramers-Brillouin (WKB) approximation includes the effect of a varying potential within the barrier region [Wolf, 1985]. This approximation involves solving the Schrödinger equation for the barrier, noting that it breaks down at the

classical turning points of the particles, and then interpolating solutions on either side of each turning point to produce a smooth wave function [Powell, 1961]. This allows the derivation of the transmission coefficient, as shown by Equation (2.5).

$$T = \exp\left(\frac{-2}{\hbar} \int_0^a \sqrt{2m(U(x) - E)} dx\right) \quad (2.5)$$

2.1.1.2 Current density calculation

The current density may be obtained by two methods: either the transfer Hamiltonian or the stationary state model [Wolf, 1985]. The latter method is discussed here, as it is simple and self-contained. However, real junction effects such as spin flip and resonant barrier levels are better described in the transfer Hamiltonian method[†]. It is assumed that each metal can be described by an equilibrium Fermi function:

$$f(E) = \left[\exp\left(\frac{E_1 - \mu_1}{kT}\right) + 1 \right]^{-1}, \quad (2.6)$$

$$f(E + eV) = \left[\exp\left(\frac{E_2 - \mu_2}{kT}\right) + 1 \right]^{-1}.$$

The Fermi energies μ_1 and μ_2 are measured from the bottom of the respective bands, as are the energies E_1 and E_2 on the left and right of the junction respectively. Following convention, the application of a positive bias, V , lowers the Fermi level of the right hand electrode (Figure 2.2). Current may pass in either direction, $J = J_{12} - J_{21}$, where J is the total current density, J_{12} and J_{21} are the current densities from one to two and vice versa. J_{12} is the integral of the electron charge multiplied by the group velocity, transmission

[†] For completeness the Hamiltonian method is summarised:

Consider a perturbation, $H(t)$ to the harmonic approximation to the system, $H_1 + H_2$. The time dependent Schrödinger equation must be solved to find the wave function, $\Psi(t)$:

$$i\hbar \frac{\partial \Psi(t)}{\partial t} = (H_1 + H_2 + H(t))\Psi(t)$$

$\Psi(t)$ is expanded in terms of the eigenstates of H_0 . Transitions occur between 1 and a range of final states, 2, with density of states $g(E_2)$ per unit energy around E_2 , the energy of the destination state. From Fermi's Golden Rule, for the transition rate Γ_{12} :

$$\Gamma_{12} = \frac{2\pi}{\hbar} |\langle \phi_2 | H | \phi_1 \rangle|^2 g(E_2) \delta(E_2 - E_1)$$

the matrix element H'_{21} is identified to be that of the current density operator.

Further details and a derivation of the resultant current density are available in [Wolf, 1985].

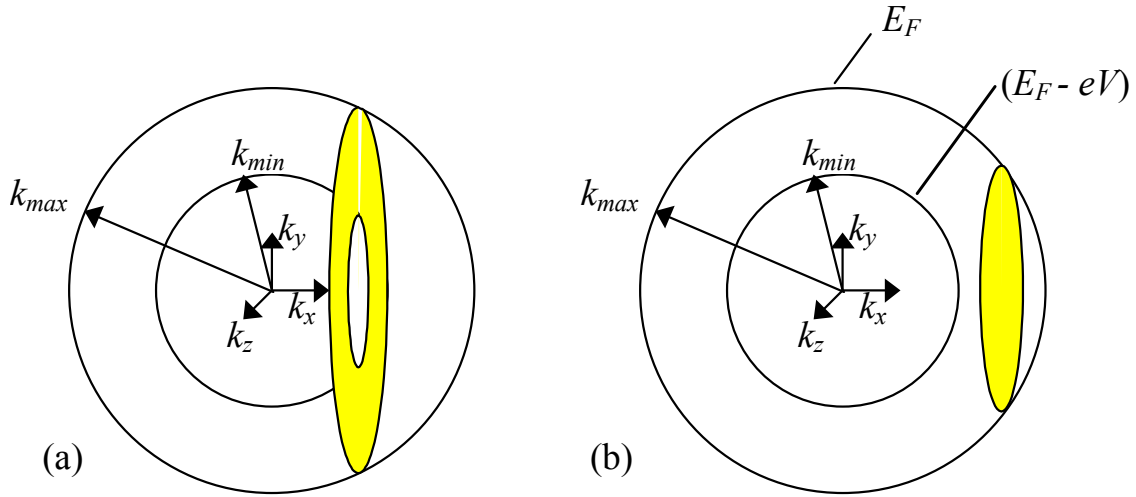


Figure 2.3: The integral may be split into two regions in k space, represented by an annulus (a) or disk (b).

coefficient, T and Fermi functions specifying that transport occurs between a full and an empty state over all available states in k -space:

$$J_{12} = \frac{2}{(2\pi)^3} \iiint e \left(\hbar^{-1} \frac{\partial E}{\partial k_x} \right) T (f(E) [1 - f(E + eV)]) dk_x dk_y dk_z, \quad (2.7)$$

where the factor 2 represents the spin degeneracy and $1/(2\pi)^3$ normalises to the number of states per unit volume in k -space. J_{21} may be derived similarly. The total current density can be calculated by changing the integration variable:

$$J = \frac{2e}{(2\pi)^3 \hbar} \int_0^\infty dE_x [f(E) - f(E + eV)] \iint T dk_y dk_z. \quad (2.8)$$

Equation (2.8) may be developed further by considering that in this model, where thermal excitation is neglected, electrons between the Fermi energy, μ_1 and $\mu_1 - eV$ are able to tunnel to the right. Figure 2.3 shows that as we integrate in k -space the areas are represented as either an annulus or disc, the integral is therefore separated into parts with appropriate limits. Since $dk_y = dk_z = dk_t$ in the transverse direction, a transverse density of states, ρ_t , may be defined:

$$d^2k_t = 2\pi k_t dk_t = \frac{2\pi m_t}{\hbar^2} dE_t = (2\pi)^2 \rho_t dE_t. \quad (2.9)$$

Substituting Equation (2.9) and the limits into Equation (2.8) leads to:

$$J(V) = \frac{2e\rho_t}{h} \left[eV \int_0^{\mu_1 - eV} T(E, V) dE + \int_{\mu_1 - eV}^{\mu_1} T(E, V) (\mu_1 - E) dE \right]. \quad (2.10)$$

2.1.2 Normal metal - insulator - normal metal junctions

J.G.Simmons used a very similar method to that in Section 2.1.1 to derive the current density for a normal metal-insulator-normal metal (NIN) junction [Simmons, 1963(a)]. He considered an arbitrary shaped barrier, with mean barrier height $\bar{\phi}$ and transmission coefficient shown below:

$$\begin{aligned} \bar{\phi} &= \frac{1}{a} \int_0^a \phi(x) dx, \\ T &= \exp\left(-A(\bar{\phi} - E + \mu_1)\right), \\ J &= J_0 \left\{ \bar{\phi} \exp\left(-A\sqrt{\bar{\phi}}\right) - (\bar{\phi} + eV) \exp\left(-A(\bar{\phi} + eV)^{1/2}\right) \right\}, \end{aligned} \quad (2.11)$$

$$\text{where } J_0 = \frac{e}{2\pi h(\beta a)^2}, \quad A = \frac{4\pi\beta a}{h}(2m)^{1/2},$$

and β is a correction factor close to unity. For low voltages, when taking $\beta = 1$, this reduces to:

$$\begin{aligned} J(V) &= \alpha V + \gamma V^3 + \dots \\ G(V) &= \alpha + 3\gamma V^2 + \dots \end{aligned} \quad (2.12)$$

$$\text{Where: } \alpha = \frac{(2m)^{1/2}}{a} \left(\frac{e}{h}\right)^2 \sqrt{\bar{\phi}} \exp\left(-A\sqrt{\bar{\phi}}\right) \quad \text{and} \quad \frac{\gamma}{\alpha} = \frac{(Ae)^2}{96\bar{\phi}} - \frac{Ae^2}{32\sqrt{\bar{\phi}}}. \quad (2.13)$$

The predicted conductance, $G(V)$, is parabolic with applied voltage bias, but Simmons' derivation incorrectly predicts it to be centred at zero. In Chapter 4 the results for NIN tunnel junctions are presented demonstrating a negligible zero offset, due to the fact that both metallic electrodes were niobium. The barrier height and width, a , can be conveniently calculated using a graphical interpretation of the above theory, which is discussed in Chapter 4.

2.1.2.1 Stratton's theory

Stratton modelled the same problem, using a different transmission coefficient, T [Stratton, 1962]. For the purposes of this work, it is sufficient to consider the results:

$$J(V) = \frac{4\pi em \exp(-b_1)}{h^3 c_1^2} [1 - \exp(-c_1 V)]$$

where $b_1(V) = \sqrt{\frac{8m}{\hbar}} \int_0^a \left(\phi(x) - \frac{eVx}{a} \right)^{1/2} dx$ (2.14)

and $c_1(V) = \sqrt{\frac{2m}{\hbar}} \int_0^a \left(\phi(x) - \frac{eVx}{a} \right)^{-1/2} dx$.

Stratton's theory leads to the temperature dependence of the tunnel current more readily than Simmons' theory:

$$\frac{J(V, T)}{J(V, 0)} = \frac{\pi c_1 k_B T}{\sin(\pi c_1 k_B T)} \approx 1 + \frac{1}{6} (\pi c_1 k_B T)^2 + \dots$$
 (2.15)

Equation (2.15) is commonly used to investigate the temperature dependence of tunnelling conductance in NIN junctions. This relation is used to examine the temperature dependence of tunnel junctions in Chapter 4.

2.1.2.2 Effect of the image force

An electron leaving or approaching a metal surface will experience an image force which is strongly dependent on the dielectric constant and thickness of the barrier. This problem has been treated in detail by Sommerfeld and Bethe [Sommerfeld, 1933] and applied to the NIN junction by Simmons [Simmons, 1963(b)]. Figure 2.4 shows the effect of the image force on a trapezoidal barrier, where the thickness and height of the barrier are reduced and the edges rounded off. Brinkman *et al.* applied the approximated barrier form to produce conductance curves as shown in Figure 2.5 [Brinkman, 1970]. The resultant changes to the conductance are a slight reduction of the zero offset and steeper rate of increase with voltage. They concluded that the effects were minor and subsequent authors have generally ignored image forces.

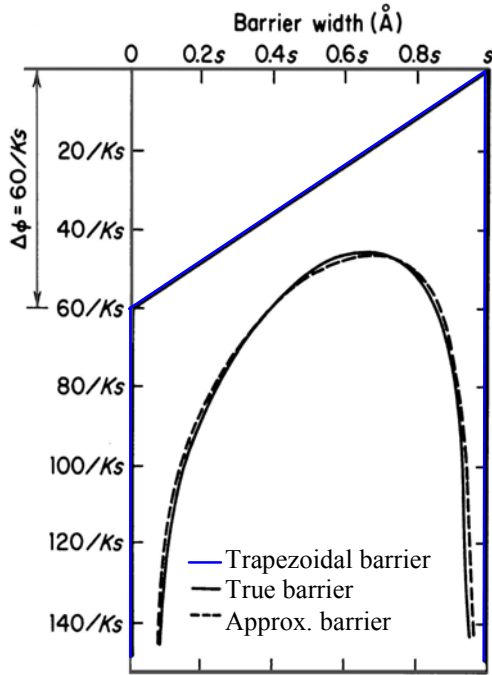


Figure 2.4: Effect of the image force on the trapezoidal barrier. Where K =dielectric constant and s =barrier thickness (\AA) [Simmons, 1963(b)].

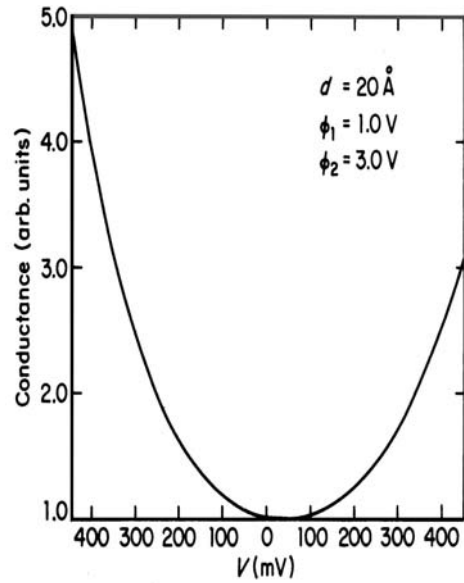


Figure 2.5: Conductance plot showing the minimal effect of the image force [Brinkman, 1970].

2.1.3 Superconductivity – a brief review

In order that junctions containing a superconducting component may be understood, it is first necessary to review some concepts of superconductivity. In 1911 Kamerlingh Onnes noticed the resistance of mercury vanished as temperature decreased below a critical temperature, T_c [Onnes, 1911]. A superconductor does not only have zero resistance, but it also exhibits perfect diamagnetism. On cooling through T_c magnetic field is expelled from the superconductor, if it is below some critical field, H_c . This is known as the Meissner effect [Meissner, 1933]. In the 1950's it was determined that superconducting materials can be separated into two categories exhibiting different behaviour, type I and type II.

When type I materials in their superconducting state are subjected to a magnetic field, a surface current is generated producing an internal magnetic field which cancels the external field. This current flows in the characteristic penetration depth, λ . The Meissner effect implies there is a critical magnetic field, H_c beyond which the external field will penetrate the material and superconductivity is destroyed. At H_c the energy per unit

volume associated with preventing external field penetration equals the condensation energy:

$$\frac{H_c^2(T)}{8\pi} = f_n(T) - f_s(T), \quad (2.16)$$

where $f_n(T)$ and $f_s(T)$ are the Helmholtz free energies per unit volume of the normal and superconducting states respectively. For type I superconductors this is a first order transition. Such materials are generally pure single element materials, with a low T_c , long electron mean free path, l and $\lambda < \xi$. ξ is the coherence length measuring the average size of the electron pairs and the minimum length scale over which the superconducting wave function may change.

In type II materials a mixed state follows the Meissner state on increasing the external magnetic field, before reaching the normal state. A second order transition occurs, where singular magnetic flux quanta penetrate in the form of vortices, starting at H_{c1} . Superconductivity generally persists to higher magnetic fields than for type I materials, to the upper critical field, H_{c2} . Here λ is the size of circulating currents around the vortices and ξ the core diameter. Type II materials are alloys or dirty, short mean free path materials, where $\lambda > \xi$.

Superconductors in SIF junctions may be tested in a high magnetic field, to measure the polarisation of the ferromagnet (Section 2.1.4.1). As stated in Section 2.1.4.1, the superconducting electrode is generally aluminium, minimising spin orbit scattering, which increases according to Equation (2.17).

$$\text{Spin orbit scattering} \propto (Z)^4 \quad (2.17)$$

Where Z is the atomic mass. However, in its pure state aluminium is a type I superconductor and the bulk material only withstands the small field of 100 Oe. Thin films are dirty compared to the bulk material and are therefore type II superconductors. The increase of the critical field by decreasing the aluminium thickness is discussed in an excellent review by Meservey and Tedrow [Meservey, 1994], they found that 4 nm thick films should have $H_{c2} = 48000$ Oe. H_{c2} values are a direct result of film deposition

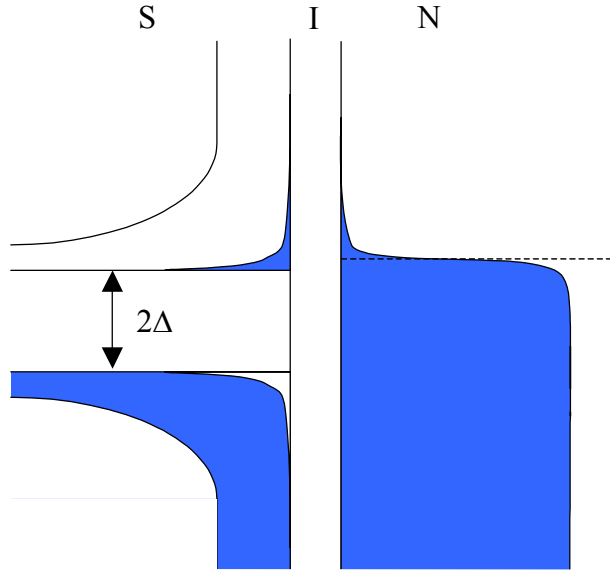


Figure 2.6: Semiconductor model of a SIF junction in zero magnetic field.

techniques and the aluminium thickness required for SIF junctions should be investigated experimentally.

2.1.3.1 The BCS density of states

In 1957 Bardeen, Cooper and Schrieffer produced an extremely successful electron pairing theory of superconductivity [Bardeen, 1957]. The fundamental concept is that of the Cooper pair, where weak interactions bind two electrons into a pair state. The Fermi sea of electrons is unstable to the formation of such a pair, producing a distribution of pair states, described by the Bardeen-Cooper-Schrieffer (BCS) density of states. They also predicted that in order to break the pair ground state into conducting quasiparticle excitations, some energy, 2Δ , must be exceeded where Δ is the energy gap. The BCS density of states, ρ_s , represented by Equation (2.18), is used throughout this analysis of superconducting tunnel junctions.

$$\rho_s = \begin{cases} \frac{\rho_s(0)|E|}{(E^2 - \Delta^2)^{1/2}} & |E| \geq \Delta \\ 0 & |E| < \Delta \end{cases} \quad (2.18)$$

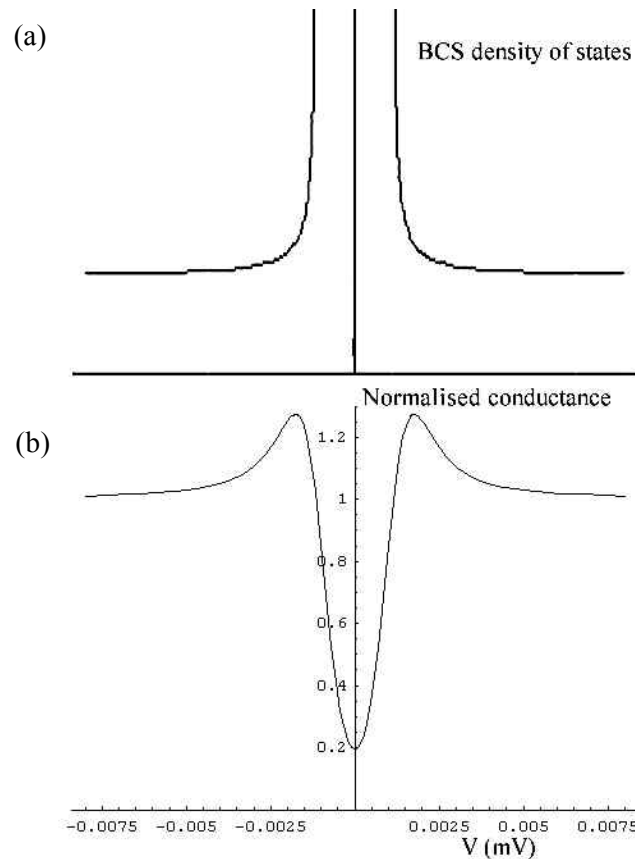


Figure 2.7: (a) The BCS density of states and (b) normalised conductance for an SIF junction in zero magnetic field.

Figure 2.7(a) illustrates the BCS density of states. A full treatment of BCS theory is beyond the scope of this thesis and the reader is advised to refer to one of the many standard texts for further information [e.g. Tinkham, 1996].

2.1.4 Superconductor-insulator-ferromagnet

In zero applied magnetic field, SIF devices behave as superconductor-insulator-normal metal (SIN) tunnel junctions. In this case, the conductance may be deduced from the results of Section 2.1.1.2 and a knowledge of the density of states of the superconductor, ρ_s . The semiconductor model is a convenient representation of a superconductor close to equilibrium and is shown in Figure 2.6. The band gap is twice the superconductor energy gap, Δ . For simplicity, it is assumed that the density of states of the ferromagnetic electrode is independent of energy, Equation (2.8), which represents the current flowing in a tunnel junction, may be rewritten:

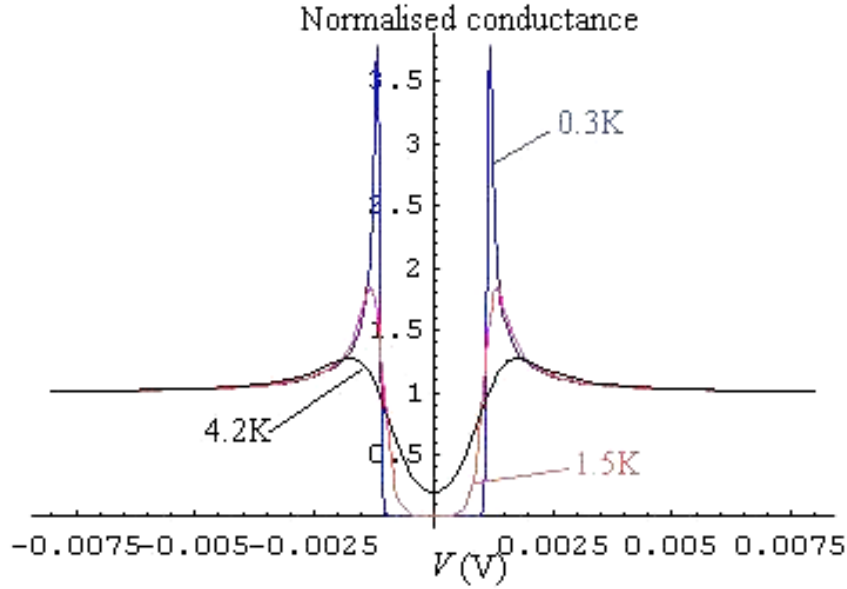


Figure 2.8: The effect of temperature on the normalised conductance of a SIF tunnel junction in zero magnetic field.

$$I_{SIF} = C_N \int_{-\infty}^{\infty} \rho_s(E) [f(E) - f(E + eV)] dE \quad (2.19)$$

C_N is the conductance of the junction when the superconductor is in its normal state, where its density of states, $\rho_s(0)$ is assumed to be independent of energy. BCS density of states is assumed to apply to the superconductor, as introduced in Section 2.1.3.1.

The normalised conductance of such junctions may be calculated using the Fermi functions of Equation (2.6) and differentiating (2.19) with respect to V :

$$\sigma(V) = \frac{\frac{dI_{SIF}}{dV}}{\frac{dI_{NIN}}{dV}} = \int_{-\infty}^{\infty} \rho_s(E) \left(\frac{\beta \exp(\beta(E + eV))}{(1 + \exp(\beta(E + eV)))^2} \right) dE, \quad (2.20)$$

where $\beta = 1/k_B T$ and I_{NIN} is the current in the normal state. Figure 2.7(b) illustrates the result of this integral, performed using Mathematica, at 4.2 K. When $|eV| < \Delta$ quasiparticle states are filled by thermal excitation, but current rapidly increases when $|eV|$ exceeds the energy gap. This corresponds to the BCS density of states shown in Figure 2.7(a). The current approaches a linear dependence on voltage well beyond the energy gap, this is the same as for NIN junctions in low bias (at high bias we see the

characteristic parabolic conductance). The density of states of real electrodes may be investigated using such conductance measurements.

We now consider the effect of temperature on SIF junction conductance in zero bias, as shown in Figure 2.8. It is clear that thermal excitation decreases as the temperature is reduced, leading to less ‘smearing’ of the conductance, i.e. lower zero bias conductance, steeper walls and a higher peak in conductance. Temperature also has a dramatic effect on junction leakage, represented by the ‘figure-of-merit’ (the conductance in the normal state divided by the conductance at zero bias.), which is discussed in Chapter 4.

2.1.4.1 SIF in a magnetic field

The treatment for SIF junctions in zero magnetic field, above, is identical to that for superconductor-insulator-normal metal junctions. However, in a large applied field, the conductance characteristics of SIF devices deviate from those of SIN devices. The polarisation of the ferromagnet can be deduced from the conductance against voltage curves of SIF junctions in a high magnetic field. Firstly, it is necessary to consider the effect of a magnetic field, H , on the superconductor. Aluminium is used to minimise the effect of spin orbit scattering, which increases according to Equation (2.17). H is applied in the plane of the junction. The quasiparticle energies are shifted by $\pm\mu_m H$ where μ_m is the absolute value of the magnetic moment of an electron. This leads to a modified BCS density of states:

$$\rho_s(E) = \rho_\uparrow(E) + \rho_\downarrow(E) = \frac{1}{2}[\rho_s(E + \mu_m H) + \rho_s(E - \mu_m H)], \quad (2.21)$$

where $\rho_\uparrow(E)$ and $\rho_\downarrow(E)$ are the density of states of the up and down spins respectively. The problem is simplified by assuming the barrier is perfect and that negligible scattering sites exist in the interface layer, therefore spin is conserved during tunneling. It is also assumed that the probability of tunneling is different for each spin state and these values are constant within the region of interest, about 10^{-3} eV of the Fermi energy. The normalised conductance should be a sum of the conductance in the independent spin directions, so Equation (2.20) leads to:

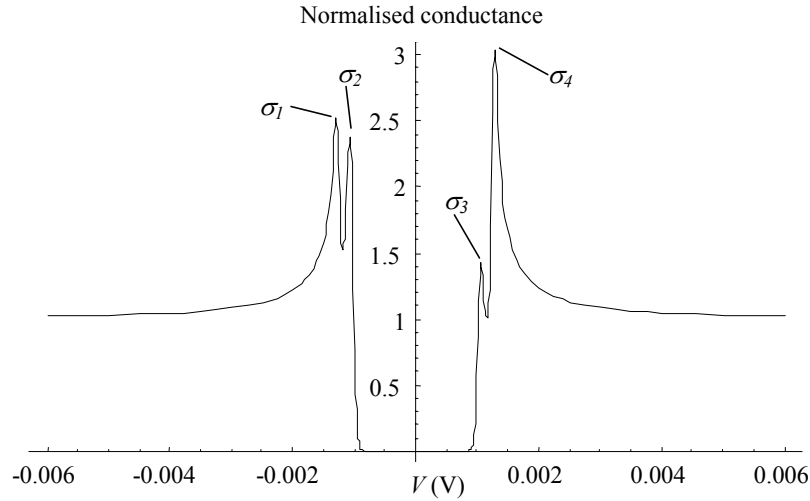


Figure 2.9: Conductance, normalized to the normal state conductance, as bias is increased for an SIF tunnel junction, polarisation 50% at 0.3 K in a magnetic field of 20000 Oe. σ_1 , σ_2 , σ_3 and σ_4 are measured at the peaks in conductance.

$$\begin{aligned} \sigma(V) = & \int_{-\infty}^{\infty} a \rho_s(E + \mu_m H) \left(\frac{\beta \exp(\beta(E + eV))}{(1 + \exp(\beta(E + eV)))^2} \right) dE \\ & + \int_{-\infty}^{\infty} (1-a) \rho_s(E - \mu_m H) \left(\frac{\beta \exp(\beta(E + eV))}{(1 + \exp(\beta(E + eV)))^2} \right) dE \end{aligned} \quad (2.22)$$

The difference in tunneling probability in the spin-up and spin-down directions is represented by a , the fraction of tunneling electrons whose magnetic moment is in the direction of the magnetic field (majority carriers). The polarisation of the ferromagnet, P , can therefore be defined as $P = 2a - 1$. The normalised conductance of an SIF junction is shown in Figure 2.9 and was calculated using a magnetic field of 20000 Oe, at 0.3 K to reduce thermal broadening. The conductances σ_1 , σ_2 , σ_3 and σ_4 are defined on the diagram and Equation (2.23) can be used to recover the polarisation of the ferromagnet [Meservey, 1994].

$$P = 2a - 1 = \frac{(\sigma_4 - \sigma_2) - (\sigma_1 - \sigma_3)}{(\sigma_4 - \sigma_2) + (\sigma_1 - \sigma_3)} \quad (2.23)$$

This technique has been used to measure the polarisation of the ferromagnets. Table 2.1 shows polarisation values from the literature, a range of values have been observed for each ferromagnetic material. This technique is sensitive to fabrication quality. In

particular, scattering sites in the barrier or interface can cause spin-flip and reduce measured polarisation. Additionally, certain problems are inherent in this method, that measurements take place at 0.4 K, 40000 Oe and low bias of a few mV. In a magnetic tunnel junction the relevant polarisation is at room temperature, or above in read heads, small magnetic field, <200 Oe, and at a bias of up to 200 mV. It is also not possible to determine the effect of the superconducting electrode on measured polarisation, as only aluminium is suitable due to spin orbit coupling. The practical problems of this technique are discussed in Chapter 4.

<i>Material</i>	<i>Polarisation by tunneling at 0.4 K (%)</i>	<i>Polarisation by field emission for crystal directions shown (%)</i>	<i>Polarisation by photoemission (%)</i>	<i>Polarisation by Andreev reflection (%)</i>
Fe	40 ⁱ , 44 ⁱⁱ , 37 ⁱⁱⁱ	(100): 25 ^v , (111): 20 ^v , (110): 5 ^v	54 ^{viii}	45 ^{xi} , 46 ^{xi} , 42 ^{xi}
Co	35 ⁱ , 33 ⁱⁱ , 35 ^{iv}		21 ^{viii}	42 ^{xi}
Ni	23 ⁱ , 11 ⁱⁱ , 8.5 ⁱⁱⁱ	13 ^{vi} , (100): 3 ^v , (110): 5 ^v	15 ^{viii} , 15.5 ^{ix}	46.5 ^{xi} , 43 ^{xi} , 44 ^{xi}
Gd	14 ⁱ	8 ^{vii}	5.5 ^x	
Ho	7.5 ⁱ			
Tb	6.5 ⁱ			
Er	5.5 ⁱ			
Dy	7.0 ⁱ			
Tm	2.7 ⁱ			
Co ₅₀ Fe ₅₀	47 ^{iv}			
Ni ₅₀ Fe ₅₀	45 ⁱⁱⁱ			
Ni ₈₄ Mn ₁₆	9.8 ⁱⁱⁱ			
Ni ₈₉ Ti ₁₁	3.6 ⁱⁱⁱ			
Ni ₆₈ Cu ₃₂	4.8 ⁱⁱⁱ			
Ni ₈₇ Cr ₁₃	0.9 ⁱⁱⁱ			

Table 2.1: Polarisation of the ferromagnets.

ⁱ [Meservey, 1994], ⁱⁱ [Meservey, 1974], ⁱⁱⁱ [Paraskevopoulos, 1977], ^{iv} [Mooodera, 1998], ^v [Landolt, 1978], ^{vi} [Gleich, 1971], ^{vii} [Hofmann, 1967], ^{viii} [Busch, 1971], ^{ix} [Banninger, 1970], ^x [Busch, 1969], ^{xi} [Soulén, 1998].

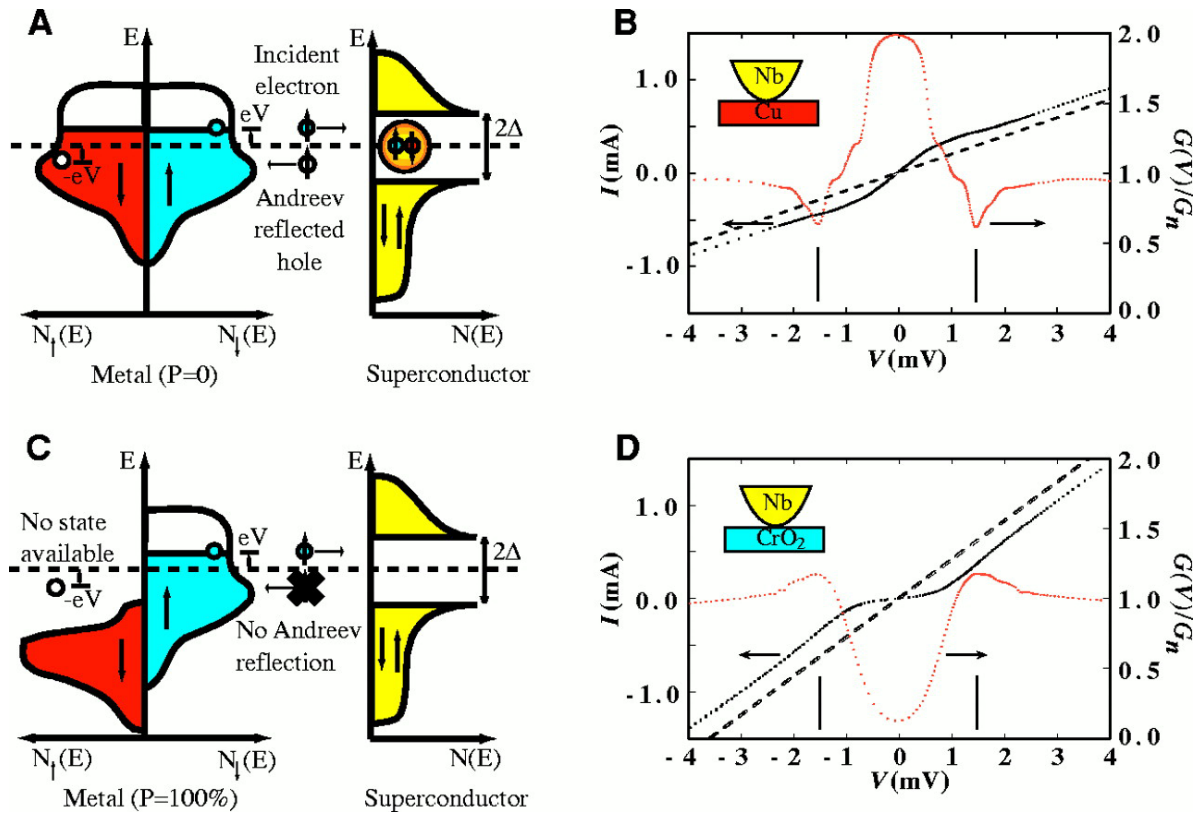


Figure 2.10: (A) Schematic when $P=0$, and Andreev reflection is unhindered by a minority spin population at the Fermi energy (E_F). Solid circles denote electrons and open circles holes. (B) Experimental measurement at $T=1.6\text{K}$, via a superconducting Nb contact on Cu. The dashed line is normal state Nb. (C) Schematic for $P=100\%$, when no supercurrent conversion occurs at the interface. (D) Experimental results for a Nb point contact on CrO_2 at 1.6K . The dashed line is for Nb in its normal state. [Soulen, 1998].

2.1.4.1.1 Alternative techniques for measuring polarisation

A large number of techniques have been suggested to measure the polarisation of ferromagnets. Meservey reviewed measurements taken by field emission, photoemission, electron capture spectroscopy, secondary electron emission, spin-polarised metastable-atom de-excitation spectroscopy and photodetection of injected electron spins [Meservey, 1994]. Recently, Andreev reflection has been used to measure the polarisation of ferromagnets [Soulen, 1998]. Measurements of the polarisation by Andreev reflection have been made via pinholes, as discussed in Section 4.1.2.1 [Akerman, 2000]. Table 2.1 displays some values from the literature.

Andreev reflection occurs at the conversion of normal current to superconducting current at a metallic interface. A superconducting point contact onto a ferromagnet allows the

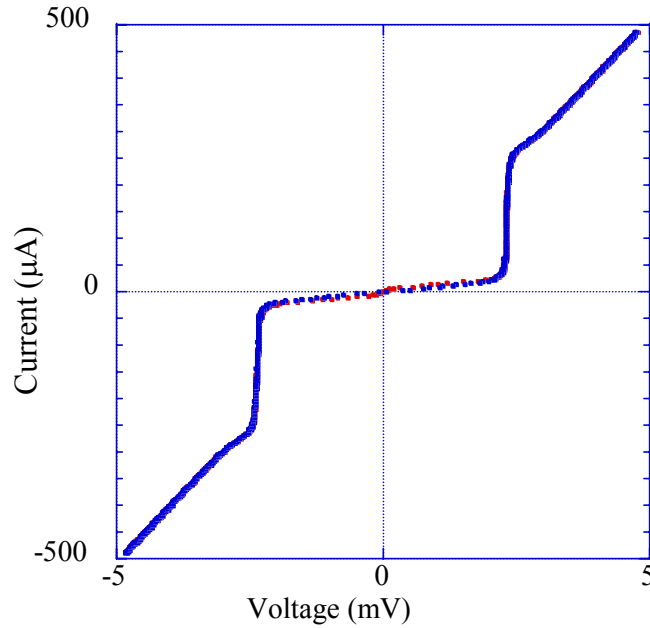


Figure 2.11: Typical SIS current-voltage characteristic.

estimation of polarisation without applying a magnetic field. Consider an electron approaching the interface, as shown in Figure 2.10(A). Electron pairs are required, so the metal donates an electron. However, a corresponding hole state is created, which moves away from the interface in the opposite direction to the electron. Therefore when the applied voltage is less than the energy gap, the conductance is doubled as compared to the normal state, as shown in Figure 2.10(B). A Cooper pair comprises of a spin-up and spin-down electron, obeying the Pauli exclusion principle. An incident spin-up electron requires a spin-down electron to be donated by the metal and a spin-up hole is Andreev reflected back into the metal. If the polarisation, P , is 100%, as shown in Figure 2.10(C), no minority spin carriers exist near the Fermi energy in the metal to provide the second electron for pairing. Andreev reflection is therefore prevented and only single particle excitations can conduct across the interface. Due to the energy gap, conductance is suppressed, as shown in Figure 2.10(D). The polarisation may be deduced from Equation (2.24), given the conductance at zero bias, $G_{v=0}$, and the conductance in the normal state, G_N [Soulen, 1998].

$$P = 1 - \frac{G_{v=0}}{2G_N} \quad (2.24)$$

2.1.5 Superconductor-insulator-superconductor

Consider superconductor-insulator-superconductor (SIS) junctions with identical metal electrodes, as fabricated during this work. Taking a BCS density of states for both electrodes (Section 2.1.3.1), the current flowing through the junction, I_{SIS} , on application of a potential, V , may be deduced from Equation (2.8):

$$I_{SIS} = C_N \int_{-\infty}^{\infty} \text{Re} \left\{ \frac{|E|}{\sqrt{E^2 - \Delta^2}} \right\} \text{Re} \left\{ \frac{|E + eV|}{\sqrt{(E + eV)^2 - \Delta^2}} \right\} [f(E) - f(E + eV)] dE, \quad (2.25)$$

where symbols have the same meaning as in Section 2.1.4. Typical current-voltage characteristics of a SIS junction are shown in Figure 2.11. When $|eV| < 2\Delta$, assuming no leakage through the barrier, transport occurs by thermally excited quasiparticles. At $|eV| \approx 2\Delta$ there is a rapid increase in current corresponding to the peak in the BCS density of states. For $|eV| \gg 2\Delta$, tunneling reverts to the behaviour of NIN junctions discussed in Section 2.1.2.

2.1.5.1 The Josephson effect

SIS junctions in zero bias voltage display a current, I , known as the Josephson current [Josephson, 1962]. The Josephson current is usually suppressed with a magnetic field for determination of junction quality, as discussed in Chapter 4, but is an important characteristic worth consideration. When two superconductors are separated by a weak link, such as the insulating barrier in SIS devices, the two wave functions couple to produce a constant phase difference, φ . Josephson deduced the results from BCS theory:

$$I = I_{Jc} \sin \varphi \quad \text{and} \quad \frac{d\varphi}{dt} = \frac{2e}{\hbar} V, \quad (2.26)$$

where I_{Jc} is the Josephson critical current of the junction and V is the voltage. A magnetic field in the barrier, \mathbf{B} , causes a modulation in the phase, given by Equation (2.27).

$$\nabla_{xy} \varphi = \frac{2ed}{\hbar} \mathbf{B} \times \mathbf{n}_z \quad (2.27)$$

Where \mathbf{n}_z is the unit vector normal to the plane of the junction and d is the magnetic thickness of the barrier:

$$d = 2\lambda_L + t, \quad (2.28)$$

t is the actual barrier thickness and λ_L the London penetration depth (as defined by the London theory equations) [London, 1935]. The application of such a magnetic field may be used to modulate I_{Jc} .

2.2 Magnetism

The aspects of magnetism of principal concern to ferromagnetic tunnel junctions and thin films of ferromagnetic metals are discussed in this section, beginning with an overview of some key concepts and the units of magnetism. Models of ferromagnetism are then considered, followed by electron spin polarisation, domains and, briefly, magnetic tunnel junctions. A detailed review of magnetic tunnel junctions is presented in Chapter 6.

2.2.1 Basic magnetism reviewed

A material's magnetic moment, susceptibility and magnetisation show its response to a magnetic field. The magnetic moment, \mathbf{m} , of a material is defined in terms of the torque $\boldsymbol{\tau}$ it experiences under the influence of a magnetic field and the magnetic induction, \mathbf{B} :

$$\boldsymbol{\tau} = \mathbf{m} \times \mathbf{B}. \quad (2.29)$$

The magnetisation, \mathbf{M} , of a material is its magnetic moment per unit volume. The susceptibility, χ , of a material is the ratio of the magnitude of the magnetisation to the magnetic field strength, \mathbf{H} , when the magnetisation and field are parallel. None of the above properties are constant for a material. Strongly magnetic materials have a high susceptibility.

The units of magnetism and notation are frequently confused and confusing. Here, Gaussian (CGS) units are used in accordance with the majority of literature on magnetic tunnel junctions. Table 2.2 shows the units and corresponding expressions for magnetism

in the SI (Sommerfeld) and Gaussian systems. A good review of magnetism can be found in Jiles [Jiles, 1996].

<i>Quantity</i>	<i>SI</i>	<i>CGS (Gaussian)</i>
Field, \mathbf{H}	A m ⁻¹	Oersted
Induction/Flux density, \mathbf{B}	Tesla	Gauss
Magnetisation, \mathbf{M}	A m ⁻¹	emu cc ⁻¹ or (gauss = 4 π M)
Flux, Φ	Weber	Maxwell
Field equation	$\mathbf{B}=\mu_0(\mathbf{H} + \mathbf{M})$	$\mathbf{B}=\mathbf{H} + 4\pi\mathbf{M}$
Energy of magnetisation, E, due to applied field, \mathbf{H} , in free space.	$E = -\mu_0 \int \mathbf{M} \cdot \mathbf{H} dv$	$E = -\int \mathbf{M} \cdot \mathbf{H} dv$

Table 2.2: Units of magnetism.

2.2.2 Ferromagnetism

Ferromagnetism arises when the magnetic moment of adjacent atoms or ions are strongly coupled in parallel. A spontaneous magnetic moment can exist in the absence of an external magnetic field. Three theories of ferromagnetism are considered. Firstly, the molecular field theory of ferromagnetism is useful in developing an understanding of this phenomenon. However, it does not describe the system well. The itinerant electron model will then be presented. Finally, the hybridisation of the s and d bands of ferromagnetic materials is discussed, this demonstrates aspects of both localisation and de-localisation.

2.2.2.1 Molecular field model of ferromagnetism

Weiss suggested the molecular field to describe ferromagnetism in 1907, since when it has been extensively developed [Weiss, 1907]. Spontaneous magnetisation in a material was speculated to be caused by a very strong molecular field, $H_{molecular}$, proportional to the magnetisation. The magnitude of this field may be estimated by equating the thermal energy to the molecular field energy at the Curie temperature, T_{Curie} . The Curie temperature is that at which ferromagnetic alignment is no longer favoured and the material becomes paramagnetic.

$$\mu_B H_{\text{molecular}} = kT_{\text{Curie}} \quad (2.30)$$

Where $\mu_B = \left(\frac{eh}{4\pi mc} \right)$ is one Bohr magneton, k is the Boltzmann constant, e the electronic charge, h is Planck's constant, c the speed of light and m the mass of an electron. This field is 6.4×10^6 Oe for iron, which is too large to be explained by magnetostatic fields from adjacent atoms, or ions in the case of a crystal. The spontaneous magnetisation, M_s , is described in terms of the maximum possible magnetisation, M_m and the maximum dipole moment of the atoms or ions, μ_m :

$$M_s = M_m B_J \left(\frac{\mu_m H}{kT} \right), \quad (2.31)$$

where B_J is the Brillouin function. In an applied field, H_a , the magnetic field acting on the spontaneous magnetisation, H , is given by:

$$H = H_a + \gamma M_s, \quad (2.32)$$

where γ is the molecular field constant and therefore γM_s is the molecular field. As shown above, the molecular field is much higher than a realistic applied field, so H_a may be neglected:

$$\frac{M_s}{M_m} = B_J \left(\frac{\mu_m \gamma M_s}{kT} \right). \quad (2.33)$$

The solution may be extracted using a graphical method or modelled numerically.

The molecular field theory is particularly successful in representing the variation of M_s/M_m with temperature. However, its key problem is that it predicts that the magnetic moments of the transition metal at low temperatures are integer multiples of the Bohr magneton (as shown in Table 2.3). The non-integer values observed cannot be explained by the molecular field theory.

<i>Ferromagnetic moment per atom</i>	<i>Fe</i>	<i>Co</i>	<i>Ni</i>
Molecular field model, assuming a Landé splitting factor of 2 and total angular momentum quantum number, $J = \frac{1}{2}$	1	1	1
Itinerant electron model	2.6	1.6	0.6
Experimental values	2.2	1.72	0.6

Table 2.3: Predicted and experimental values of ferromagnetic moment.

2.2.2.2 Itinerant electron model of ferromagnetism

The itinerant electron model for ferromagnetism, also known as the collective electron model, was initially developed by Stoner and Slater [Stoner 1933; Slater 1936]. They reasoned that electrons in unfilled shells, contributing to the magnetic moment, are usually outer electrons. These electrons are unlikely to be localised and instead they are conduction electrons in energy bands. Figure 2.12 shows schematic density of states (DOS) diagrams for the 3d bands of cobalt, nickel and iron. For comparison, the DOS calculated for nickel is shown in Figure 2.13 [Hodges, 1966]. The lower energy levels also form bands, but do not contribute to ferromagnetism, apart from 4s electrons. All states are filled up to the Fermi level, in accordance with the Pauli exclusion principle (neglecting thermal effects) and the number of states filled is equal to the area of the shaded region in Figure 2.12. The number of filled spin-up states is not equal to the number of spin-down states, leading to the polarisation of ferromagnets and consequently the magnetoresistance of ferromagnetic tunnel junctions. The bands are shifted by the electrostatic exchange interaction, which is caused by the overlap between electron wave functions.

Clearly, the complex band structure shown in Figure 2.13 is unlikely to produce integer values for the magnetic moment, m . If the number of 3d + 4s electrons is n and the number of 4s electrons per atom is x , then Equation (2.34) represents the magnetic moment.

$$m = [10 - (n - x)] \mu_B \quad (2.34)$$

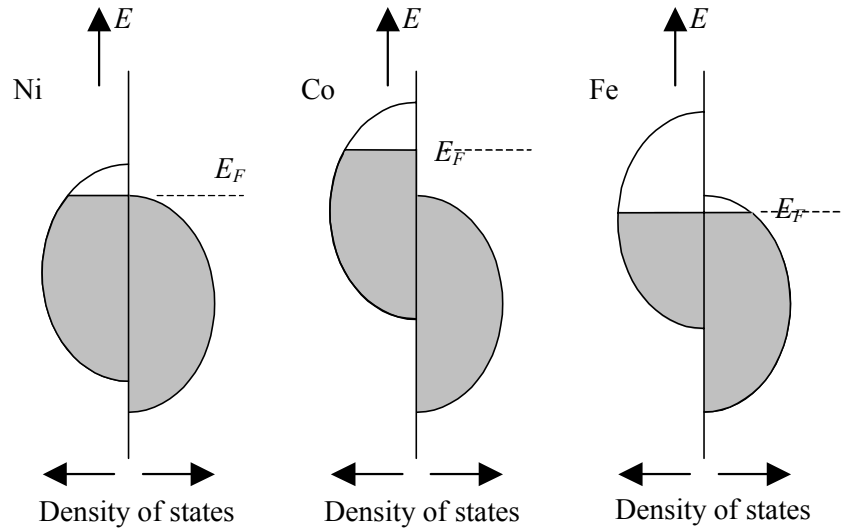


Figure 2.12: Schematic representations of the 3d bands of nickel, cobalt and iron. E is the energy and E_F the Fermi energy. Adapted from Comstock [Comstock, 1999]

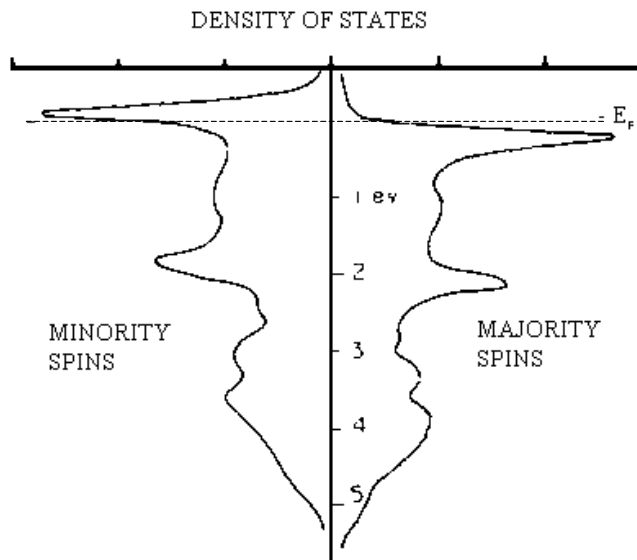


Figure 2.13: Calculated density of states of nickel [Hodges, 1966].

Experimentally, $x = 0.6$ for nickel. If it is assumed that x is constant, $m = (10.6 - n)\mu_B$, and the values shown in Table 2.3 can be derived. Agreement between theory and experiment is good, but significant problems arise in the prediction of polarisation.

2.2.2.2.1 Polarisation

The electron spin polarisation of a ferromagnet, P , is defined as:

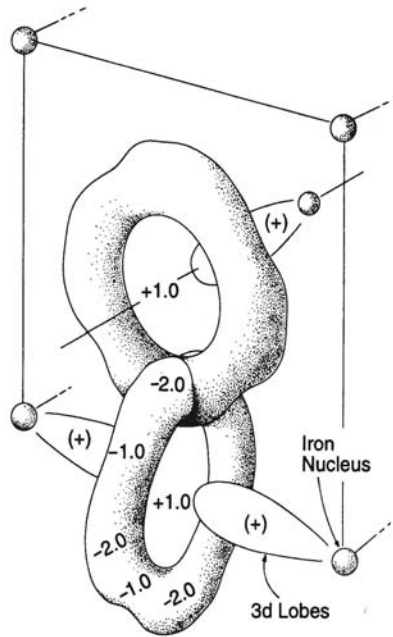


Figure 2.14: Magnetisation distribution in a unit cell of iron as determined by neutron scattering [Shull, 1966].

$$P = \frac{n_{\uparrow} - n_{\downarrow}}{n_{\uparrow} + n_{\downarrow}}, \quad (2.35)$$

where n_{\uparrow} is the number of spin-up electrons and n_{\downarrow} the number of spin-down electrons. Electrons close to the Fermi energy are expected to contribute to the tunneling current. Figure 2.13 shows the DOS of nickel, it is mismatched in the up and down spin directions at the Fermi energy so a polarisation is expected. The majority carrier at the Fermi energy is spin-down, however tunneling electrons are found to be mainly spin-up. For tunneling, in SIF and magnetic tunnel junctions, the spin polarisation and dominant spin direction are not explained by the itinerant electron theory of the d band. Figure 2.14 illustrates the distribution of magnetisation within an iron unit cell, [Shull, 1966]. The diagram shows some localisation and some itinerant behaviour, indicating that simple localisation and itinerant models cannot describe the electronic configuration. Hybridisation of the s and d bands is used to describe the system more accurately; the most commonly quoted model was suggested by Stearns [Stearns, 1977].

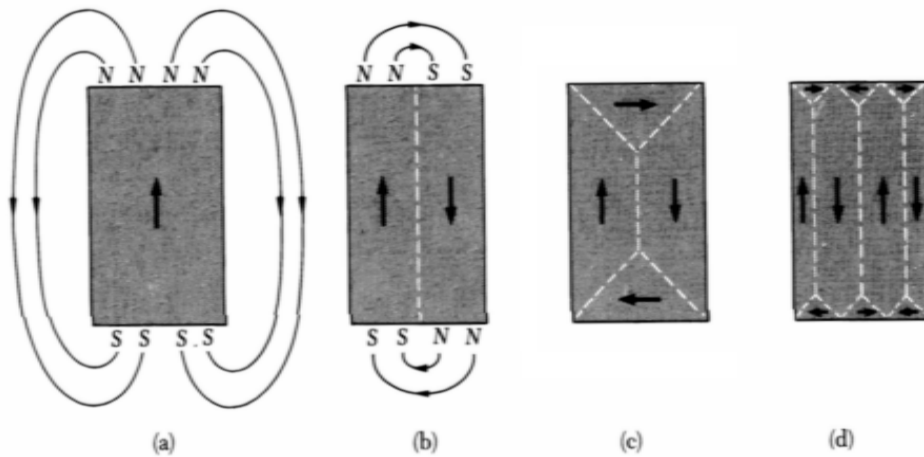


Figure 2.15: Simple domain structures. Adapted from [Kittel, 1996].

2.2.2.3 Domains

The above treatment of ferromagnetism suggests that such materials should always exhibit a net magnetisation, which is not observed. Weiss suggested that ferromagnets consist of a domain structure, where magnetisation is aligned within each domain but the magnetisation can be aligned differently in adjacent regions [Weiss, 1907]. Landau and Lifschitz showed that domains decrease the magnetic energy of the system [Landau, 1935]. The single domain structure of Figure 2.15(a) has high magnetic energy (defined in Table 2.2), due to the large spatial extent of the field outside the crystal. In Figure 2.15(b) the magnetic energy is reduced to approximately half the value in (a) by dividing the crystal into two domains pointing in opposite directions. The magnetic energy of the system is minimised in the presence of closure domains, shown in Figure 2.15(c) and (d). Domain structures can be very complicated, but minimise the magnetic energy of the system wherever possible.

In an applied magnetic field, the magnetic moment of the sample increases by means of three processes. At low field domain walls distort reversibly, increasing the volume of favourably aligned domains. In moderate field the volume of domains favourably aligned to the field increases at the expense of those unfavourably oriented by means of irreversible processes. Domain wall motion occurs. In strong fields, the domain magnetisation rotates towards the direction of the field.

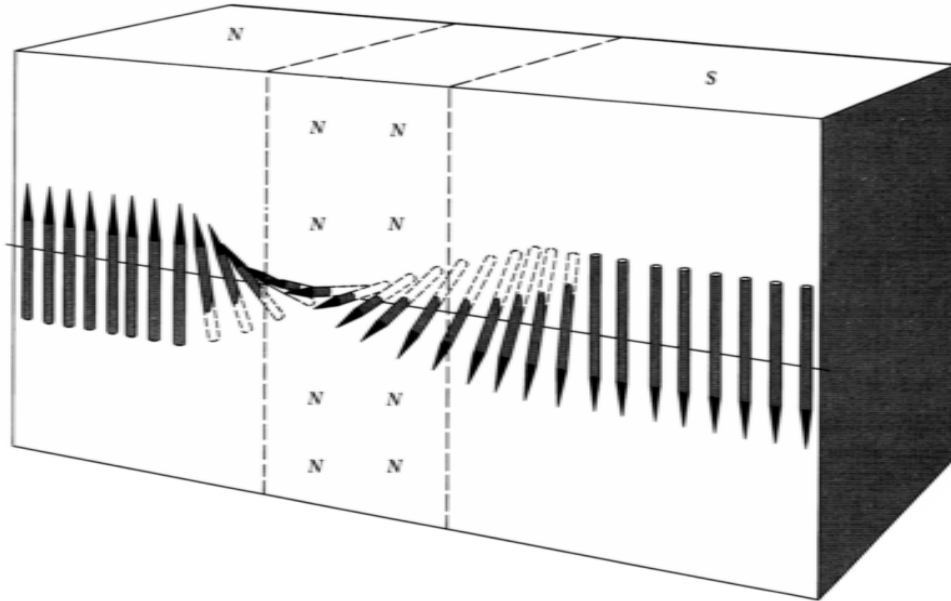


Figure 2.16: Magnetisation rotation in a Bloch wall between magnetic domains.
[Kittel, 1996]

Magnetisation does not jump discontinuously between domains, instead domain walls exist, over which the magnetisation gradually rotates. Figure 2.16 shows a 180° Bloch wall [Bloch, 1932]. The total angular displacement of magnetisation across a domain wall is often 90° or 180° in cubic crystals, as assumed below.

2.2.2.3.1 Exchange energy

The interaction between magnetic moments produces an exchange interaction, with energy, E_{ex} :

$$E_{ex} = -\mu_0 \mathbf{m} \cdot \mathbf{H}_e, \quad (2.36)$$

where \mathbf{H}_e is the interaction field and \mathbf{m} the magnetic moment. Considering nearest neighbours only (i and j), with interaction J , the exchange energy becomes:

$$E_{ex} = -\mu_0 z J \mathbf{m}_i \cdot \mathbf{m}_j, \quad (2.37)$$

where z is the number of nearest neighbours. For an angle, ϕ between magnetisations and approximating to small ϕ :

$$E_{ex} = -\mu_0 z J m^2 \cos \phi = \mu_0 z J m^2 \left(\frac{\phi^2}{2} - 1 \right). \quad (2.38)$$

If a total change of π (180° domain wall) occurs in N equal steps, over $N+1$ atoms and there are $1/a^2$ lines of atoms normal to the plane of the wall, where a is the lattice constant:

$$\sigma_{ex} = \frac{\mu_0 J m^2 \pi^2}{N a^2}, \quad (2.39)$$

where σ_{ex} is the exchange energy per unit area.

2.2.2.3.2 Anisotropy energy

The anisotropy energy, or magnetocrystalline energy, directs the magnetisation along certain crystallographic orientations, the directions of easy magnetisation. An anisotropy constant, K , is defined to represent the effect for specific crystallographic arrangements. The anisotropy energy per unit area, σ_a , is of the order of the anisotropy constant, K , times the thickness of the wall:

$$\sigma_a \approx K N a \quad (2.40)$$

2.2.2.3.3 Total energy

The total domain wall energy per unit area, σ_w , is the sum of the anisotropy and exchange contributions, given by Equations (2.39) and (2.40). Energy is minimised in the system leading to an expression for the number of atoms involved in the domain wall:

$$\frac{\partial \sigma_w}{\partial N} = 0 = -\frac{\pi^2 J m^2 \mu_0}{N^2 a^2} + K a$$

$$\therefore N = \sqrt{\frac{\pi^2 J m^2}{K a^3}} \quad (2.41)$$

2.2.2.3.4 Néel walls

Figure 2.17 shows that in thin films the magnetisation of Bloch walls is normal to the plane of the material, causing a high demagnetisation energy. However, magnetisation

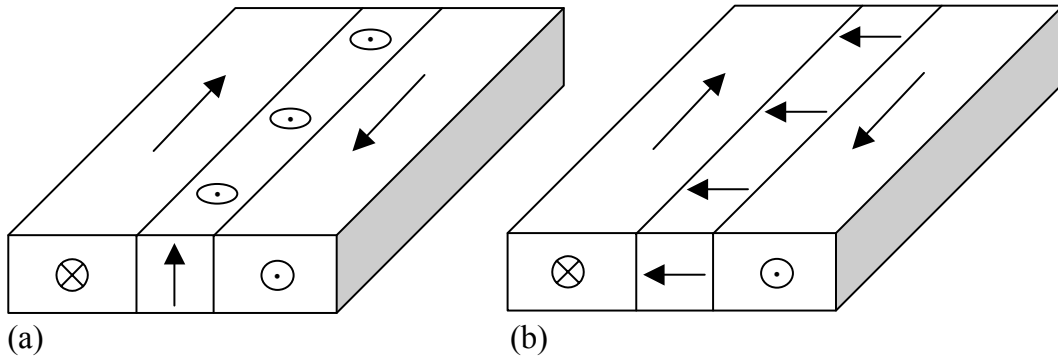


Figure 2.17: (a) Bloch domain wall (b) Néel wall. After [Jiles, 1998].

rotates in the plane for Néel walls. The demagnetisation energy in the Néel wall itself is high, therefore such domain walls are only formed in thin films, where the demagnetisation energy of the Bloch wall becomes larger than that in the Néel wall.

2.2.3 Magnetic tunnel junctions

The above introduction to tunneling and magnetism leads to the exciting phenomenon of large magnetoresistance (MR) in magnetic tunnel junctions. MR is defined in Equation (2.42), also termed the tunneling magnetoresistance, TMR.

$$\text{MR} = \frac{R_{\max} - R_{\min}}{R_{\min}} \quad (2.42)$$

Where R_{\max} is the maximum resistance and R_{\min} the minimum resistance recorded during a magnetic field sweep. A basic magnetic tunnel junction consists of two ferromagnets separated by an insulator. Firstly, in the absence of a magnetic field this device behaves in the same manner as the NIN junctions described in Section 2.1.2. In the presence of a magnetic field and in the absence of spin-flip events, spin is conserved during tunneling. Most of the electrons involved in tunneling originate from close to the Fermi level. An imbalance in the number electrons in majority and minority spin states occurs at the Fermi level (Section 2.2.2.2.1). Consider the situation illustrated by Figure 2.13, where the DOS for minority carriers is high and the DOS of majority states low at the Fermi level. When the magnetisation of the ferromagnets is parallel, minority electrons tunnel into vacant states of the minority band in the second electrode. The number of vacant states in the second electrode and the number of occupied states in the first electrode is

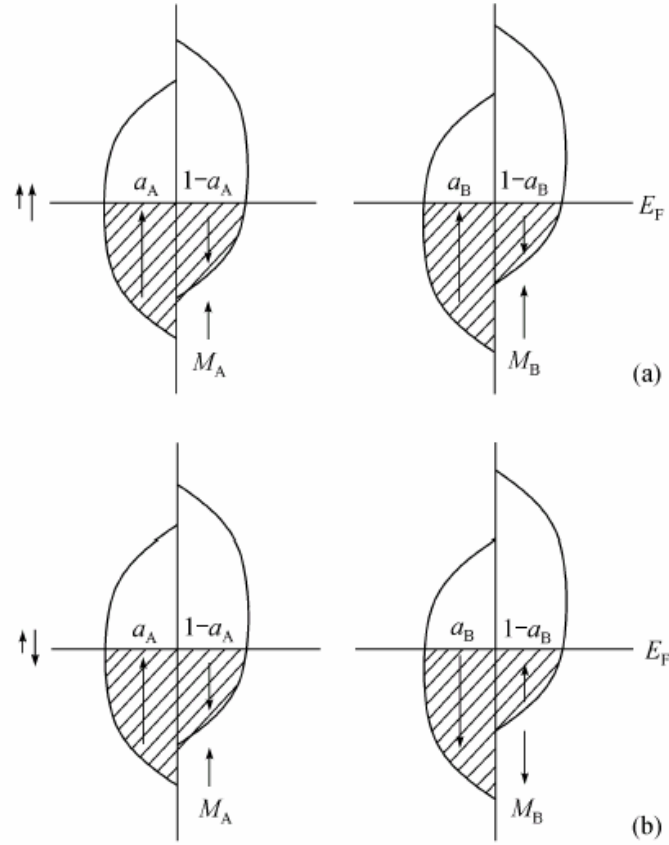


Figure 2.18: Band structures of two ferromagnets, magnetisations M_A and M_B respectively in a magnetic tunnel junction (a) parallel alignment of magnetisation (b) antiparallel magnetisation alignment. [Haili, 2001]

maximised, as is conductance. However, if the magnetisations are aligned antiparallel, electrons must tunnel between minority states (high DOS) in one electrode and majority states (low DOS) in the other, conductance is minimised. Jullière suggested this simple description to provide the basis for his model for the MR of tunnel junctions, [Jullière, 1975].

For parallel magnetisation alignment, as shown in Figure 2.18(a), the conductance, $G_{\uparrow\uparrow}$, can be expressed in terms of the fraction of spin-up electrons, in the materials on either side of the barrier a_A and a_B respectively:

$$G_{\uparrow\uparrow} = \alpha [a_A a_B + (1 - a_A)(1 - a_B)], \quad (2.43)$$

where α is a constant. If the magnetic moment of one of the magnetic layers is reversed, for example electrode B, the majority and minority bands interchange spins, as shown by Figure 2.18(b). The conductance is given by Equation (2.44).

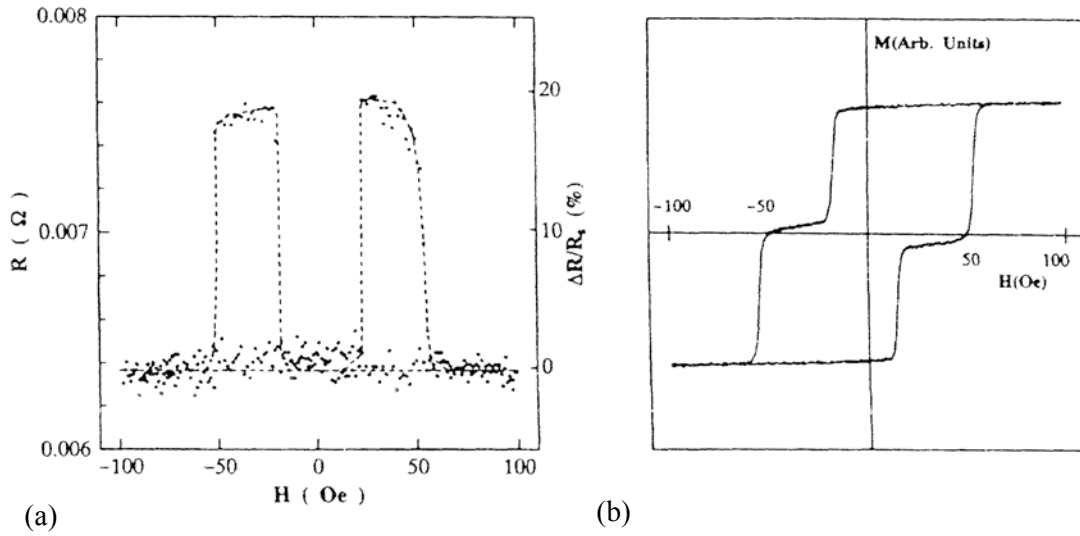


Figure 2.19: (a) Magnetoresistance of a tunnel junction and (b) corresponding hysteresis loop [Miyazaki, 1995].

$$G_{\uparrow\downarrow} = \alpha [a_A(1 - a_B) + a_B(1 - a_A)] \quad (2.44)$$

The difference in conductance ΔG between the parallel and antiparallel alignments is:

$$\Delta G = \alpha(2a_A - 1)(2a_B - 1) = \alpha P_A P_B, \quad (2.45)$$

where $P_A (= 2a_A - 1)$ is the polarisation in the first electrode and $P_B (= 2a_B - 1)$ is the polarisation in the second electrode. The TMR is then given by:

$$\frac{\Delta R}{R_{\uparrow\uparrow}} = \frac{G_{\uparrow\downarrow}^{-1} - G_{\uparrow\uparrow}^{-1}}{G_{\uparrow\uparrow}^{-1}} = \frac{2P_A P_B}{1 - P_A P_B}, \quad (2.46)$$

where ΔR is the difference in resistance between parallel and antiparallel alignment and $R_{\uparrow\uparrow}$ the resistance when the magnetisation in electrodes is parallel.

Hysteresis curves for magnetic tunnel junctions support Jullière's theory. A hysteresis curve and resistance plot for magnetic tunnel junctions is shown in Figure 2.19. The main changes in resistance correspond to the steps in the hysteresis curve. Resistance is minimised when the magnetisation of the two ferromagnetic layers is parallel, and is maximum for antiparallel alignment. The steps in the hysteresis loop suggest that the ferromagnetic layers are able to switch independently, with minimal coupling. Hysteresis

curves from magnetic tunnel junctions have been studied to investigate the mechanism of tunneling. A detailed review of magnetic tunnel junctions is presented in Chapter 6.

2.3 Summary

This chapter has introduced the concepts of tunnel junctions and magnetism required as a background to understand the experimental work of Chapters 4 and 6. The treatment of NIN devices in Section 2.1.2 is used in Chapter 4 to investigate the relationship between the normal and superconducting state characteristics of SIS and SIF devices. Magnetic tunnel junctions are considered in detail in Chapter 6, where an understanding of magnetism is essential. The knowledge of the theory presented in this chapter is assumed in Chapters 4 and 6 and where necessary, development of the basic theory is undertaken.

Chapter 3:

Experimental methods

“The thing with high-tech is that you always end up using scissors.”

- David Hockney (artist)

The principal experimental methods employed during the course of this work are introduced in this Chapter. However, Chapters 5 and 7 concentrate on the development of new experimental methods, to test read heads at high frequency and identify pinhole and weak-links in insulators, respectively. Fabrication techniques for devices are considered broadly in the order in which they were employed. In Section 3.1 substrate choice and cleaning methods are discussed. Deposition procedures and issues are then considered, followed by photoresist, lithography, ion milling, silica and contact pad deposition. A large number of devices have been produced over the course of the study. Specific depositions and mill times are discussed in the appropriate experimental chapters. Testing methods are then discussed in Section 3.4, starting with the analysis of thin films using the vibrating sample magnetometer (VSM) and the atomic force microscope (AFM). Device testing at low temperature is introduced in Section 3.4.2, followed by measurements in a magnetic field. Finally, nomenclature for deposition and device identification is discussed.

3.1 Substrate choice and preparation

Substrate choice is critical to the production of a good quality thin-film electronic device. The substrate should be a good insulator to avoid shorting-out high resistance devices during testing. It should also be extremely flat, have a high thermal conductivity, good stability and have good adhesion properties. Additionally, the choice is influenced by the cost and ease of handling during processing. Silicon wafers, with the surface oxidised to form SiO_2 are commonly employed as substrates, due to their favourable properties and price and were used almost exclusively during this work. The substrate consisted of 100 nm SiO_2 on 0.5 mm silicon and shall be referred to as oxidised silicon throughout this thesis. However, the earliest depositions of this work took place on r-plane sapphire, as previously used within the Device Materials Group.

Substrate preparation prior to deposition must produce clean, unscratched material of appropriate size for device production and testing. Firstly, photoresist was spun onto the wafer, to protect the surface from grease and scratching during dicing. The wafer was stuck onto a glass plate using hot wax and cut to 10×5 mm chips using a dicing saw. The

dicing saw blade was set to high rotation speed and advanced slowly, in order to prevent substrate chipping. The 10×5 mm samples were then removed and submerged in a beaker of acetone, which was agitated in an ultrasound bath for 1 hour. They were then airbrushed at close range with acetone and placed into a beaker of chloroform in the ultrasound bath for two hours, to remove grease deposits. The substrates were dried using an airgun and placed into an acetone beaker in the ultrasound bath for a further two hours. Finally, the silicon oxide chips were airbrushed with acetone and visually checked for drying marks or traces of dirt using an optical microscope. Dirty were cleaned gently using a cotton bud soaked in acetone and then airbrushed with acetone. This procedure was found to be highly effective in the production of very clean, regular substrates.

3.2 Deposition of thin films

DC magnetron sputter deposition, in an ultrahigh vacuum system was used throughout this work. Films were deposited as a whole wafer, without the use of lithography or shadow masks. Sputtering is a versatile and common technique for producing metallic thin films, due to its speed, range of possible deposition materials and homogeneity of deposits. The sputtering system and associated issues for the production of high quality tunnel junction films are discussed in this section.

3.2.1 Deposition system

The MkVII sputtering system used to deposit films is shown in Figure 3.1 and Figure 3.2. The schematic diagram shows the inner chamber, separated by a valve from the outer chamber, with liquid nitrogen jacket between the two. Sputtering takes place in the inner chamber and the chambers are cooled with liquid nitrogen. The purpose of this arrangement is to cool the chambers with liquid nitrogen during the final stage of evacuation. This cooling encourages absorption of molecules into the walls, thereby lowering the pressure. A rotary pump, followed by a turbomolecular pump, are used to evacuate the system. A needle valve connects the outer chamber to the gas reservoir, providing control of gas pressure in the system. Flowing argon gas was used during deposition, its pressure a combination of the needle valve and the gate valve settings.

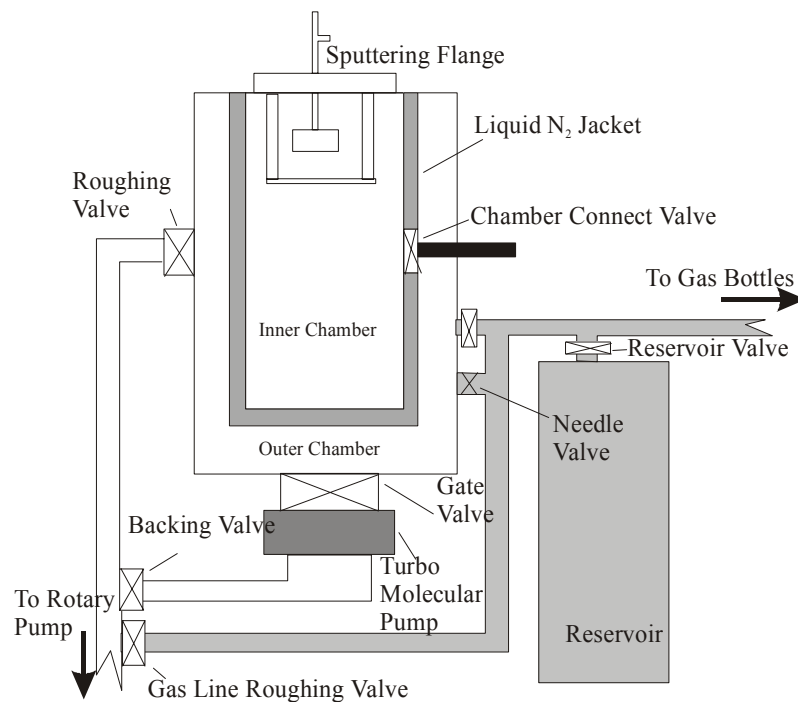


Figure 3.1: Schematic diagram of the MkVII sputtering system (courtesy of Dr G.Burnell).

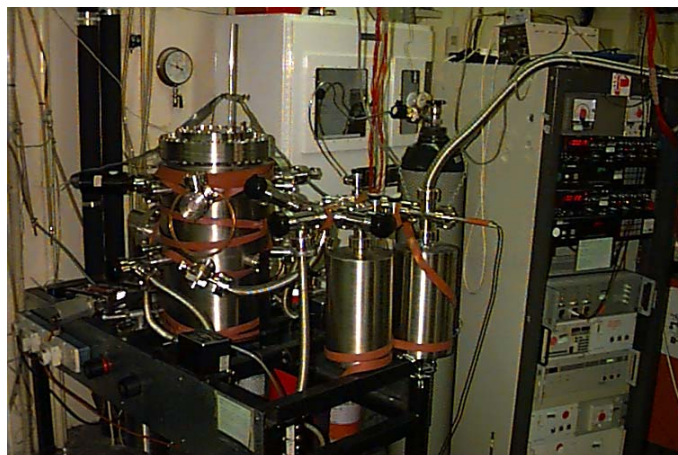


Figure 3.2: Picture of the MkVII sputtering system.

The flange consisted of four targets at 90° intervals separated by shielding, as shown in Figure 3.3. The targets used were high quality aluminium, cobalt, iron and niobium. The magnetron shields were made from the same material as the target. Prior to deposition the targets were cleaned with a copper wire brush. The aluminium target was then placed in an ultrasonic bath for 30 minutes, in a beaker containing approximately 0.1 M aqueous solution of NaOH. It was then rinsed with distilled water and dried with an air gun.

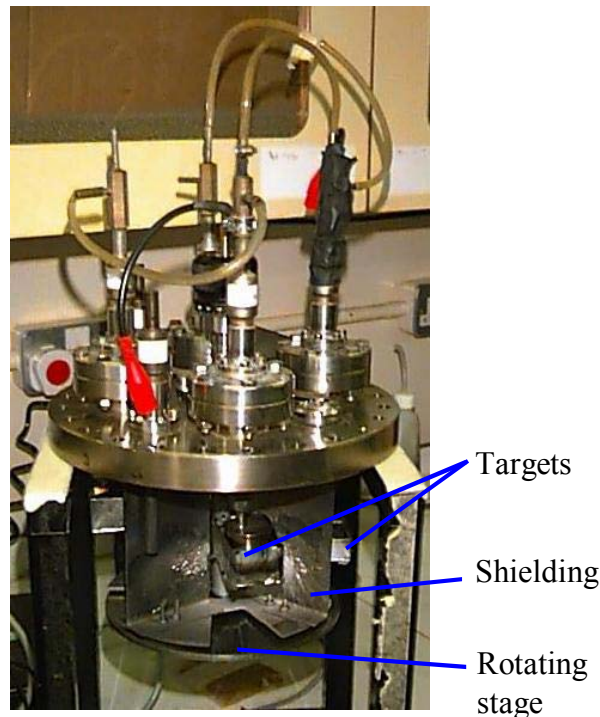


Figure 3.3: The 4-target flange.

Below the target, the substrates were placed in 20 mm wide grooves every 60° on an aluminium stage, radius 190 mm. This arrangement, in conjunction with the shielding, prevented simultaneous deposition by a target on two substrate positions. Depositions generally took place with a rotating stage. The thickness deposited was dictated by the sputtering power, rate of rotation and number of turns and was controlled by a stepper motor and computer. A stationary stage was used in the case of cobalt, the substrates lay directly below the target and thickness was controlled by the time and power. This highly flexible arrangement allowed the variation of thickness and multilayer structure during one run. Allowing for sufficient presputtering positions between substrates, up to three different junction types could be deposited in one run.

3.2.2 Evacuation of the system

The flange was bolted down onto the inner chamber, sealed with a copper gasket. The chambers were evacuated overnight with the turbomolecular pump. The chambers and gas reservoir were heated for 6 hours, to encourage out-gassing from the walls of the system and flange. In the morning the bolts holding the flange were tightened and the pressure checked with a mass spectrometer. The pressure was generally found to be

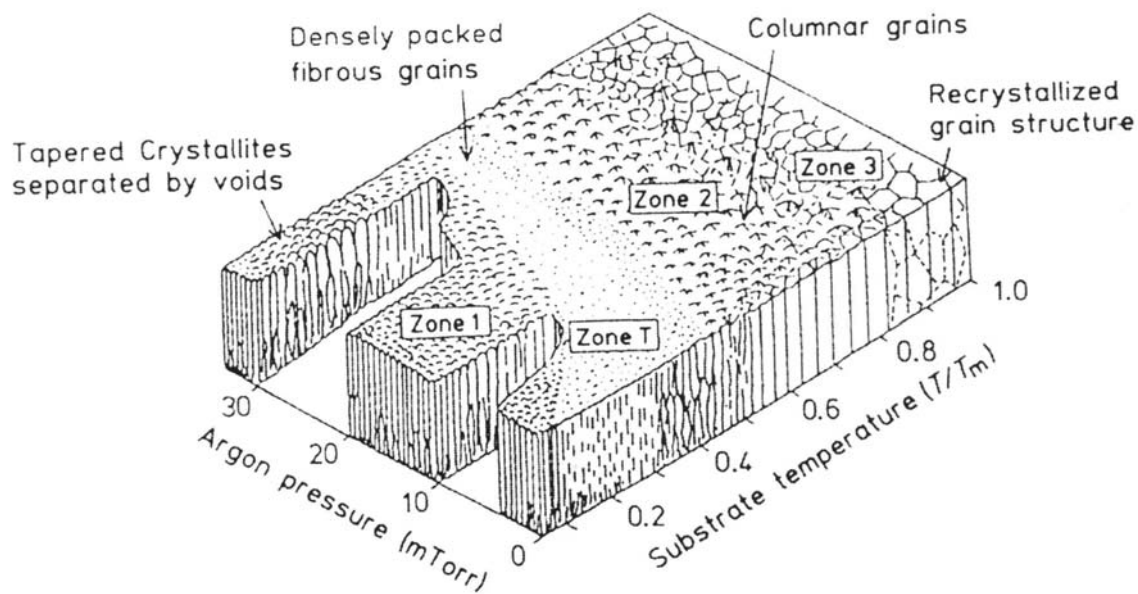


Figure 3.4: Thornton zone model of thin film deposition. T is the substrate temperature and T_m the melting point of the deposited metal. [Thornton, 1974].

approximately 5×10^{-8} mBar. The magnetron cooling water was then connected and the liquid nitrogen jacket filled. The system was pumped for a further 1.5-2 hours; the ultrahigh vacuum base pressure achieved was generally $\approx 2 \times 10^{-9}$ mBar.

3.2.3 Gas pressure

Argon gas pressure is an important sputtering parameter. The pressure must be high enough to maintain a glow discharge, but it also affects the stress and structure of the film. The Thornton zone model of film deposition provides useful insight into the effect of temperature and pressure on film structure, it is represented by Figure 3.4 [Thornton, 1974]. T is the substrate temperature and T_m the melting point of the deposited metal. Zone 1 consists of fibrous grains. Self-shadowing occurs due to the growth of cone shaped grains, voids exist between grains. Due to the low temperature, surface diffusion is insufficient to overcome shadowing. Zone 1 films have rough surfaces. Zone T, the transition zone, occurs at low pressure and higher temperature than Zone 1. Self-shadowing is significant due to the growth of cone shaped structures, but adatom mobility is sufficiently high to fill voids. Zone T structures have smooth surfaces. Zone 2 and 3 structures both consist of columnar grains which grow epitaxially.

Increased temperature encourages higher adatom mobility, bulk diffusion becomes significant in Zone 3.

Zone 2 and 3 structures are not expected in films deposited as described above, as no heating took place. Low gas pressure was used, to encourage Zone T film growth. However, it is possible to damage the barrier by the deposition of subsequent layers at low pressure, where incident atoms have high kinetic energy. The deposited material may impact the barrier with sufficient force to become embedded in the insulator. Damage was minimised by the deposition of a thin aluminium layer above the barrier. Aluminium is a light atom and therefore has low kinetic energy. High initial deposition pressure was generally also used for the top electrode, which was decreased after a short time.

3.2.4 Deposition rate calibration

A thickness monitor, initially used for deposition rate calibration was built by wrapping a band of aluminium foil around a substrate prior to deposition. The foil shadowed part of the substrate, enabling measurement of the film thickness with a profilometer. A thickness monitor was placed at each substrate position during multilayer deposition, for measurement in the event of stepper motor failure. Later, calibration took place by defining a series of parallel lines of resist on the substrate prior to deposition, using the techniques described in Section 3.3.2. Following lift-off, thickness was measured using the atomic force microscope (Section 3.4.2.1).

3.3 Processing

Standard cleanroom processing techniques were used to fabricate devices. An overview of the general route for fabrication of tunnel junctions is shown in Figure 3.5. This diagram shows that mesa junction devices are produced. The successful production of good quality devices depends on well-calibrated, reliable processes and equipment. Therefore, optimising the exact details of fabrication, modifying and developing equipment was a large part of this work.

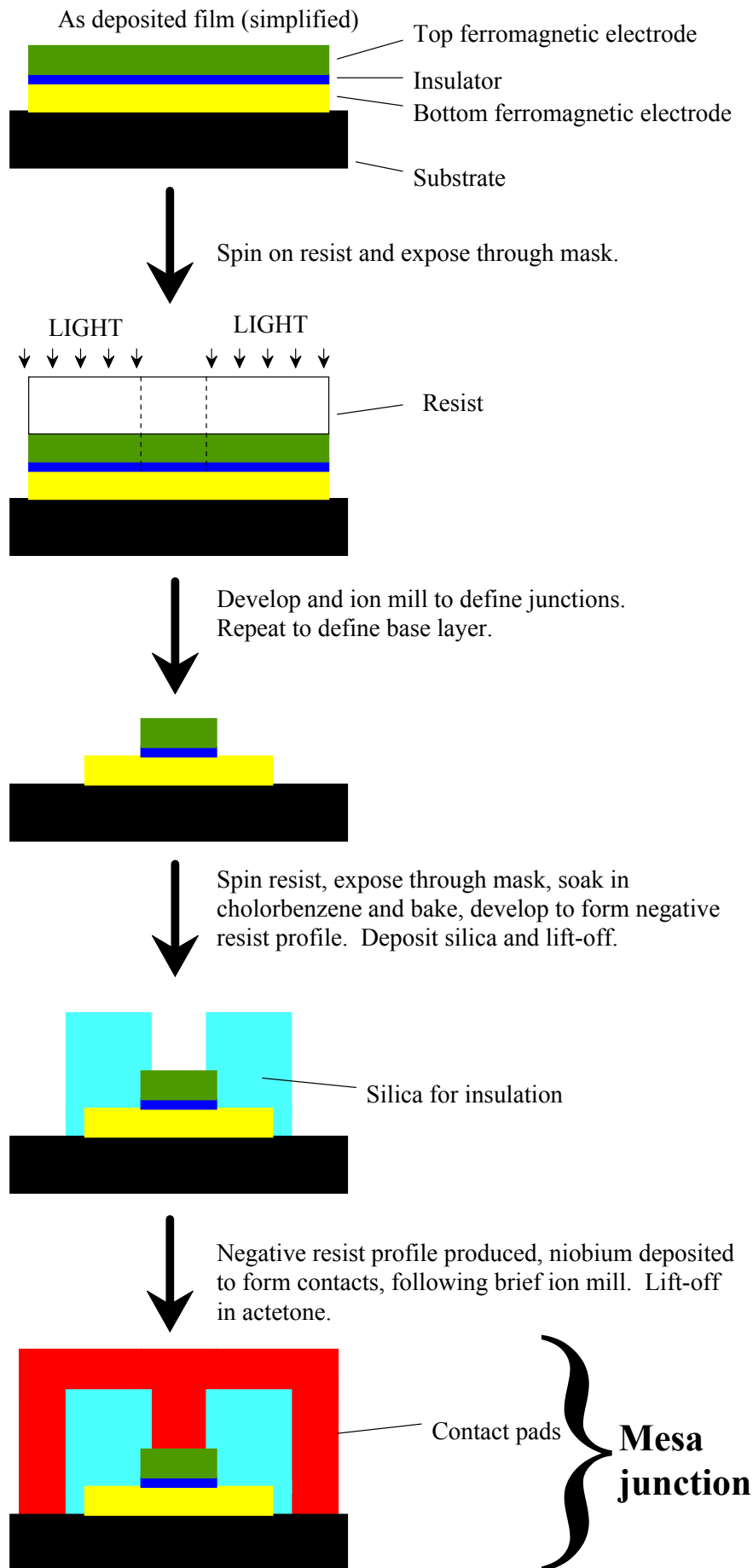


Figure 3.5: Schematic diagram of the process route.

3.3.1 Photoresist

AZ1529 photoresist was used throughout device production. It was spun on to films at 5000 rpm for 30 seconds. The films had been previously cleaned by airbrushing with acetone. Great care was taken to ensure good resist coverage and minimal defects, obtained by using clean films, resist spinner and chuck. Excess photoresist was wiped off the underside of the chip against a class 100 cleanroom wipe. The sample was then baked for 1 minute at 100°C in an oven placed on a hotplate.

3.3.2 Optical lithography

Optical lithography was undertaken on a Karl Süss contact printer, using chrome masks on glass substrate, made by CompugraphicsTM to the design of CAM30. This mask design is for simple mesa tunnel junctions, with common bottom electrode. Mesa junctions of dimensions 6×6 μm (2), 8×8 μm (4), 20×30 μm (2) and 50×100 μm (2) were produced, where the figures in brackets denote the number of junctions that size per chip. Pictures of part-fabricated devices, illustrating the mask design, are presented in Section 4.2.2.

3.3.2.1 Edge bead removal

As a consequence of spinning photoresist onto the chip, surface tension at the edges produces a thick bead of photoresist. This bead prevents flat contact to the mask, thereby reducing the resolution. The edge bead was removed by exposing a 4×9 mm mask, in close proximity to the substrate, for 40-50 seconds. Contact printing was not used as it often left traces of photoresist on the mask. The edge bead mask was usually aligned and exposed twice, removing as much excess photoresist as possible, according to the size of the final feature. Resolution is improved by removing all unnecessary photoresist. This is particularly useful for small features at the centre of the substrate e.g. mesa junctions.

The chip was developed by immersion and agitation in a solution of 80% AZ Developer, for approximately 30 seconds. Development time is critically dependent on the temperature, humidity and exposure. Cleanroom temperature and humidity was not controlled well, so immersion took place until the exposed resist was observed to disappear. The sample was then rinsed in a bath of distilled water, washed in running

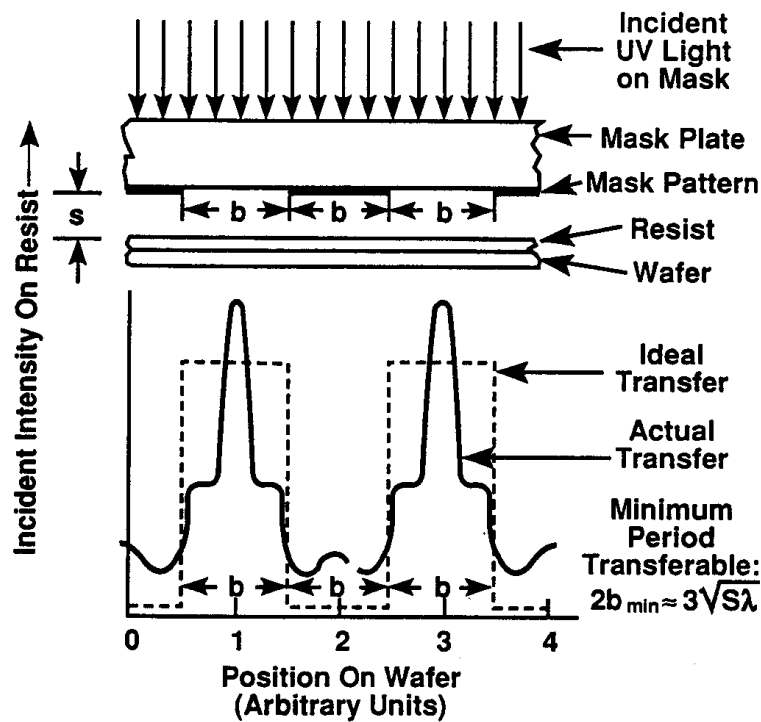


Figure 3.6: Schematic diagram of contact printing and the intensity of light diffracted by a mask. [Thompson, 1994]

distilled water to remove all traces of developer, and dried with an air gun. When a corner of edge bead remained after exposure, tweezers were used to remove it. Prolonged immersion in developer was avoided, to avoid excess thinning, swelling and distortion of patterns. To minimise the effect of swelling and to prevent wet photoresist sticking to the mask, the chips were baked at 100°C for 1 minute prior to further lithography.

3.3.2.2 Feature definition

Contact printing was used to define features on the chips, as it gives good resolution and minimises the effect of vibration. The contact printing system is represented schematically in Figure 3.6. In contact printing, the height above the mask, s , is zero. The resolution of a grating is limited by diffraction:

$$2b_{\text{minimum}} = 3\sqrt{\lambda\left(s + \frac{z}{2}\right)}, \quad (3.1)$$

where b is the period of the grating, λ is the wavelength of the light (≈ 400 nm) and z the photoresist thickness (≈ 1 μm) [Thompson, 1994]. Substituting the values into Equation (3.1): $b_{\text{minimum}} \approx 0.7$ μm . In practice the resolution is often limited by the uniformity of the resist coverage i.e. if the resist is not flat and good contact cannot be achieved, poor resolution will result. The thickness of AZ1529 resulting from spinning at 5000 rpm for 30 seconds was found to provide acceptable resolution for the features required. Minimum object size on the CAM30 mask is 4×4 μm , for silica insulation of the mesa junctions. Alignment was undertaken with great care and patience. The mask is designed for an alignment accuracy of better than ± 1 μm for the finest features. The definition of resist for silica deposition around the mesa junctions required the most accurate alignment, of 4 μm squares inside 6 μm squares. This requirement was relaxed by slight over development of the pattern, thus decreasing the resist feature size, with no adverse effect on device performance.

3.3.2.2.1 *Positive resist profile*

A positive resist profile is illustrated in Figure 3.7(a) and was used for lithography that did not require lift-off (mesa junction and base electrode definition). The resist was generally exposed for 7 seconds in the Karl Süss contact printer, followed by immersion in 80% developer solution. It was then rinsed in a distilled water bath and washed with running distilled water before being dried with an air gun. Development time was judged by observing the resist removal and was approximately 20-25 seconds.

3.3.2.2.2 *Negative resist profile for lift-off*

Lift-off is the process of depositing a film over patterned photoresist, then removing the photoresist to leave the desired device structure on the substrate. A negative resist profile, as shown in Figure 3.7(b), was used for steps requiring lift-off (silica and contact pad deposition). The negative gradient of resist edges shadows the corners of the substrate from deposition. It prevents tearing when the resist is removed and promotes acetone penetration.

The mask was exposed for 12 seconds in the Karl Süss contact printer. The chip was then soaked in chlorobenzene for 2.5 minutes, dried with an airgun and baked at 100°C for 1 minute. This process hardened the surface of the photoresist, increasing its

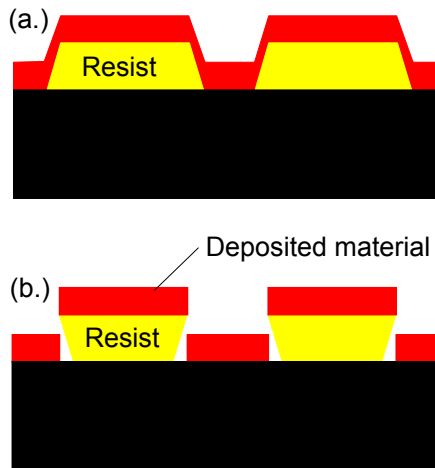


**Figure 3.7: (a.) Positive resist profile.
(b.) Negative resist profile.**

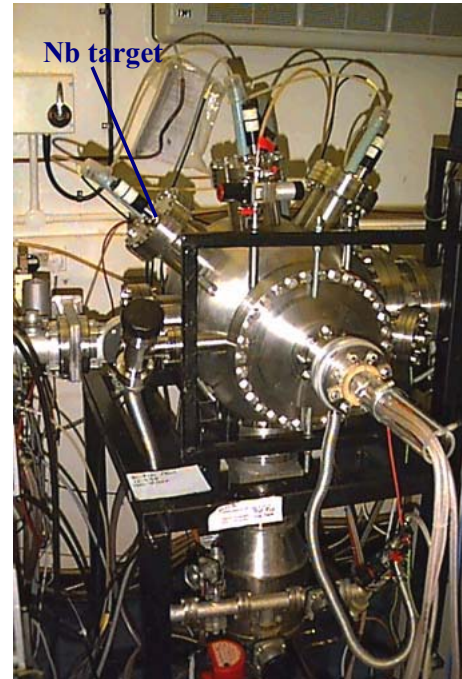


Figure 3.8: Ion milling and contact pad deposition system.

development time compared to that beneath the surface. This produced the desired profile, following the development process as described above in as above Section 3.3.2.2.2.

3.3.3 Ion milling

The ion milling system (Figure 3.6) with an 80% argon and 20% oxygen gas mixture was used to define film features. Ion milling was used as the ferromagnets cobalt and iron do not plasma-etch at a reasonable rate in CF_4 . Additionally, ion milling is a physical technique for etching materials and the roughly collimated beam of ions strike the surface vertically, producing no undercut beneath the resist. Undercut could reduce the size of the tunnel junctions to an unknown area, and may prevent satisfactory insulation around the junction during silica deposition. The disadvantages of ion milling are the lack of selectivity to materials (hence the rate must be well calibrated) and the redeposition of milled material on the sides of the junction which produces conducting shorts (Figure 3.9). To reduce the effect of redeposition, low ion milling pressure was used and the stage was angled at 15° to the normal incidence of ions. The stage was rotated throughout the ion mill. This angular ion mill was intended to clean the sides of the junction and

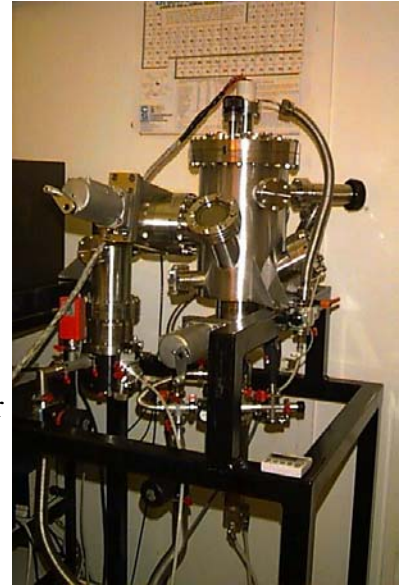
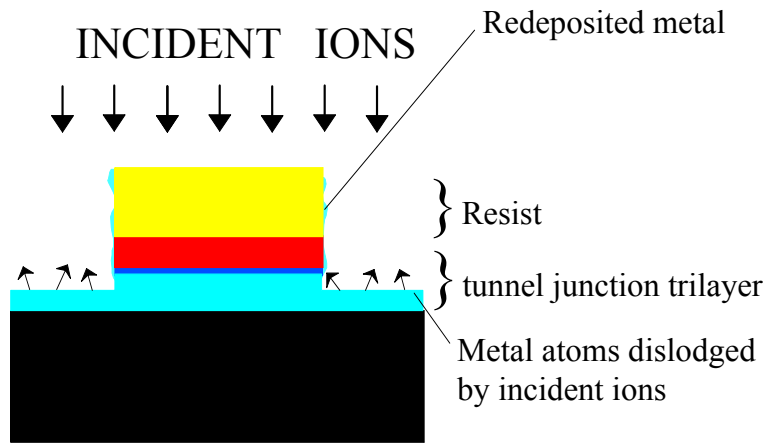


Figure 3.9: Redeposition of milled material.

Figure 3.10: The new milling system with load-lock.

proved to be highly effective in producing good quality tunnel junctions. However, the rotating stage was regularly unavailable. Ion milling with the stage at this position produced badly shorted junctions. This was improved by ion milling at normal incidence, followed by gentle chip cleaning with a cotton bud soaked in acetone. This treatment may have damaged some of the devices.

A new system (Figure 3.10) was available in the last few months of study. This system has a partial load-lock and turbomolecular pump. The pumping time has been reduced to 5 minutes, compared to a previous minimum of 1 hour. However, the mill rate varied by up to 50% between ion mills. This system was used to define the base electrode only, but not for junction definition. Rotation was powered by hand and the stage was fixed at normal incidence to the ions.

3.3.4 Silica deposition

The system used to deposit silica is shown in Figure 3.11 and was rebuilt by the author before it could be used for device fabrication. The system is far larger than required and the flange is sealed with a rubber gasket, despite which the pumping time to reach deposition pressure of approximately 5×10^{-5} mBar is 30 minutes. The chips were attached to a copper block using silver dag and inserted into the chamber. An AC power



Figure 3.11: The silica deposition system.

supply and tuner box were used to sputter the silica substrate in argon at 2.7 Pa for one minute, then at 3.2 Pa for the remainder of the deposition. Transmitted power, the difference between incident and reflected power, of 50 W was used throughout. The 30 minute deposition produced a silica film thickness of 360 ± 20 nm of silica (measured using the AFM).

Following deposition and unloading of the system, the chips were removed from the copper block by soaking in acetone. The deposited silica was found to be extremely robust and was removed by a 5 minute ultrasound bath in acetone, followed by airbrushing with acetone.

3.3.5 Contact pad deposition

Contact pads for the tunnel junction devices were made from niobium. This provided a superconducting wiring layer at 4.2 K, which minimised the effects of wiring layer and contact resistance. Niobium was deposited in the ion mill (Figure 3.6), using the indicated sputtering target. The advantage of depositing contact pads in a system which is fitted with an ion gun is the ability to pre-mill the substrate before deposition. During

processing a resistive top layer can form on the metals. This is attributed to an organic layer resulting from the photoresist and oxidation of the top layer. A large contact resistance may result, which is discussed in Chapter 4. However, a short mill prior to contact pad deposition, removes such unwanted layers.

The sample(s) were stuck to the stationary side of the stage with vacuum grease. This position is much closer to the targets than for normal ion milling and therefore increases the rate. The system was loaded, then evacuated overnight. In the morning, the liquid nitrogen trap of the diffusion pump was filled and the system pumped down for a further hour in order to produce good quality niobium. A base pressure of $\approx 5 \times 10^{-7}$ mBar was obtained and the T_c of thick niobium films was approximately 9 K. The chips were generally pre-milled at standard conditions in 80% Ar, 20% O₂ at normal incidence to the ion gun. Pure argon ion milling was unreliable. Ion mill times varied according to the milling rate and devices produced, but were in the range 15–45 seconds. Following evacuation for 20 minutes, niobium was sputter deposited at $\approx 3 \times 10^{-3}$ mBar. Niobium was deposited for 20 minutes, producing 820 ± 27 nm films. This thickness is ample to cover the 360 nm steps in the silica.

Lift-off took place in an acetone bath. The chips were soaked for up to one hour and the acetone agitated gently using a pipette. They were then dried with an air gun. Tweezers were used, under a binocular microscope, to remove niobium when it failed to lift-off from around the edges of the pattern.

3.4 Testing

A wide range of testing techniques have been used to obtain data for thin films and devices. This section outlines these methods and their practical limitations with relevance to this work.

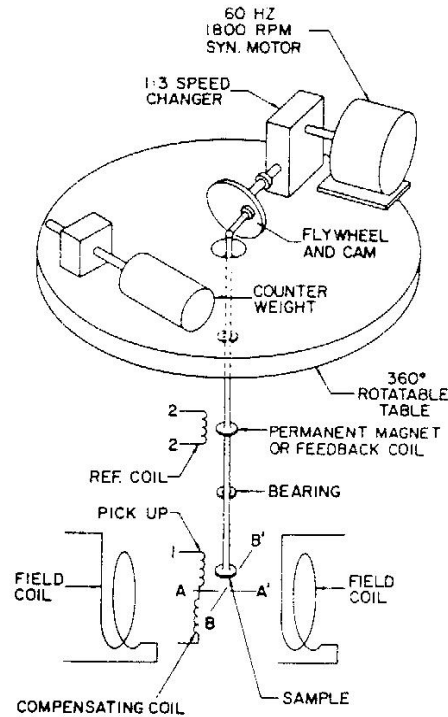


Figure 3.12: Schematic diagram of a vibrating sample magnetometer [Jiles, 1998].

3.4.1 Film characterisation

3.4.1.1 VSM

The magnetic properties of as-deposited films were investigated using a Kingston vibrating sample magnetometer (VSM). Figure 3.12 shows a simplified VSM. A VSM comprises of a field coil, to expose the sample to a variable magnetic field, and a sample holder, which is rapidly vibrated within the coil. The change in induction is recorded as the sample vibrates, giving a direct measurement of its magnetisation. The Kingston VSM has a sensitivity of 10^{-6} emu and is ideal for the investigation of thin films. However, due to the small thickness of magnetic material in a typical tunnel junction film, a reasonable signal is not be obtained for small features. Therefore the VSM may not be used to investigate fabricated devices.

The VSM was calibrated using a nickel sample of known magnetisation before use. The nickel sample is very small (500 μm square) and image charges on larger films are therefore not adequately calibrated. Film sample size tested in the VSM was usually

5×10 mm, image charges do influence such data. Additionally, samples placed with the long axis of the film transverse to the field direction are not entirely within the strongest field and magnetisation may not be fully measured. This problem was minimised by placing samples with their long axes in line with the magnetic field direction. Samples were not cut or patterned to a smaller size, in order to allow their processing into devices.

3.4.1.2 AFM

The topography of samples was investigated using a Digital Instruments Nanoscope III atomic force microscope (AFM) in tapping mode. The AFM is useful for investigating the roughness of films and assessing their quality. In tapping mode, the AFM probe is vibrated at constant frequency while the silicon cantilever scans across the surface. Atomic forces close to the sample cause the cantilever to deflect. This deflection is measured using a laser. The data may be reconstructed into a three dimensional image of a sample surface.

A film from each substrate position from every deposition was measured with the AFM to assess its surface quality. A particularly rough sample may indicate problems with substrate preparation or deposition. A large number of post-measurement analysis tools are available for the AFM, which were used with caution. For example, a data set must be flattened to return the surface from raw data. Flattening with different plane-fit or polynomial-fit order generally produces a slightly different image.

Roughness measurements are quoted in Chapters 6 and 7. Calculation of the roughness with the AFM was undertaken using the root mean square (RMS) function, providing the standard deviation of height measurements about the mean. This function does not correct for plane-fit or tilt, therefore measurements are affected by the flattening method employed. First order plane fit flattening was used throughout. Furthermore, roughness measurement depends on the area from which it is calculated and scale on which that data was collected. This results from the fact that the number of pixels, each of which represents a measurement point, is constant. A large sample area for roughness measurement does not record fine-scale variation. Roughness measurements were therefore a function of the area over which they were measured. A 1 µm square image was used throughout for roughness measurements, to provide consistency. This small

sample area also records short period variation in the height, which is expected to be significant for shadowing during deposition.

3.4.2 Device characterisation

3.4.2.1 AFM

The power of the AFM as an analysis tool was highlighted by its use to investigate the success of individual patterning steps. The AFM may be used in tapping mode without damaging devices, even when used to investigate the height of tunnel junctions. The processing of devices was therefore checked quickly, speeding up the development of techniques and calibration of ion mill and deposition rates. The particular advantage of measuring devices regularly was that equipment faults were rapidly diagnosed.

Two serious limitations exist for the use of the AFM to measure step heights of features. Firstly, the Nanoscope III software allows flattening by either plane fitting to a user defined area, or an algorithm based on the polynomial fitting of curves, usually line-by-line. Neither technique has been found to cope reliably with images incorporating large height steps. A good fit of one side of the step, producing a flat film, but severe curvature on the other side is often observed, this an artefact of flattening. In such situations the use of the in-built depth analysis tools, which compiles a histogram of the height of the sample, gives an incorrect step height. Instead, section analysis, a vertical cut through the image, was used to measure heights along the step and the results averaged. Even in this case the height is not easily defined, due to noise, roughness and curvature. These are reflected in error estimates. Secondly, AZ1529 photoresist was sometimes found to react with the surface of metals, forming thick deposits. Such layers could often be identified optically, as a darker pigment on the metal, which was found to occur more regularly for old photoresist. This problem was minimised by using the newest photoresist available and checking any large changes in ion mill rate.

3.4.2.2 Testing at 4.2 K

Prior to measurement, each chip was glued to a carrier using nail varnish. The chip carriers consisted of a printed circuit with copper back plate and either socket or plug to attach to the probe. The device contact pads were ultrasonically wire-bonded to the

circuit board contacts using 30 μm diameter aluminium wire. Measurements were made using the standard four-point technique. Samples were tested in the temperature range 4.2 - 300 K by dipping into liquid helium, using one of two probes and associated electronics.

3.4.2.2.1 Probes

The two dip probes used between 4.2 K and 300 K were very similar in design, both fitting into a 50 mm diameter dewar neck. Each probe has nineteen active signal lines and a thermometer. They are of low thermal mass and each have a heater attached below the sample holder, thereby providing temperature control. Coils may be attached to supply a moderate magnetic field, up to 300 Oe. The main practical difference between the two probes is that the older, made by Dr Wilfred Booij, is designed to accept a sample holder with 'D' plug connection, whilst the newer probe, made by Dr Philip McBrien, accepts 0.9" dual-in-line sockets.

3.4.2.2.2 Measurement electronics and control

The two probes described in Section 3.4.2.2 were used in conjunction with two different electronics systems, both designed by Dr Wilfred Booij. The older electronics system consists of a dual current supply and voltage amplifier. A National Instruments 12 bit LabPC 1200 analogue-to-digital converter was used and the signal processed with a LabVIEWTM programme, written by Dr Gavin Burnell.

The same LabVIEWTM programme as for the older electronics was also used to control measurement on the second probe. A low noise current source was driven by a National Instruments 16 bit analogue-to-digital I/O card, which also transferred measurements of current and amplified voltage to the computer. A diagram illustrating this measurement probe and electronics is shown in Figure 3.13.

3.4.2.3 Testing at 0.3 - 4.2 K

An Oxford Instruments HelioxTM He³ system was used to measure devices in the temperature range 0.3 - 4.2 K (Figure 3.14(a)). This probe fits into a 50 mm diameter liquid helium dewar neck. The older electronics and computer acquisition described in Section 3.4.2.2.2 were connected to perform measurements. The sample was mounted

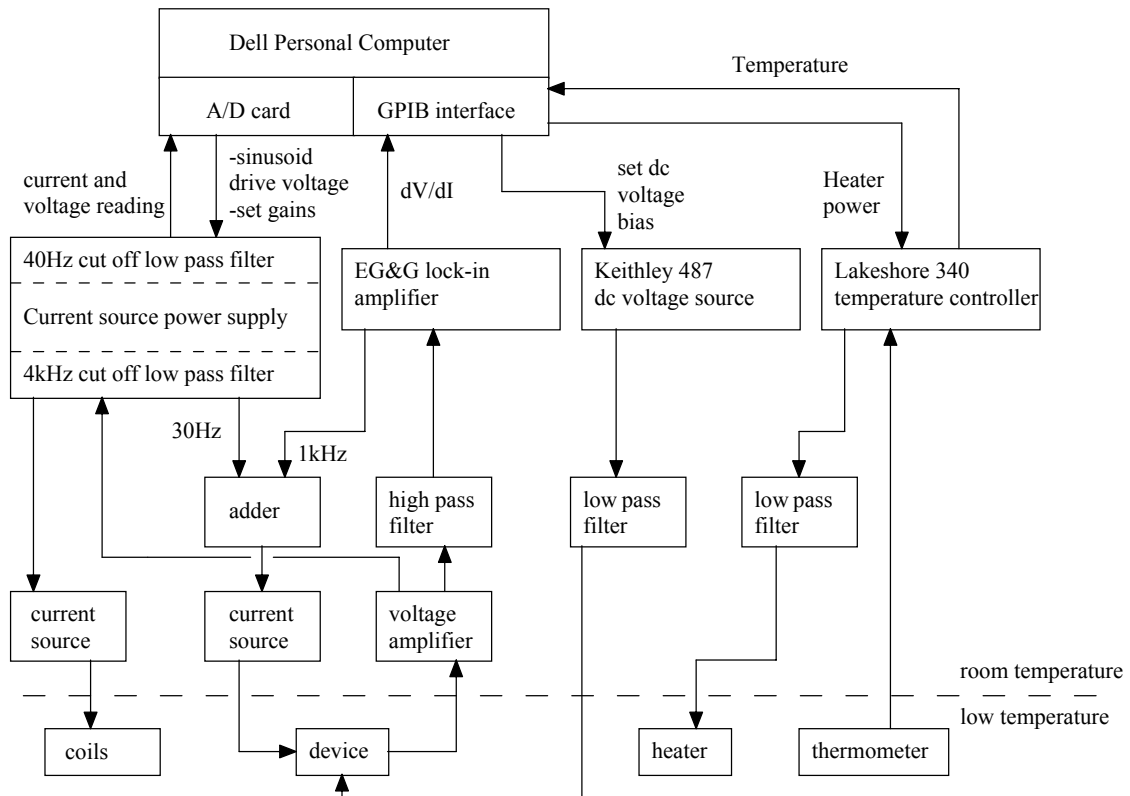


Figure 3.13: Block diagram of the ‘new’ 4.2 K testing apparatus (courtesy of Dr P. McBrien).

onto a 0.9” dual-in-line holder, although only 13 lines were available. The tailpiece was fitted and the sample space evacuated overnight using a small diffusion pump. In the morning, the tailpiece was cooled in liquid nitrogen for approximately one hour, before transferral to the liquid helium dewar, where it was cooled to 4.2 K. The temperature was further reduced to 1.5 K by filling the 1 K pot with He⁴, then pumping the pot with a rotary pump. At the same time, the He³ sorption charcoal was heated, so that it did not pump the He³. This caused the He³ to condense and run into the pot directly above the sample mount. Base temperature of 0.3 K was then obtained by switching the sorption charcoal heater off, allowing it to pump the He³. Temperatures in the range 0.3 - 1.5 K were obtained by heating the sorption charcoal to reduce its pumping efficiency.

3.4.2.3.1 20000 Oe magnet extension

A 20000 Oe Oxford Instruments magnet insert (Figure 3.14(b)) was driven by a computer controlled 50 A HP power supply. This was used to investigate the effect of magnetic field on superconductor-insulator-ferromagnet junctions. The additional length of the

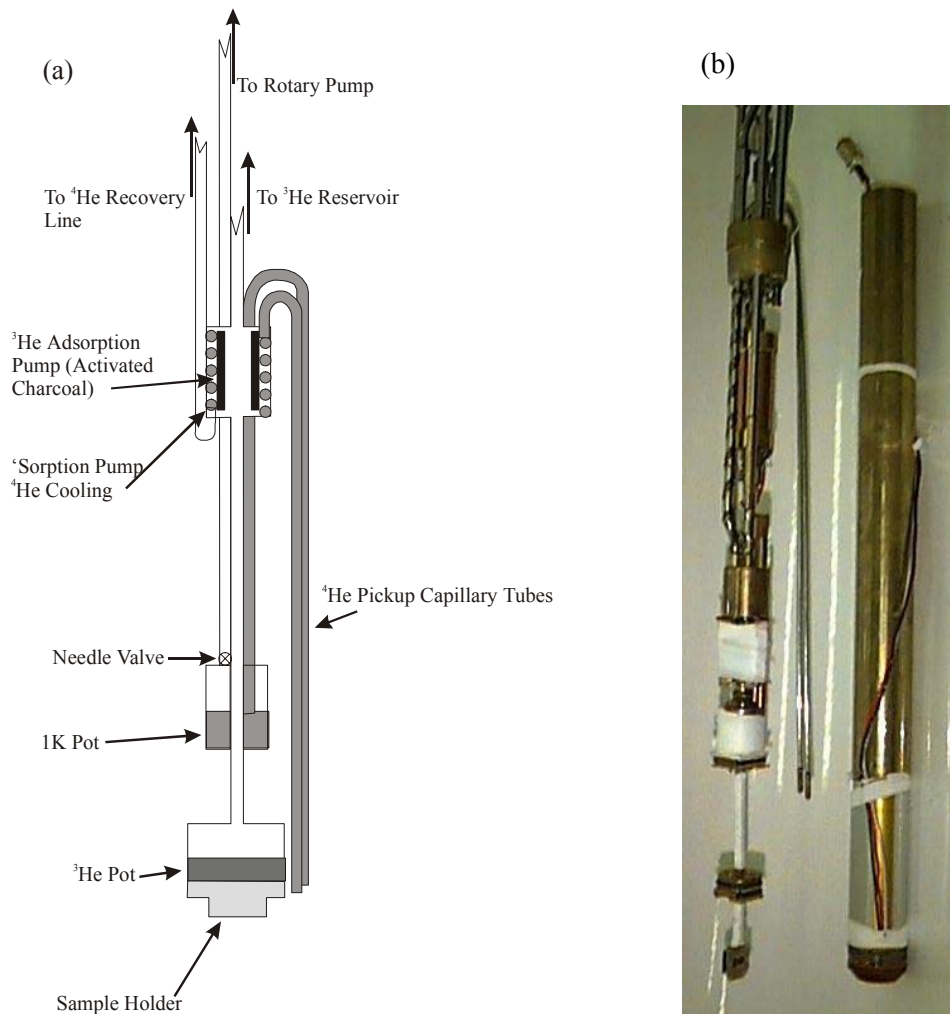


Figure 3.14: (a) Schematic diagram of the Oxford Instruments Heliox cryogenic probe. Picture courtesy of Dr G.Burnell.

(b) Heliox probe showing extensions (left) and Heliox 20000 Oe magnet tailpiece (right).

magnet necessitated extension pieces to hold the sample in the plane of the magnetic field (Figure 3.14). A 65 litre helium dewar was used to immerse the high-current magnet wiring.

3.4.2.4 Lock-in measurements

The parabolic nature of tunnelling conductance with applied voltage (Section 2.1.2) is difficult to observe for our low resistance junctions. It was therefore investigated using the newer electronics and a lock-in amplifier, which reduced noise by acting as a narrow band filter. An EG&G 5302 lock-in was used at signal amplitude of 5 mV and frequency of 1 kHz. Differential resistance was calculated using the LabVIEWTM programme.

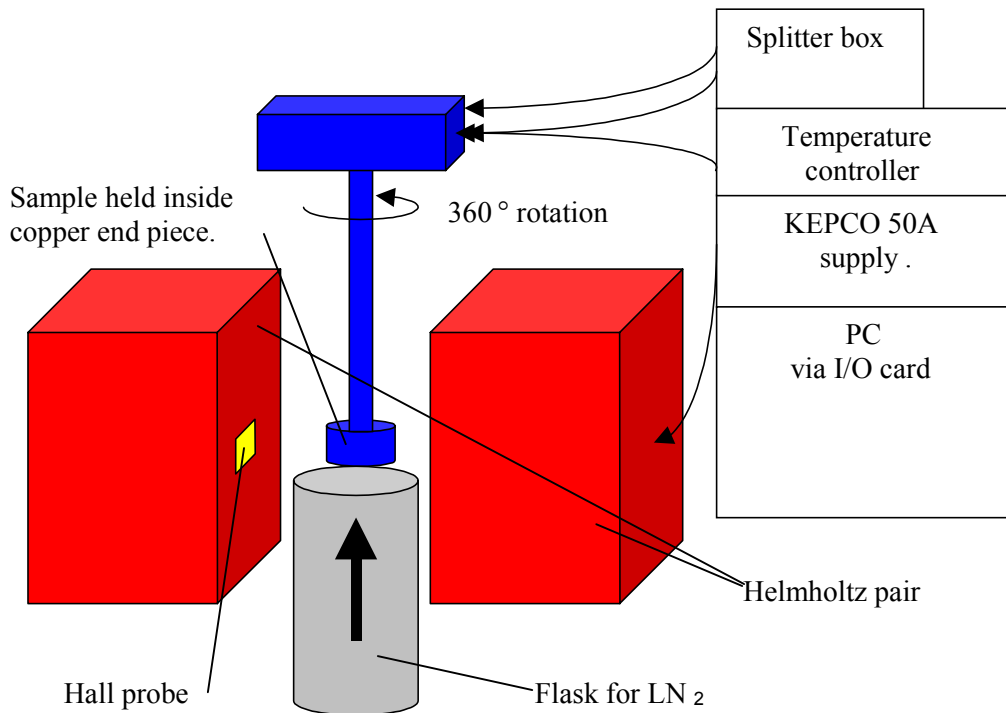


Figure 3.15: Schematic diagram of the magnetic testing apparatus.

3.4.2.5 Magnetic device testing

Magnetic properties of devices were investigated using four-point measurements in a magnetic field, provided by a Helmholtz pair (Figure 3.15). Chips were mounted and wire bonded as in Section 3.4.2.2, to the standard 0.9" direct-in-line socket sample holders. The probe is designed to allow 360° of rotation in the plane of the field. A Kepco power supply was used to achieve fields up to 3500 Oe. A LabVIEW™ programme, developed by Dr Gavin Burnell and Mr Neil Todd, was used to drive a current source and measure output from the voltage amplifier via a National Instruments 16 bit I/O card. The computer also controlled the Kepco power supply, reading the magnetic field with a hall probe which was mounted on the pole piece of one coil. A flask of liquid nitrogen could be introduced to cool the probe. A Lakeshore temperature controller was used in conjunction with a small heater and thermometer. These were mounted directly above the sample in the probe and measured temperatures in the range 77 – 300 K.

3.5 Nomenclature

Each deposition was assigned a unique identification number, using the sputtering database, in which conditions were also recorded. Six different angular positions were available on the rotating stage. Angular positions in which substrates were actually placed were numbered consecutively from one to six, unless deposition conditions were identical for all angles. For example, all substrates in the third position for deposition run 10445 are denoted 10445_3.

Chips were assigned an additional number, according to the order in which they were fabricated. The second fully fabricated chip from deposition 10445_3 is therefore denoted 10445_3_2. Tunnel junction fabrication produced ten devices along a common bar, labelled a to j. Sizes of the devices were $50 \times 100 \mu\text{m}$ (a and j), $20 \times 30 \mu\text{m}$ (b and i), $8 \times 8 \mu\text{m}$ (c, e, f and h) and $6 \times 6 \mu\text{m}$ (d and g). Continuing the above example, junction d is therefore assigned the unique code 10445_3_2d.

3.6 Summary

Experimental methods for the production and testing of magnetic tunnel junctions have been discussed in this chapter. Tunnel junctions require high quality fabrication, with well-calibrated processes. The identification of fabrication problems for superconductor-insulator-superconductor and superconductor-insulator-ferromagnet tunnel junctions is discussed in Chapter 4. Criteria to identify tunneling as the principal mechanism for conductance in normal metal-insulator-normal metal junctions are discussed.

The effect of deposition conditions on magnetic tunnel junction performance is discussed in Chapter 6. The insulating barrier is a key issue for high quality, low resistance magnetic tunnel junction fabrication. A new experimental technique to identify pinholes and weak-links in insulating films is developed in Chapter 7.

Chapter 4:

The use of SIS and SIF junctions to optimise device fabrication

Prediction is very difficult, especially about the future.

-Niels Bohr

The quality of magnetic tunnel junction device fabrication is not easily assessed. Measurements of resistance as a function of magnetic field demonstrate a good or bad magnetoresistance (MR), but give no indication of the source of problems in a non-optimal result. It is important to be able to identify reliable criteria for the assessment of device quality which are independent of MR. Many workers have found the fabrication of high MR magnetic tunnel junctions extremely difficult and have not been able to separate issues concerning the magnetic properties of the devices from simple processing problems. However, superconductor-insulator-superconductor (SIS) and superconductor-insulator-ferromagnet (SIF) tunnel junctions are well understood and their failure modes easily identified. Presented below is a practical approach to the optimisation of magnetic tunnel junction fabrication techniques using SIS and SIF junctions.

The fabrication of SIS junctions was optimised first, followed by SIF junctions. The effect of the material beneath and above the insulating barrier was observed by initially producing top electrode ferromagnet devices, and then bottom electrode ferromagnet devices. The fabrication of magnetic tunnel junctions was then possible with confidence in basic processes. Above T_C SIS and SIF devices behave as normal metal-insulator-normal metal (NIN) tunnel junctions. Techniques for assessing the quality of NIN tunnel junctions were investigated by comparing the figure-of-merit (Section 4.1.1) of SIS and SIF devices to their normal state characteristics.

4.1 Previous work

4.1.1 SIS junctions

Figure 4.1 illustrates the effect on the current-voltage characteristics of the two main failure modes associated with SIS junction fabrication. The schematics in Figure 4.1 represent idealised behaviour and real junctions are slightly less clear, but it is generally simple to identify the causes of poor junction behaviour. Contact resistance between the junction and wiring layer, discussed in Section 3.3.5, produces an increase in the observed energy gap and a non-vertical rise in the current as bias voltage approaches 2Δ . As discussed in Section 2.14, SIS junctions may be simply represented as perfect tunnel

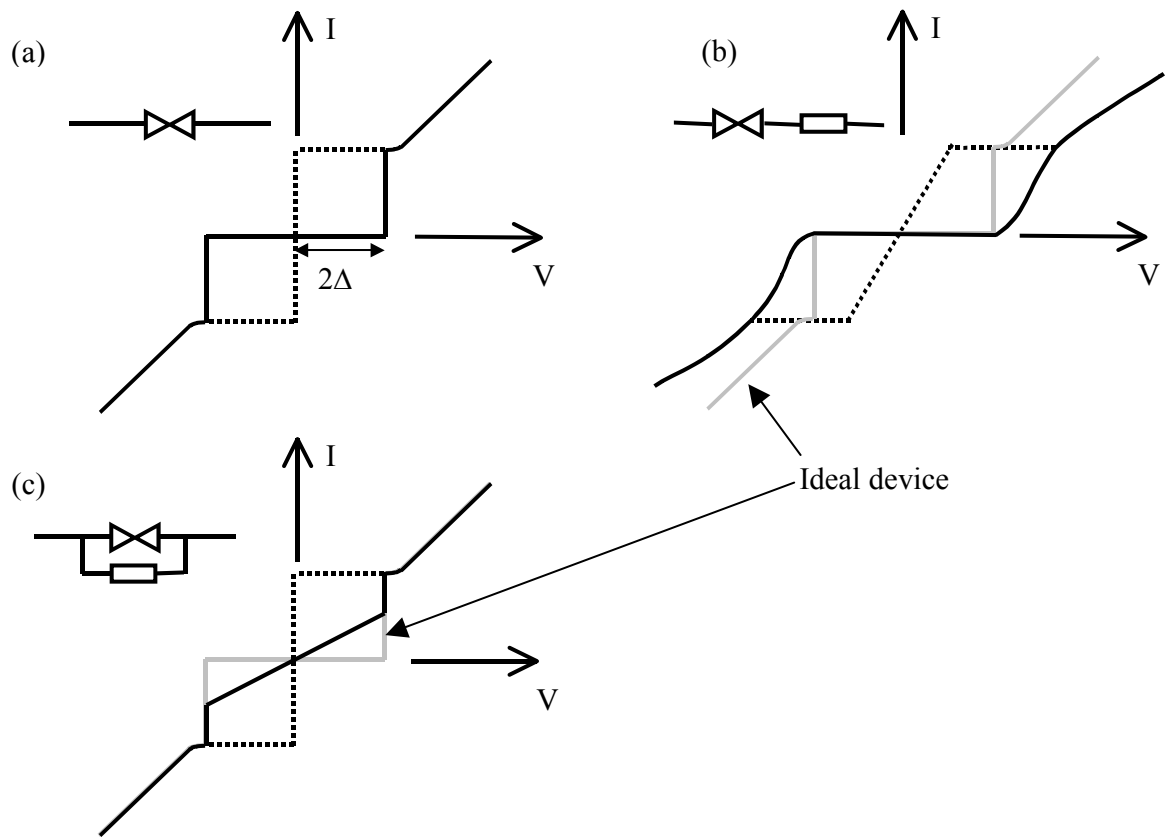


Figure 4.1: Schematics of SIS junction behaviour. (a) Perfect junction. (b) Resistance in series with junction. (c) Resistance in parallel with junction.

junctions having a BCS density of states in the electrodes. A real junction may be modelled as a circuit consisting of a perfect junction, parallel leakage resistance, R_L , and series contact resistance, R_C , as shown in Figure 4.2. The sub-gap current in a real junction at 4.2 K is often dominated by leakage and not thermal excitation. The ratio of the sub-gap resistance, R_S , to normal state resistance, R_N , is a convenient measure of junction quality, termed the figure-of-merit (FOM).

$$\text{Figure-of-merit} = \text{FOM} = \frac{R_S}{R_N} \quad (4.1)$$

An alternative measure of junction quality is the ratio of the current at the top of the gap edge ($eV > 2\Delta$) to the current just below the gap edge ($eV < 2\Delta$), the latter value is typically measured at a bias voltage of ~ 2 mV for niobium, where $2\Delta = 2.3$ meV.

Values of FOM commonly quoted in the literature for niobium electrode SIS junctions with aluminium oxide barrier at 4.2 K up to 40 [Blamire, 1988]. The figure-of-merit has

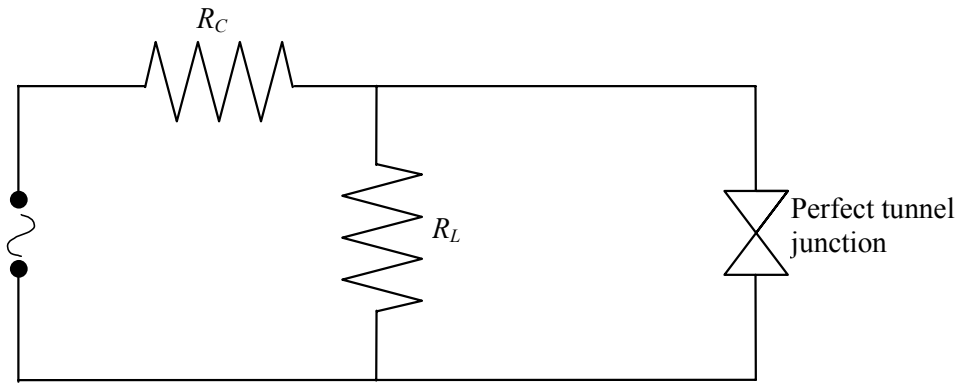


Figure 4.2: Circuit model of a real tunnel junction.

been developed as a measure of the leakage of SIS and SIF tunnel junctions by many authors. However, the correlation of such values with measurable quantities in the normal state have not been widely investigated. Superconducting tunnel junctions were fabricated regularly throughout the course of the study to test the fabrication route, particularly following equipment failure.

4.1.1.1 Fabrication of high quality SIS junctions

The production of high quality Nb/Al₂O₃/Nb SIS junctions is reviewed, with particular reference to previous work performed within the Device Materials Group in Cambridge. Pertinent issues are surveyed concerning the effect of available equipment and techniques on junction quality. The effectiveness of the barrier as a defect-free insulator has often been highlighted as the primary limit to tunnel junction quality. The Al₂O₃ barrier can be damaged by the incidence of high kinetic energy atoms or ions during the deposition of subsequent layers, as discussed in Section 3.2 [Goodchild, 1996; Gurvitch, 1983]. Goodchild *et al.* demonstrated the effect of decreasing the pressure of argon during niobium deposition above the barrier using the MkVII sputtering system discussed in Section 3.2. Figure 4.3 shows that the deposition of a 4-6 nm buffer layer of niobium at 6 Pa following barrier oxidation, significantly decreases sub-gap current compared with deposition at the ‘normal’ pressure of 1.3 Pa, increasing the FOM and the resistance-area product (RA). They go on to calculate the decrease in barrier thickness due to deposition induced damage using the oxygen pressure time product, on the basis of Equation (4.2) [Lehnert, 1992].

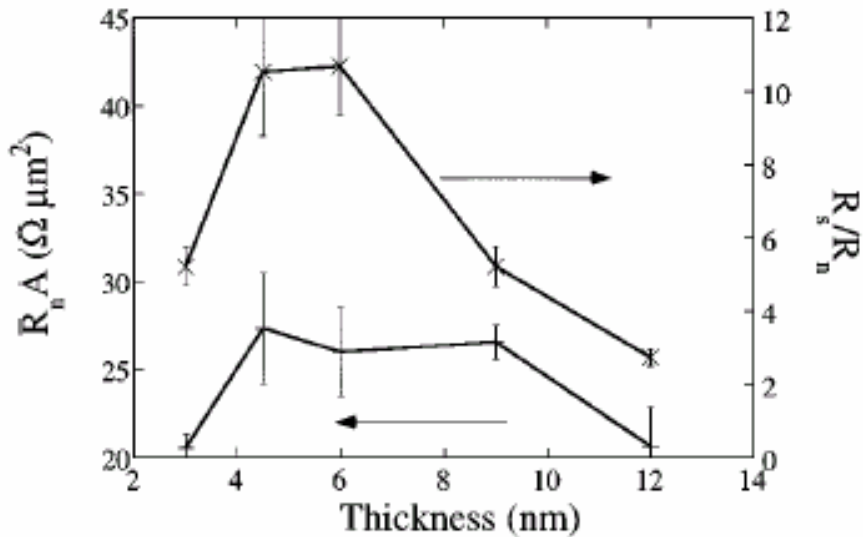


Figure 4.3: The effect of the thickness of niobium buffer layer deposited above the barrier on RA and FOM. [Goodchild, 1996]

$$\frac{R_2}{R_1} \approx \exp\left(\alpha\sqrt{\phi}\left(1-\frac{\phi}{2E_g}\right)\delta s\right) \quad (4.2)$$

Where $\frac{R_1}{R_2}$ is the ratio of the resistances, ϕ the barrier height, E_g is the energy gap of the insulating barrier and δs the difference in barrier thickness. They estimated $\delta s = 0.5 \text{ \AA}$, by assuming $\phi = 2 \text{ eV}$ and $E_g = 4 \text{ eV}$. Considering calculations in Section 4.3.1.3, below, estimating the barrier height and thickness using Simmons theory, this value should be considered an aid to thought, not an accurate prediction of thickness changes. Gurvitch *et al.* suggested an alternative solution to reducing barrier damage, by the inclusion of a thin aluminium buffer layer above the barrier [Gurvitch, 1983]. The proximity effect in the Nb-Al bilayer may result in a suppression of measured Δ [Golubov, 1988]. Gurvitch *et al.* did not note any decrease of Δ for aluminium thickness up to 3 nm.

4.1.1.1.1 Anodisation

The tunnel junction area can be defined by the selective niobium anodisation process (SNAP) [Kroger, 1981]. Devices may either be defined entirely by anodisation or by either etching or ion milling to form mesas, followed by anodisation around the edges. Kroger used a solution of ammonium pentaborate (156 g), ethylene glycol (1120 ml) and

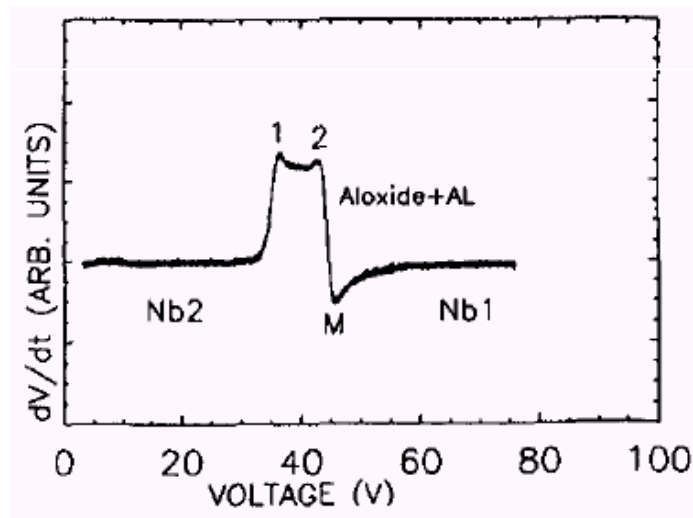


Figure 4.4: Anodization spectroscopy of SIS trilayer [Lehnert, 1991].

distilled water (760 ml) to anodise at constant current of about $1 \mu\text{A}$, recording the voltage. The huge advantage of anodisation to insulate tunnel junctions is that it eliminates a major source of shorting in mesa junctions, the metal redeposited on the junction sides during ion milling, as discussed in Section 3.3.3. Definition of the junctions by the selective niobium electing process (SNEP) does not lead to redeposition and has produced high quality SIS tunnel junctions. However, etching of ferromagnets is very slow and this technique cannot be applied to magnetic tunnel junctions. Some authors have adopted the voltage characteristics of anodisation as an indicator of trilayer quality [Blamire, 1993]. Figure 4.4 shows an example of such measurements, the rise in dV/dt at the Nb2/aluminium oxide interface followed by a maximum (1) was attributed to a homogeneous aluminium oxide barrier and a well-defined transition to the counter electrode free of niobium oxide and impurities [Lehnert, 1991]. A sharp decrease at the Al/Nb1 interface followed by a pronounced minimum, M, was interpreted as uniform coverage of the base niobium electrode with aluminium and low interdiffusion at the interface. However, anodisation is not well suited to magnetic tunnel junction fabrication, due to possibility of spalling of the ferromagnetic oxides. Anodisation was investigated, but not used in the production of devices for this work.

4.1.1.1.2 Effect of deposition temperature

Blamire *et al.* used a heated stage during the deposition of Nb/Al₂O₃/Al/Nb devices to investigate the effect on junction quality of substrate temperature during the bottom

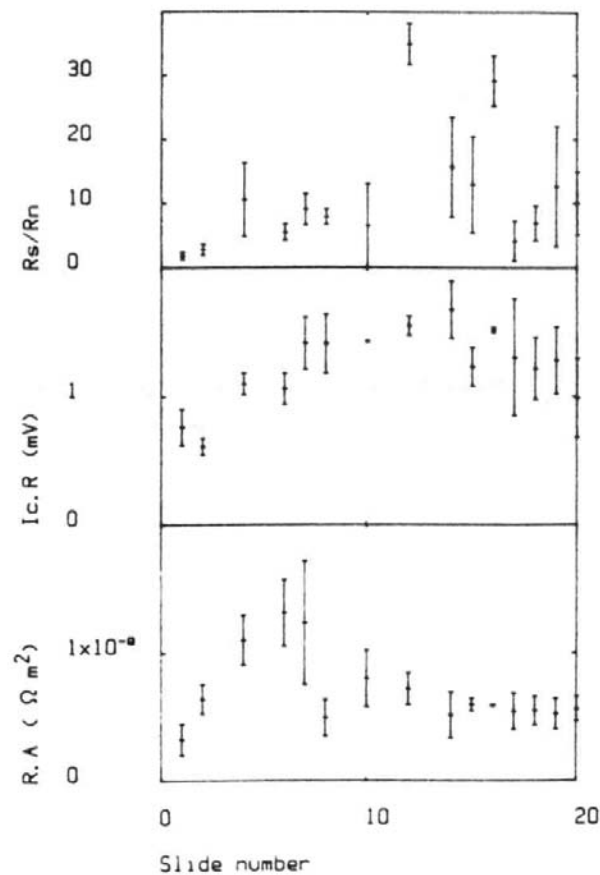


Figure 4.5: Effect of substrate temperature on SIS tunnel junction characteristics [Blamire, 1988].

niobium layer deposition [Blamire, 1988]. Figure 4.5 shows a summary of some of the results presented; the approximate temperature of each slide number is listed in Table 4.1. Temperatures were estimated using an optical pyrometer and are approximate. Their results may be summarised by three findings. Firstly, devices fabricated with a cool base layer of niobium have a poor quality, highlighted by the low FOM and low RA. When the base layer is deposited on moderately heated substrates, device characteristics reach a maximum. Finally, at the hottest temperatures there is a possible decrease in device quality, though this is not clear. The authors suggest that the aluminium forms a layer of variable thickness and poor device performance may be due to a decrease in the minimum aluminium thickness within the film. Whilst Blamire’s study highlights an important consideration for the growth of tunnel junction multilayers, the optimum substrate temperature for base layer deposition must be investigated for each material used.

<i>Temperature of each slide (°C)</i>													
Slide number	1-5	6	7	8	9	10	11	12	13	14	15	16	17-20
	200/	600/	620/	640/	660/	680/	700/	720/	740/	760/	780/	800/	800
	500	550	570	590	610	630	650	670	690	710	730	750	

Table 4.1: Temperature of the substrate during bottom niobium electrode deposition.

4.1.2 SIF junctions

Replacing the top superconducting electrode with a ferromagnet should not significantly degrade tunnel junction quality. Naturally, proper fabrication is assumed, with well-defined junctions and no sticking problems during the deposition of insulation and contact pads. This provides a smooth transition between SIS and SIF tunnel junctions. The effect of base electrode on tunneling characteristics may then be observed by fabricating SIF devices with ferromagnetic bottom electrode. Similarly to SIS tunnel junctions, the ratio of the resistance at zero bias to that in the normal state is a convenient measure of the quality of SIF tunnel junctions and is again termed the figure-of-merit (FOM).

As discussed in Section 2.1.3.1 above, quoted spin polarisation values of ferromagnets vary widely in the literature. The effective polarisation of a magnetic tunnel junction electrode is the combination of intrinsic material properties, defect levels and device structure. Production of appropriate SIF tunnel junctions and subsequent testing in high magnetic field, to determine the ferromagnet's spin polarisation, could indicate electrode quality. The polarisation values obtained are likely to be representative of the effective density of states contributing to spin polarised transport in similarly fabricated magnetic tunnel junctions, allowing better comparison between theory and experiment.

4.1.2.1 Criteria to indicate tunneling

Rowell suggested a series of criteria to which junctions are expected to adhere if their conductance is dominated by tunneling [Rowell, 1969]. These 'Rowell criteria' have been quoted recently in work investigating the reliability of methods to identify tunneling as the main source of conduction in a device. It is important to note that Rowell clearly

states that these criteria are necessary, but not sufficient, to identify tunneling. Firstly, at liquid nitrogen temperatures, the resistance of different sized junctions should be roughly inversely proportional to the area. Clearly the resistances of many devices adhere to this principle, such as junctions where leakage originates from a number of randomly distributed pinholes and metallic junctions. Secondly, on cooling to liquid helium temperatures the junction resistance should increase slightly and hence ‘an appreciable decrease in (the resistance of) any junction should eliminate it from further consideration’, indicating metallic shorting of the junction. 4.2 K is below the critical temperature, T_C , of niobium, whereas Rowell commented on junctions with lead, tin, indium, tantalum and aluminium electrodes, which all have T_C lower than 4.2 K. The criteria may therefore be redefined to incorporate niobium electrodes: an increase in the resistance of tunneling devices should be observed when temperature is reduced. Thirdly, an energy gap must be observed for superconducting tunnel junctions. Fourthly, good quality SIF junctions at 1 K should display an $\frac{R_S}{R_N}$ of 1000. Moreover, he suggests that values of less than 10 are unacceptable. The effect of thermal smearing on SIF junctions is discussed in Section 2.1.3, where it was shown that such values cannot be obtained at 4.2 K. Finally, he suggests that for SIS junctions the increase in resistance at $\Delta_1 + \Delta_2$ should be sharp. A non-vertical increase in current at $\Delta_1 + \Delta_2$ has been discussed in Section 4.1.1 and is generally attributed to a series resistance. With different superconducting materials acting as the electrodes above and below the barrier, a cusp in the current-voltage characteristic should be well defined at $\Delta_1 - \Delta_2$, an effect which we may not observe in Nb/Al₂O₃/Nb junctions.

A series of papers have been published by Akerman *et al.* investigating the ‘Rowell criteria’, of which they list three for non-superconducting tunnel junctions [Akerman, 2001; Rabson, 2001; Akerman, 2000]. Firstly, they claim that an exponential dependence of the conductance on the insulator thickness must be present for tunneling dominated transport. Secondly, they identify the parabolic dependence of conductance on applied bias voltage which can be fitted to theoretical models [Simmons, 1963; Stratton, 1962]. Finally, a weak insulator-like temperature dependence of the conductance must be present. Rowell does not suggest the first two of these criteria in the article cited and discussed above, to which they are credited. However, many authors do

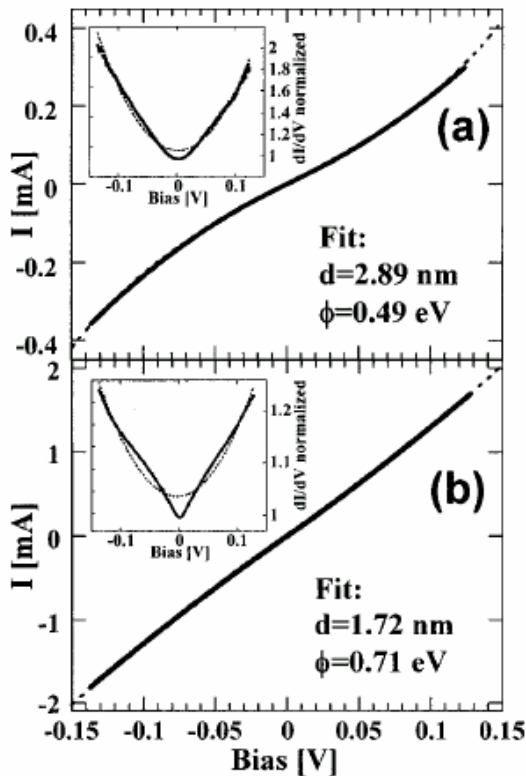


Figure 4.6: Current-voltage characteristics for (a) Sample A, at 90 K. (b) Sample B, at 77 K. [Akerman, 2000]

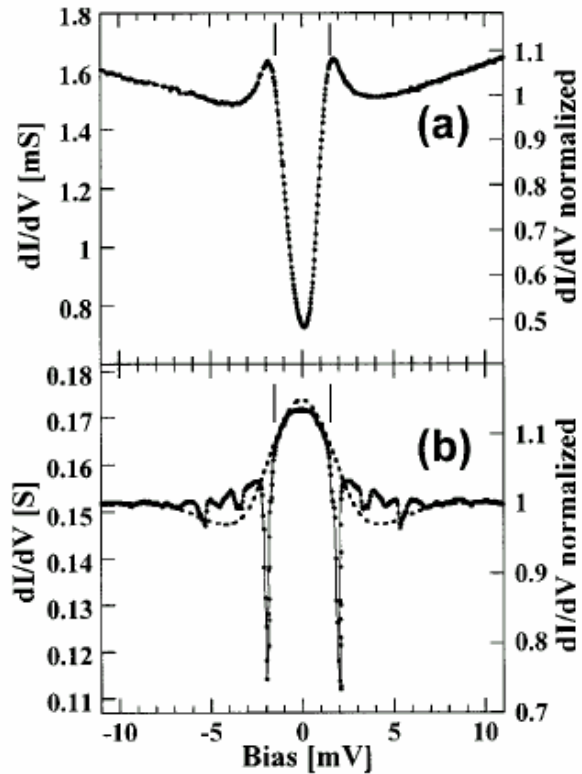


Figure 4.7: Conductance at 4.2 K for (a) Sample A. (b) Sample B. [Akerman, 2000]

use these two well-documented properties of tunneling conduction as ‘proof’ that tunneling is the main source of conduction in their magnetic tunnel junctions. Again, it should be noted that these characteristics are necessary, but not sufficient, to identify tunneling as the cause of conductance. For example, many electronic devices display non-linear current-voltage characteristics at low applied bias, which may be fitted by a parabolic curve. Rowell states: ‘the only test of tunneling is to put a superconductor on one side of the junction’; the identification of an energy gap and good FOM indicate tunneling. However, the results of Akerman *et al.* provide insight into the issues associated with the identification of tunneling in magnetic tunnel junctions.

Platt *et al.* propose that non-linear current-voltage (I-V) characteristics allow the distinction between conduction through pinholes and conduction by tunneling [Platt, 1997]. They argue that conduction through pinholes is metallic, resulting in linear I-V characteristics, but conduction by tunneling follows the predictions of Simmons and other workers [Simmons, 1963(a)]. However, Akerman *et al.* show that junctions demonstrating a non-linear I-V characteristic, modelled adequately by Simmons’ theory,

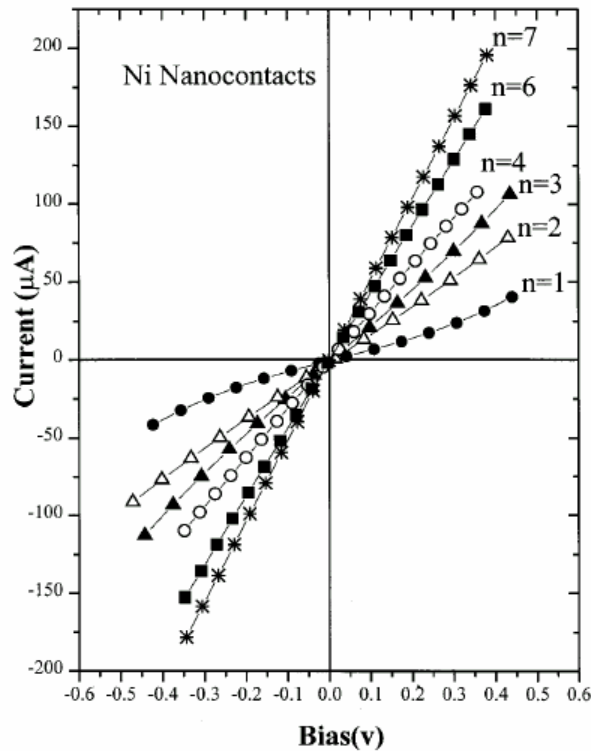


Figure 4.8: Experimental curves for ballistic Ni contacts for n quanta of conductance, $n=1-7$. Non-linear IV is observed for small contacts. [Garcia, 2000]

may actually contain pinholes, as shown by Figure 4.6. Andreev reflection was observed for Sample B, for which modelling by Simmons theory produced reasonable values of barrier height, 0.71 eV, and thickness, 1.72 nm. Measurements of polarisation from Andreev reflection are discussed in Section 2.1.4.1.1. Using Equation (2.23) the polarisation of the iron was estimated as 43%, in good agreement with values from the literature (see Table 2.1). Clearly a parabolic conductance dependence on voltage is a necessary, but not sufficient, requirement for the identification of tunneling as the main mechanism for electron transport. Additionally, Garcia claims that non-linear I-V characteristics may be attributed to transport through nanocontacts (small pinholes) [Garcia, 2000]. His results are shown in Figure 4.8, representing the I-V curves for nanocontacts of size 1-7 conduction quanta in nickel. The trends become increasingly linear as contact size increases. He further claims that magnetoresistance effects in magnetic tunnel junctions may be described by conduction through pinholes, which is not a generally accepted description of the origin of MR.

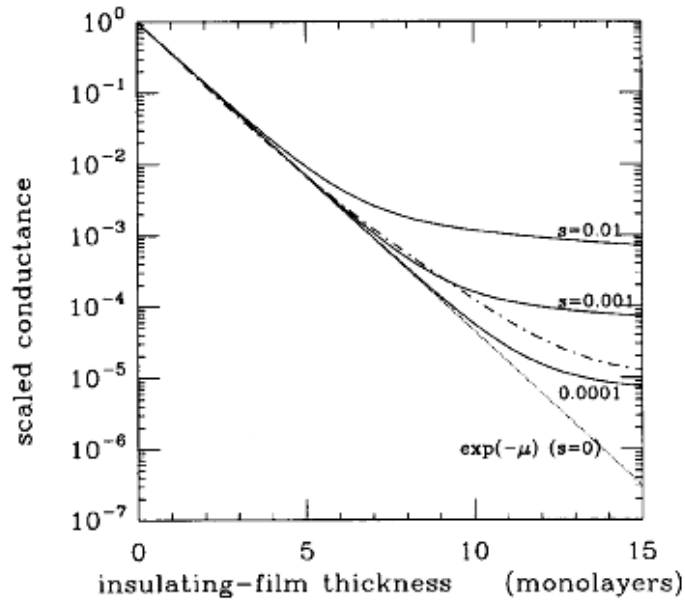


Figure 4.9 : The dependence of conductance on insulator thickness. $s = R_0/R$, deviation from exponential dependence (straight line) occurs as s increases. [Rabson, 2001]

Rabson *et al.* have shown that the exponential dependence of conductance on barrier thickness may be explained not only by tunneling but also by transport through pinholes [Rabson, 2001]. Barrier growth is modelled two dimensionally as a random deposition of blocks of insulating material, leaving some pinholes. The ratio of the metal-metal resistance R_0 to the insulator resistance, R , influences the conductance dependence on thickness. An exponential dependence of conductance on insulator thickness results from blocks of a perfect insulator. However, as the ratio $s = R_0/R$ increases, the dependence of conductance on thickness deviates from exponential behaviour, as shown in Figure 4.9. No suggestion is made of the practical values of R and R_0 . At a practical barrier thickness of 2 nm, roughly 10 monolayers of Al_2O_3 , such an exponential dependence could be observed for conduction by pinholes.

The third criterion of Akerman *et al.*, initially suggested by Rowell, is that resistance should increase as temperature is decreased for tunneling dominated conductance. Studies by Akerman *et al.* and also by Rudiger, claim that resistance-temperature measurements are a reliable test for tunneling dominated conduction [Akerman, 2000; Akerman, 2001; Rudiger, 2001]. Consider a magnetic tunnel junction which has been undermilled, but displays a large contact resistance to the wiring layer due to organic

deposits (Section 3.3.3). The resistance of such a device is expected to increase as temperature decreases, yet the magnetic tunnel junction does not work. The presence of increasing resistance with decreasing temperature is not sufficient to indicate a working tunnel junction.

The above experimental evidence supports Rowell's claim that the only way to identify tunneling as the main cause of conduction in a device is by fabricating junctions with at least one superconducting electrode. Below are the results of investigations into the relationship between the figure-of-merit of a SIS or SIF device and its parabolic I-V characteristics, resistance-area product, and dependence of resistance on temperature. A relationship between the quality of superconducting tunnel junctions and their normal state characteristics should prove to be a useful analysis tool for magnetic tunnel junctions. This study was initiated prior to the publication of the recent papers identified above by Akerman, Rudiger and Garcia.

4.2 The fabrication of SIS and SIF tunnel junctions

4.2.1 Deposition of films

Films were deposited on 5×10 mm oxidised silicon substrates by whole wafer DC sputtering using the MkVII system. The substrate preparation, deposition system and procedure are described in Section 3.2. Thirteen depositions took place specifically for the production of tunneling devices. Conditions associated with devices presented in this chapter are summarised in Table 4.2 and Table 4.3. Care was taken to provide consistency throughout the course of study, particularly in deposition procedure, substrate and target cleaning. The total electrode thickness was maintained on introducing the ferromagnetic material for SIF and magnetic tunnel junctions, providing good comparison between devices from different depositions. Therefore a larger thickness of niobium was used for the SIS devices and the superconducting electrode of SIF devices than is required to provide a good quality superconducting electrode.

<i>Material</i>	<i>Deposition power (W)</i>	<i>Deposition Rate (nmW⁻¹min⁻¹)</i>	<i>Target-stage distance (mm)</i>
Aluminium	10	0.004/0.166	37
Niobium	60	0.038	57
Cobalt	30	0.225	68
Iron	27	0.039	68

Table 4.2 : Deposition power, rate and target stage distances for deposited materials. Aluminium rate changed dramatically after replacing the worn-out 1mm target with a new 2mm target.

Table 4.2 and Table 4.3 indicate the unexpected dramatic increase in deposition rate observed on changing the aluminium target. The value of a thickness measurement to identify problems with deposition rates is highlighted by such results. The films of 11247 were used for device fabrication to test the viability of the processing route for aluminium electrodes. The problems associated with the fabrication of Al/Al₂O₃/Al/Co/Nb devices to investigate the spin polarisation of cobalt are discussed in Section 4.4.3.

<i>Material</i>	<i>Condition</i>	<i>10075</i>	<i>11150</i>	<i>10397 1/2/3</i>	<i>10445 1/2/3</i>	<i>10696 1</i>	<i>11247 1</i>
Niobium	Passes, speed	2, 2× and 32, 2×	2, 2× and 32, 2×	1, 1× and 15 1×	2, 2× and 14, 2×	2, 2× and 14, 2×	-
	Pressure (Pa)	0.7	0.32 and 0.7	0.31 and 0.72	0.32 and 0.7	0.3 and 0.7	-
	Thickness (nm)	38.8	38.8	36.5	19.4	19.4	-
Cobalt	Time (s)	-	-	-	82/123/164	104	-
	Pressure (Pa)	-	-	-	1	1	-
	Thickness (nm)	-	-	-	9.2/13.8/18.5	11.7	-
Aluminium	Passes, speed	6, 1×	6, 1×	6, 1×	6, 1×	6, 1×	8, 2× and 22, 2×
	Pressure (Pa)	0.7	0.7	0.71	0.71	0.71	0.29 and 0.7
	Thickness (nm)	2.4	2.4	2.4	2.4	2.4	1.6/6.6 and 4.4/18.3 *
Oxidation		1 hour, 1kPa	1 hour, 1kPa	1 hour, 1kPa	1 hour, 1kPa	1 hour, 1Pa	1 hour, 1kPa
Aluminium	Passes, speed	4, 1×	4, 1×	4, 1×	4, 1×	4, 1×	8, 2×
	Pressure (Pa)	0.95	0.95	0.99	1.02	0.94	0.94
	Thickness (nm)	1.6	1.6	1.6	1.6	1.6	1.6/6.6 *
Cobalt	Time (s)	-	-	82/123/164	-	-	104
	Pressure (Pa)	-	-	4 – 1.4	-	-	5-1
	Thickness (nm)	-	-	9.2/13.8/18.5	-	-	11.7
Niobium	Passes, speed	2, 2× and 20, 2×	2, 2× and 20, 2×	6, 1×	1, 1× and 11, 1×	1, 1× and 11, 1×	3, 1×
	Pressure (Pa)	4 and 0.7	4 and 0.7	0.68	4 and 0.72	4 and 0.72	0.7
	Thickness (nm)	25.1	25.1	13.7	27.4	27.4	6.8

Table 4.3: Deposition conditions for SIS and SIF films discussed below. * A new Al target was used for this deposition and surprisingly the deposition rate was significantly increased, from $0.04\text{nmW}^{-1}\text{min}^{-1}$ to $0.166\text{nmW}^{-1}\text{min}^{-1}$

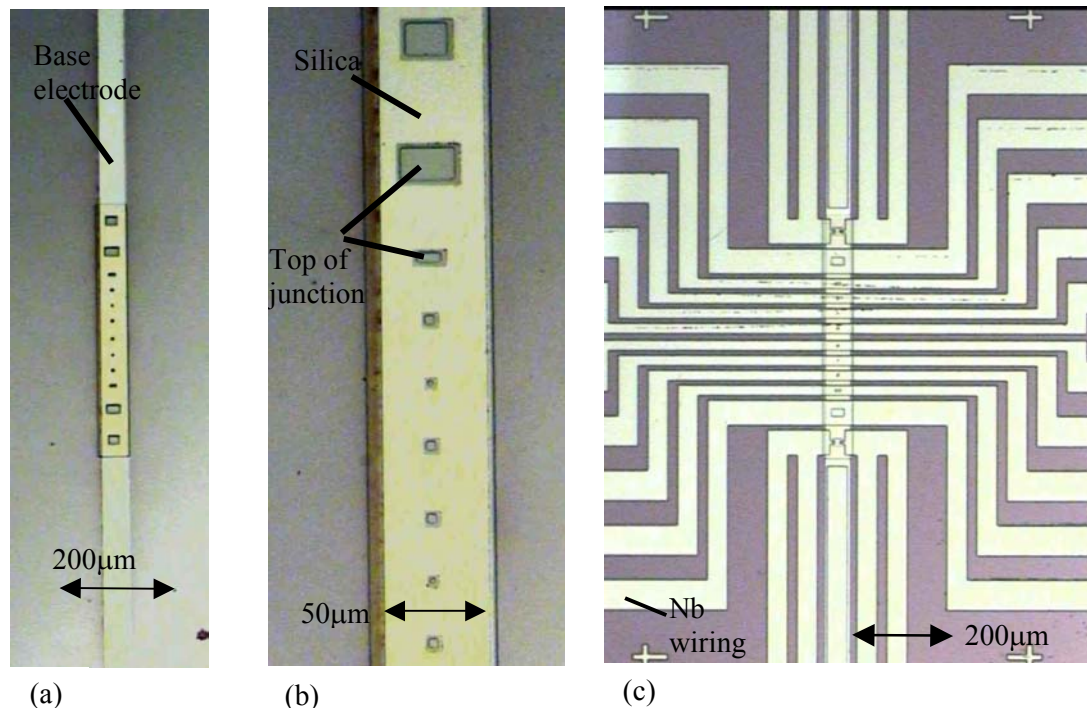


Figure 4.10: Pictures of device fabrication (a) base electrode and junctions defined, silica deposited (b) greater detail of the silica and junctions (c) fully built device with Nb wiring layer.

4.2.2 Fabrication of devices

Devices were fabricated using standard contact lithography and processing techniques as described in Section 3.3. For convenience, the fabrication route is summarised below. Firstly, the junction area was defined by contact lithography on as-deposited films, the mask-set CAM30 was used throughout. The mesa junctions were defined by ion milling on the NOAR system, the majority of films were fabricated without use of the rotating stage. The base layer was defined to the pattern shown in Figure 4.10(a) by lithography followed by ion milling. The lift-off profiled lithography structure was defined for silica insulation of the junctions, followed by deposition, resulting in the features shown in Figure 4.10(b). Finally, the wiring layer was defined and, following a brief pre-mill, deposition of niobium contacts took place in the NOAR, as shown in Figure 4.10(c).

4.2.3 Variation in the fabrication route

Every effort was made to maintain good and repeatable practice during film deposition and processing, but the very nature of the deposition systems and processing techniques lead to unavoidable variation in conditions. Certain depositions were undertaken at large intervals. For example, the SIS depositions 10075 and 11150 were performed almost two years apart, over which time the system was used extensively for other materials. System cleanliness therefore changed slightly over the course of study, but any variation was minimised by the use of the same flange, used only for this work.

Lithography is a complex variable of temperature, humidity, bulb calibration, developer and photoresist age. In the cleanroom used to fabricate devices, temperature and humidity was subject to seasonal variation. A great deal of time was spent optimising lithography, and times altered accordingly to minimise differences in junction area. The age of developer and photoresist was monitored and it was regularly replaced. AFM measurements of junction height were used to check milling time and calibration also took place following a filament change. Devices on separate chips are therefore considered very similar, but not identical.

4.3 Results

4.3.1 SIS tunnel junctions

Superconductor-insulator-superconductor devices fabricated from the deposition runs 10075 and 11150, as described above, were tested using the low temperature probes described in Section 3.4. Figure 4.11 shows the SIS current-voltage characteristics of 10075_4d, 6×6 μm junction, measurements in zero magnetic field and with the Josephson current suppressed by a magnetic field are shown. The presence of the energy gap, Δ , clearly identifies tunneling as the primary transport mechanism within the junction. The energy gap estimated from the diagram is $\Delta \approx 1.15$ meV, significantly lower than the bulk value for niobium at 0 K, 1.5 meV, but similar to previous results for thin films [Goodchild, 1996]. The figure-of-merit of 11.7 is fair and typical of the devices produced

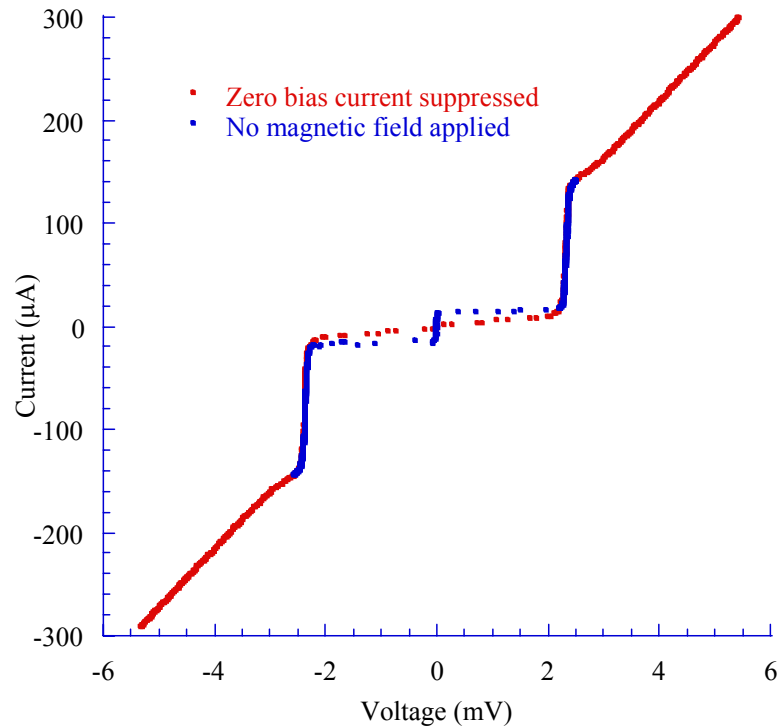


Figure 4.11: Current-voltage characteristic for 10075_4d SIS tunnel junction. The zero voltage bias current (Josephson current) is shown, in addition to a measurement when it is suppressed with a magnetic field.

at 4.2 K. The rapid increase in current at the energy gap indicates that there is no significant series resistance.

4.3.1.1 The effect of resistance-area product on FOM

A large number of devices have been fabricated, primarily to improve and test the processing route. Series resistance was generally insignificant and, neglecting devices where it was large, we expect leakage and tunnel current to dominate transport, leading to an increase in figure-of-merit as the resistance-area (RA) product rises. FOM is plotted against RA in Figure 4.12. RA was used to normalise the effect of junction area, A , using the normal state resistance, R_N . Modelled FOM is also shown on the graph, assuming a simple leakage model, as discussed below.

Consider one device assumed to consist of a perfect tunnel junction, resistance R_J , and parallel leakage, resistance R_L . Here we use the device 10075_4d. The normal state resistance of the junction, R_N is then described by Equation (4.3).

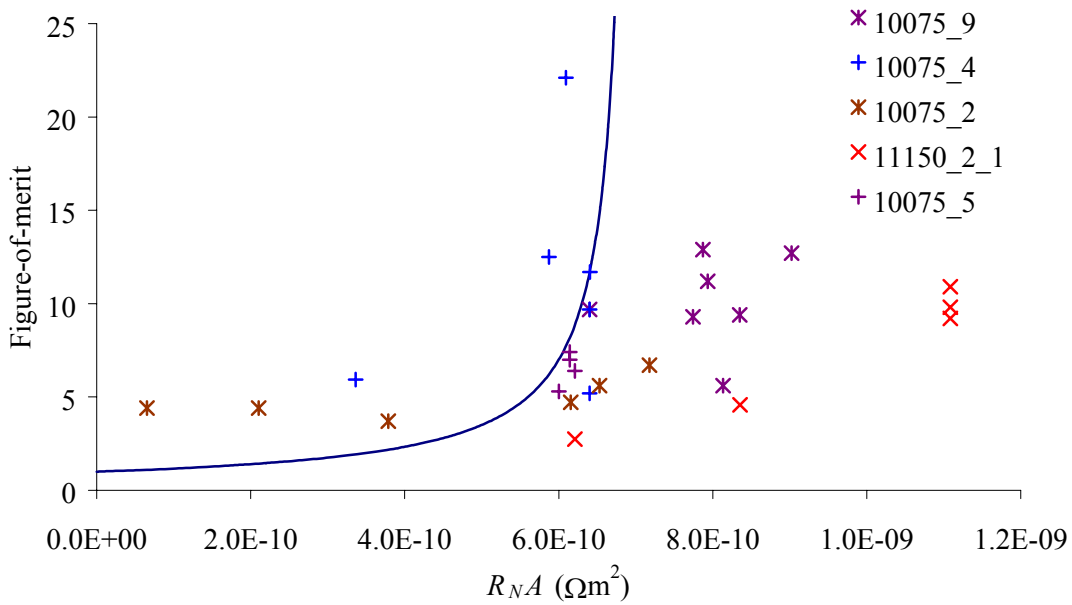


Figure 4.12: Figure-of-merit against resistance-area for SIS tunnel junctions. Solid line is the result of modelling 10075_4d as a perfect junction and parallel leakage resistance.

$$R_N = \frac{R_J R_L}{R_J + R_L} \quad (4.3)$$

Figure-of-merit is defined by Equation (4.1). Assuming conduction by thermal excitation is negligible compared to junction leakage, and that R_L is not voltage dependent, $R_S = R_L$, from which we derive Equation (4.4).

$$\text{FOM} = 1 + \frac{R_L}{R_J} \quad (4.4)$$

FOM and R_N are known from device measurements. Values for the leakage and true junction resistance may be derived using this model. Substituting $R_N = 17.79 \Omega$ and FOM = 11.7 into (4.3) and (4.4), as experimentally observed for 10075_4d and solving, we find $R_L = 208 \Omega$ and $R_J = 19.45 \Omega$. This calculation reveals that even a small leakage, corresponding to high resistance, can lead to considerable reduction in the quality of the junction. Extremely high quality tunnel junction fabrication is required to produce a good FOM. Having calculated the model junction parameters, the leakage resistance may be varied, and the figure-of-merit calculated and as shown in Figure 4.12.

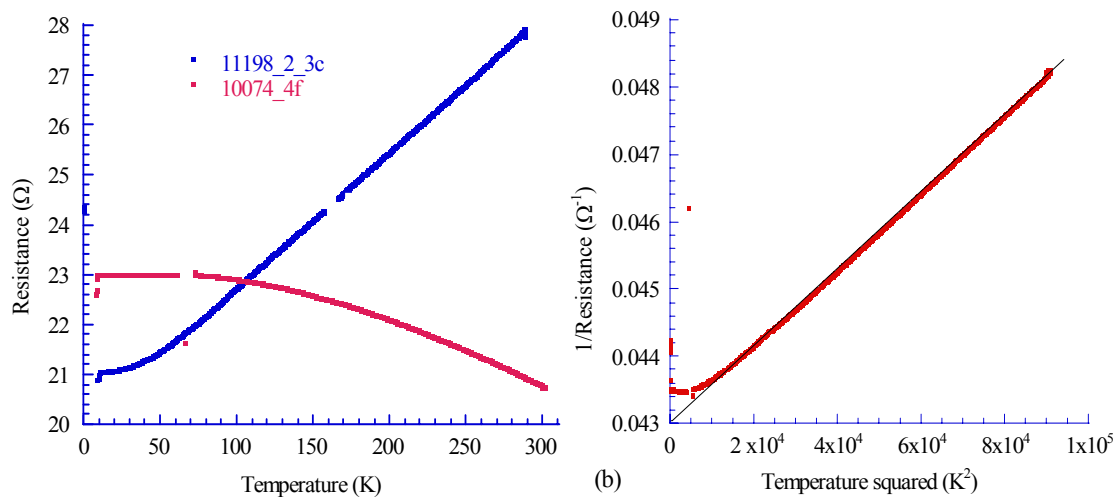


Figure 4.13: (a) Variation of resistance with temperature for a good SIS tunnel junction, 10075_4f and shorted junction, 11198_2_3c, a SIF device. (b) 1/resistance against temperature squared for 10075_4f, the line is drawn as a guide to the eye.

The high scatter of points in Figure 4.12 indicates that a simple model of a real tunnel junction consisting of a perfect junction and leakage in parallel does not explain the variation in FOM of real junctions. A certain amount of ‘clumping’ of results from devices on each chip is evident. Though the trend is not clear, FOM does appear to increase as the resistance-area product rises. This simple model neglects a number of important parameters, such as thermal transport and voltage dependent transport through the barrier. Weak-links through the insulator may significantly affect transport properties. Transport through real SIS tunnel junctions is clearly complex and significant variation is evident, even for devices on the same chip.

This model does not differentiate between shorting due to pinholes and redeposition of metal during ion milling. To identify significant redeposition, normal state resistance at 300 K was plotted against junction area, during cooling to liquid helium temperatures. With minimal redeposition, junction resistance scales as the inverse of area. This is a useful, quick test for ion milling problems.

4.3.1.2 Temperature dependence of resistance

The temperature dependence of the resistance is commonly used to indicate that tunneling dominates junction conductance, as discussed in Section 4.1.2.1. Figure 4.13(a) illustrates the contrast between a working and shorted junction. The shorted junction,

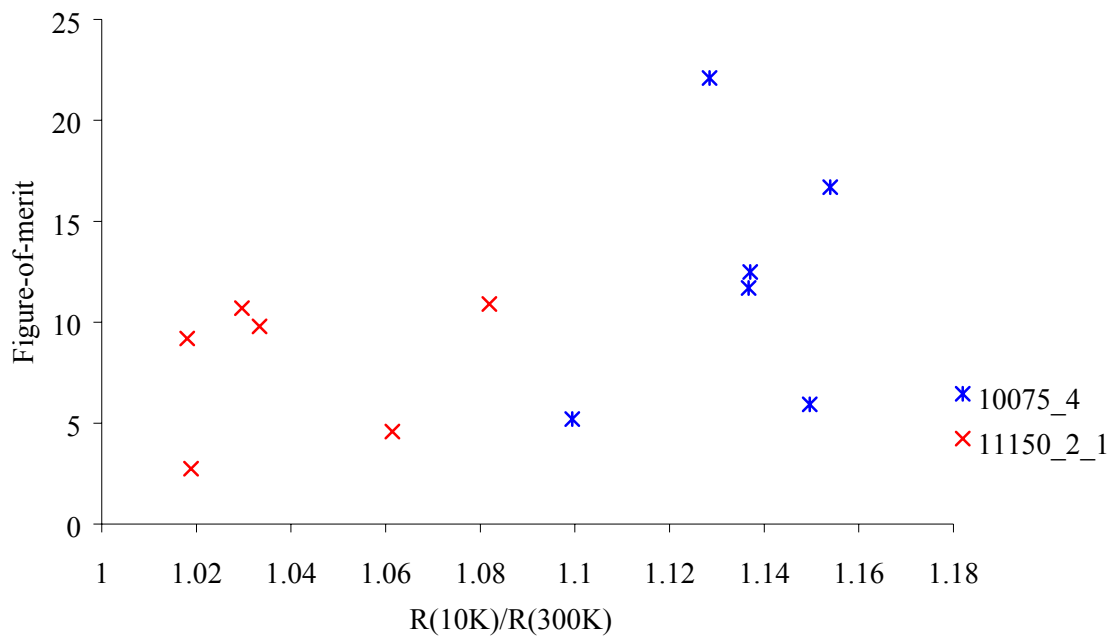


Figure 4.14: The correlation between FOM and $R(10K)/R(300K)$.

11198_2_3c, displays an approximately linear decrease in resistance as temperature falls for most of the range, as expected for a metallic device. Resistance increases as temperature drops for the good device, 10075_4f, as expected. All working junctions displayed an increase in resistance as temperature decreased.

Stratton's theory, discussed in Section 2.1.2.1, predicts an increase in resistance with decreasing temperature. From Equation 2.15, this theory suggests that a graph of $1/\text{resistance}$ against temperature squared should be linear. Figure 4.13(b) shows the results from 10075_4f, where the data may be adequately fitted to a straight line at temperatures above 50 K. Fitting data to Stratton's theory to indicate the variance of resistance with temperature appears to be a reliable technique to identify tunneling as the principal cause of conduction in the junction.

The relationship between the resistance increase with decreasing temperature for working SIS tunnel junctions and FOM was investigated by plotting the ratio of resistance at various low temperatures to that at room temperature. Figure 4.14 shows figure-of-merit plotted against a ratio of the resistance at 10 K, $R(10K)$, to that at 300 K, $R(300K)$. No trend is clear on the graph, though FOM possibly increases as $R(10K)/R(300K)$ increases. However, the resistance-temperature characteristics for SIS devices displaying a series

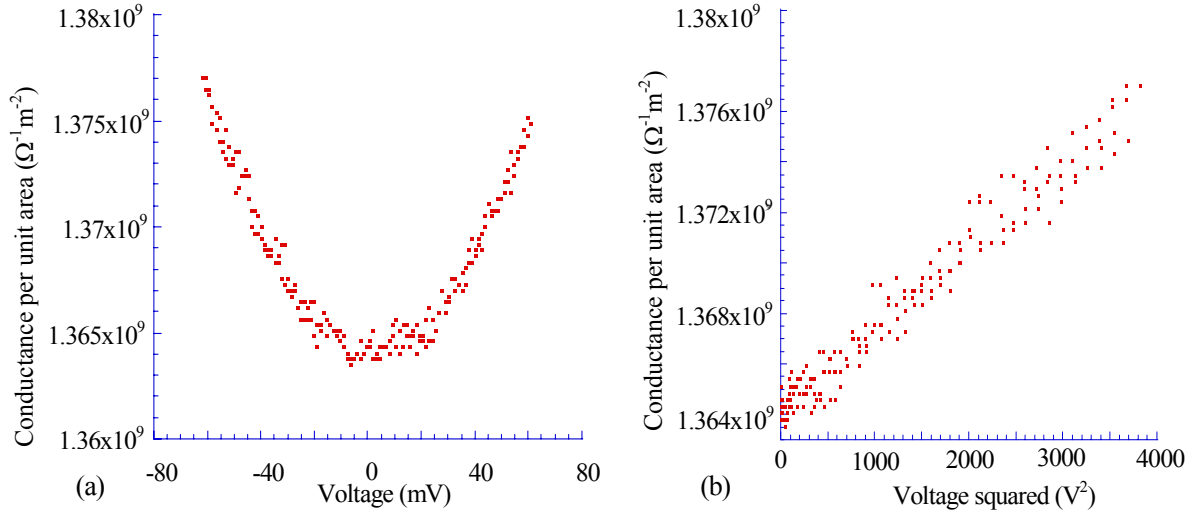


Figure 4.15 : (a) Conductance per unit area against voltage and (b) conductance per unit area against voltage squared for SIS tunnel junction, 10075_2g.

resistance were not measured, such series resistance could lead to a significant increase in $R(10K)/R(300K)$ with decreasing temperature.

4.3.1.3 Simmons' theory fits as an indication of junction quality

The junction height, ϕ , and thickness, t , are predicted by Equation 2.12, derived by Simmons' theory of tunneling in NIN structures. A variant on the graphical method suggested by Simmons to determine ϕ and t was used to recover barrier characteristics from measurements taken using the lock-in described in Section 3.4.2.4 [Simmons, 1963(c)]. Figure 4.15(a) shows a typical conductance versus voltage plot for a SIS tunnel junction, 10075_2g. No shorted devices displayed the parabolic dependence of conductance on bias voltage. From Equation 2.12 we may write:

$$\text{Differential conductance} = G = \frac{dJ}{dV} = \beta + 3\beta\gamma V^2 \quad (4.5)$$

$$\text{Where } \beta = \frac{3}{2t} \left(\frac{e}{\hbar} \right)^2 \sqrt{(2m\phi)} \exp\left(-\frac{4\pi t}{\hbar} \sqrt{(2m\phi)} \right) \quad (4.6)$$

$$\text{and } \gamma = \frac{\pi m \hbar^2}{3\phi (et)^2}$$

t and ϕ may be recovered from Equations (4.7) and:

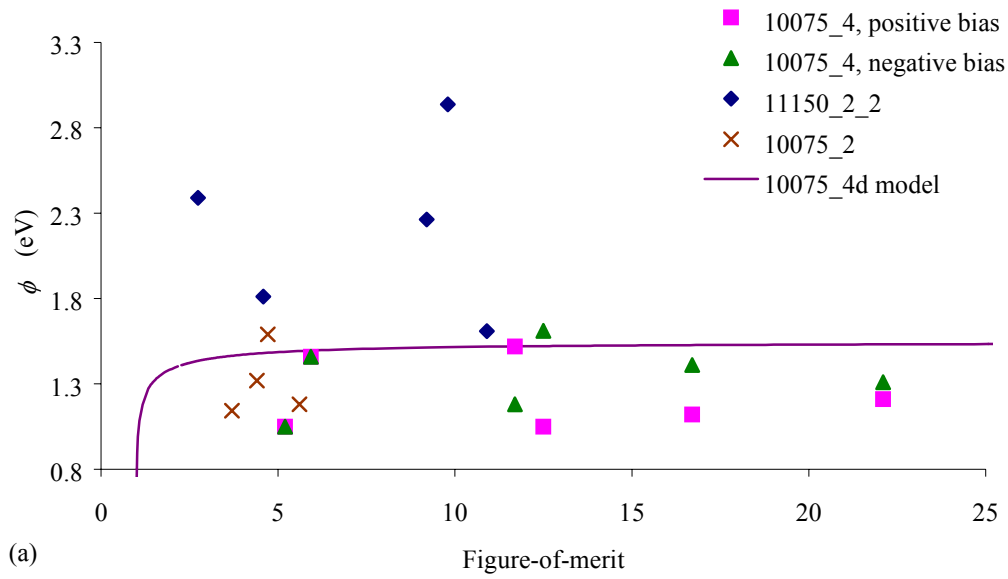
$$t = 4.94\gamma^{\frac{1}{4}}L^{\frac{1}{2}}, \quad (4.7)$$

$$\phi = \left(\frac{0.266}{\gamma^{\frac{1}{2}}} \right) L, \quad (4.8)$$

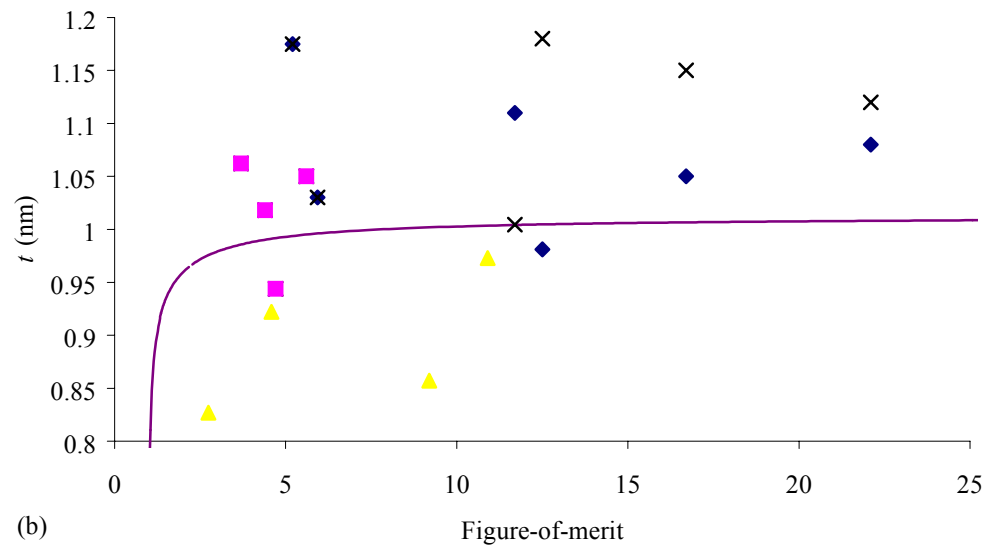
where $L = \log_{10} \left(\frac{4.87 \times 10^{13}}{\beta\gamma^{\frac{1}{2}}} \right)$. For tunneling devices adequately described by Simmons’

theory, a plot of differential conductance against bias voltage squared should be linear, with y-intercept β and gradient $3\beta\gamma$. The corresponding plot of differential conductance against voltage squared for device 10075_2g is shown in Figure 4.15(b). Generally, no distinction could be made between tunnel junction performance in positive and negative bias. Despite the prediction by Simmons’ theory that the parabolic conductance dependence on bias voltage should be centred at zero bias, we discussed in Section 2.1 that an offset is usually present. However, such an offset was not visible, due to a number of factors. Firstly, since these devices have nominally identical electrodes, minimal offset is expected. Due to the low resistance of devices, measurements became quantised and additionally, the applicable voltage range before destroying the device was small. Calculated values for 10075_2g are $\phi = 1.39$ meV and $t = 1.02$ nm, which appear reasonable.

Graphical analysis, followed by calculation of the barrier parameters was carried out for a number of SIS devices. The dependence of figure-of-merit on calculated barrier height and thickness is shown in Figure 4.16(a) and (b). No correlation is evident between figure-of-merit and either t or ϕ . Also shown in Figure 4.16 is the variation of barrier height and thickness for 10075_2g, according to the model presented in Section 4.3.1.1, where a real device is pictured as a perfect tunnel junction and parallel leakage resistance. As found in Section 4.3.1.1, this model does not adequately explain the behaviour of the system. Values of barrier thickness and height calculated by Simmons’ theory are not adequate indicators of tunnel junction quality. Furthermore, it is likely that the calculated values do not represent the actual barrier height and thickness within a real junction and are, instead, effective barrier height and thickness.



(a)



(b)

Figure 4.16 : The variation of the barrier height and thickness, calculated using a variation of Simmons' graphical method, for SIS tunnel junctions with figure of merit.

4.4 SIF tunnel junctions

4.4.1 Superconducting bottom electrode

A typical conductance against voltage curve for a tunnel junction of the nominal structure Nb/Al₂O₃/Al/Co/Nb is shown in Figure 4.17. A solid line representing the theoretical

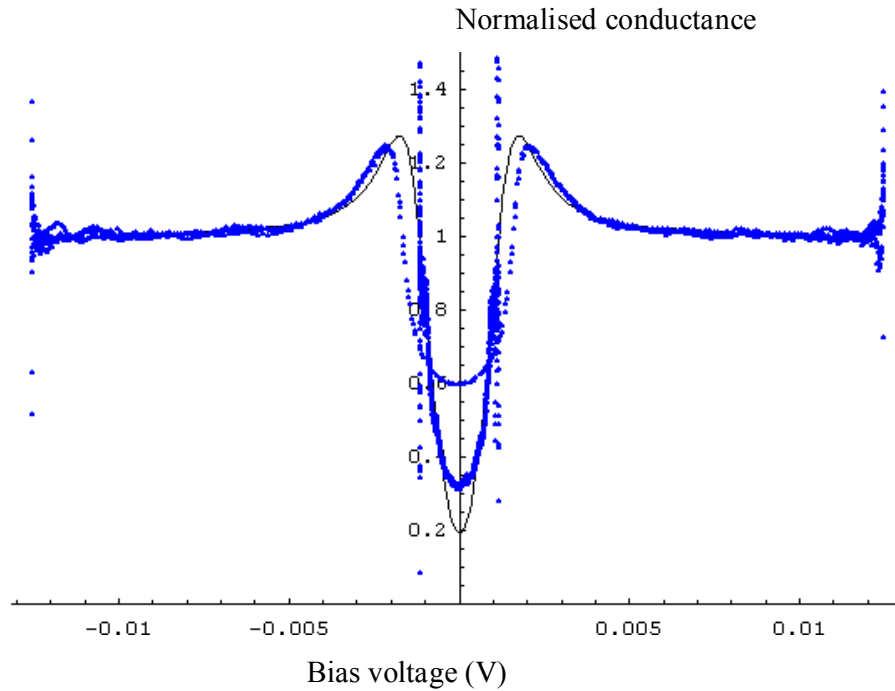


Figure 4.17: Normalised conductance against applied bias for 10397_1f SIF tunnel junction showing the theoretical solid curve.

conductance of an SIF junction with niobium superconducting electrode in zero magnetic field at 4.2 K is also shown. The curve was calculated from the model presented in Section 2.1.3, and uses the value of $\Delta = 1.15$ meV, found for SIS devices above (Section 4.3.1). The figure-of-merit of this junction, 10397_1f, is 3.16. The two sets of data evident near zero bias result from measuring the device at low and high current. At low bias, the sub-gap structure is observed with minimal junction heating, but the high bias, necessary to observe the normal behaviour of the junction, causes self-heating and a decrease in FOM. A small series resistance may cause the deviation from theoretical curve at the peaks in conductance.

Figure 4.18(a) illustrates the effect of series resistance on conductance curves of SIF tunnel junctions. The peak in conductance is raised well above the known energy gap of the niobium superconducting electrode. Figure 4.18(b) shows the effect of leakage on a SIF tunnel junction: the conductance at bias voltage below the energy gap is significantly increased. The cause of leakage is known to be poor barrier formation, produced by oxidising the aluminium at only 1 Pa, instead of 1000 Pa, the resistance of junctions on the chip scaled as the inverse of their area.

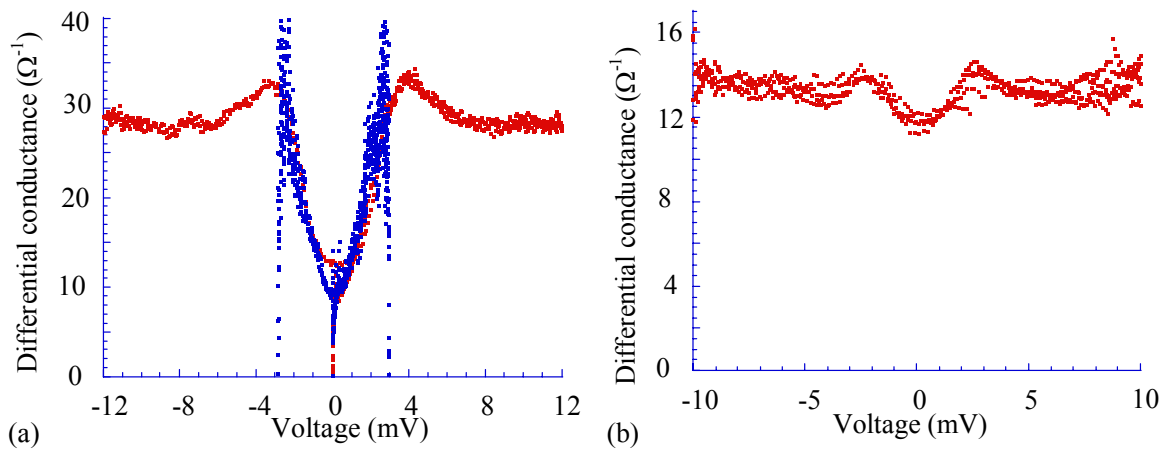


Figure 4.18: Conductance against voltage for (a) high leakage device, 10696_1g (b) device with series resistance, 10397_2b. Differential conductance is that calculated by numerical differentiation of dI/dV .

4.4.1.1 Temperature dependence of conductance in SIF junctions

A useful measure of the quality of an SIF junction is the variation of the normalised conductance at zero bias as temperature, T , decreases. The temperature dependence of the conductance at zero bias may be deduced from Equation 2.21:

$$\left. \frac{G_{SIF}}{G_N} \right|_{V \rightarrow 0} \propto \exp\left(-\frac{\Delta}{k_B T}\right), \quad (4.9)$$

where G_{SIF} is the conductance of the SIF junction at zero voltage bias and G_N is the normal state conductance. Measurements were taken between 0.34 K and 4.2 K using the Oxford Instruments HelioxTM cryogenic probe. Figure 4.19 shows normalised conductance at zero bias versus $1/T$ for 10397_1f and a line representing the relationship of Equation (4.9). G_N is assumed constant over the temperature range; at the value recorded at 4.2 K, changes shown by RT graphs are generally insignificant at such low temperatures. Deviation from the theoretical line occurs at about 2 K for 10397_1f, at which point leakage or self-heating dominates the conductance of the device. A respectable FOM of 98 was observed at 0.34 K. This technique could provide useful insight into device quality, encouraging the optimisation of deposition and processing conditions. However, the time taken to measure each chip with the HelioxTM probe is

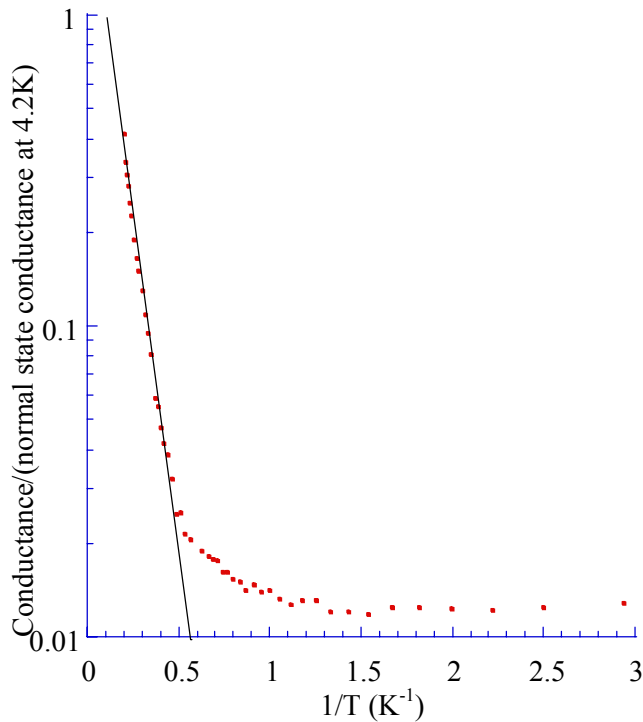


Figure 4.19 : Variation of normalised conductance with inverse temperature. Straight line indicates perfect theoretical behaviour.

prohibitive for rapid device development, and this technique is not directly applicable to magnetic tunnel junctions.

4.4.1.2 Nb/Co/Al₂O₃/Al/Nb devices in a large magnetic field

A good quality SIF chip, 11175_3, with the nominal structure Nb/Co/Al₂O₃/Al/Nb was tested using the Oxford Instruments HelioxTM cryogenic probe with 20000 Oe magnet pole piece. The purpose of this experiment was to test the apparatus and computer programme. It was also hoped to observe some inflection in the band edge of a device at 0.3 K and 20000 Oe. Unfortunately, the magnet wiring (pictured in Figure 3.16) did not work to the manufacturer's specified level and burnt out at a current just below the 50 A required to obtain 20000 Oe. Following shortening of the magnet wiring, the device was tested again, but the wiring failed at 30 A. The magnet was returned to the manufacturer for repair, causing considerable delay to the work of Section 4.4.3

4.4.2 SIF, ferromagnet bottom electrode

Initially, junctions fabricated with a ferromagnetic bottom electrode were unsuccessful, demonstrating very poor figures-of-merit, generally below two. The deposition of aluminium on top of cobalt was identified as the cause, since this was the only critical stage changed. The SIS junctions verified the deposition of niobium on top of the barrier. The problem was overcome by allowing the samples to cool for 30 minutes in 50 Pa argon between cobalt and aluminium deposition, decreasing the aluminium mobility, and lessening structural rearrangement. Junctions were obtained with good FOM at 4.2 K, up to 4.5, better than previously obtained for a superconducting bottom electrode.

4.4.3 Al/Al₂O₃/Al/Co/Nb tunnel junctions

Al/Al₂O₃/Al/ferromagnet/Nb tunnel junctions may be used in conjunction with a large magnetic field to investigate the spin polarisation of the ferromagnetic electrode, as discussed in Section 2.1.3.1. The basic procedure for film deposition and device fabrication is described above in Section 4.2. However, devices appropriate for spin polarisation measurements must have thin aluminium electrodes, in the range 5-10 nm. Such devices are generally defined by deposition through shadow masks, eliminating difficult processing [Meservey, 1994]. Three particularly challenging steps are present in the fabrication route. Firstly, the deposition of superconducting thin aluminium films, less than 10 nm, requires optimisation of the deposition conditions. However, given the high vacuum and cleanliness of the system used, this requirement can be easily met. Secondly, milling fully through the top electrode, yet stopping within roughly 1 nm in order to provide a thick enough bottom contact is extremely difficult, particularly with no rotation on the milling system. This issue is aggravated by the final significant problem, that the pre-contact pad deposition mill must remove the aluminium oxide and organic deposits, but not significantly thin the electrode. The milling rate of aluminium is high, generally 1.5 times that of niobium, but that of the oxide and organic deposits was found to be low.

Careful ion mill calibration took place, followed by milling and subsequent AFM measurements to indicate mill depth. Milling depth was repeatably controlled to within 1 nm. Calibration of the pre-deposition mill rate was also performed and found to be

approximately 3.5 times the rate of feature definition mills. This difference is due to the fact that the ‘reverse’ of the stage, required to bring the sample close to the magnetron for depositions, is also much closer to the ion gun than the rotation stage. Several chips were fabricated and the results of testing the junctions as normal metal-insulator-normal metal junctions are summarised below, in addition to characterisation at 0.3 K.

4.4.3.1 Testing the Al/Al₂O₃/Al/Co/Nb junctions

The criteria listed above (Section 4.1.2.1) were used to try and identify working tunnel junctions. The results highlight the fact that whilst such criteria are satisfied if tunneling is the principal conduction mechanism, they are not sufficient to indicate working devices. However, the identification of shorted junctions, not displaying series resistance is, possible.

11247_3_1 was tested using the lock-in and the resistance of junctions found to be slightly lower than previously, $\approx 16 \Omega$ at 300 K for $6 \times 6 \mu\text{m}$ devices, as opposed to the $\approx 22 \Omega$ generally observed. The resistance of the junctions did not scale in proportion to the inverse of their areas. No parabolic dependence of the conductance on the voltage bias was observed and resistance decreased approximately linearly with temperature. This behaviour is characteristic of a shorted device, due to undermilling of the mesa junction.

Devices from 11247_1_2 and 11247_3_2 displayed similar resistances to previous working tunnel junctions and resistance was inversely proportional to junction area. Devices were tested using the lock-in to investigate the dependence of conductance on bias voltage. Figure 4.20(a) shows the increase in conductance with increasing bias of a typical device, which may be fitted adequately by a parabolic curve. Device resistance increased as the temperature was reduced, as shown in Figure 4.20(b). This behaviour indicates that tunneling may be the principal conduction mechanism in the junctions.

11247_1_2 was mounted on the extension for field-in-plane measurements and tested in the Oxford Instruments HelioxTM cryogenic probe, with the 20000 Oe magnet tailpiece in place, as described in Section 3.4.2.3. No characteristic SIF properties were observed, and furthermore, measurements of the aluminium base electrode demonstrated no superconductivity, even at 0.3 K. This highlights the fact that tests on NIN junctions do

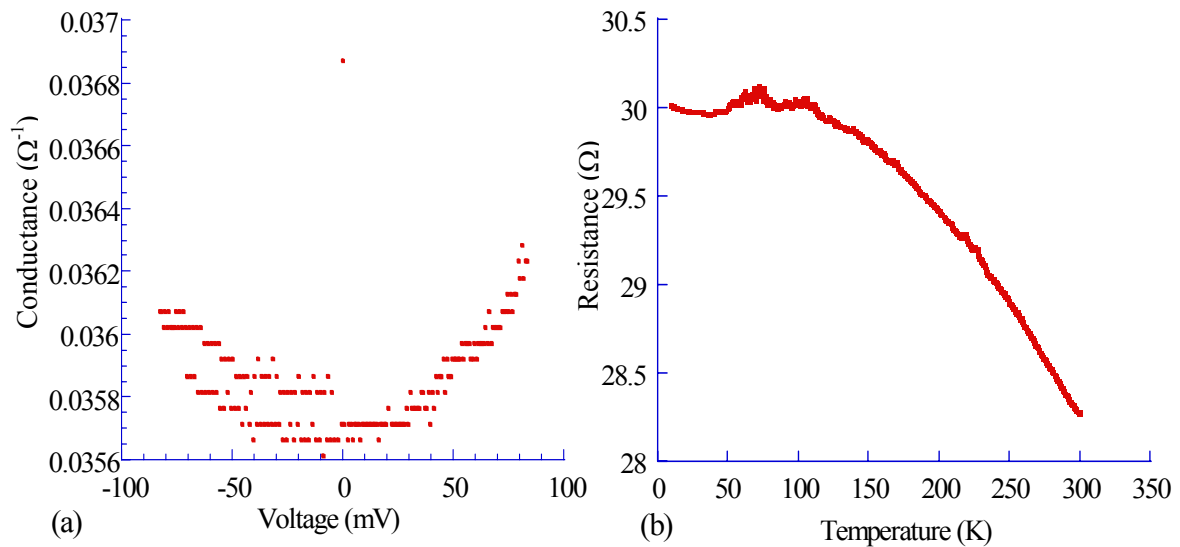


Figure 4.20 : (a) Conductance against bias voltage for 11247_1_2f (b) Resistance against temperature for 11247_1_2f. ‘Glitches’ on both graphs are due to a loose contact in the probe head.

not indicate that a tunnel junction works. The likely cause of device failure is the formation of an oxide or organic layer prior to contact pad deposition, which was not removed adequately by the pre-deposition ion mill.

The observed device failure suggests two areas for improvement and study. Firstly, the device structure should be altered, incorporating a non-superconducting under-layer such as copper or gold. This layer serves two purposes. Most importantly, the demanding requirement on milling times is avoided and the aluminium can be completely milled through. Secondly, a smooth, inert under-layer would protect the aluminium from oxygen diffusion from the substrate. Depositing Cu/Al layers of different thickness and testing their superconducting properties should also be undertaken. The critical field of thin aluminium films could then be investigated.

4.5 Conclusions

The work presented above indicates that the only reliable method to identify tunneling as the principal mechanism for conduction in a tunnel junction is to observe the characteristic I-V relationships for SIS and SIF devices. The observation of an energy gap indicates that tunneling is present. Additionally, the figure-of-merit may be used to estimate the quality of a junction. This finding supports the route suggested above to aid

the production of high quality magnetic tunnel junctions, where SIS and SIF junctions are first fabricated and the effect of changing the electrodes on the FOM observed. Since the analysis of the characteristics of SIS and SIF junctions is simple, they may be used to check and optimise the fabrication route. The production of a stock of known good quality films is recommended for such work.

Certain criteria must be met to make testing of a ‘tunnel junction’ worthwhile. Failure to meet any of the criteria listed below indicates that the device does not work properly, yet satisfying all criteria does not indicate a working device. Firstly, the resistance of devices should be approximately inversely proportional to the expected junction area. The resistance-area product of devices should be similar to previous working tunnel junctions produced on the fabrication route. Junction resistance should increase as temperature decreases, a drop in resistance indicating the presence of a conducting short. The conductance of the device should increase parabolically with bias voltage. Additionally, the prediction of Stratton that junction conductance increases as a function of temperature squared seems to hold.

Investigation of the correlation between properties of normal metal-insulator-normal metal junctions and SIS figure-of-merit indicates that such measurements are unlikely to accurately predict junction quality. The simple model of a device with no series resistance present, but as a perfect tunnel junction and parallel leakage resistance does not fit data well. However, this model does provide the useful insight that a small leakage, represented by a large parallel resistance, significantly decreases junction quality. The correlation between SIS figure-of-merit and either $R(10K)/R(300K)$ or RA is not clear. However, in general, FOM does appear to increase as both RA and $R(10K)/R(300K)$ rise. No trend in FOM is visible with changes in the barrier height and thickness derived by a variation on Simmons’ graphical method. Whilst further work may indicate clear trends in the FOM of SIS junctions with the NIN characteristics measured above, this study shows that such results may not be considered a reliable indicator of junction quality in all cases.

Chapter 5:

High frequency testing of read heads and capacitors

“What I did on my summer holidays”

– Cliff Elwell, age 24.

The development of magnetic materials for read head sensors has been a driving force for magnetic thin film research over the past ten years. Increased storage capacity must be accompanied by faster data transfer, to satisfy the growing demand for high capacity drives in applications such as streamed video and other multimedia. The response speed of a read head is generally measured by full read and write head build. This requires well over 100 processing steps, followed by mounting to slider and associated electronics, it is then tested over a hard disk. This technique provides a huge amount of information, including error rates, side-reading and rate of response. However, the time from the initiation of reader build to testing is prohibitively long for rapid device development. A need has arisen to identify a test, to provide preliminary data, which is quick to perform and does not require full wafer build. High frequency testing of read heads at wafer level, using a network analyser, could be an appropriate, fast, technique. This chapter details the theory and practice of network analyser operation, followed by results obtained during three months study at Seagate Technology Springtown. Models of the electronic system are developed, followed by their relation to those suggested in the literature. The implications of the results on read head design are discussed. The use of a network analyser to measure the dielectric properties of materials is then considered and results are presented.

5.1 Introduction to high frequency testing

The fundamental concepts of transmission lines and network analyser operation are introduced below. Firstly, wave propagation along a transmission line is considered, followed by the important concept of line termination. S-parameters are introduced as a convenient tool for investigating the high frequency characteristics of devices. Finally, the basic operational concept of network analysers, their limitations and errors are discussed.

5.1.1 Transmission lines

A system of two conductors separated by dielectric and capable of maintaining a rapidly oscillating potential difference and current may be modelled as a transmission line.

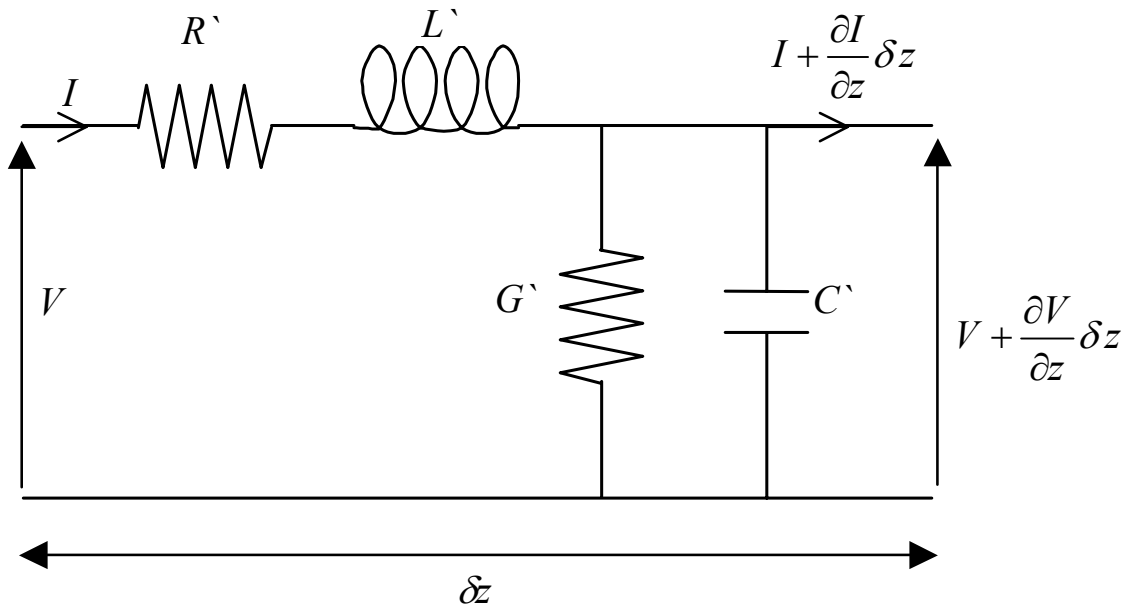


Figure 5.1: Schematic representation of a length of transmission line.

Consider the generalised section of transmission line illustrated by Figure 5.1. L' and C' are the inductance and capacitance per unit length respectively. G' is the leakage resistance per unit length, due to losses through the dielectric and R' is the resistance per unit length of the line. Applying Kirchoff's laws for a small section of the line, δz , the following expressions for the current, I and voltage, V are obtained:

$$V - \left(V + \frac{\partial V}{\partial z} \delta z \right) = L' \delta z \frac{\partial I}{\partial t} + IR' \delta z \Rightarrow \frac{\partial V}{\partial z} = - \left(L' \frac{\partial I}{\partial t} + IR' \right) \quad (5.1)$$

$$I - \left(I + \frac{\partial I}{\partial z} \delta z \right) = C' \delta z \frac{\partial V}{\partial t} + VG' \delta z \Rightarrow \frac{\partial I}{\partial z} = - \left(C' \frac{\partial V}{\partial t} + VG' \right). \quad (5.2)$$

For a sinusoidal variation in voltage and current with time, t :

$$I = I_0 \exp(i\omega t) \quad \text{and} \quad V = V_0 \exp(i\omega t), \quad (5.3)$$

where ω is the angular frequency of oscillation and V_0 and I_0 are constants. Assuming a sinusoidal variation of voltage and current in the transmission line, differentiating (5.1) with respect to z and substituting Equation (5.2) into the result, produces Equation (5.4).

$$\frac{\partial^2 V}{\partial z^2} = (R' + i\omega L')(G' + i\omega C')V \quad (5.4)$$

This is the general form for a wave equation and is solved by:

$$V = A \exp(i\omega t - \gamma z) + B \exp(i\omega t + \gamma z),$$

$$\gamma = \sqrt{(R + i\omega L)(G + i\omega C)}, \quad (5.5)$$

where A and B are arbitrary constants and γ is the propagation constant. Equation (5.5) is substituted into (5.2) to find I . The characteristic impedance of the transmission line, Z_0 , is deduced using Ohm's law:

$$Z_0 = \sqrt{\frac{R + i\omega L}{G + i\omega C}}. \quad (5.6)$$

5.1.1.1 Termination of transmission lines

The impedance Z_T is the termination load of a transmission line. Consider the simplified term for the voltage, $V = V^+ + V^-$, where V^+ and V^- are the incident and reflected contributions to the voltage respectively. Similarly $I = I^+ + I^-$, using Ohm's law and noting that reflected current has the opposite sign to incident current:

$$I = \frac{V^+}{Z_0} - \frac{V^-}{Z_0}. \quad (5.7)$$

The termination impedance, Z_T must satisfy the circuit parameters and solving to find the reflection coefficient, Γ Equations (5.8) and (5.9) are deduced.

$$Z_T = \frac{V}{I} = \frac{V^+ + V^-}{V^+/Z_0 - V^-/Z_0} \quad (5.8)$$

$$\therefore \Gamma = \frac{V^-}{V^+} = \frac{Z_T - Z_0}{Z_T + Z_0} \quad (5.9)$$

The termination load dictates the reflection coefficient of the current and voltage signals. Three key regimes of reflection behaviour are important. Firstly, when the circuit is open, $Z_T = \infty$, so $\Gamma = 1$, total reflection of the wave. Conversely, when the transmission line is terminated with a short circuit, $Z_T = 0$, so $\Gamma = -1$ and all the voltage is reflected, with negative phase compared to the incident voltage. Finally, the impedance matched

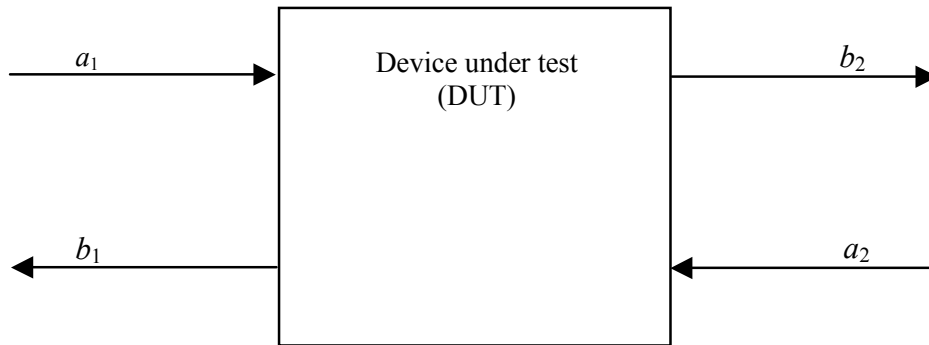


Figure 5.2: Incident and transmitted waves for a two-port network analyser.

case, of particular importance to network analysers, occurs when $Z_T = Z_0$, so $\Gamma = 0$ and all the incident power is transmitted.

5.1.2 Basic network analyser theory

The operation of a network analyser is discussed below. The S-parameter method of characterising termination loads of transmission lines is introduced followed by an introduction to network analyser hardware and limitations.

5.1.2.1 S-parameters

Measuring total voltage or current at high frequency is difficult. The probe impedance and difficulty of placing the probes in the necessary positions effectively make it impractical. Furthermore, such measurements often require the application of a short or open circuit, which has the tendency to destroy devices. However, the response of a device terminating a transmission line may be conveniently represented by scattering (S-) parameters, as recorded by network analysers. S-parameters should not be confused with the Laplacian operator, s , which is widely used in the modelling of high frequency electronics. Consider a normalised input and output wave, $a(z, t)$ and $b(z, t)$ respectively, defining both voltage and current:

$$a(z, t) = \frac{1}{2} \left(\frac{V(z, t)}{\sqrt{Z_0}} + \sqrt{Z_0} I(z, t) \right) \quad (5.10)$$

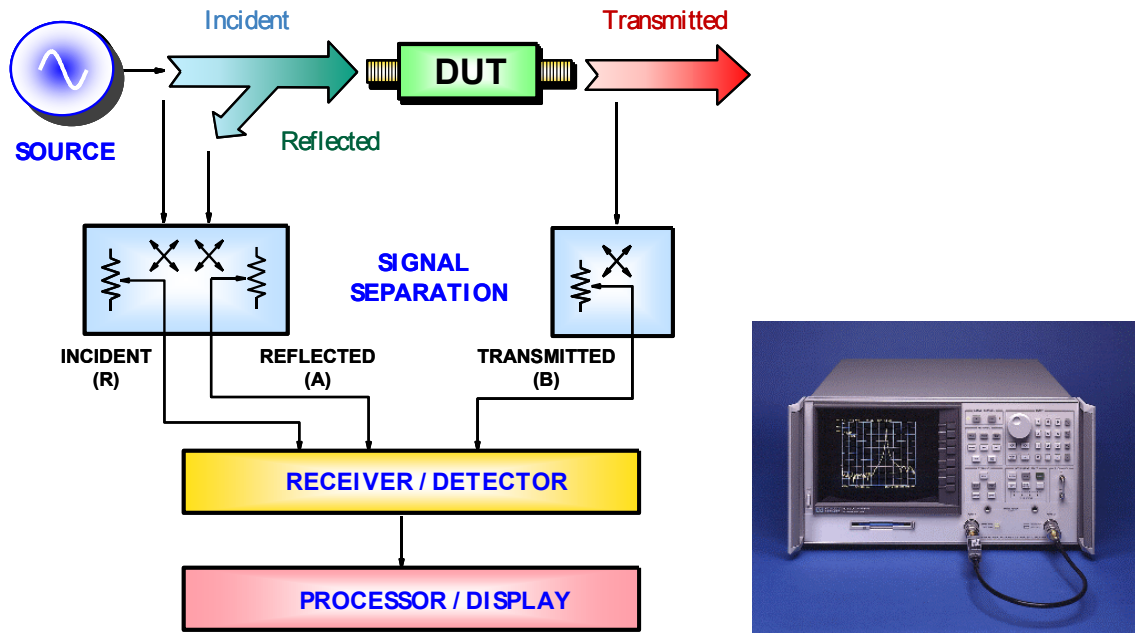


Figure 5.3: Block diagram and picture of a network analyser. DUT is the device under test.

$$b(z,t) = \frac{1}{2} \left(\frac{V(z,t)}{\sqrt{Z_0}} - \sqrt{Z_0} I(z,t) \right). \quad (5.11)$$

Figure 5.2 illustrates the incident and transmitted waves for a two-port network analyser. The S-parameters are defined as:

$$\begin{aligned} S_{11} &= \left. \frac{b_1}{a_1} \right|_{a_2=0} & S_{12} &= \left. \frac{b_1}{a_2} \right|_{a_1=0} \\ S_{21} &= \left. \frac{b_2}{a_1} \right|_{a_2=0} & S_{22} &= \left. \frac{b_2}{a_2} \right|_{a_1=0} \end{aligned} \quad (5.12)$$

S_{11} is the reflection coefficient and S_{21} the transmission coefficient at port 1; S_{22} the reflection and S_{12} the transmission coefficient at port 2. The condition $a_2 = 0$ represents the termination of port 2 with a matched load so the reflection is zero, and similarly for $a_1 = 0$. The reflection coefficient for the transmission line (Section 5.1.1.1) may be redefined for port 1, $\Gamma = S_{11}$. For a network analyser transmission line, $Z_0 = 50 \Omega$. The complex impedance of the termination can be deduced from S_{11} , using Equation (5.9). It is important to realise that S-parameters do not provide a measurement of individual devices in a circuit. Instead, S-parameters measure the combined impedance of a circuit, which must be modelled to retrieve values of inductance, resistance and capacitance.

5.1.2.2 Network analyser hardware

A network analyser is illustrated by the block diagram and photo in Figure 5.3. An internal source is used for modern network analysers. Signal separation is required for two functions. Firstly, splitters or directional couplers are used to measure a portion of the incident signal, providing a reference. Secondly, the incident and reflected waves are separated for input to the device under test (DUT). Signal separation is a major cause of error in measurements, due to the requirements of high isolation, directionality and low loss. Errors are discussed below in Section 5.1.3.1. Generally, couplers are best for both separation purposes as they meet the above requirements, but they are difficult to make. Tuned receivers are used to detect signals; bandpass filters improve sensitivity and reduce noise. An analogue-to-digital converter and digital signal processing are then used to extract magnitude and phase information.

5.1.3 Errors and limitations

5.1.3.1 Error analysis

Systematic errors occur due to imperfections in the analyser and test apparatus. Random errors are due to instrument noise, repeatability or drift over time. Systematic errors are characterised during calibration and mathematically removed from the measurements. Calibration is performed with short circuit, open circuit and matched load, connections being identical to those used during testing of the device. Two-port calibration allows the determination of twelve error terms, producing an extremely accurate result. However, the test setup available was a one-port system, where three error terms may be calculated: directivity, source match and reflection tracking. Accurate calibration requires good termination at port two of the device, which occurs internally for the HP8753es network analyser used in this study. Figure 5.4 shows the effect of one-port calibration. Initially a characteristic ripple pattern dominates the measurement, which is removed by calibration. The effect of poor calibration producing such ripples is reconsidered in Section 5.2.3.6.1 below.

Random errors originate from instrument noise and the difficulty of obtaining identical contacts, particularly because the test apparatus for devices on a wafer requires touch-down contacts. Drift errors are principally caused by temperature variation. These may

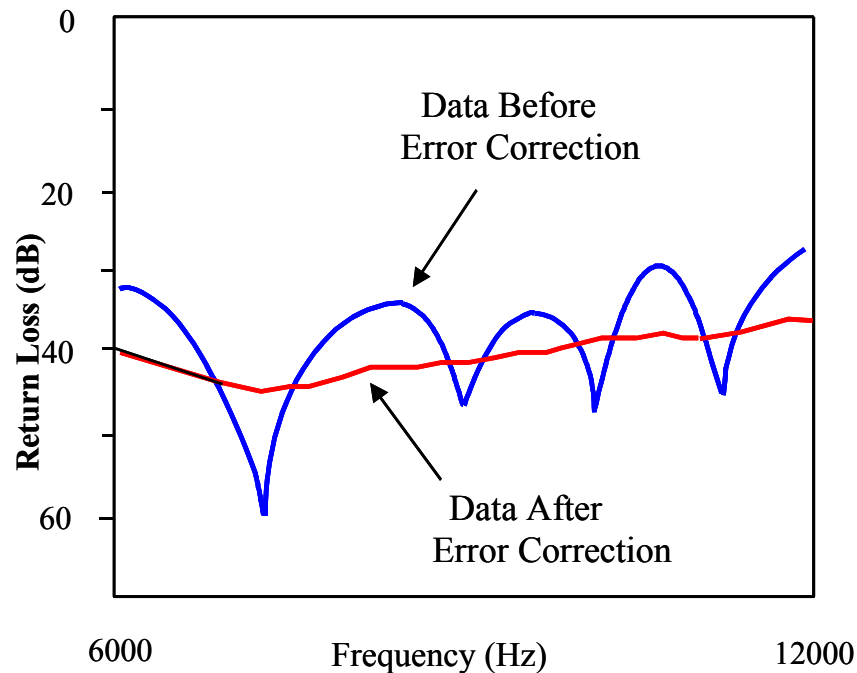


Figure 5.4: The effect of error correction on measurements [HP, 1999].

be eliminated by regular calibration and a temperature controlled environment. Additionally, the network analyser should warm up for two hours, allowing the internal temperature to reach equilibrium.

5.1.3.2 Limitations of the technique

The fundamental limitation of the use of network analyser measurements to identify the characteristics of a circuit has been mentioned in Section 5.1.2.1, but must be stressed again. Values for resistance, inductance and capacitance recovered from measurements are not actual values, but are determined by modelling the circuit. Measurement of S-parameters does not separate components of a device: it measures the whole device response. A simple model may fit the data adequately, but the actual device may be considerably more complex.

5.2 High frequency response of read heads

The high frequency read-back response of the full build reader assembly has received much research by hard disk manufacturers. Owing to corporate secrecy, only a small

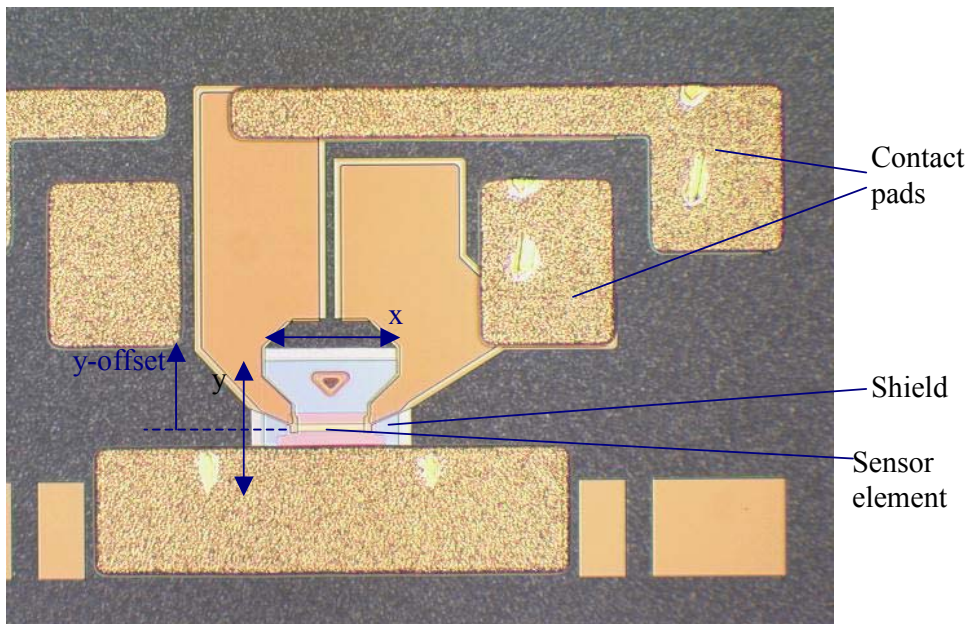


Figure 5.5: A simple reader with square shield of dimensions $x = 100 \mu\text{m}$, $y = 100 \mu\text{m}$ and $y\text{-offset} = 0$.

amount of research has been published, but the fundamental concepts are widely accepted and summarised below.

A simple part-built reader is pictured in Figure 5.5. Fabrication has taken place up to ‘second half gap’; the bottom shield, insulation, wiring layer and sensor have all been deposited. A thin layer of insulation above the sensor element is also defined; this layer is termed the second half gap. Figure 5.5 shows that wiring passes over the shield, the two separated by an insulator (InsA). InsA is not deposited in the region of the sensor element, where the first half gap insulates the sensor from the bottom shield and second half gap lies above it. A simple electrical circuit model of a fully built reader is illustrated by Figure 5.6 [Mallinson, 1996]. Read-back signal is significantly influenced by the manner of amplification, the following treatment considers the effect of amplification on reader response. Circuit resistance is dominated by the sensor, due to its small dimensions compared to the leads. The sensor has resistance R_0 in zero magnetic field, with a magnetically induced change δR . The read head with its associated inductance, L , is shunted by the stray capacitance, C_s . The circuit may be operated with two types of read amplifier: a high internal resistance voltage amplifier, as depicted in Figure 5.6(a), or a low internal resistance current amplifier, shown in Figure 5.6(b). When a high internal impedance amplifier is used, the open circuit voltage, V_{OC} , is measured. The signal

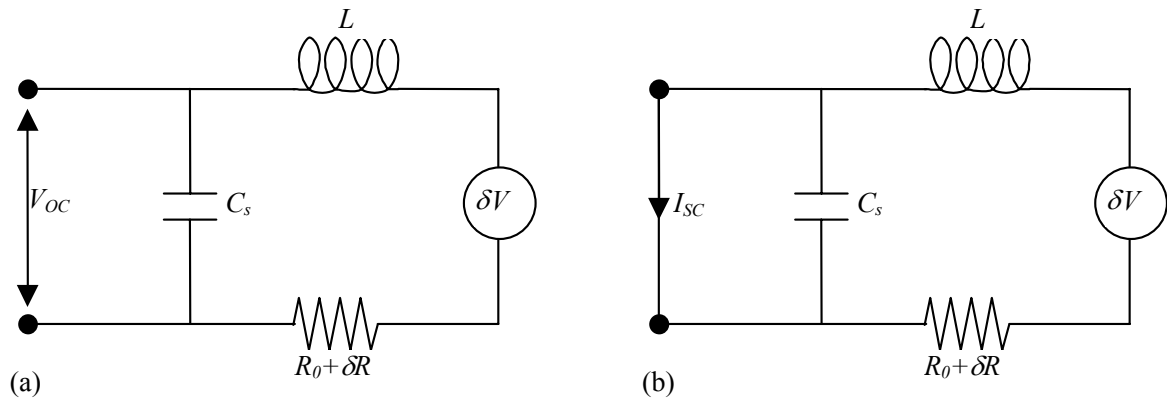


Figure 5.6 : Electrical circuit models of a read head for (a) voltage sensing and (b) current sensing.

current in the loop, I , and the output voltage are represented by Equations (5.13) and (5.14).

$$i = \frac{\delta V}{(R_0 + \delta R) + j\omega L + \frac{1}{j\omega C_s}} \quad (5.13)$$

$$V_{oc} = \frac{i}{j\omega C_s} = \frac{\delta V}{j\omega C(R_0 + \delta R) + (1 - \omega^2 LC_s)} \quad (5.14)$$

An undesirable resonance occurs at angular frequency $\omega = \frac{1}{\sqrt{LC_s}}$, causing oscillation in the output voltage. The inductance in magnetoresistive read heads (those using magnetoresistance, giant magnetoresistance or magnetic tunnel junctions) is low, generally less than 20 nH, compared with inductive heads where it is ~ 1000 nH. The resonant frequency for magnetoresistive read heads is therefore higher than inductive heads, further evidence of their superiority. Constant current is used for this mode of operation and it is therefore often termed the current-forcing, voltage-sensing mode.

Figure 5.6(b) illustrates an amplification configuration with low internal impedance. It is termed the voltage-forcing, current-sensing mode. The short circuit current, I_{sc} , is measured and represented by Equation (5.15); it does not depend on the stray capacitance. No resonance is present and an improved high frequency response is observed.

$$I_{sc} = \frac{\delta V}{(R_0 + \delta R) + j\omega L} \quad (5.15)$$

This latter configuration requires large gain for amplification of the signal and is therefore subject to higher noise than the current-forcing, voltage-sensing mode. High amplifier impedance is generally used, although real amplifiers are significantly more complicated than suggested above. The shunting effect of stray capacitance is extremely important for device performance.

5.2.1 Roll-off frequency

The roll-off frequency of a read head is the frequency at which the return loss falls to -3dB of the DC value. The return loss, or attenuation, is generally displayed by the network analyser and defined by Equation (5.16).

$$\text{Attenuation} = 20 \log \left(\frac{|Z|}{Z_{DC}} \right) \quad (5.16)$$

The roll-off frequency is equivalent to the half-power of the circuit, at which point a signal may no longer be distinguished from noise. This occurs when the impedance falls to $\frac{\text{DC value}}{\sqrt{2}}$. Substituting into Equation (5.16), the attenuation is 3.010 (to 3 d.p.) at the half-power point. Clearly data may often be read below the -3dB point, with the use of filtering and data processing. However, determination of the -3dB point is widely used to provide a measure of the limit of data measurement.

5.2.2 Experimental procedures

Considerable effort has been made to investigate the frequency response of read heads, but such work is based on fully built devices, which are time consuming to fabricate. The experimental methods employed in this study to investigate the frequency response of a part-built reader are discussed below. Not only does this technique drastically reduce the time to investigate reader configurations, but also read heads and writers may be built up piece-by-piece to determine the effect of each layer on the frequency response. Full build is still required for the determination of error and side reading rates, but the ability to

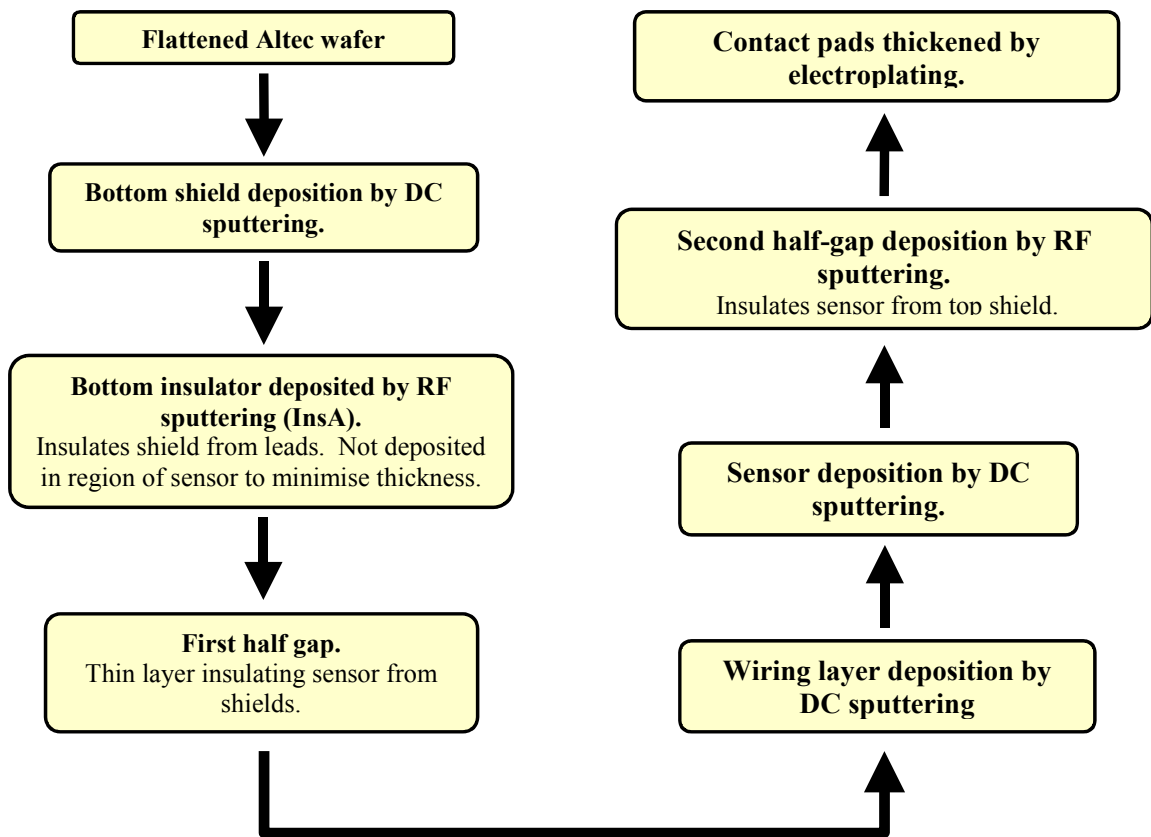


Figure 5.7: Overview of the fabrication route of the Y6 read head wafers.

dissect read and write heads could dramatically improve understanding of the system. The giant magnetoresistive or tunnel junction sensor structure is regularly changed in industrial research making measurements of read-back from a hard disk difficult to compare. However, measurement of readers with a network analyser does not depend significantly on the magnetic structure of the sensor element, thus allowing better comparison of wafers.

5.2.2.1 Production of devices

Read heads were fabricated up to second half gap, as described in Section 5.2 above. Figure 5.5 illustrates the terminology and standard reader configuration tested. Standard lithography and processing techniques were used. Figure 5.7 illustrates the key processes of device fabrication, excluding lithography, seed layers and other minor steps. Details of precise processes are not included, in accordance with the wishes of Seagate Technology. The shields, read element, wiring and contact pads seed layer were deposited by DC magnetron sputtering. Insulators were deposited by AC sputtering and the contact pads

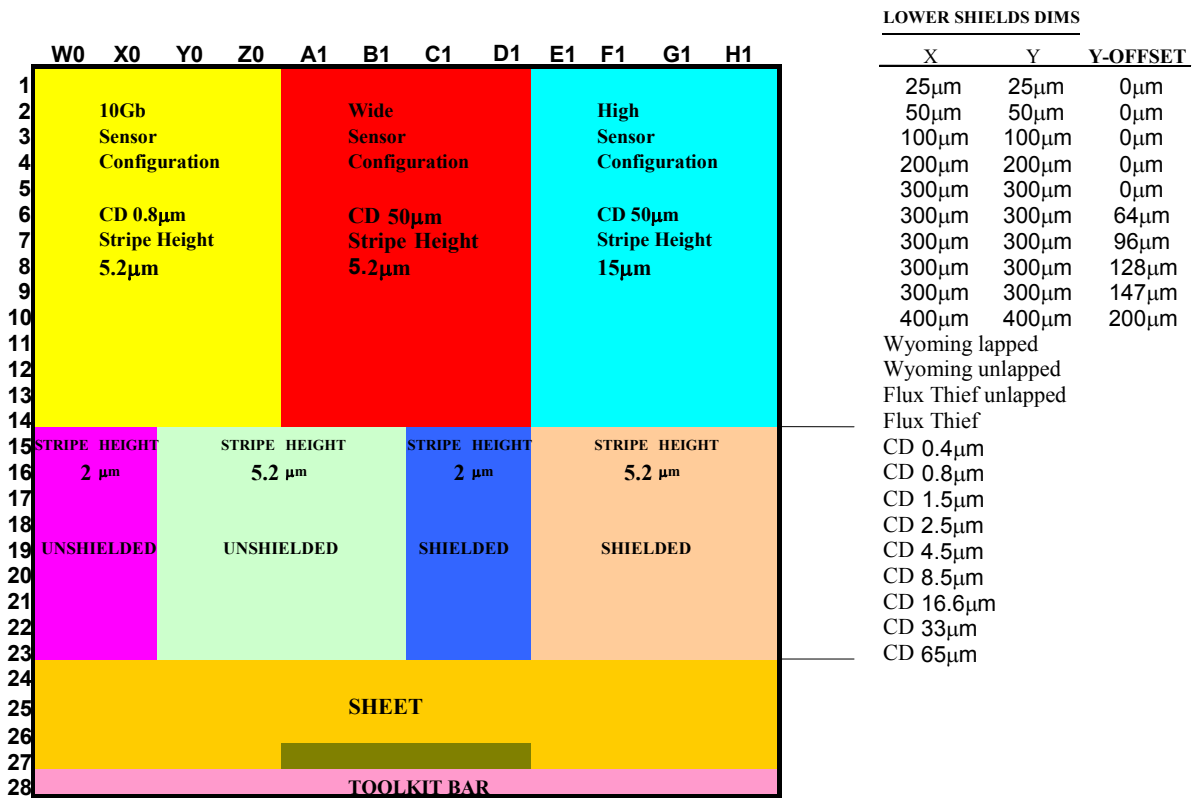


Figure 5.8: CAD design for one quadrant of the Y6 wafers. One read head lies at each coordinate. For example, the device at C115 is shielded, with 2 µm stripe height and 0.4 µm CD.

electroplated with copper to make them more robust. The read element on all heads was a giant magnetoresistance (GMR) spin valve structure. The magnetic properties of some devices were investigated using a Kerrscope and prober, but are not presented here.

Figure 5.8 illustrates the device layout for the wafers tested. Each quadrant, A, B, C or D, consists of tessellations of this layout, with device numbers continuing incrementally so that each reader is assigned a unique name within the wafer. The length of the sensor is termed the critical dimension, CD and stripe height is the width of the read head, as indicated in Figure 5.9(a). The Flux-thief and Wyoming shield designs are illustrated in Figure 5.9(b) and (c) respectively. Such designs have been devised to improve the magnetic shielding of the sensor from stray fields. Lapped geometry approximates the configuration in the read head by removal of the shield and insulator below the sensor element, as shown in Figure 5.9(d). The size and y-offset of square shields, as shown in Figure 5.5, were also varied. Y-offset is defined as the displacement of the centre of the square shield from the sensor.

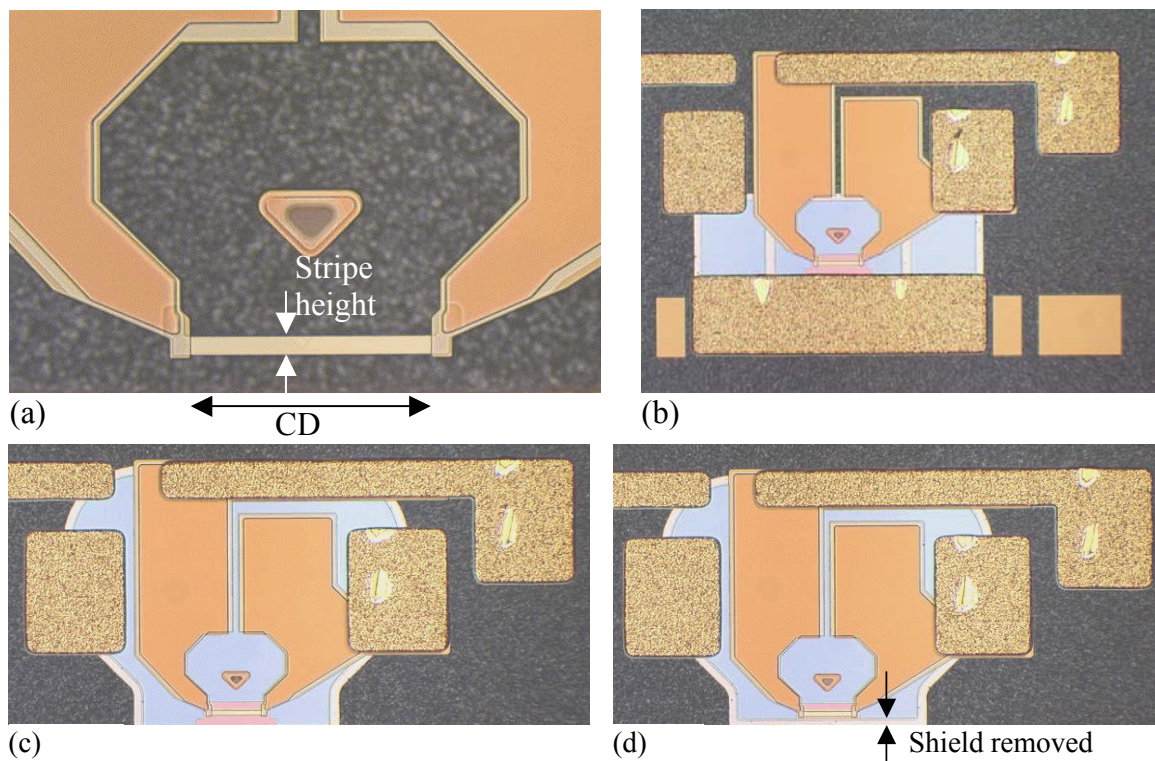


Figure 5.9: Pictures of the reader geometry. (a) stripe height and CD on an unshielded reader. (b) The Flux-thief shield design (in blue). (c) Wyoming shield, unlapped. (d) Wyoming shield, lapped.

The mask-set is designed to provide a large quantity of data regarding the effect of shield and reader dimensions on the performance of a reader. In addition to design alterations of the geometry, wafers were produced with different thickness insulating layers and copper instead of magnetic shields. A summary of the differences between wafers studied is shown in Table 5.1, below. A batch of wafers with varying InsA were started to measure directly the effect of the capacitance between the leads and shield. However, due to other priorities within the facility and the difficulty of passing non-standard wafers through the cleanroom, they were not completed.

5.2.2.2 Testing procedure

An HP8753es network analyser was used to test devices at wafer level as shown in Figure 5.10. A simple two-probe touch-down contact with micrometer adjustment was used, with a microscope enabling alignment to contact pads. Wafers were clamped firmly during measurement using a rising stage. A constant probe pitch of 150 μm was used, matching the contact pad separation, as shown in Figure 5.11.

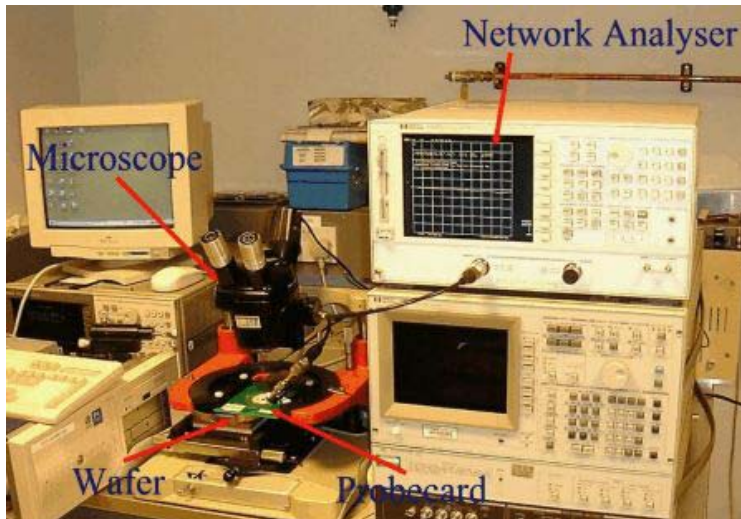


Figure 5.10: The measurement apparatus.



Figure 5.11: Probe tips, measuring the matched resistance calibration sample.

<i>Wafer code</i>	<i>First half gap (nm)</i>	<i>Other difference</i>
Y50196_Y6HJ0	26.4	
Y50316_Y6HL0	50.0	
Y50386_Y6HLS	51.4	
Y50326_Y6HL4	21.4	
Y50616_Y6H0C	42.8	
Y50646_Y6H00	42.8	
Y50486_Y6HMW	49.6/26.3	
Y50476_Y6HMS	26.7	
Y50426_Y6HN8	9.4	
Y50986_Y6HLK	51.2	Copper shields
Y50566_Y6HNS	48.6/43.1/41.5	
Y50546_YH NK	42.8/48.1	

Table 5.1: Differences between the wafers presented. Multiple values of the first half gap indicate measurement problems due to elipsometer or operator error.

Thermal drift was minimised by the air-conditioned environment and by allowing the apparatus to warm up for two hours before use, as recommended in the manual and discussed in Section 5.1.3.1. The network analyser was calibrated for one-port operation before use, using a short circuit, open circuit and matched load of 50Ω . The GG Industries CS-8 calibration substrate was used, over the range 1 MHz to 6 GHz. The

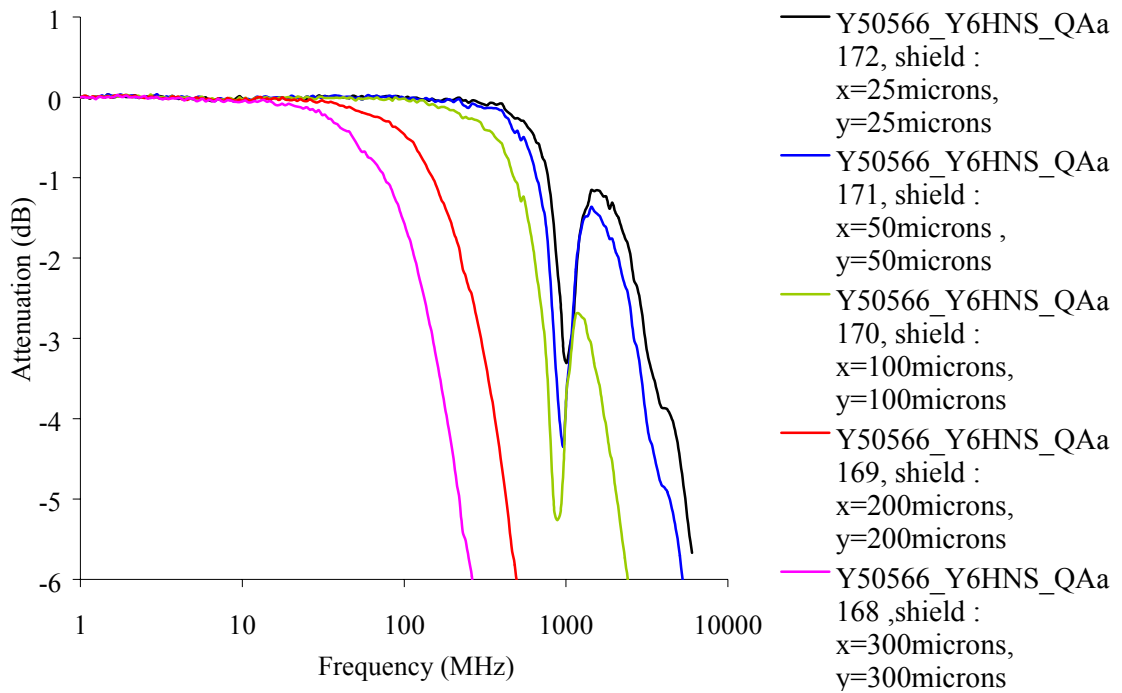


Figure 5.12: Attenuation vs frequency as shield size is increased.

second port was terminated internally with a $50\ \Omega$ matched load to minimize error. Errors introduced by variance in the exact positioning of the touch-down probes on the contact pads were investigated by aligning and measuring devices repeatedly. No variation in attenuation characteristics was observed. Additionally, ten devices on the wafer Y50566_Y6HNS were tested regularly over a period of one month, over which time no changes were detected in the attenuation of readers, indicating consistent calibration. The probe was used in S-parameter mode with a moderate rate of frequency increase during measurements in order to ensure an effectively constant frequency over the electrical length of the device. Measured S-parameters were recorded on a computer and Equation (5.9) (where $\Gamma = S_{11}$) was used to recover the complex impedance. The attenuation (Equation (5.16)) was recorded graphically.

5.2.3 Results and discussion

5.2.3.1 The effect of shield area on roll-off frequency

Figure 5.12 shows attenuation against frequency for readers with increasing shield size for Y50566_Y6HNS, devices A168 to A172. As shield size increases, roll-off frequency

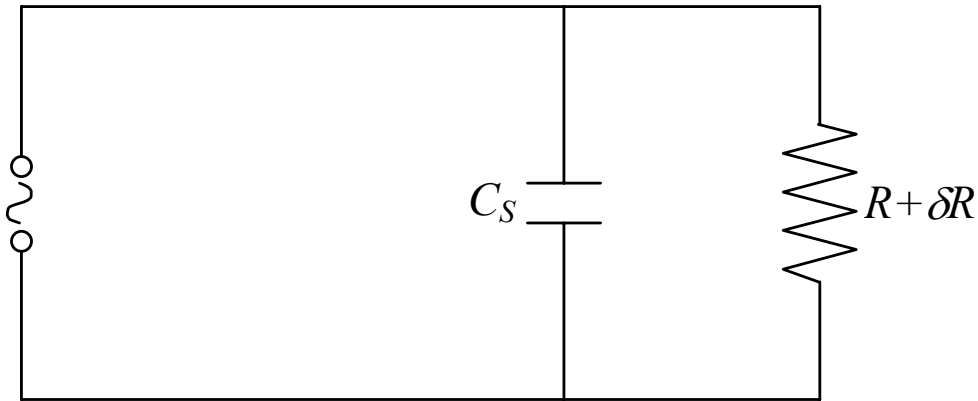


Figure 5.13: Capacitively shunted model for a read head

decreases. At high frequency, the presence of a resonant peak is characteristic of LCR circuits and will be discussed below (Section 5.2.3.6). Using a one-port system, only two system variables can be calculated; and therefore the simple RC circuit shown in Figure 5.13 was used to model the behaviour. The roll-off frequency for such an RC circuit is calculated by inserting the half-power criterion into the equation for the impedance of the reader. At zero frequency, the shunt capacitance has no effect and the circuit impedance is simply the resistance of the wires and reader, $R + \delta R$, from which Equation (5.17) is derived.

$$Z_{roll-off} = \frac{\delta R + R}{\sqrt{2}} = \frac{1}{\sqrt{(2\pi f_{3dB} C_S)^2 + 1/(\delta R + R)^2}}$$

$$\therefore f_{3dB} = \frac{1}{2\pi C_S (\delta R + R)}, \quad (5.17)$$

where f_{3dB} is the roll-off frequency and C_S the shunt capacitance. The capacitor is expected to originate from the wiring-shield sandwich, with InsA and first half gap dielectric. Assuming this is the sole cause of capacitance, Equation (5.18) should be applicable to the system.

$$C_S = \frac{\epsilon_0 \epsilon_r A}{d}, \quad (5.18)$$

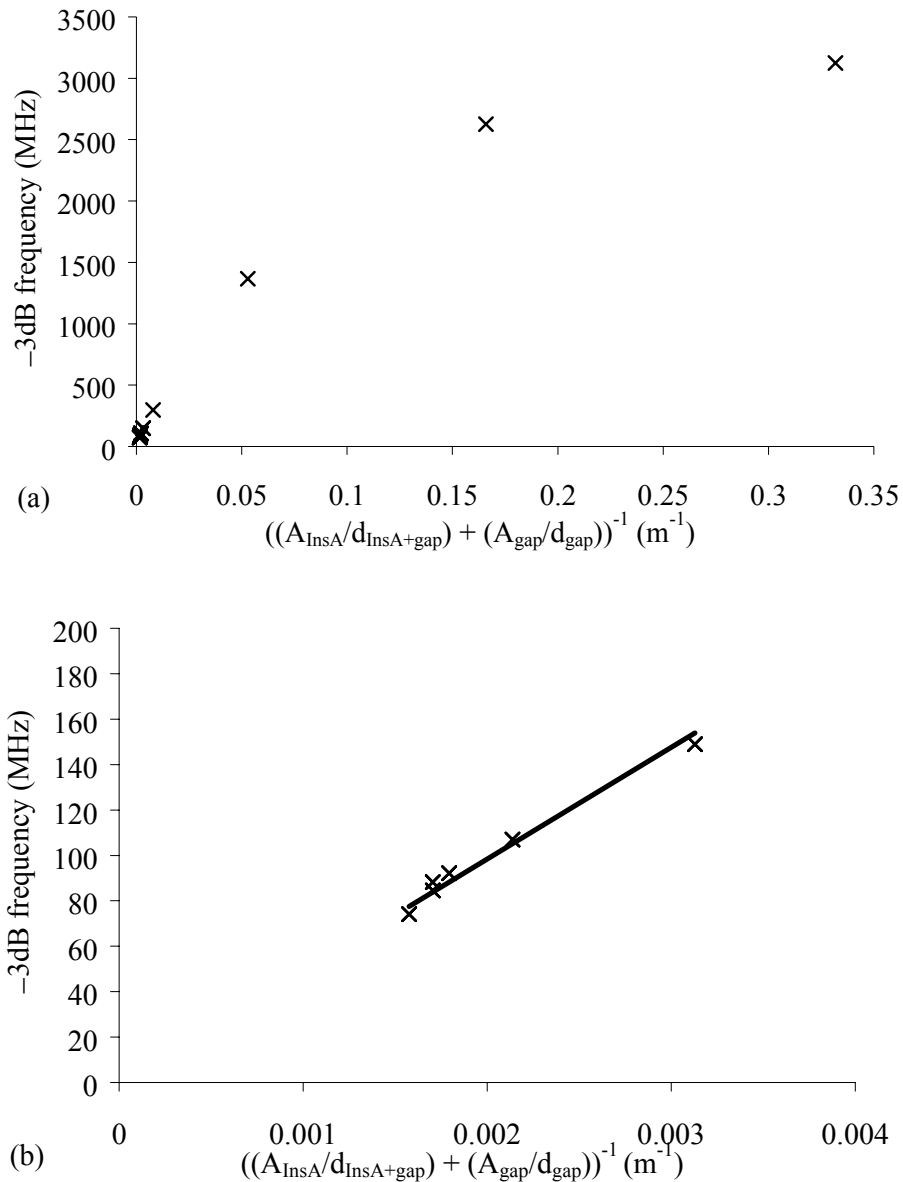


Figure 5.14: The effect of overlap of shields with wiring on -3dB frequency. (a) The data for all areas. (b) Data for large area only.

where ϵ_r is the relative permittivity of the dielectric, ϵ_0 is the permittivity of free space, A the area and d is the separation of capacitor plates. The area of contact leads overlapping the shield and separated by $InsA$, A_{InsA} , was calculated using the CAD for each configuration. The area of the sensor separated from the shield by the first half gap, A_{gap} , was also measured. The effect of these two different areas and thickness is to replace the single capacitor in Figure 5.13 by two in parallel. Total capacitance, C_{tot} , is the sum of the sum of the capacitance formed by the overlap between the shields and wiring with

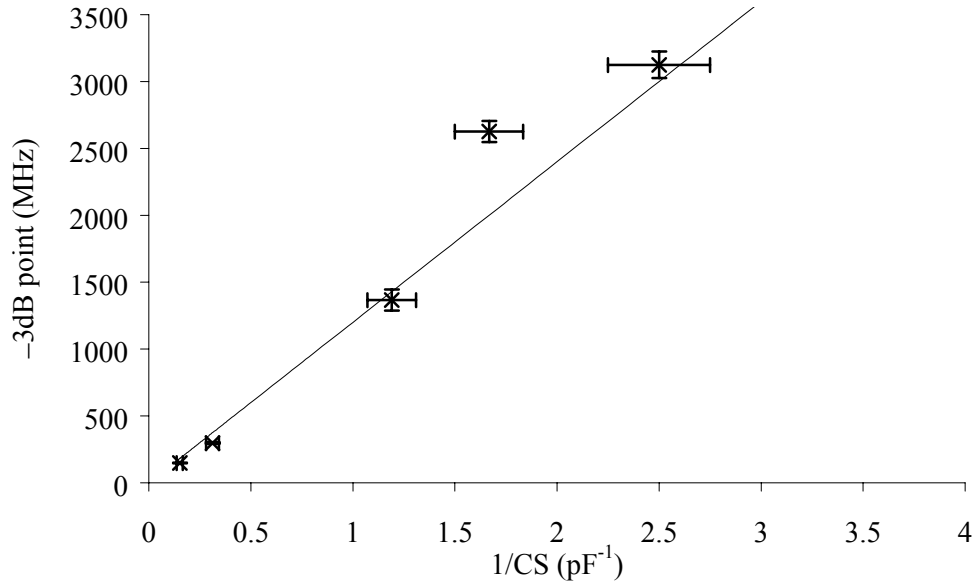


Figure 5.15: –3dB point against capacitance, calculated from the impedance data.

dielectric InsA, C_{InsA} , and that formed by the overlap between sensor and shield with first half gap as the dielectric, C_{gap} . Using Equations (5.17) and (5.18):

$$f_{3dB} \propto \frac{1}{C_{InsA} + C_{Gap}} \propto \left(\frac{A_{InsA}}{d_{InsA}} + \frac{A_{Gap}}{d_{Gap}} \right)^{-1}, \quad (5.19)$$

where d_{InsA} and d_{gap} are the thickness of InsA and the first half gap, respectively. Roll-off frequency was estimated from the data by taking the measurement point nearest to –3dB attenuation. Figure 5.14 shows the roll-off frequency plotted against the expression of Equation (5.19). This model fits the data well for large areas, as shown by Figure 5.14(b), but at low area the increase of roll-off frequency flattens (Figure 5.14(a)). Consider a further, small, capacitance in parallel to that formed between the shield and wiring. At high shield area this extra capacitance is insignificant compared to $C_{InsA} + C_{gap}$. However, at low area C_{InsA} has dropped dramatically and the extra capacitance becomes significant, eventually dominating the device response and the roll-off frequency falls below that predicted by Equation (5.19). Figure 5.15 shows the roll-off frequency against $1/C_S$, as calculated from the impedance data. The linear trend to high frequency suggests that roll-off of the impedance is due to capacitive shunting of the sensor element. The linear trend exhibited by Figure 5.15 at frequencies above those at

which Figure 5.14 deviates from linearity also suggests that an extra capacitance is present in the system. The origin of this second capacitance is investigated in Section 5.2.3.6.

5.2.3.1.1 Shield design

Optimisation of the magnetic shielding of the sensor element has led to the development of a wide range of shield designs; Figure 5.9 shows the Flux-thief and Wyoming shields. Roll-off frequency decreased as shield area increased, in agreement with the capacitively shunted reader model. As expected, no difference was observed between lapped and unlapped geometry. Wafer level testing is not significantly affected by shield areas not directly below the wiring or sensor.

5.2.3.2 The effect of sensor length on roll-off frequency

Figure 5.16(a) shows the effect of reader length (CD) on roll-off frequency. Measurements were taken for shielded devices Y50566_Y6HNS_V050-58 (see Figure 5.8). The linear trend in Figure 5.16(a) supports the capacitively shunted reader model presented in Section 5.2.3.1, where roll-off is described by Equation (5.17). No magnetic field is applied during measurement, so $\delta R = 0$. Predicted roll-off frequency $\propto 1/R$ and sensor resistance $\propto CD$. R was also deduced from the real part of Equation (5.9) using S-parameter measurements. Roll-off frequency is plotted against calculated $1/R$ in Figure 5.16(b). The linear correlation at high resistance supports the use of the capacitively shunted reader model at large CD. At low CD, both graphs deviate from the straight line predicted, but curve in different directions. This indicates that the model breaks down at low resistance; recovery of the resistance from the impedance using Equation (5.17) is no longer valid. The circuit is more complicated than shown in Figure 5.13, which may be an artefact of measurement errors. Improvements to the model are discussed in Section 5.2.3.6.

5.2.3.3 Stripe height

Stripe height is the width of the sensor as shown in Figure 5.5. Equation (5.17), representing the capacitively shunted reader model, predicts that roll-off frequency is proportional to reader width. Only two comparable stripe heights were available, as

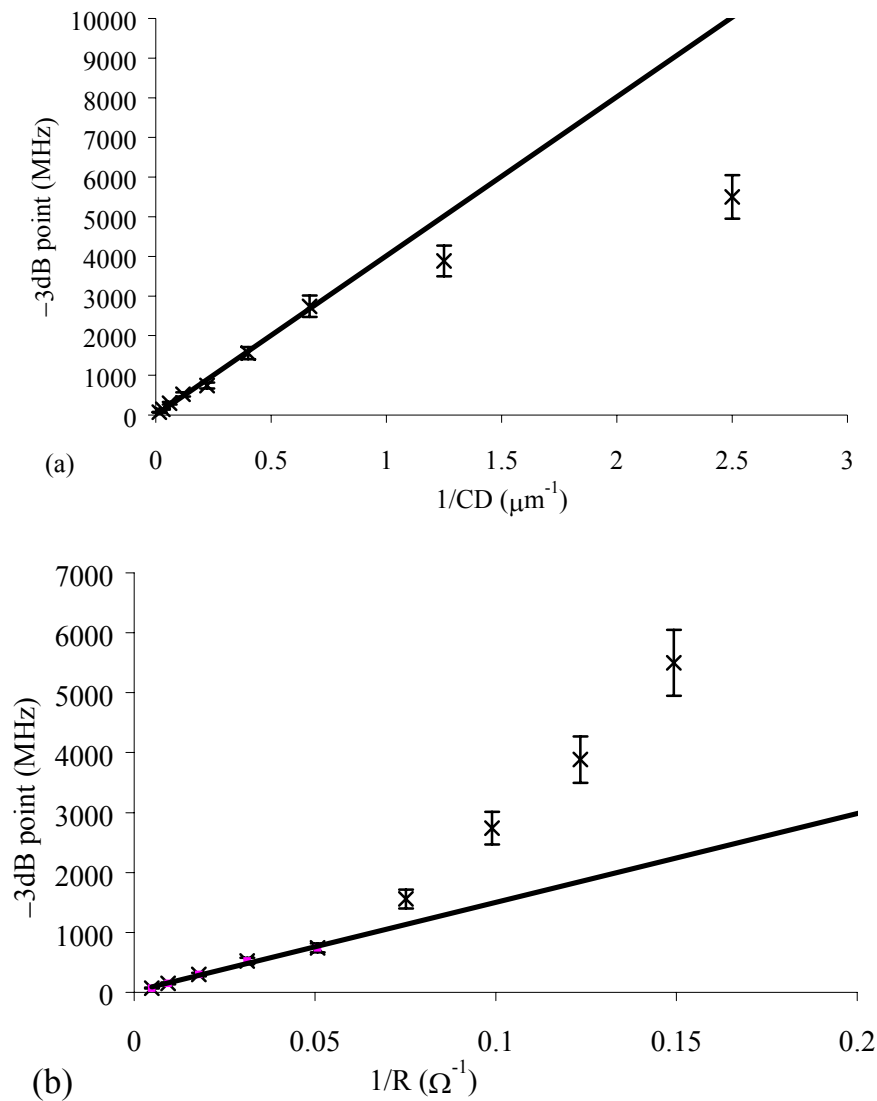


Figure 5.16: (a) The effect of CD on the roll-off frequency. (b) –3dB point versus resistance, as calculated from the impedance.

shown by Figure 5.8. Roll-off frequency was observed to be consistently higher for larger stripe height readers.

5.2.3.4 Gap thickness

Equation (5.19) indicates that if the capacitance in the region of the sensor is significant, roll-off frequency should rise as the first half gap thickness increases. Measurements of first half gap, using an ellipsometer, for available wafers are shown in Table 5.1. The range of measured first half gap values for some wafers indicates that the measurements were either incorrectly performed or the ellipsometer poorly calibrated. This occurred

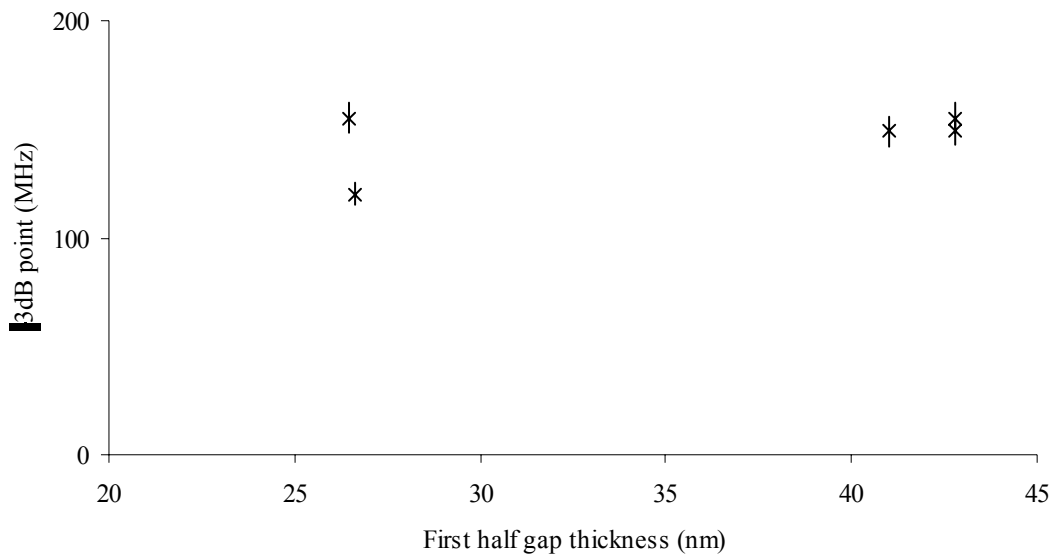


Figure 5.17: No trend is evident in roll-off frequency as gap thickness changes. Changes in sensor stack lead to variation in device resistance; only readers of similar resistance are shown.

because the wafers were not standard production lots and therefore some processes were not properly optimised or performed. Figure 5.17 shows that no trend in roll-off frequency is evident as first half gap thickness changes. Device resistance was checked and only devices of similar resistance presented. Changes in to the sensor deposition are responsible for the changes in resistance. The sensor-to-shield capacitance is not significant for such resistance and shield configuration. First half gap thickness could be significant for other geometries.

5.2.3.5 Temperature dependence of roll-off frequency

Read heads operate at up to 200°C and the demands of higher data transfer imply an increase in rotation speed, raising the head temperature. The temperature dependence of read-back characteristics is critical to read head performance. The effect of temperature on the devices was investigated by mounting the wafers on a Phasemetrics prober where measurements took place between 20°C and 100°C. Roll-off frequency is plotted against $1/(\text{temperature})$ in Figure 5.18. The line shown is a linear regression of the data, with r^2 of 94%, a reasonable fit. The r^2 value represents the proportion of the variation of the data which is described by the linear regression. The resistance of the metallic sensor

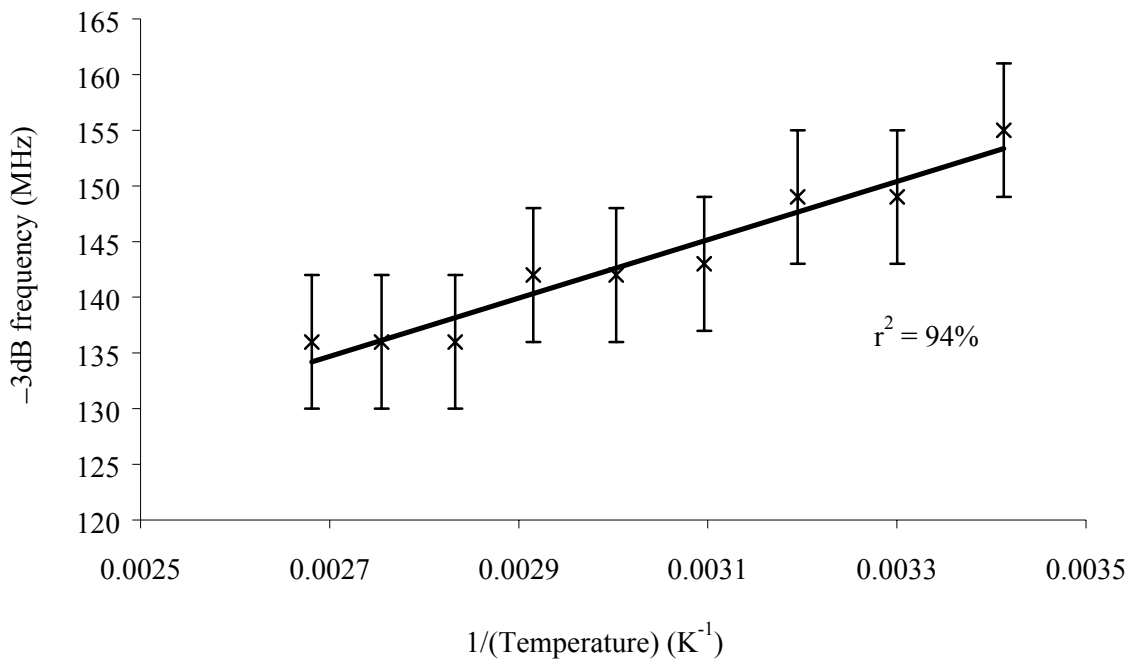


Figure 5.18: Dependence of the roll-off frequency on temperature for device Y50566_Y6HNS_QAA168.

element is expected to increase linearly with temperature. Figure 5.18 is therefore in agreement with the capacitively shunted model, where resistance is inversely proportional to roll-off frequency. However, visible quantisation of the data is evident, as reflected by the error bars, and other effects may contribute to the temperature characteristics.

5.2.3.6 Modification of the model

At low capacitance and resistance, behaviour of the read heads deviates from that predicted by the capacitively shunted model as discussed in Sections 5.2.3.1 and 5.2.3.2. The attenuation against frequency graphs at low capacitance and resistance exhibit a resonant peak, as shown Figure 5.12. As frequency increases the impedance of a capacitor always decreases attenuation (making it more negative), but the impedance of an inductor increases, causing a rise in attenuation. The observed resonant peak indicates that contributions are present from at least two capacitors and one inductor. However, it is likely that the circuit is considerably more complicated.

Figure 5.14(a) indicates that a second capacitance is present in parallel to the sensor, as discussed in Section 5.2.3.1. The origin of this capacitance was investigated by measuring devices with no shields. Figure 5.19 shows the attenuation against frequency

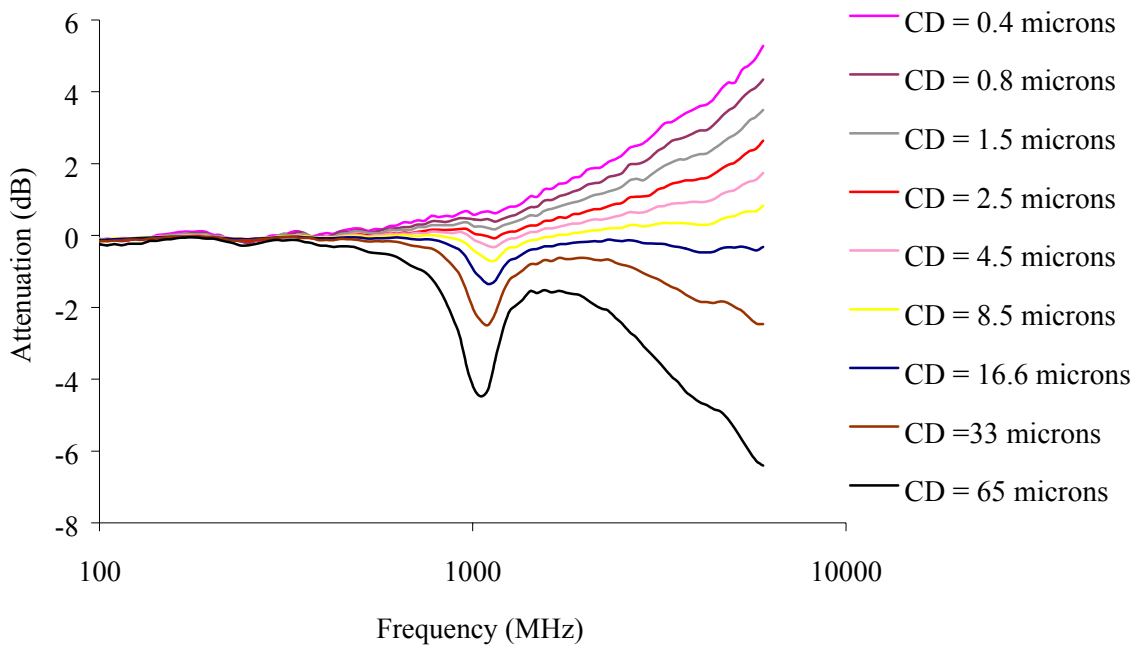


Figure 5.19: The effect of CD on attenuation for unshielded devices.

curves for unshielded devices of varying CD, Y50566_Y6HNS_QAA150-55. Capacitive roll-off of read head performance is still observed for high resistance sensors. This indicates that a second capacitance, in parallel to the sensor is indeed present. As expected, roll-off frequency is significantly higher than with shields present. To account for the effect of this capacitor and the inductance in the system, the model is modified to that shown in Figure 5.20. Two possible causes for the additional capacitance are the wiring-to-substrate geometry and calibration error.

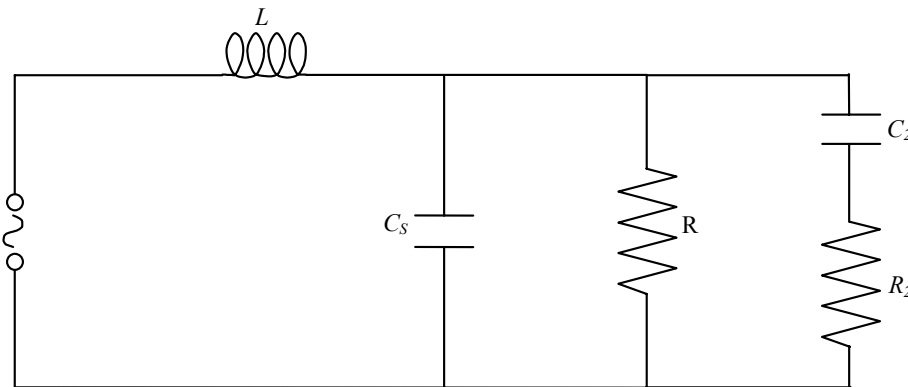


Figure 5.20: Model for the read head including inductance and extra capacitance (C_2) an extra resistance, R_2 is added for the case of substrate resistance.

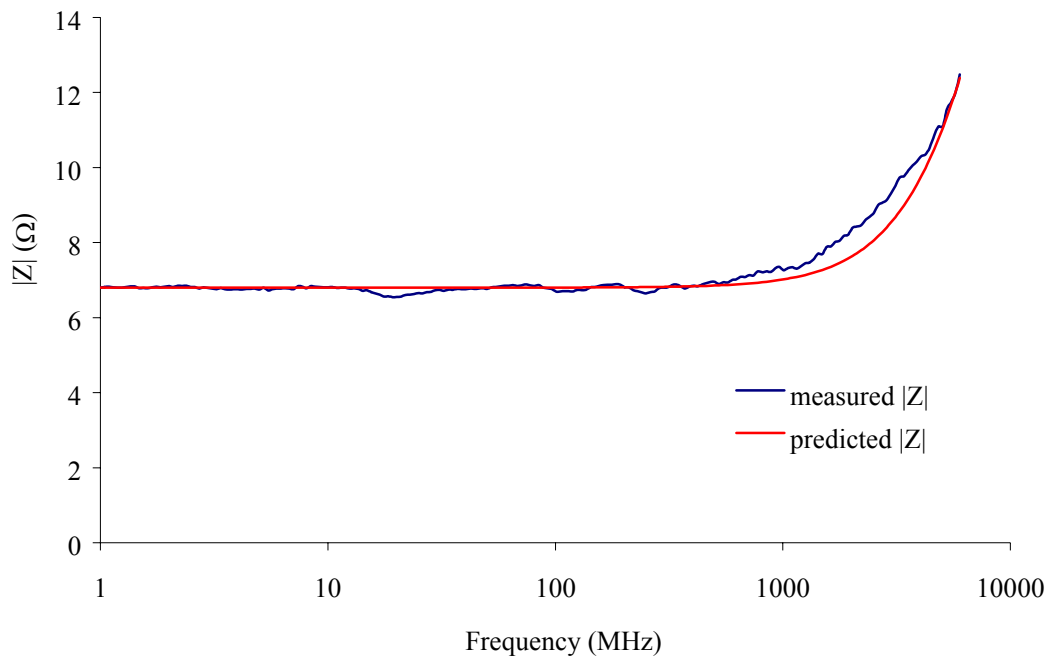


Figure 5.21: The variation of the magnitude of the impedance and modelled impedance for an unshielded device with $CD = 0.4 \mu\text{m}$, Y50566_Y6HNS_QAA158.

The contribution to capacitance from the wiring-to-substrate area was estimated from Equation (5.17) and the known device properties. The substrate used was AltecTM, a relatively low resistance yet versatile and durable material. The resistance of the AltecTM was assumed to be negligible. Estimates took place for the highest resistance, $65 \mu\text{m}$ CD, assuming a dielectric constant of 8.5 for the alumina and dielectric thickness 50 nm. The device resistance was measured and wiring layer area calculated from the mask-set design. When substituted into Equation (5.17), these values produce a roll-off frequency of 650 MHz, lower than that observed (930 ± 15 MHz).

The model shown in Figure 5.20 was used to investigate the substrate resistance required to produce the observed roll-off frequency. Inductance was neglected. Using the same values as above, two complex roots were derived for the impedance: $Z_{Altec} = 5723 + 151784i$ and $Z_{Altec} = 5309 + 140753i$. Whilst a real root is expected, the imaginary component is extremely high impedance. The values of the real root are high and may be appropriate for the AltecTM substrate. Since roll-off was observed with no shields present, a high resistance substrate, such as silicon oxide, may eventually be required to improve performance.

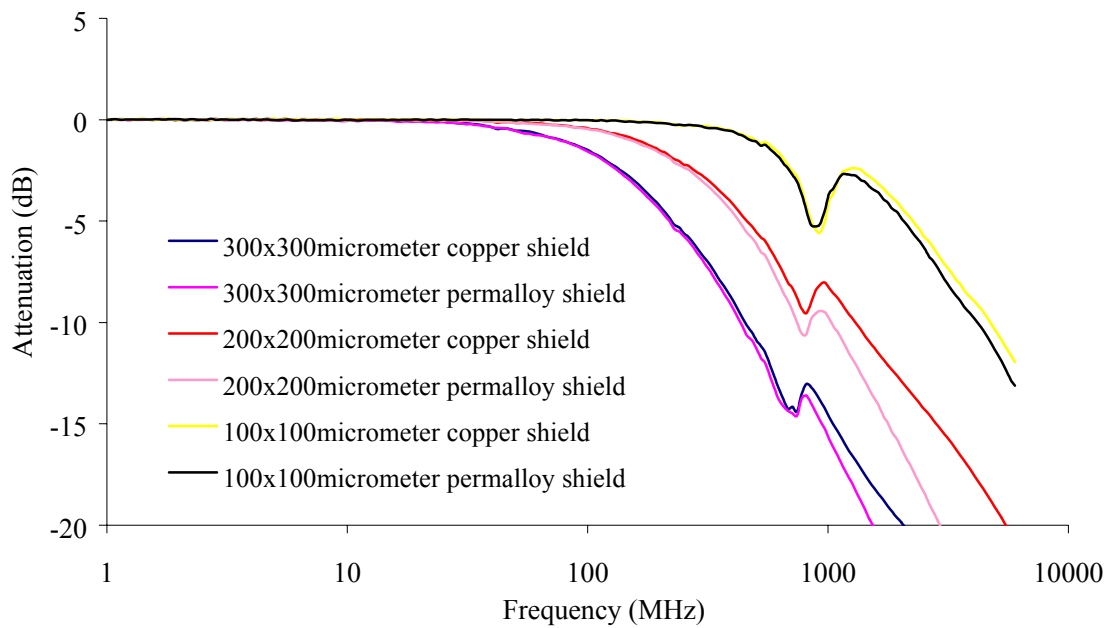


Figure 5.22: The effect of copper versus magnetic shields. Differences between comparable devices are attributed to sensor resistance variation.

Figure 5.19 shows that unshielded devices with small CD and therefore low sensor resistance, display an increase in impedance. This is inductive behaviour. No resonant peak is present for $CD = 0.4 \mu\text{m}$ and the circuit may be modelled as a resistor and inductor in series, as described by Equation (5.20).

$$Z = R + i2\pi fL \quad (5.20)$$

Solving Equation (5.20) at 6 GHz, produces the very small inductance, $L = 2.75 \times 10^{-10} \text{ H}$. Using this value for inductance, modelled impedance is plotted against frequency in Figure 5.21. The modelled values correlate well with experimental results.

5.2.3.6.1 Origin of the inductance

The inductance present in the circuit may be due to measurement artefacts, lead configuration or magnetic effects. The effect of the shield material on the inductance was investigated by replacing the permalloy shields with copper. The roll-off characteristics for equivalent devices with copper and magnetic shields were not found to be significantly different, as shown by Figure 5.22. The inductance is not a result of magnetic effects in the shields.

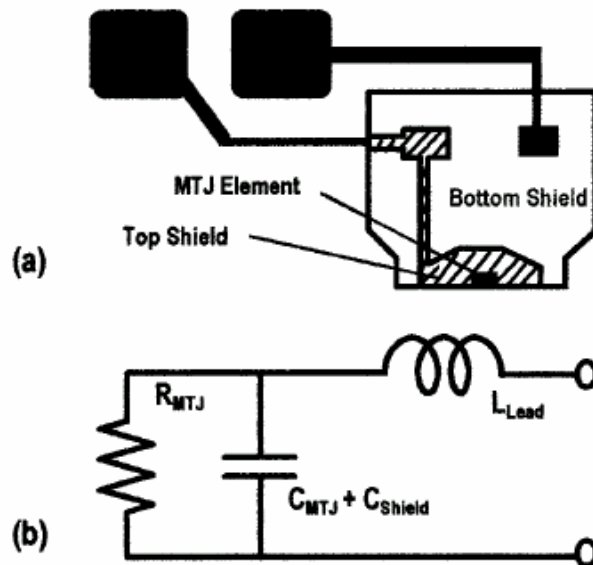


Figure 5.23: (a) Reader geometry and (b) circuit model used by Shimazawa. [Shimazawa, 2001]

Calibration error is a possible source of the inductance since one-port calibration only corrects three error terms opposed to the twelve of two-port calibration, as discussed in Section 5.1.3.1. Figure 5.4 shows that calibration error may lead to ‘ripples’ in the observed attenuation. Given that the inductance calculated above is so small, it is possible that it is an artefact of measurement and not a device characteristic. The network analyser performance was further investigated by measuring resistors in the toolkit of the mask (Figure 5.8). The characteristics of inductance were observed in attenuation measurements, despite the simple structure and short device wiring leads. This implies that the principal origin of the inductance is calibration errors, though inductance could be significant for other reader configurations.

5.2.4 Subsequent literature

The frequency response of magnetic tunnel junction read heads of the geometry shown in Figure 5.23(a) has been investigated by Shimazawa *et al.* [Shimazawa, 2001]. They propose the model shown in Figure 5.23(b) to explain the frequency response, based on the work presented by Mallinson and discussed above in Section 5.2 [Mallinson, 1996]. Measurements of read-back data from a hard disk were made. Two tunnel junction areas were measured, varying the resistance of the reader. The effect of dielectric was also

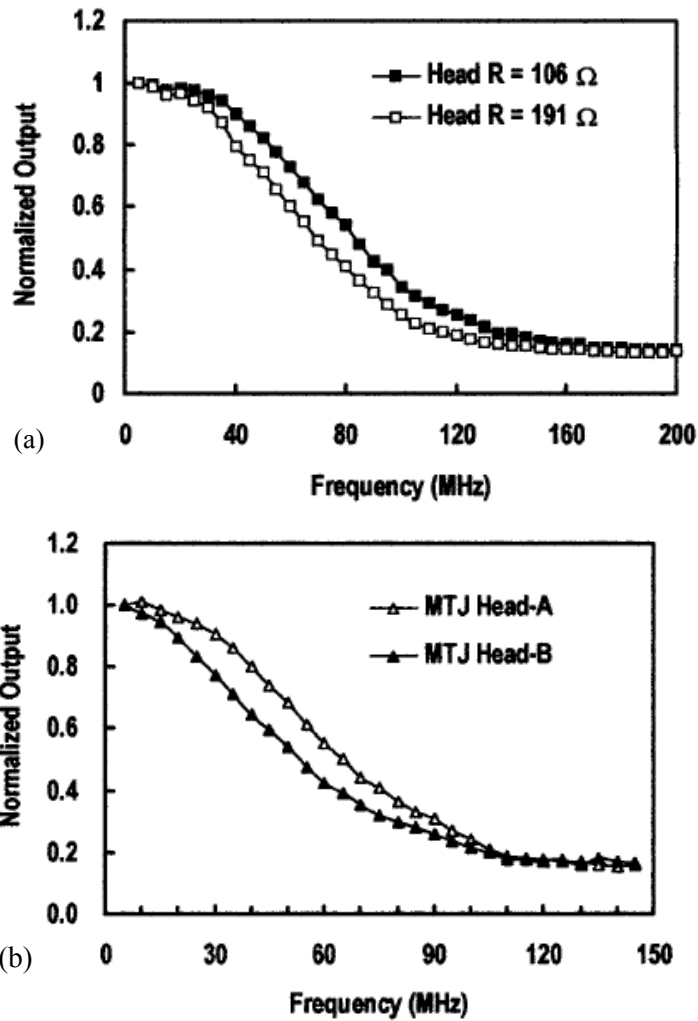


Figure 5.24: (a) Effect of resistance on read-back.
(b) Effect of insulator material on read-back. [Shimazawa, 2001]

investigated. Values of inductance, capacitance and resistance were estimated using an impedance tester, following fitting to the model. The inductance obtained was 8.2 nH, much larger than that discovered above (Section 5.2.3.6). This was present when the measurement leads were shorted with a wire and therefore assumed to be parasitic. The inductance was attributed to the measurement apparatus, as concluded in Section 5.2.3.6.1, and subsequently omitted from the reader model. Curves produced by the impedance analyser were not presented and the effect of removing the top shield was not investigated. Figure 5.24(a) shows that increased reader resistance decreases the roll-off frequency, as found above (Sections 5.2.3.2 and 5.2.3.3).

Shimazawa *et al.* found that roll-off frequency increased when the Al_2O_3 (head B) insulator was replaced with SiO_2 (head-A), as shown by Figure 5.24 (b). This is expected

from Equations (5.17) and (5.18) which suggest that $f_{3dB} \propto 1/\epsilon_r$. The dielectric constant of Al_2O_3 is higher than that of SiO_2 and whilst Shimazawa *et al.* do not suggest values for these materials, we note from the literature that $\epsilon_r = 3.5-5$ for SiO_2 and 8.5 for Al_2O_3 . Exact dielectric constant values cannot be estimated due to the effect of deposition technique and impurities. They suggest a low impedance amplifier configuration for magnetic tunnel junctions (see Section 5.2) for operation at 400 MHz, corresponding to 800 Mbps data transfer rate. Jury and Wang suggest that improved performance is possible using a buffer amplifier [Jury, 2002].

The particular significance of the work presented by Shimazawa *et al.* is that results on the basis of full wafer build and read-back from a hard disk support the conclusions of this study, performed using a network analyser on wafer level devices. Further work is required to identify the exact relationship between the two measurement processes and limitations of the network analyser technique.

5.2.5 Implications for read head design

Network analyser measurements of part-built readers suggest a number of design considerations for read heads. Increased read head sensor resistance decreases the roll-off frequency, therefore low resistance readers are desirable. Decreasing the resistance of magnetic tunnel junctions is essential to their application to high-density hard disk read heads. Whilst manufacturers strive to increase the bit density of hard disks, sensor size decreases, increasing their resistance and decreasing the maximum data rate. Shield size should be minimised and innovations such as the ‘Flux-thief’ pictured in Figure 5.9, where a break in the metal between sides of the sensor element promotes isolation, may improve read head performance. Shunt capacitance between wiring and substrate could become significant. A high resistance substrate such as silicon oxide is recommended.

The development of suitable insulators with low dielectric constant is important, in order to decrease the shunt capacitance. The requirement of low capacitance is in direct conflict with that of high-density recording, as the reader size and insulator thickness must be reduced. Finally, we note that the inductance of leads may be significant and should be minimised.

5.3 The high frequency performance of insulators

The insulator between shields and wiring layer significantly affects high frequency read head performance. In particular, a low dielectric constant is required (Section 5.2.4) and good insulation should be maintained, regardless of the decrease of thickness required to obtain a larger bit density. The dielectric properties of insulators were investigated by fabricating simple parallel plate capacitors for high frequency testing. The characteristics of capacitors at high frequency are reviewed, followed by literature investigating the high frequency dielectric properties of materials. Experimental procedure employed during this study is discussed, together with the results, implications and limitations of this technique.

5.3.1 Capacitors at high frequency

Equations (5.17) and (5.18) indicate that at high frequency, with constant dielectric thickness and capacitor area, relative permittivity of the dielectric is critical to device performance. Permittivity is not necessarily constant as frequency increases. Consider the loss tangent of the dielectric, defined as:

$$\tan \delta = \frac{2\sigma}{\epsilon f}, \quad (5.21)$$

where σ is the conductivity of the material and f the frequency. The loss tangent measures the proportion of capacitor input converted into heat. The absolute value of the loss tangent is not an appropriate measure for insulator applications in the reader, since both low conductivity and low dielectric constant are required. However, research on dielectric materials for high frequency applications generally concentrates on developing capacitors, hence the loss tangent is often quoted. The dielectric constant is often approximately constant in the range 1 Hz to 10 GHz, in which case the loss tangent can be considered a measure of the conductivity over frequency.

5.3.2 The dielectric properties of insulators

Dielectric properties of insulators have been the subject of considerable research, but studies generally measure sintered materials using a resonant cavity. Figure 5.25 shows

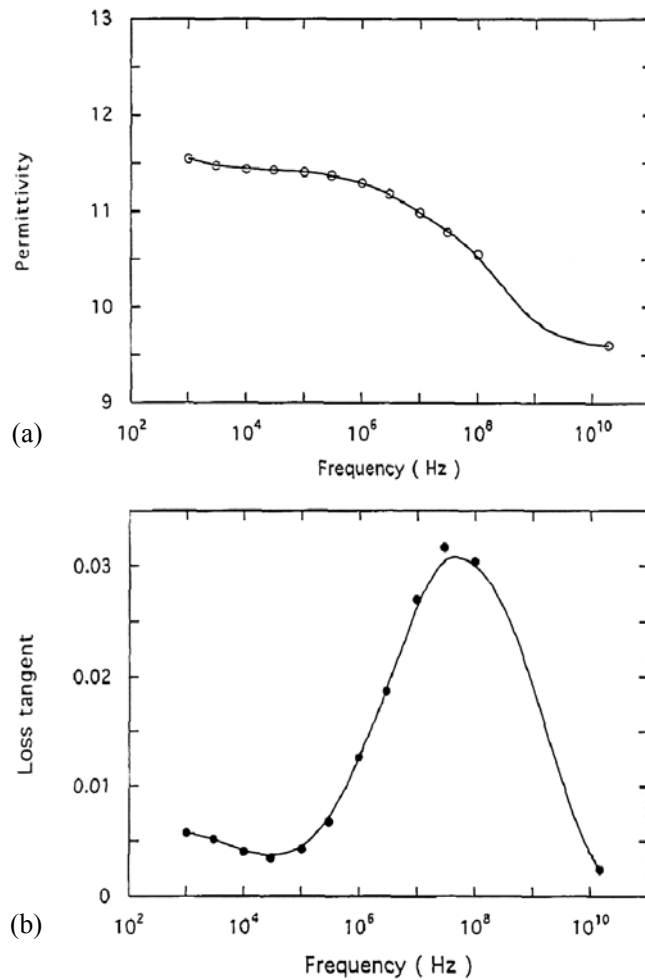


Figure 5.25: (a) Frequency dependence of the permittivity of 99.7% sintered Al₂O₃ (b) Frequency dependence of the loss tangent of 99.7% sintered Al₂O₃. [Molla, 1995]

the variations with frequency of permittivity and loss tangent of 99.7% sintered alumina [Molla, 1995]. Measurements were made on cylinders of sintered material with a height of 30 mm and diameter of 30 mm, using a resonant cavity. Both loss tangent and permittivity change considerably over the frequency range of importance to reader performance (100 MHz and above). Bulk sintered material is structurally and chemically different from sputtered thin films, so these results do not necessarily indicate the trend in permittivity and loss tangent within read head insulators. However, it is likely that loss tangent and dielectric constant vary as read-back frequency increases, affecting the -3dB point measured.

Maeda *et al.* investigated the dielectric characteristics of metal-insulator-metal capacitors using a network analyser. Plasma-enhanced chemical vapour deposition was used to

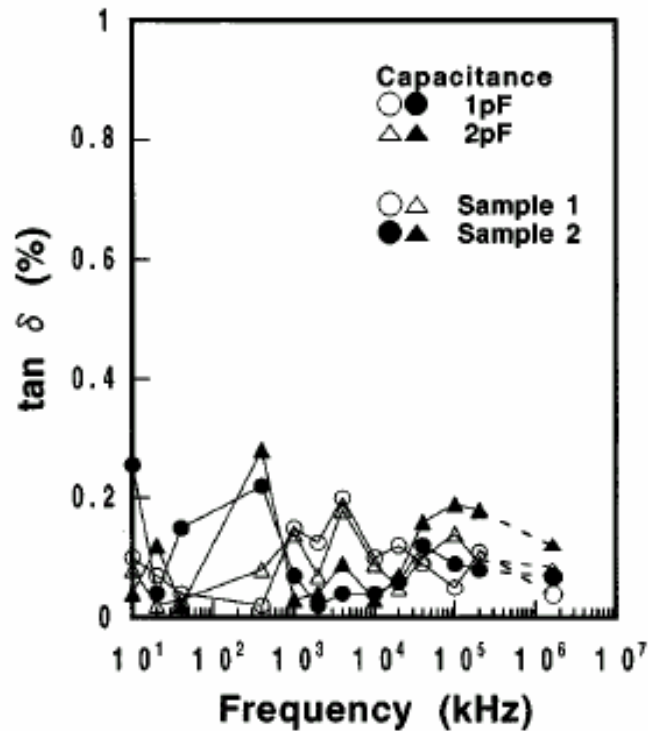


Figure 5.26: Variation in loss tangent of silicon nitride as frequency is increased [Maeda, 1999]

produce silicon nitride thin films in the range 0.1 μm to 0.66 μm . Measurements were made from 10 kHz to 100 MHz using an LCR meter and a network analyser in the range 100 MHz to 1.4 GHz. The recovery of appropriate values of capacitance, inductance and resistance requires a circuit model, but no model is quoted. They show that capacitance is directly proportional to the area of the plates and inversely proportional to dielectric thickness at 1 MHz. Higher capacitance was observed for silicon nitride deposited onto a heated substrate than at room temperature, which was attributed to an increase in roughness and a corresponding rise in effective surface area. However, such measurements do not prove the validity of their model at high frequency, where stray inductance often becomes significant. Figure 5.26 shows calculations of loss tangent, based on measurements of the system and subsequent modelling; no clear trend is visible in loss tangent. Owing to the lack of explanation of the model used, Figure 5.26 cannot be assumed to represent dielectric behaviour and not measurement related artefacts. The peak in loss tangent at approximately 100 MHz is a characteristic of parasitic inductance.

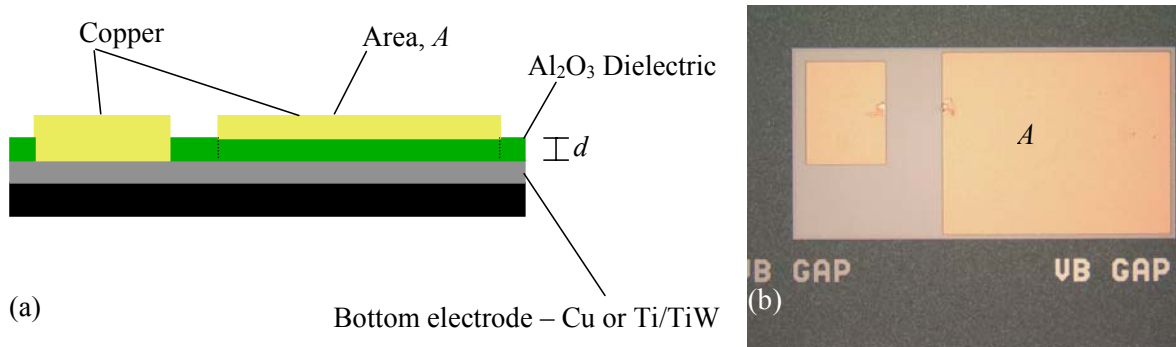


Figure 5.27: (a) Cross-section of capacitor. (b) Picture of a tested capacitor.

5.3.3 Experimental Procedure

Parallel plate capacitors were fabricated using standard lithography and processing techniques. Figure 5.27 pictures a typical capacitor, the area, A , of which is indicated. The copper contact pads were deposited by DC magnetron sputtering a seed layer, followed by electroplating to provide thick, durable contacts. The Ta/TiW or copper bottom electrode was deposited by DC magnetron sputtering. Alumina dielectric was produced by either ion beam deposition (with the Nordiko IBD) or chemical vapour deposition (ALCVD). Table 5.2 shows the wafers measured during this study, noting the alumina deposition thickness and system. The wafers were tested with the network analyser, as described in Section 5.2.2.2.

<i>Wafer</i>	<i>Predicted dielectric thickness (nm)</i>	<i>Alumina deposition system</i>
S5024O_SOHKO	20	ALCVD
S50260_SOHLO	20	ALCVD
S50330_SOHLO	30	Nordiko IBD
S5037O_SOHM4	20	Nordiko IBD
S5059O_SOHOK	50	ALCVD
S5060O_SOHOO	75	ALCVD
S5061O_SOHOS	125	ALCVD
S5062O SOHOW	200	ALCVD

Table 5.2: Capacitor wafer dielectric thickness and deposition system.

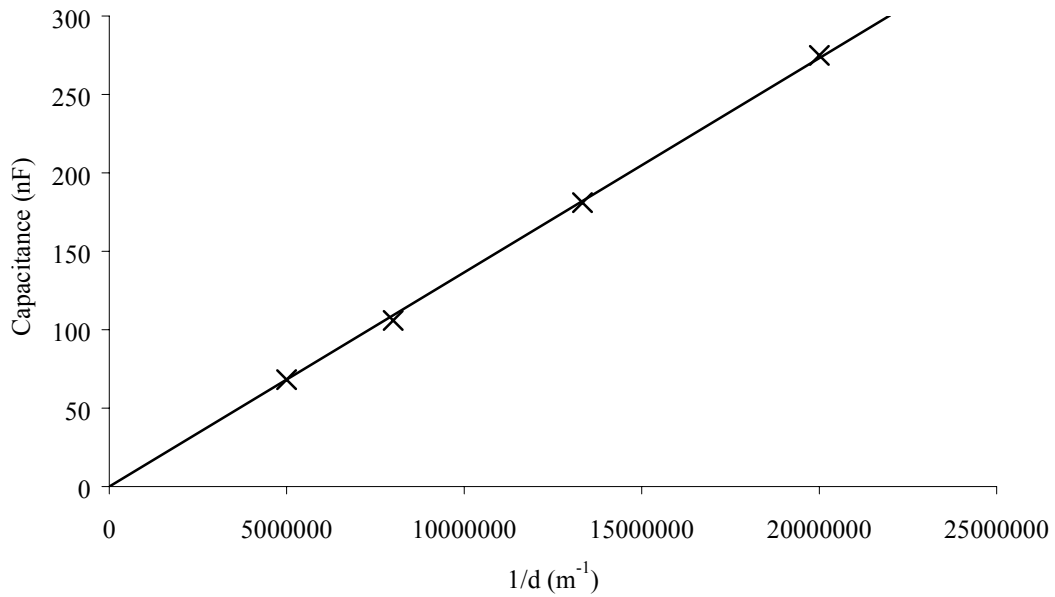


Figure 5.28: Variation of capacitance with $1/d$. Capacitance was modelled at 1MHz for a capacitor and parallel resistor. Includes wafer series S50959-62O only, where the insulator was deposited with the same rate calibration.

5.3.4 Results and Discussion

Figure 5.28 shows the variation of capacitance as dielectric thickness, d , increases, calculated at 1 MHz. Values were obtained by modelling the circuit as a capacitor in parallel with a resistor. As expected, capacitance increases linearly with $1/d$, verifying the model at low frequency. The magnitude of the impedance, $|Z|$, of a circuit consisting of a parallel resistor, R , and capacitor, C is described by Equation (5.22).

$$|Z| = \frac{R}{\sqrt{\omega^2 C^2 R^2 + 1}} \quad (5.22)$$

A typical plot of measured impedance against frequency is shown in Figure 5.29. The S-parameter values at 1 MHz were used to calculate the expected impedance changes according to Equation (5.22). This model neglects the effect of permittivity and resistance changes. When calculated from the data, the permittivity falls rapidly at 100 MHz to less than 1. Clearly, the permittivity is not accurately represented by this model. Impedance levels-out as frequency increases at around 1 GHz. This behaviour is characteristic of a series resistance, limiting the minimum measured impedance.

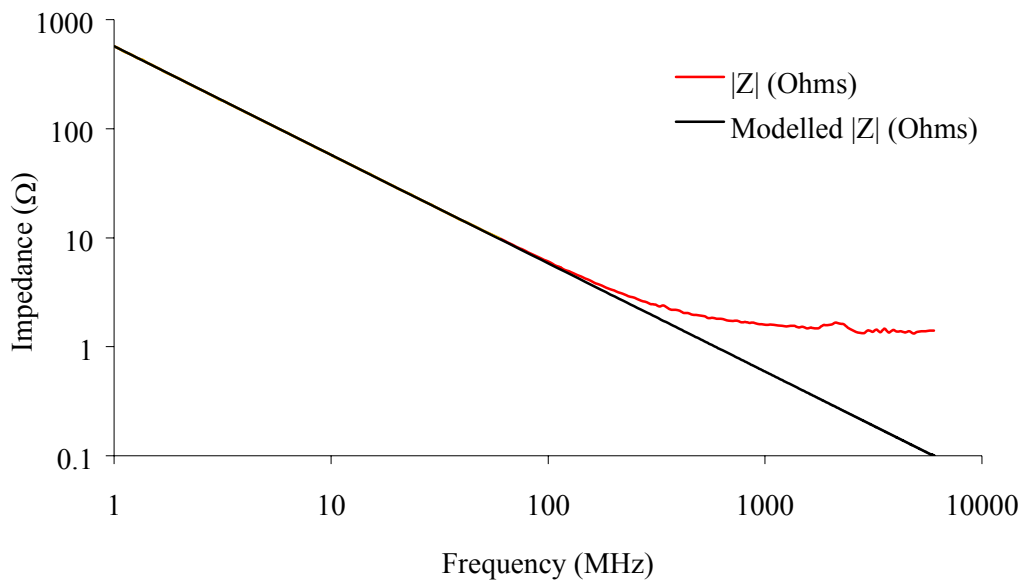


Figure 5.29: Magnitude of impedance for a real capacitor, S50590_SOHOK_QCZ078 and that expected by modelling the circuit as a resistor and capacitor in parallel.

However, incorporation of a series resistance into the model was no more successful in describing the data. High frequency calibration error of the one-port network analyser is likely to be responsible for these problems. Measurement with a two-port network analyser is required to provide more accurate calibration and may be suitable for investigating the high frequency properties of dielectrics.

Attempts to determine the effect of deposition technique on the dielectric properties of alumina at low frequency were unsuccessful due to inaccuracies in deposition rate calibration. Large variations were observed in the properties of capacitors on wafers where the insulator was deposited with the same method. Since plate areas and fabrication route were not changed, this suggests that alumina deposition rate was not consistent. It was not possible to measure accurately the alumina thickness on fabricated wafers, since the films were too thin, either for determination with the ellipsometer, or by slicing the cross-section with a focussed ion beam followed by scanning electron microscopy.

5.4 Conclusions

The high frequency characteristics of read heads can be investigated using a network analyser at wafer level, and the results correlate well to those obtained via hard disk read-back from fully built devices. Testing at wafer level has significant advantages over measurement at full build. The effect of individual components may be isolated by building the wafer towards completion layer-by-layer, promoting better understanding of the electronic properties of the system. Wafer level testing dramatically decreases the time taken to investigate the effect of changing device geometry and composition, since full reader build and testing is very time consuming. Hard disk read-back measurements are required to determine cross-reading and error rates. The technique could be also be used to assist write head development. However, one-port network analyser measurements are not suitable for the investigation of the high frequency properties of dielectrics.

A simple model of a capacitor and resistor in parallel satisfactorily represents a low roll-off frequency read head built to first half gap. The capacitor is formed between the wiring layer and shield. For readers capable of higher frequency response, a more complex model is required to account for an extra capacitance and inductance. Two-port network analyser measurements should allow more accurate calibration and the determination of more system parameters, allowing better characterisation of the read head.

Roll-off frequency decreases as sensor resistance increases, and for high resistance readers the -3dB frequency is inversely proportional to resistance. Reader length (CD) is directly proportional to sensor resistance, hence minimising CD increases the roll-off frequency and is necessary as bit density increases. -3dB frequency rises as sensor width increases. Raising read head temperature increases sensor resistance and decreases roll-off frequency, which is an important consideration as future heads may operate at over 200°C . Roll-off frequency increases as stray capacitance decreases, and for large overlap area between shields and wiring the -3dB point is inversely proportional to area and capacitance. No correlation was found between roll-off frequency and first half gap thickness, the insulator between shield and sensor, which is attributed to its small area. A read head designed to operate at high frequency should have a low resistance sensor and

minimal shield size, which may incorporate insulation between the sensor sides. The requirement of low resistance demonstrates the importance of the development of low resistance magnetic tunnel junctions for read head applications.

Chapter 6:

Magnetic tunnel junctions

“Our patience will achieve more than our force”

-Edmund Burke

Research into magnetic tunnel junctions has been driven by their potential application to read heads and magnetic random access memory (MRAM). Large magnetoresistance (MR) at room temperature for magnetic tunnel junctions was first demonstrated seven years ago [Miyazaki, 1995]. Since then, significant improvements have been made to both the understanding of the effect, and MR. However, the fabrication of high quality magnetic tunnel junctions is still problematic. Many research groups struggle to obtain junctions with a significant magnetoresistance.

The basic properties of magnetic tunnel junctions have already been introduced in Section 2.2.3. Developments in the field of magnetic tunnel junctions are reviewed in this chapter. Particular note is made of the problems associated with producing high quality devices. The techniques employed to fabricate tunnel junctions during the course of this study are then presented. The MR obtained from magnetic tunnel junctions (MTJ's) with different ferromagnetic electrodes is discussed. Atomic force microscope (AFM), vibrating sample magnetometer (VSM) and superconductor-insulator-ferromagnet (SIF) tunnel junction measurements are used to investigate trends in MR. Transmission electron microscopy (TEM) images are then presented, providing useful insight into the structure of the deposited films.

6.1 Literature review

In 1975 Jullière discovered significant spin polarized tunneling between two ferromagnets separated by an insulating barrier [Jullière, 1975]. He observed a 14% junction magnetoresistance (Equation (6.2)) for Fe/Ge/Co tunnel junctions at 4.2 K and in zero voltage bias. MR decreased monotonically as voltage bias increased. Jullière suggested the model discussed in Section 2.2.3, where MR is attributed to the difference in occupation level of the spin-up and spin-down energy bands at the Fermi level. Equation (6.1) represents the tunneling magnetoresistance (TMR), derived using Jullière's theory.

$$\text{TMR} = \frac{\Delta R}{R_{\min}} = \frac{2P_1P_2}{1 - P_1P_2} \quad (6.1)$$

where ΔR is the maximum difference in resistance observed over the field range and R_{\min} is the minimum resistance, which corresponds to a state in the electrodes of parallel magnetisation. P_1 and P_2 are the spin polarisation of the top and bottom electrodes respectively. Jullière's simple prediction has been widely investigated and developed and is generally considered an upper limit for tunnel junction performance. Experimentalists commonly compare their results to predictions from Equation (6.1).

It was 20 years after the first demonstration of magnetic tunnel junctions before reproducible devices were produced, with significant MR at room temperature. In 1991 Miyazaki *et al.* demonstrated a 2.7% TMR at room temperature for $\text{Ni}_{82}\text{Fe}_{18}/\text{Al}-\text{Al}_2\text{O}_3/\text{Co}$ [Miyazaki, 1991], later improving the value to 18% [Miyazaki, 1995]. However, these values were not reproducible and it was found later that the results were influenced by geometrical enhancement of the MR (Section 6.1.7.4) [Moodera, 1999]. In 1995, Moodera *et al.* announced a consistent room temperature magnetoresistance of over 10% for $\text{CoFe}/\text{Al}_2\text{O}_3/\text{Co}$ [Moodera, 1995]. The following year they reported a TMR of 22% for $\text{CoFe}/\text{Al}_2\text{O}_3/\text{Co}$ tunnel junctions [Moodera, 1996(a)].

The properties, theory and problems associated with fabricating magnetic tunnel junctions are discussed below. Hundreds of papers have been written about magnetic tunnel junctions since 1995. This review presents the most significant results and theories.

6.1.1 The definition of magnetoresistance

The concept of MR was introduced in Section 1.2, however clarification is required as two definitions are in use in the literature. This work follows the most commonly used definition of the MR as the TMR (Equation (6.1)). However, some authors and particularly Jullière use the junction magnetoresistance (JMR), defined as:

$$\text{JMR} = \frac{\Delta R}{R_{\max}} = \frac{2P_1P_2}{1 + P_1P_2}, \quad (6.2)$$

where R_{\max} is the maximum resistance, and ΔR , P_1 and P_2 have the same meaning as in Equation (6.1). At R_{\max} the magnetisation in the electrodes is aligned in opposite directions.

TMR values are higher than JMR values, causing some confusion in the field, particularly as some authors appear to use both terms interchangeably. Some significant results in the literature were presented in terms of JMR, without sufficient data to reconstruct the TMR. These are highlighted in the text and are included as they provide some useful insight into the properties of magnetic tunnel junctions.

6.1.2 Ferromagnetic electrodes

Equation (6.1) indicates that the magnetoresistance of junctions should increase as the polarisation of the ferromagnets rises. Many different combinations of ferromagnetic electrode materials have been investigated by different authors. However, it is difficult to identify the effect of ferromagnetic electrodes on TMR due to differences in the fabrication route. In particular, both the barrier preparation and thickness vary widely. At low temperatures, values approaching the prediction of Jullière have been obtained. Moodera demonstrated a TMR of 37% at 77 K compared to the predicted value of 37.2% for Co/Al₂O₃/Ni₈₀Fe₂₀ tunnel junctions [Moodera, 1998]. Amongst the highest room temperature TMR recorded is 41% for CoFe/Al₂O₃/CoFe/MnIr following annealing at 300°C [Cardoso, 2000]. Taking the polarisation of CoFe to be 47%, the predicted value is 56.7%.

6.1.3 Exchange bias

Well-defined switching at low magnetic field can be obtained by exchange biasing one electrode of the magnetic tunnel junction, termed the ‘pinned layer’. The other ferromagnetic electrode is then termed the ‘free layer’. Exchange biased structures exploit the uniaxial anisotropy of an antiferromagnetic layer to pin the magnetisation of the ferromagnetic electrode in one direction. This direction is specified during deposition by the application of an external magnetic field. Figure 6.1 illustrates the effect of exchange bias on both the resistance and hysteresis characteristics of an MTJ [Lu, 1998]. Exchange biased structures exhibit abrupt changes in resistance and a flat top of the resistance peaks, compared to those without exchange bias. These abrupt changes create a more linear response, as required for read head applications [Mallinson, 1996]. The exchange biased tunnel junction behaves more like a single domain structure.

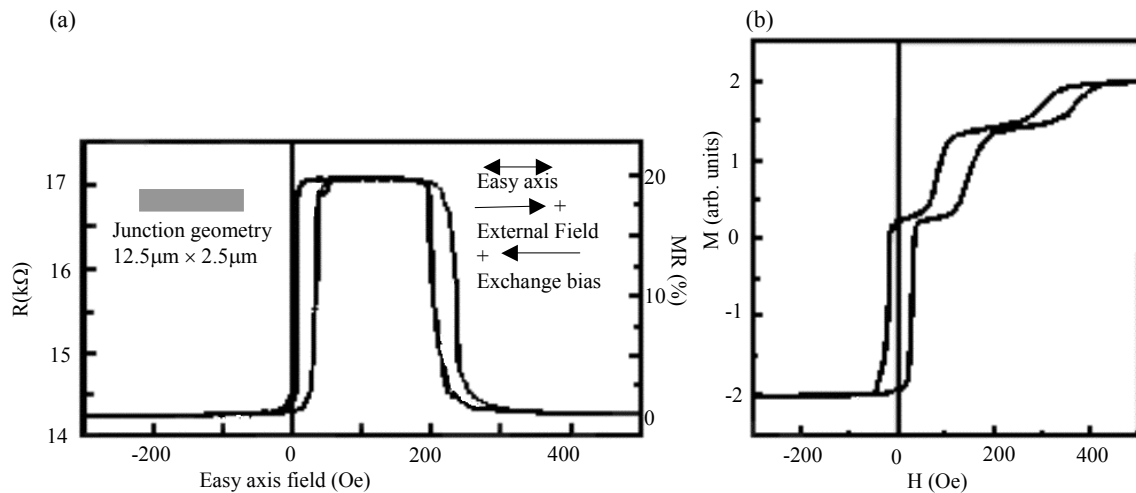


Figure 6.1: (a) Resistance and MR versus field of an exchange biased magnetic tunnel junction at room temperature. Structure $\text{Pt}/\text{Ni}_{80}\text{Fe}_{20}/\text{FeMn}/\text{Ni}_{80}\text{Fe}_{20}/\text{Al}_2\text{O}_3/\text{Co}/\text{Pt}$. [Lu, 1998].

(b) hysteresis curve for the as-deposited film corresponding to (a). [Lu, 1998].

The effect of exchange bias on the hysteresis curve of a ferromagnet can be visualised by assuming an exchange interaction at the ferromagnet-antiferromagnet interface. Consider a bilayer consisting of a ferromagnet (F) and antiferromagnet (AF). F has a Curie temperature, T_C , below which ferromagnetic alignment occurs. AF has a Néel temperature, T_N , below which antiferromagnetic alignment occurs. At a temperature, T , such that $T_N < T < T_C$, and in the presence of a magnetic field larger than the coercivity, the spins of F are aligned parallel to the field. As the temperature is decreased, until $T < T_N$, the top layer of AF aligns with the field, whilst the other spin planes within it align to produce zero net magnetisation. On reversal of the field F spins start to rotate. However, for sufficiently large antiferromagnetic anisotropy, the AF spin state remains unchanged. The exchange interaction therefore acts to maintain parallel alignment of the spins at the F-AF interface. The material behaves as if an internal bias field is present, thus shifting the hysteresis curve on the field axis. Many different antiferromagnetic materials have been investigated for the purpose of exchange bias, including synthetic antiferromagnets. A good review of current materials for exchange bias was written by Nogués and Schuller [Nogués, 1999].

Gider *et al.* presented results indicating that exchange biasing significantly increased the stability of junctions to magnetic switching [Gider, 1998]. They investigated the switching properties of magnetic tunnel junctions which had either a hard ferromagnetic

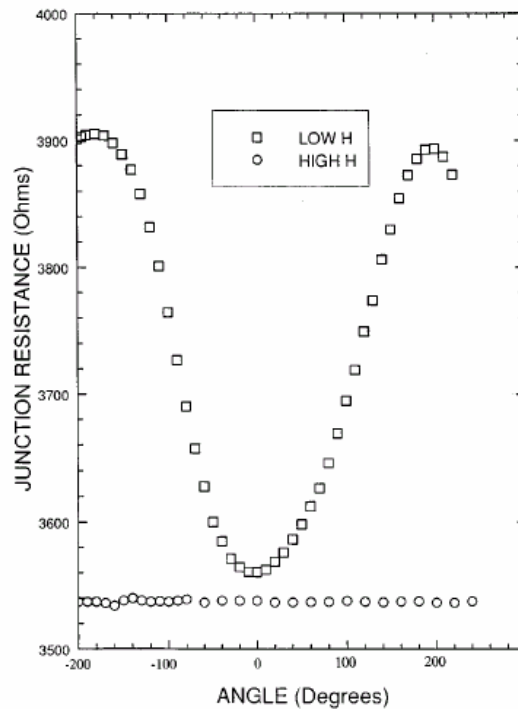


Figure 6.2: The angular dependence of magnetoresistance, illustrated by the changes in resistance at high and low field [Moodera, 1996(a)].

electrode or an exchange biased electrode. The junctions were exposed to fields less than that required to switch the hard ferromagnetic layer's spin direction. This simulated the effect of a writer in close proximity to a read head that incorporates a reference layer. They found that the magnetisation of the exchange biased structure was stable for over 10^7 cycles. However, the magnetisation of the hard structure tunnel junction decayed logarithmically with the number of field cycles. The reference layer in a read head is required to withstand millions of cycles, making exchange biased tunnel junctions more desirable than those with a hard ferromagnetic electrode.

6.1.4 Angular dependence of MR

Figure 6.2 illustrates the angular dependence of MR [Moodera, 1996(a)]. The junction was subjected to a high field, which was greater than the switching field of both layers, aligning their magnetisation. The field was then reversed to a low value, below that at which peak resistance occurred. The sample was rotated and the junction resistance recorded every 5-10°, for both high and low field. Figure 6.2 shows a periodic variation of the resistance at low field. This is expected when the field is larger than that required

to rotate the magnetisation of the softer film, but not the hard electrode. Resistance reaches a maximum value when the magnetisation of the two layers is antiparallel.

Slonczewski developed the first model of magnetic tunnel junctions to consider the ferromagnet-insulator-ferromagnet trilayer as a single quantum mechanical system [Slonczewski, 1988]. He predicted the observed angular dependence of the magnetoresistance. He modelled the system as a rectangular barrier (Section 2.1), with the ferromagnets described by parabolic bands. It was assumed that the electrodes consisted of free electron metals with momentum conserved across the junction. This model results in Equation (6.3) which represents the angular dependence of the conductivity, G .

$$G = G_{12} (1 + P_1 P_2 \cos \theta), \quad (6.3)$$

where G_{12} is the mean surface conductance and θ is the angle between the magnetisation direction of the electrodes. P_1 and P_2 are the effective polarisations of the top and bottom ferromagnetic layers respectively. This relation agrees with the experimentally observed angular dependence of the magnetoresistance shown in Figure 6.2.

6.1.5 MR dependence on voltage

Figure 6.3 shows the decrease in MR of magnetic tunnel junctions as the bias voltage is increased [Moodera, 1998]. This diagram shows the JMR rather than TMR (Section 6.1.1). Device applications require a stable response to voltage and the use of small voltages is undesirable due to increased measurement noise. Little variation in the MR is observed at a low bias, ~ 10 mV, particularly at room temperature.

Figure 6.4 shows variation of the conductance with bias at room temperature and at 4.2 K for a magnetic tunnel junction [Moodera, 1996(a)]. At room temperature the curve shape is as expected from Simmons theory, discussed in Section 2.1.2 [Simmons, 1963(a)]. However, at 4.2 K a zero bias dip is observed in conductance. The zero bias anomaly has been recorded by a number of authors for tunnel junctions with one or more ferromagnetic electrode [Wolf, 1985]. It has been proposed that a decrease in spin independent tunneling with temperature is responsible for the zero bias anomaly [Moodera, 1996(a)]. Sources of spin independent transport include spin-flip scattering

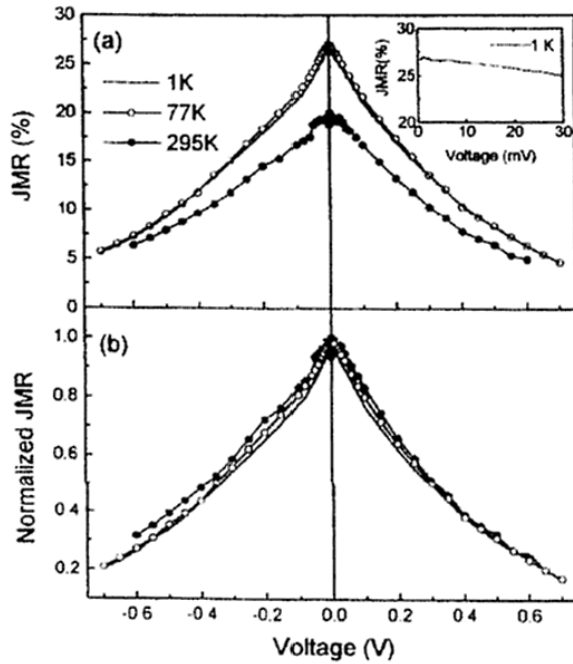


Figure 6.3: (a) JMR against bias voltage (b) normalized JMR against bias voltage. Note this paper quotes the JMR, not TMR [Moodera, 1998].

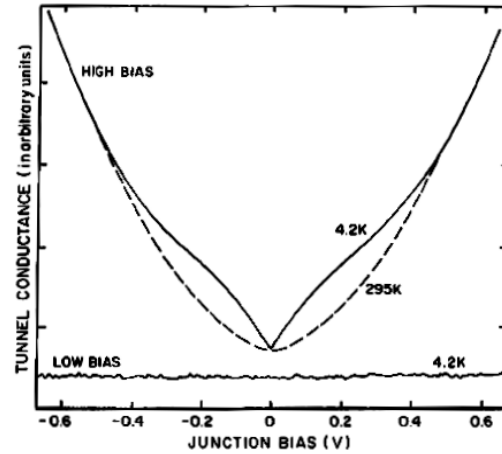


Figure 6.4: Tunnel conductance dependence on bias at 4.2K and 295K. [Moodera, 1996(a)].

caused by magnetic impurities, magnons, localisation effects, multistep tunneling, the presence of metal particles, and states in the barrier or at the interface. Wolf discusses the zero bias anomaly in detail [Wolf, 1985], however no clear explanation exists for this effect. It seems likely that the true mechanism is a combination of the factors listed above and depends on the precise deposition conditions of the tunnel junction.

The rapid decrease in MR with increasing bias voltage (Figure 6.3) is still not fully understood. Figure 6.3(b) shows the normalised JMR versus voltage. It indicates that the shape of the MR dependence, apart from the zero bias effects, is independent of temperature. A number of suggestions have been made to model the decrease of MR as voltage bias increases. The most popular theories are the excitation of magnons, which are inelastic excitations of spin waves, [Zhang, 1997], bias dependence of the effective barrier height [Slonczewski, 1988], two stage spin-flip tunneling [Zhang, 1998] and energy dependence of the polarisation [Moodera, 1995]. The decrease in the effective barrier height with increasing bias voltage raises the probability of minority spin tunneling. This decreases the effective spin polarisation. However, the predicted variation in MR from this model is low and can account for less than 1% of the observed rapid decrease in MR [Moodera, 1995]. Zhang and White showed that the inclusion of

defects into the barrier increases the rate of MR decay as voltage bias increases [Zhang, 1998]. They modelled this as two stage spin-flip tunneling via defect states in the barrier. Bratkovsky included phonon contributions to the magnon interactions suggested by S. Zhang *et al.*, shows good agreement with the data [Zhang, 1997; Bratkovsky, 1998]. Recently, a great deal of research has centred on the effect of the barrier interface states, further developing the phonon-magnon theory. Clear implications may be inferred from the theoretical treatment of the MR dependence on voltage bias: the barrier must be high quality and the barrier/ferromagnet interface clean and abrupt.

6.1.6 MR dependence on temperature

The temperature dependence of MR in a typical magnetic tunnel junction is shown by Figure 6.5 [Shang, 1998]. Two contributions to the temperature dependence of the MR must be considered: intrinsic material behaviour, and extrinsic behaviour due to defect or interface effects. Intrinsic behaviour was not initially thought to significantly contribute to the MR temperature dependence as Fermi smearing and magnetisation changes for the 3d ferromagnets are small below 300 K [Moodera, 1995; Zhang, 1998]. A number of researchers have suggested that spin independent tunneling makes a significant contribution to the temperature dependence of MR [Moodera, 1998; Zhang, 1998]. Zhang and White suggested a two stage tunneling mechanism via defect states in the barrier, producing spin independent transport [Zhang, 1998]. They presented results supporting this theory showing that as temperature increased, magnetic tunnel junctions with a large number of defects experienced a more rapid MR decrease than those with fewer defects. Shang *et al.* suggested that polarisation changes, principally caused by surface effects in the ferromagnetic electrodes, are the main cause of the decrease in MR [Shang, 1998]. They predicted that the polarisation changes as:

$$P(T) = P_0 \left(1 - \alpha T^{\frac{3}{2}} \right). \quad (6.4)$$

P_0 is the polarisation at 0 K, T is the temperature and α is a material dependent constant. Figure 6.5 shows the results of this model. They found a less significant second source of conductance, due to spin independent tunneling, which was proportional to $T^{1.35 \pm 0.15}$. This is supported by Hagler *et al.*, who found that only 10% of conduction at room

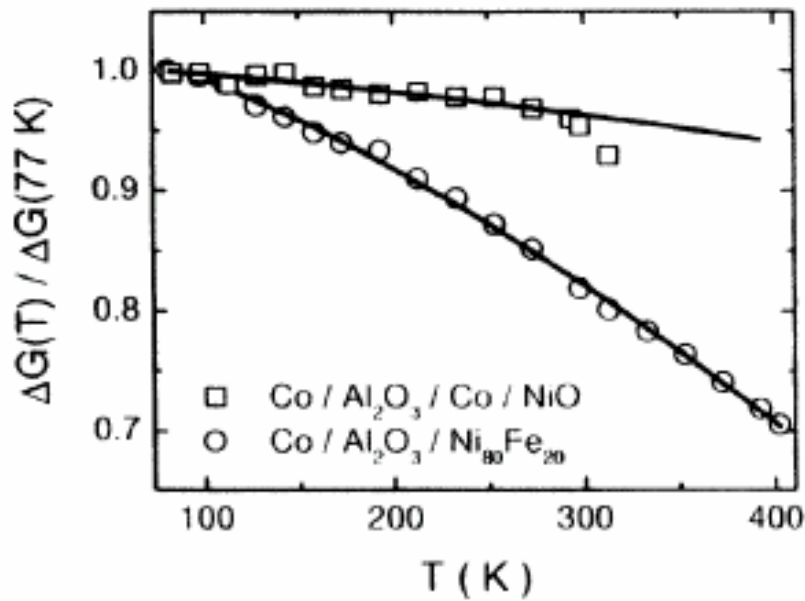


Figure 6.5: Temperature dependence of MR, $\Delta G(T)$ and $\Delta G(77\text{ K})$ are the difference between minimum and maximum conductance on sweeping the magnetic field at temperature T and 77 K , respectively [Shang, 1998].

temperature in tunnel junctions was attributable to spin independent tunneling [Hagler, 2001]. Davis *et al.* have modelled the effect of Fermi smearing and exchange splitting on the temperature dependence of MR [Davis, 2001]. They found that such effects could account for 33% of the drop in MR between 0 K and 300 K for the tunnel junctions fabricated by LeClair *et al.* [LeClair, 2000].

Spin independent tunneling is dependent upon junction quality. The lack of significant room temperature MR between 1975 and 1995 may indicate the presence of significant spin-flip events due to poor barrier quality. It is likely that all the above effects contribute to the temperature dependence of MR in different proportions, depending on the barrier and ferromagnetic electrode quality.

6.1.7 Problems of magnetic tunnel junction fabrication

6.1.7.1 Barrier production

Barrier quality is critical to magnetic tunnel junction performance. Ideal requirements for the barrier are stringent. It should be homogeneous, have no pinholes, be defect free and be fully oxidised, yet not over oxidised. The resistance-area product (RA) has been

adopted as a convenient measure for the comparison of barrier resistance. The lowest possible RA is required. Values of less than $1 \text{ k}\Omega\mu\text{m}^2$ may be suitable to permit rapid frequency response in read head applications, as discussed in Chapter 5. This suggests that that barrier should be thin and its height as low as possible whilst maintaining tunneling dominated conductance. Pinholes and weak-links are more likely to occur for thin barriers (Chapter 7) and are detrimental to device performance. Barrier materials, aluminium deposition thickness for Al_2O_3 barriers, oxidation technique and barrier defects are discussed in Sections 6.1.7.1.1 to 6.1.7.1.4.

6.1.7.1.1 Barrier material

A number of materials have been investigated for use as a magnetic tunnel junction barrier. Al_2O_3 is most commonly used, but other insulators include CoO, NiO, AlN, MgO, Ta_2O_5 and ZnS. The lowest RA for a magnetic tunnel junction with Al_2O_3 barrier and large TMR ($\approx 20\%$) is $\approx 1 \text{ k}\Omega \mu\text{m}^2$ (Section 6.1.7.1.3) [Boeve, 2001]. Various studies investigated the performance of magnetic oxides, such as CoO and NiO as tunnel barriers [Platt, 1997]. However, in the light of theoretical developments as described in Sections 6.1.5 and 6.1.6, it seems likely that magnetic scattering centres within the barrier led to the observed poor device performance. Guth *et al.* recently demonstrated a room temperature TMR of 5.16% for a junction with ZnS barrier and CoFe electrodes [Guth, 2001]. They estimated a barrier height of 0.56 eV with a thickness of 1.4 nm by fitting the I-V characteristics to the Brinkmann model [Brinkmann, 1970]. The RA products for the devices were in the range 2-3 $\text{k}\Omega\mu\text{m}^2$ and therefore higher than the lowest values for Al_2O_3 . The low barrier height makes junctions more susceptible to spin independent tunneling than Al_2O_3 barriers. This is reflected in the low MR reported. Currently, ZnS barriers offer no improvement over Al_2O_3 .

Ta_2O_5 has recently been shown to exhibit 10% room temperature TMR, with a high RA of approximately $100 \text{ M}\Omega\mu\text{m}^2$ [Gillies, 2001]. Gillies *et al.* reported a lower barrier height of 0.9 eV, compared with that generally reported for Al_2O_3 , 1.5-2 eV. However, tantalum expands by 125% during oxidation, compared to only 26% for aluminium, and therefore extremely thin tantalum layers must be deposited to form an acceptable barrier. Whilst it may be possible to reduce the RA for tantalum oxide barriers, the technological

challenge of depositing thinner layers of tantalum than aluminium, without pinhole formation or over oxidation, currently seems prohibitive to their development.

MgO barriers have been demonstrated with lower TMR than that of Al₂O₃ junctions but a barrier height of only 0.9 eV [Moodera, 1996(a); Platt, 1997]. Moodera *et al.* measured the dependence of the MR on bias voltage for Al₂O₃ and MgO. They found the MR decay of MgO to be much more rapid than that of Al₂O₃. This poor performance of MgO barriers is likely to be predominantly due to the susceptibility of the lower barrier height to spin independent tunneling. However, Moodera did not present any data from MgO barriers. Platt presented magnetic tunnel junctions with TMR of over 20% at 77 K, but huge RA ($\approx 1 \text{ G}\Omega\mu\text{m}^2$). This was due to the large barrier thickness required to eliminate pinholes.

AlN is currently showing promise for low resistance magnetic tunnel junction barriers. Magnetic tunnel junctions with AlN barriers have been presented with room temperature TMR in the range 13-33% [Wang, 2001]. The corresponding RA was in the range $73 \text{ }\Omega\mu\text{m}^2 - 8.5 \text{ k}\Omega\mu\text{m}^2$, with barrier height 0.7-2 eV. Bias and temperature dependence of MR was not investigated. Further research is required to investigate whether this barrier material offers any advantages over Al₂O₃ barriers. Most current research concentrates on Al₂O₃ barriers due to their repeatability, high MR, and voltage and temperature dependence. However, lowering RA is still a priority.

6.1.7.1.2 Aluminium thickness

The oxide barrier is generally produced by the deposition of aluminium, followed by oxidation, as discussed in Section 6.1.7.1.3. The optimum aluminium thickness required for oxidation to form high quality Al₂O₃ barriers has been investigated. Three causes of decreased TMR can be identified. Oxidation of the bottom ferromagnetic electrode may occur if the aluminium is too thin. The significant contributions to spin scattering at the interface caused by such surface defects have been discussed in Sections 6.1.5 and 6.1.6. This effect considerably decreases the TMR at room temperature, as shown by Figure 6.6. A second consequence of thin aluminium is the possible formation of pinholes or weak-links through the barrier. Such defects cause device failure. However, large thickness leads to excess nonmagnetic, unoxidised material at the interface. Investigation into the

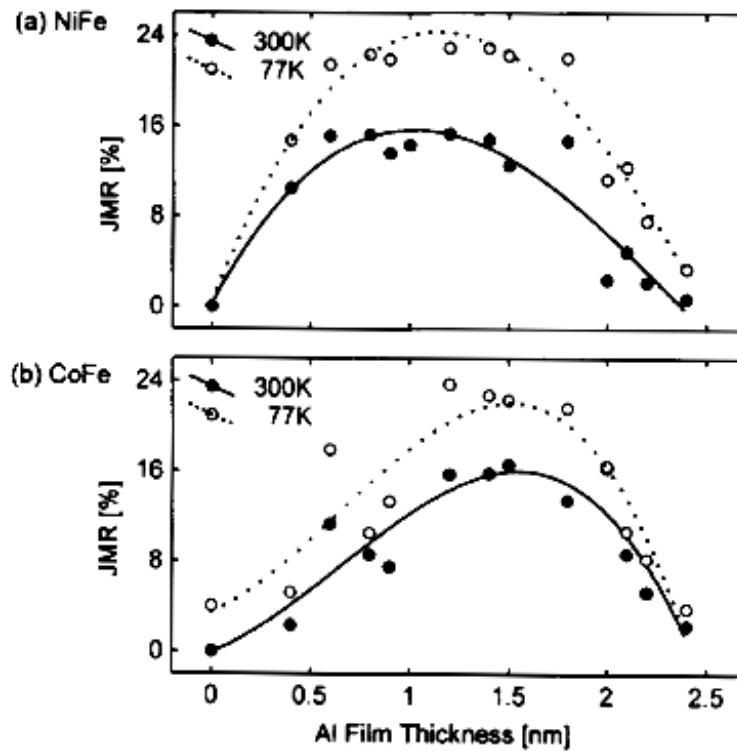


Figure 6.6: JMR variation as aluminum thickness is changed for (a) NiFe top electrode and (b) CoFe top electrode. [Moodera, 1997].

effect of nonmagnetic layers was performed by inserting thin films of Au or Cu above the bottom electrode of ferromagnet-insulator-superconductor tunnel junctions [Pierce, 1974; Moodera, 1989]. The inclusion of such layers led to the rapid reduction of effective polarisation. For example, a decrease from 40% to 3% was observed when 0.6 nm of Au was introduced between an iron electrode and barrier [Moodera, 1989]. Polarisation was inversely proportional to the thickness of normal metal. Excess aluminium is expected to behave similarly, by reducing the electrode polarisation and thus lowering the MR of a magnetic tunnel junction. An aluminium buffer layer is often deposited above the barrier (Section 4.1.1.1), this is also expected to reduce the effective polarisation of the ferromagnetic electrode.

A very thick oxide may be formed, for example by the multiple deposition of thin aluminium followed by oxidation (Section 6.1.7.1.3). Single step tunneling probability decreases as oxide thickness increases and multi-step, spin-independent transport becomes significant. However, thick oxides produce a large RA and are not suitable for magnetic tunnel junction applications in MRAM or read heads. Figure 6.6 shows the

effect of aluminium thickness on the JMR of a series of tunnel junctions [Moodera, 1997]. The films of composition Co/Al₂O₃/Ni₈₀Fe₂₀ and Co/Al₂O₃/Co₅₀Fe₅₀ were deposited by thermal evaporation and the oxidation performed by glow discharge plasma.

Figure 6.6 illustrates that the use of different top electrodes requires different optimum aluminium thickness. This variation may be caused by damage to the barrier during top electrode deposition. Different deposition techniques and conditions will also change the observed behaviour. Additionally, the oxidation method will influence the over-oxidation of junctions. Moodera *et al.* used oxygen glow discharge. This is a vigorous technique which generally forms thick oxides. Natural oxidation may lead to less over-oxidation. The aluminium thickness required for optimum tunnel junction performance is likely to be specific to the materials, techniques and equipment used.

6.1.7.1.3 Oxidation technique

A number of different oxidation techniques have been investigated for the fabrication of the Al₂O₃ insulating barrier. This barrier is most commonly used in magnetic tunnel junctions. Natural oxidation has been investigated in atmosphereⁱ, pure oxygenⁱⁱ and ozoneⁱⁱⁱ, in addition to multiple deposition and oxidation in pure oxygen^{iv}. Oxidation has also been undertaken by RF or DC plasma^v, and sputter deposition of aluminium in the presence of oxygen^{vi}. Plasma oxidation of the aluminium layer in an RF or DC bias is the most common method used in the fabrication of magnetic tunnel junctions. This technique generally leads to high TMR but also a very high RA (~10 MΩμm²). Sousa *et al.* have produced one of the lowest RA for tunnel junctions fabricated using this method, averaging 25 kΩμm² for a TMR of 21% before annealing [Sousa, 1999].

Miyazaki *et al.* performed oxidation by opening the deposition chamber to air after aluminium deposition [Miyazaki, 1995]. This produced the reasonable RA of 6.4×10³ Ωμm² and TMR of 1.2% (corrected for geometrical enhancement from 18%, see

ⁱ [Miyazaki, 1995]

ⁱⁱ [Boeve, 2001]

ⁱⁱⁱ [Park, 2001]

^{iv} [Wong, 1998]

^v [Moodera, 1997]; [Sousa, 1998]

^{vi} [Tondra, 1998]

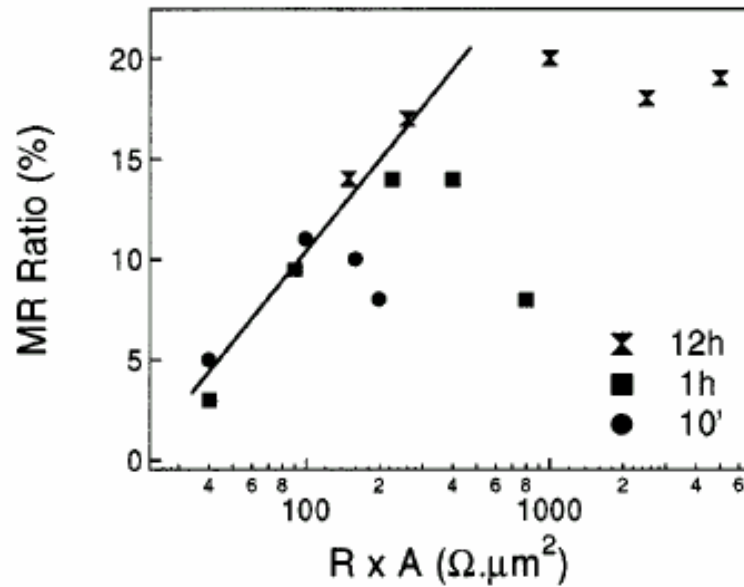


Figure 6.7: MR variation with RA, showing time of oxidation in 13.3 kPa oxygen. [Boeve, 2001]

Section 6.1.7.4). However, this oxidation was performed for 24 hours, which is not practical for industrial application. The time taken to evacuate the system twice is also prohibitive. Surface contamination of the aluminium oxide is difficult to avoid in air and could severely reduce the TMR. Natural oxidation in-situ, using ‘pure’ oxygen has been investigated by a number of authors. This technique generally produces a lower RA than plasma oxidation. As an example, Figure 6.7 shows TMR versus RA for tunnel junctions with naturally oxidised barriers [Boeve, 2001]. Oxidation took place for different times in 13.3 kPa O_2 . Maximum observed TMR was 20% with an RA of approximately $1 \text{ k}\Omega\mu\text{m}^2$.

Barrier production by sputtering aluminium in an atmosphere of argon with a small (unspecified) amount of oxygen has been used to produce tunnel junctions with 20% TMR and RA of $110 \text{ M}\Omega\text{m}^2$ [Tondra, 1998]. However, sputtering aluminium in an atmosphere containing some oxygen is likely to cause intermixing at the interface, due to the incident kinetic energy of oxide molecules. Boeve *et al.* were unsuccessful in their attempts to produce working magnetic tunnel junctions, producing the barrier by sputtering aluminium in an atmosphere of 85% argon and 15% oxygen [Boeve, 2001]. The zero TMR recorded was attributed to oxidation of the ferromagnetic electrode, and was identified by TEM.

A barrier may be fabricated by multiple oxidation. Wong *et al.* used this method to demonstrate a TMR of 6.2% and RA of $0.96 \text{ k}\Omega\mu\text{m}^2$ at room temperature [Wong, 1998]. A thin aluminium layer was deposited and oxidised naturally in 1 kPa O_2 . This was followed by further thin aluminium layers and oxidation thus minimising the thickness of unoxidised aluminium. TMR values were limited by the inclusion of an aluminium layer above the barrier, to protect the oxide from damage (Sections 4.1.1.1 and 6.1.7.1.2). Park and Lee demonstrated magnetic tunnel junctions with Al_2O_3 barrier produced by aluminium oxidation in an atmosphere of ozone [Park, 2001]. They recorded TMR values of approximately 20% with RA of $8 \text{ M}\Omega\mu\text{m}^2$. The RA value is too high for read head sensor applications, although shortened oxidation times may lower this value.

The low RA produced by natural oxidation, or multiple natural oxidation is attractive for the application of tunnel junctions to read heads. Although higher MR has been obtained for plasma oxidation, large RA is generally produced. Further investigation is required into oxidation technique to produce repeatable, low RA, high TMR magnetic tunnel junctions.

6.1.7.1.4 Barrier defects

Theories discussing the voltage and temperature dependence of the TMR in magnetic tunnel junctions have highlighted the significance of defects in the barrier [Zhang, 1997; Zhang, 1998]. These defects provide spin scattering sites or encourage two-stage spin-flip tunneling. High MR requires the dominance of spin dependent transport over spin independent transport. Pinholes and weak-links in the barrier also decrease TMR. Incorporation of sub-monolayer amounts of cobalt, palladium, copper and nickel into the middle of the barrier has been investigated (Figure 6.8) [Jansen, 1998]. Figure 6.8 represents results for the JMR as insufficient data was available to convert to TMR. As expected, the diagram shows that MR decreases with increasing impurity concentration. Jansen *et al.* derived Equation (6.5) to represent the effect of scattering and spin-flip tunneling caused by impurities in the barrier.

$$\text{MR} = \frac{(1 - 2f) \text{MR}^0}{1 - (f \cdot \text{MR}^0)}, \quad (6.5)$$

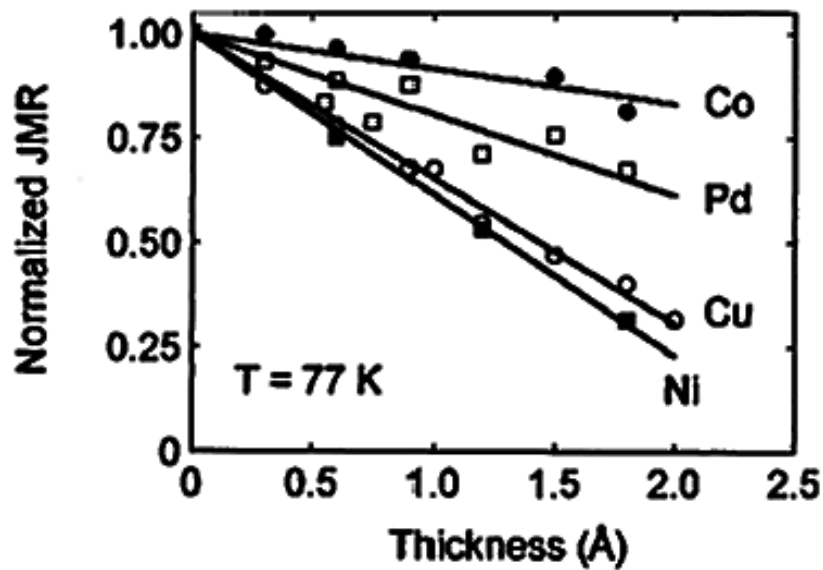


Figure 6.8: Decrease in normalized JMR as the thickness of various defects incorporated into the center of the barrier increases [Jansen, 1998].

where f is the fraction of spin-flip events and MR^0 the magnetoresistance in the absence of spin flip.

The formation of pinholes is detrimental to device performance, as discussed in Chapter 4 and Chapter 7. Generally, pinholes are pictured as regions in which aluminium deposition has not occurred, thus allowing metallic contact between the top and bottom electrodes. Pinholes act in parallel to the tunnel junction and, due to their low resistance, electrically short circuit the tunneling conductance. Aluminium oxide barriers are generally amorphous [Dunin-Borkowski, 1999; Portier, 2001] and therefore produce a smooth layer. The approximately 26% volume increase on oxidation of aluminium reduces the incidence of pinholes [Portier, 2001]. However, an inhomogeneous aluminium thickness may lead to weak-links in the barrier. Such weak-links are not pinholes, but are thin oxide regions and therefore provide a lower resistance current path. They generally result from the use of extremely thin layers, underlayer roughness or deposition problems. Weak-links are sometimes termed ‘hot-spots’ due to the higher currents carried and associated heating effects. They break down rapidly on the application of a voltage bias, thereby leading to junction shorting.

Tests to identify a tunnel junction with pinholes were investigated (Chapter 4). It was found that a decrease in resistance as temperature drops is a reliable characteristic of

pinholes. Due to the requirements of a low resistance barrier, insulator thickness must be minimised. This leads to a severe risk of pinhole and weak-link formation. An increase in the number of randomly distributed pinholes and weak-links causes a decrease in the yield of working tunnel junctions. Schad *et al.* proposed the decoration of pinholes and weak-links with copper, allowing identification by scanning electron microscopy (SEM) [Schad, 2000; Allen, 2001]. A bottom electrode/barrier structure was deposited on a silicon wafer, covered with 200 nm of silicon nitride. The electrodeposition of copper then took place in a copper sulphate solution. Pinholes in the barrier act as a conducting path and copper plating occurs, leading to the build up of cauliflower-like copper features. Dielectric breakdown of the thin insulator at weak-links leads to the formation of conducting paths, where electrodeposition may also occur. The copper features produced are easily identified in an SEM by their bright contrast due to their low resistance. This allows the determination of the number of pinholes and weak-links per unit area. This technique is discussed in depth in Chapter 7, where the cause of weak-links and pinholes has been investigated using the electrodeposition of copper.

6.1.7.2 Effect of electrode roughness

Roughness of the bottom ferromagnetic electrode leads to two problems with the fabrication of high quality magnetic tunnel junctions. These are magnetic coupling through the barrier and a non-uniform oxide layer. Dipolar or orange peel coupling can prevent ferromagnetic electrodes from switching independently [Néel, 1962]. Néel derived Equation (6.6) for the coupling energy, J , between two ferromagnetic films. M and M' are the saturation magnetisation of the films, which are separated by a barrier thickness t . The interface roughness is described by a two dimensional sinusoidal relation with amplitude h and wavelength λ .

$$J = \frac{\pi^2}{\sqrt{2}} \frac{h^2}{\lambda} (\mu_0 M M') \exp\left(\frac{-2\pi t \sqrt{2}}{\lambda}\right), \quad (6.6)$$

where μ_0 is the permeability of free space. The coupling field, H_{CP} of the free ferromagnetic layer, with thickness t_f and magnetisation M is then predicted by Equation (6.7) [Kools, 1996]:

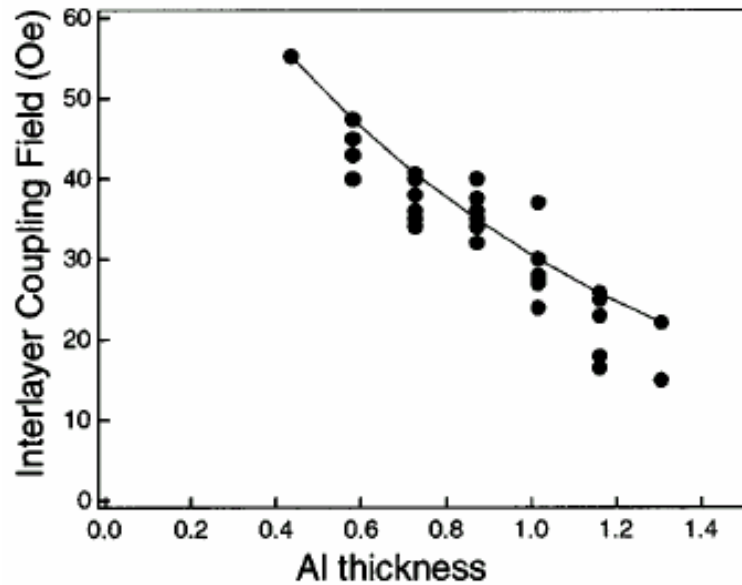


Figure 6.9: The variation of interlayer coupling field with aluminium thickness [Boeve, 2001].

$$H_{CP} = \frac{J}{\mu_0 M t_f}. \quad (6.7)$$

Boeve *et al.* used Equations (6.6) and (6.7) to fit data for naturally oxidised tunnel junctions of the structure $\text{Co}_{90}\text{Fe}_{10}/\text{AlO}_x/\text{Co}_{90}\text{Fe}_{10}/\text{Ni}_{80}\text{Fe}_{20}$ [Boeve, 2001]. x represents the degree of oxidation of the aluminium. Figure 6.9 shows the variation of interlayer coupling field with aluminium thickness. They found values of $h = 0.22$ nm and $\lambda = 12.5$ nm, which they assigned to the barrier thickness variation and grain size respectively. However, their films were extremely regular and flat, as demonstrated by transmission electron microscope (TEM) images. The results presented in Section 6.3.2 and those of other authors show films with rough bottom electrodes [Bruckl, 2001; Clark, 1999; Portier, 2001]. Therefore the roughness of the bottom electrode generally dominates the height variation of the barrier. Such roughness is also likely to induce thickness variation in the aluminium barrier. This indicates that the switching fields of magnetic tunnel junctions may be shifted due to orange peel coupling [Boeve, 2001]. Furthermore, the ferromagnetic layers may be strongly coupled preventing independent switching. Orange peel coupling is discussed further in Section 6.3.1.1.2.

The second problem associated with rough ferromagnetic electrodes is the non-uniformity of aluminium thickness due to deposition self-shadowing effects. This leads to either incomplete coverage of the electrodes or weak-links in the insulator. As discussed in Section 6.1.7.1.4, weak-links are likely to form ‘hot-spots’ and cause the barrier to break-down at low voltage. The relationship between electrode roughness and the number of weak-links and pinholes per unit area is discussed in Chapter 7.

6.1.7.3 Annealing and temperature stability

The effect of annealing magnetic tunnel junctions has been investigated by measuring device characteristics and studying TEM images. A number of authors have identified an improvement in TMR after annealing at modest temperature, $<230^{\circ}\text{C}$. However, TMR drops for higher temperature annealing, as illustrated by Figure 6.10 [Sousa, 1999]. This figure shows the results of annealing exchange biased junctions of the structure Ta/NiFe/CoFe/Al₂O₃/CoFe/MnRh/Ta, with relatively low RA, in the range 25-60 kΩμm². Annealing took place for one hour in the presence of an external magnetic field. Sousa *et al.* presented Rutherford backscattering data to indicate the barrier oxygen content during annealing. They suggested that the cause of the increase in MR for annealing at temperatures up to 200°C was the diffusion of oxygen from the CoFe/Al₂O₃ interface into the barrier, thus increasing the effective polarisation and decreasing scattering. At higher temperatures they suggested that the changes in barrier height and thickness indicated structural change (Figure 6.10). However, effective barrier height and thickness are calculated values rather than physical quantities. It is likely that the diffusion of defects caused the changes in the effective barrier height and thickness.

A number of research groups have investigated the annealing of magnetic tunnel junctions. It is clear that the dependency of TMR on annealing depends on the deposition conditions and defect concentrations. Generally, annealing for one hour in the presence of an external magnetic field at temperatures up to 230°C increases TMR. Parkin *et al.* observed improvements in TMR at annealing temperatures up to 300°C [Parkin, 1999]. The improvement in TMR is due to homogenisation of the barrier and diffusion of oxygen from the barrier interfaces to its bulk. The decrease in TMR caused by annealing at high temperature has been attributed to the diffusion of atoms from the electrode metal into the barrier [Moodera, 1998].

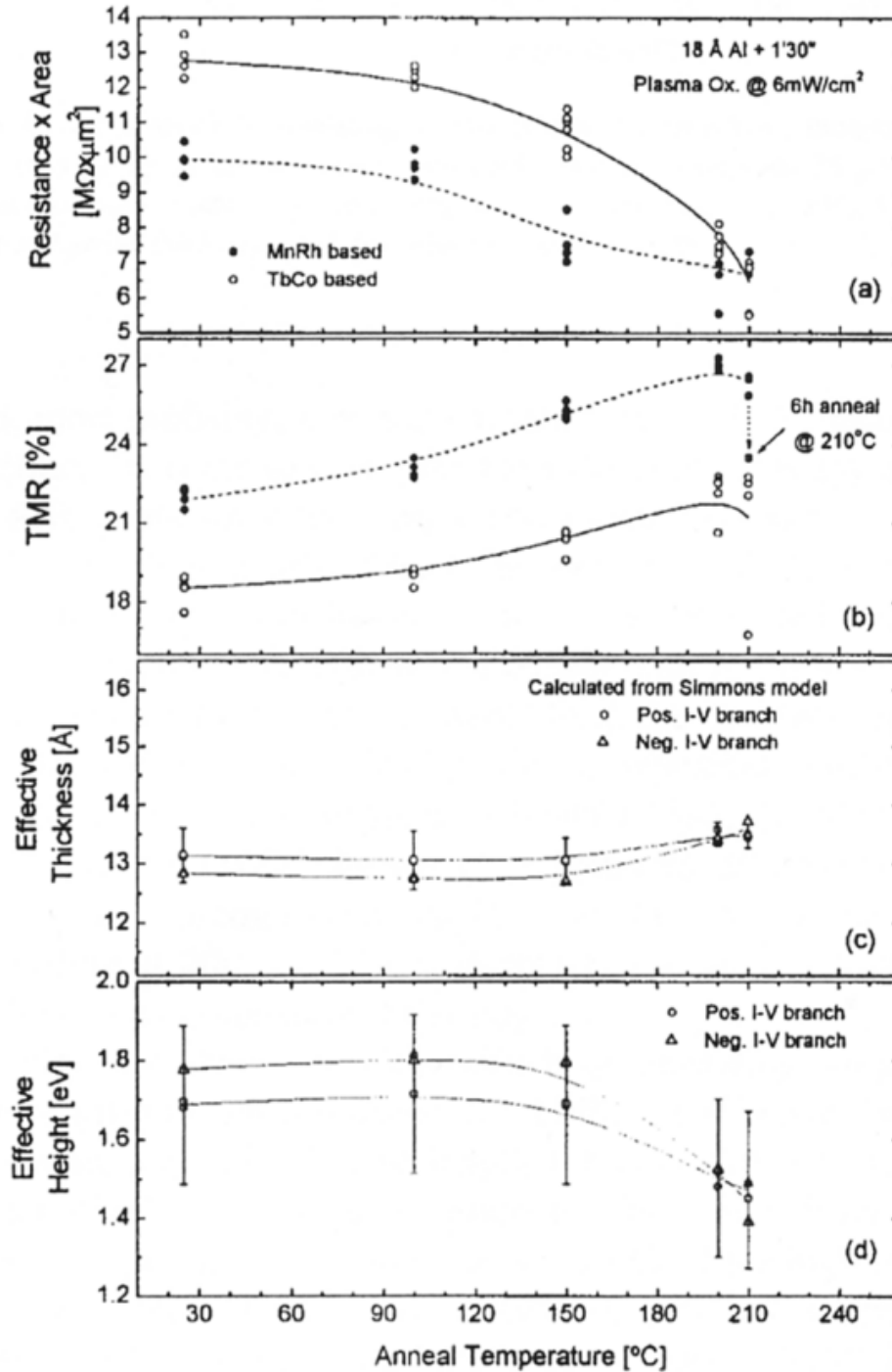


Figure 6.10: The effect of annealing on junction parameters (a) RA product (b) TMR (c) effective barrier thickness and (d) effective barrier height. [Sousa, 1999]

6.1.7.4 Geometrical enhancement

Geometrical enhancement of the TMR may be observed when the actual junction resistance, R_T , becomes comparable to the resistance of the leads over the junction area,

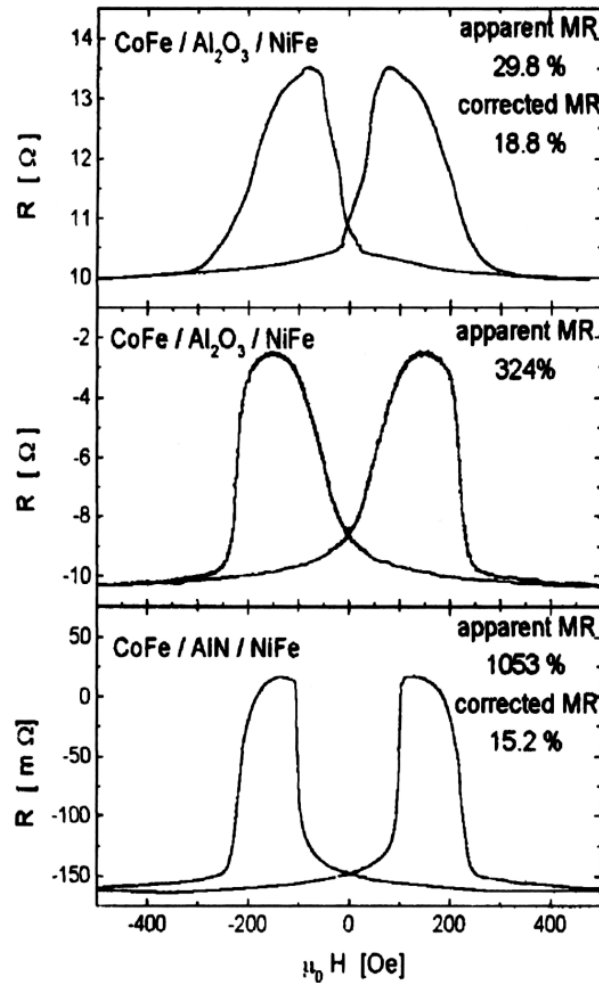


Figure 6.11: Geometrical enhancement of MR [Moodera, 1996(b)].

R_L [Pederson, 1967]. When this occurs, the measured junction resistance, R_J , is less than R_T , due to non-uniform current flow. Figure 6.11 shows the effect of such geometrical effects on the TMR for magnetic tunnel junctions [Moodera, 1996(b)]. Pederson and Vernon developed a one-dimensional model of coplanar tunnel junctions to explain this effect [Pederson, 1967]. They predict that when $R_L < 30R_T$ geometrical enhancement is negligible and when $R_L > 30R_T$ negative values for R_J may be observed, as shown in Figure 6.11 [Moodera, 1996(b)]. Van de Veerdonk *et al.* modelled the non-uniform electrode current distribution, which can lead to significant voltage drop in the electrodes [Van de Veerdonk, 1997]. For a cross-geometry tunnel junction, when R_L becomes comparable to R_J , the current flow becomes largest in the corner where the two leads meet. When the leads are good quality and thick geometrical enhancement should not occur.

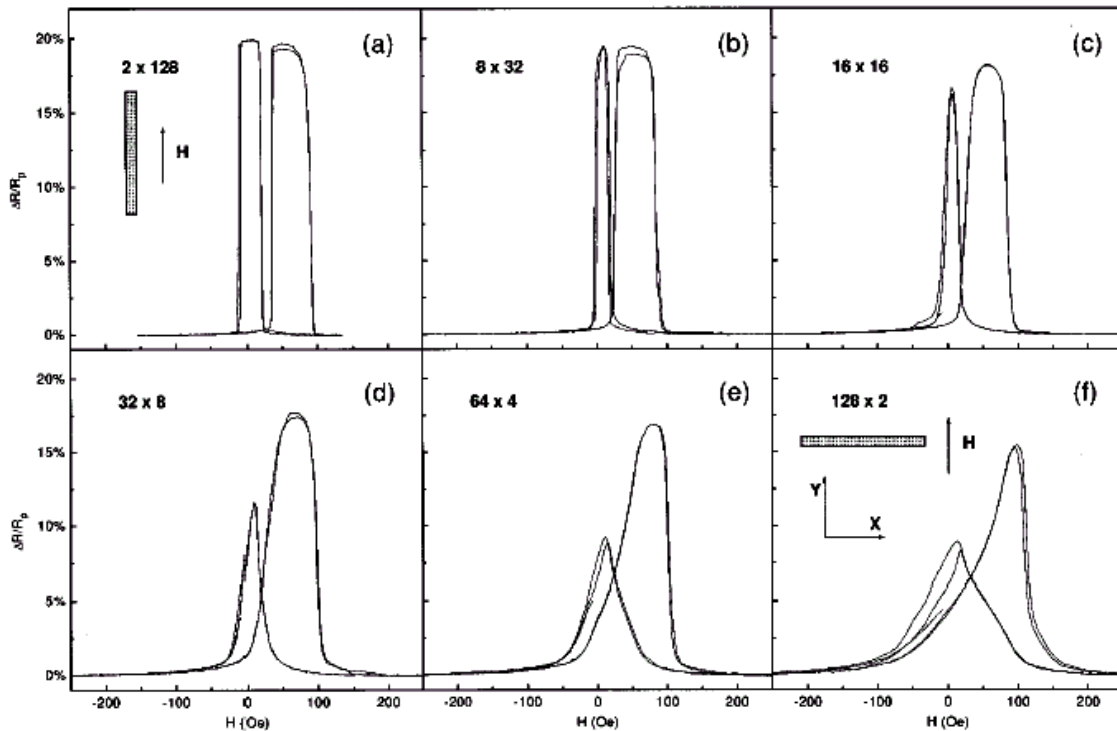


Figure 6.12: The effect of shape on magnetic tunnel junction response as the aspect ratio of junctions changes from (a) $2 \times 128 \mu\text{m}^2$ to (f) $128 \times 2 \mu\text{m}^2$ [Gallagher, 1997].

6.1.7.5 Shape anisotropy

Magnetic tunnel junction shape can affect the switching response. This is shown in Figure 6.12 [Gallagher, 1997]. Gallagher *et al.* deposited the film structure: Cu/Py/MnFe/Py/Al₂O₃/Py/Pt, where Py represents permalloy. Junctions shown in the figure have the same area but different aspect ratios in relation to the magnetic field. Switching is most abrupt when magnetic field is aligned along the easy axis of the electrode. The demagnetising field depends on shape anisotropy, intrinsic anisotropy, domain structure and inhomogeneities such as edge roughness.

6.2 Fabrication and testing of magnetic tunnel junctions

The fabrication and testing procedures for magnetic tunnel junctions have been discussed in Chapter 3. Specific conditions for films and devices presented in this chapter are listed

in this section. A review of the deposition and processing route is included for convenience.

Films suitable for SIF devices were deposited and subsequently fabricated to check the integrity of each magnetic tunnel junction deposition run. The rotating stage and shielding on the flange allowed the deposition of up to three different types of device during one run, as discussed in Section 3.2.1. The ability to deposit and subsequently fabricate magnetic tunnel junctions and SIF devices with ferromagnet bottom and top electrode during the same run was a considerable aid to MTJ development. The use of SIF devices to characterise deposition and device fabrication quality was discussed in Chapter 4

6.2.1 Film deposition

Films were deposited on 5×10 mm oxidised silicon substrates by whole wafer DC magnetron sputtering, except run 9617 which used 3.5×12.5 mm r-plane sapphire substrates. Substrate preparation and deposition procedure are described in Section 3.2. Tables 6.1 and 6.2 show the deposition conditions and layer thickness for films presented in this chapter. Consistent procedures and rate calibrations were used throughout the study, deposition rates are shown in Table 4.2. Table 6.2 shows that two depositions were undertaken with CoFe electrodes. CoFe was deposited by co-sputtering the cobalt and iron targets, each at 13.5 W power, whilst rotating the stage rapidly. The deposition rate from iron and cobalt is the same to within the experimental error. The CoFe deposition rate was 0.096 nmW⁻¹min⁻¹. The requirement of presputtering positions whilst depositing from two targets at once was prohibitive. Therefore it was not possible to produce SIF films in addition to magnetic tunnel junctions. CoFe was not pursued as an electrode of ferromagnetic tunnel junctions, but VSM investigation into magnetic coupling through the thick aluminium layers is presented below.

6.2.2 Device fabrication

Standard processing and lithography techniques were used to fabricate devices. These are described in Section 3.3 and part-built devices are shown in Figure 4.10. The processing route may be summarised as:

1. Junction area defined by optical lithography, mesa junctions produced by ion milling.
2. Base layer defined by optical lithography followed by ion milling.
3. Negative resist profile for lift-off defined by optical lithography followed by silica insulation deposition and lift-off in acetone.
4. Negative resist profile defined by optical lithography followed by a brief ion mill, niobium wiring deposition and lift-off in acetone.

All optical lithography took place on the Karl Süss contact printer, using AZ1529 photoresist spun at 5000 rpm for 30 seconds. Lithography conditions are a complex function of temperature, humidity, bulb calibration, age of resist and age of developer. Some variation in device definition is expected, as discussed in Section 4.2.3. The effects of changes in the lithography, milling and deposition rates were minimised.

Layer	Condition	9716_3	11336_(1/2/3)	11363_(1/2/3/4)
Niobium	Passes, speed	16, 1×	2, 2× and 15, 2×	2, 2× and 15, 2×
	Pressure (Pa)	0.74	0.3 and 0.7	0.3 and 0.7
	Expected thickness (nm)	36.5	19.4	19.4
Cobalt/Iron	Ferromagnet	Fe	Fe	Co
	Passes, speed	10, 1×	10, 1×	104 secs stationary
	Pressure (Pa)	2.7	2.7	1.02
	Expected thickness (nm)	10.5	10.5	11.7
Aluminium	Passes, speed	2, 1×	3, 2× (_1/2) or 0.5× (_3)	3, 2×
	Pressure (Pa)	0.67	0.7	0.7
	Expected thickness (nm)	0.8	2.5 or 10	2.5
Oxidation	Pressure (Pa), time (mins).	1000, 60	1000, 60	1000, 60
Aluminium	Passes, speed	5, 1×	1, 1×	1, 1×
	Pressure (Pa)	0.81	0.7	0.7
	Expected thickness (nm)	2	1.7	1.7
Cobalt/ Iron/ Permalloy	Ferromagnet	Ni ₈₀ Fe _{15.5} Mo _{4.5}	Co (_2 and _3 only)	Fe (_1/2/3 only)
	Passes, speed	10, 1×	104 secs stationary	10, 1×
	Pressure (Pa)	0.59	4 reduced to 1	4 reduced to 2.7
	Expected thickness (nm)	8.7	11.7	10.5
Niobium	Passes, speed	4, 1×	1, 1× and 11, 1× (_1) or 2× (_2/3)	1, 1× and 11, 2× (_1/2/3) or 1× (_4)
	Pressure (Pa)	0.85	4 and 0.7	4 and 0.7
	Expected thickness (nm)	9.12	27.4 (_1) or 13.7 (_2/3)	13.7 (_1/2/3) or 27.4 (_4)

Table 6.1: Deposition conditions for MTJ and SIF films presented in Section 6.3

Layer	Condition	11198_1	11259_1	11464_(2/3/)
Niobium	Passes, speed	2, 2× and 15, 2×	2, 2× and 15, 2×	2, 2× and 15, 2×
	Pressure (Pa)	0.3 and 0.7	0.3 and 0.7	0.3 and 0.7
	Expected thickness (nm)	19.4	19.4	19.4
Cobalt/Iron	Ferromagnet	Co	Co	Co (_2) or Fe (_3)
	Passes, speed	104 secs stationary	104 secs stationary	104 secs stationary or 10,1×
	Pressure (Pa)	1.04	1.04	1 or 2.7
	Expected thickness (nm)	11.7	11.7	11.7 or 10.5
Aluminium	Passes, speed	24, 4×	24, 2×	0.5×
	Pressure (Pa)	0.7	0.7	0.7
	Expected thickness (nm)	10	20	7.5
Oxidation	Pressure (Pa), time (mins).	1000, 60	1000, 60	1000, 60
Aluminium	Passes, speed	8, 2×	8, 2×	-
	Pressure (Pa)	0.7	0.7	-
	Expected thickness (nm)	6.6	6.6	-
CoFe	Passes, speed	4, 2× and 16, 2×	4, 2× and 16, 2×	-
	Pressure (Pa)	4 and 2.7	4 and 2.7	-
	Expected thickness (nm)	13	13	-
Niobium	Passes, speed	1, 1× and 11, 2×	1, 1× and 11, 2×	-
	Pressure (Pa)	0.7	0.7	-
	Expected thickness (nm)	13.7	13.7	9.12

Table 6.2: Deposition conditions for films presented in Section 6.6

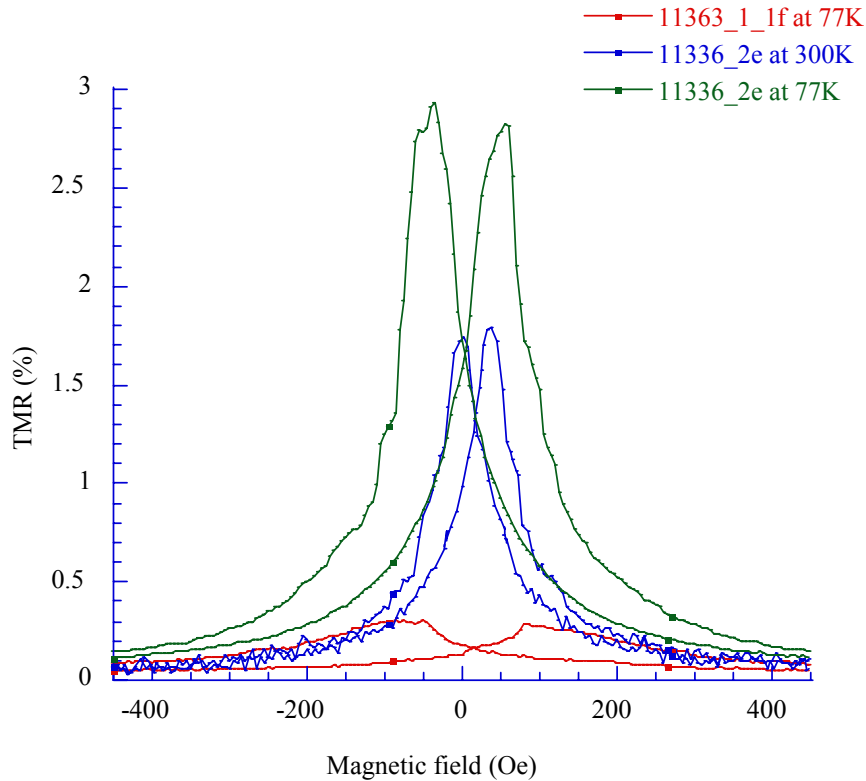


Figure 6.13: TMR of devices 11336_2_1d and 11363_1_1g, Fe bottom and top electrodes respectively.

6.3 Results

6.3.1 The effect of bottom electrode

Figure 6.13 shows the TMR obtained from devices 11336_2_1d and 11363_1_1g. These $6 \times 6 \mu\text{m}$ magnetic tunnel junctions were tested at 77 K and room temperature. Devices were fabricated from the film 11336_2 which was of the structure Nb/Fe/Al₂O₃/Al/Co/Nb. These junctions exhibited 2.9% TMR (2.8% JMR) at 77 K, and 1.8% TMR at room temperature. Devices from 11363_1, of the structure Nb/Co/Al₂O₃/Al/Fe/Nb with Co bottom electrode, showed much smaller TMR of about 0.3% at 77 K and negligible TMR at room temperature. SIF devices were fabricated from both deposition runs and were reasonable quality with figure-of-merit (FOM) in the range 2.5-4 at 4.2 K. FOM is the ratio of the conductance of the SIF junction in the normal state to that at zero bias (Section 4.1.2). This indicates that tunneling was the principle transport mechanism at 4.2 K and that the fabrication route was satisfactory.

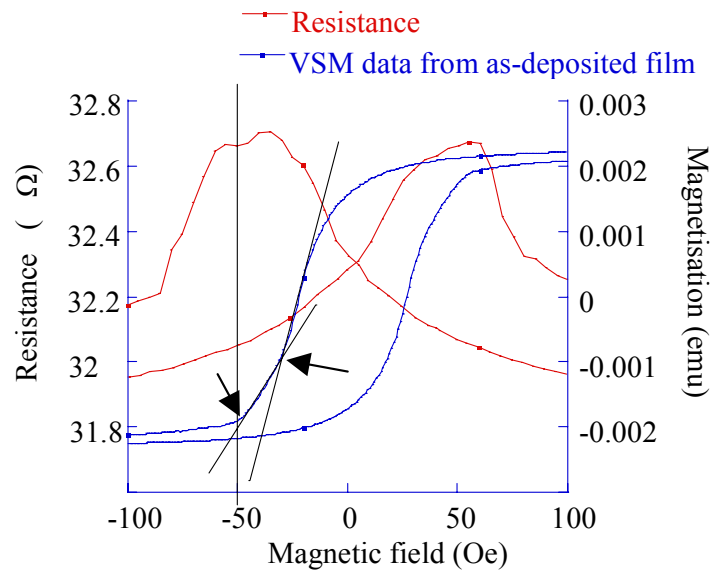


Figure 6.14: The resistance-field characteristics for 11336_2_1d at 77K and the hysteresis curve for 11336_2. Lines and arrows indicate possible inflections in the hysteresis curve.

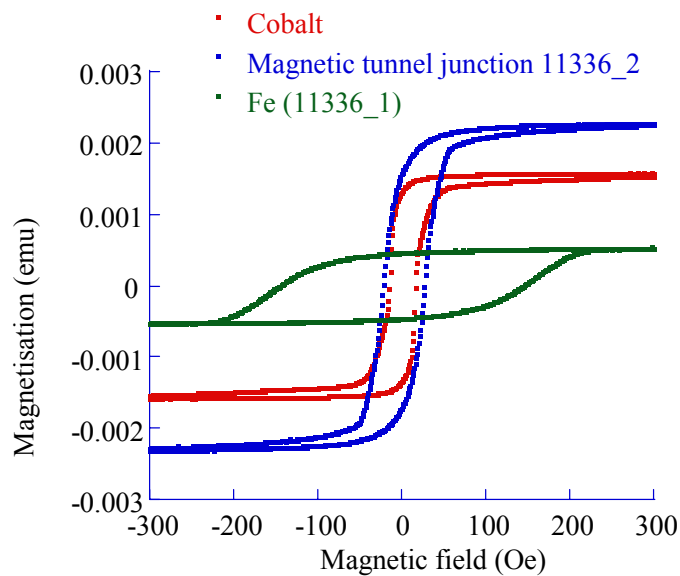


Figure 6.15: Hysteresis curves at room temperature for 11336_2 magnetic tunnel junction film and corresponding individual magnetic layers.

6.3.1.1 Film characteristics

The difference in TMR caused by changing the bottom electrode from iron to cobalt was investigated using VSM and AFM measurements on as-deposited films. Figure 6.14 shows the hysteresis curve for the film 11336_2 as well as resistance-field measurements at 77 K for the corresponding device, 11336_2_1d. Unlike Figure 2.19, there is no clear

independent magnetic switching of the layers is clear. The straight lines act as visual aids which identify two slight inflections in the curve on each branch of the hysteresis loop. Figure 6.15 shows the hysteresis curve for the Nb/Fe/Al₂O₃/Al/Co/Nb trilayer in addition to those for iron, in the film Nb/Fe/Al₂O₃/Al/Nb and cobalt in the film Nb/Al₂O₃/Al/Co/Nb. The volume of each ferromagnetic material in the SIF junctions is the same as that found in the respective layer of the magnetic tunnel junction films. The relative saturation magnetisation of cobalt and iron in the SIF films suggest the proportion of the magnetic tunnel junction trilayer saturation magnetisation for which these materials are responsible. Possible switching in the magnetic tunnel junction trilayer does not appear to correspond to the magnetisations suggested by results from the SIF films. Figures 6.14 and 6.15 indicate that the magnetic layers in the film 11336_2 are strongly coupled. Similar curves were observed for 11636_1 and other magnetic tunnel junction films.

AFM measurements made on the films 11336_2 and 11363_1 indicated a negligible difference in roughness between the complete multilayers. Films were deposited to the barrier and not beyond (deposition 11464) to investigate the roughness at the barrier and the number of pinhole and weak-links per unit area. Figure 6.16 shows cross-sections of images measured with the AFM for these films. The diagram shows that a cobalt bottom electrode produces a considerably rougher interface at the barrier than iron. Roughness values estimated using the AFM (Section 3.4.1.2) are 1.8 nm for a cobalt bottom electrode and 0.3 nm for an iron bottom electrode. Measurements were made in a 1 µm square to measure short range height variation. The layers deposited above the barrier for tunnel junction films homogenise the profile thereby decreasing the observed roughness. Increased electrode roughness can produce two problems (discussed in Section 6.1.7.2), higher pinhole or weak-link formation and increased orange peel coupling.

6.3.1.1.1 Copper decoration

The effect of the choice of bottom electrode on pinhole and weak-link density was investigated by copper decoration (Section 6.1.7.2). This technique, which is the subject of Chapter 7, involves the electrodeposition of copper onto films deposited up to the barrier (deposition run 11464). The method is based on the work of Schad *et al.* [Schad, 2000]. The experimental technique, apparatus and issues are discussed in detail

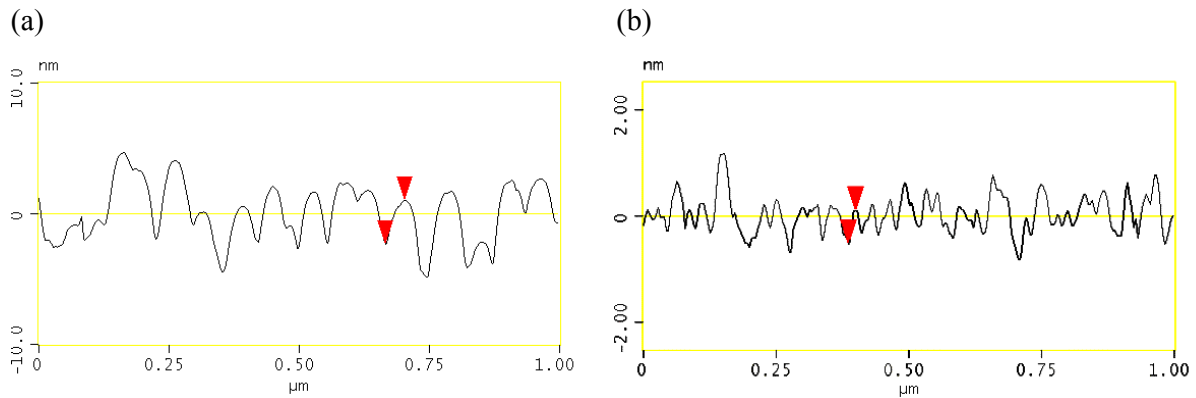


Figure 6.16: Cross-sections of the surface, measured by AFM. (a) 11464_2, Co bottom electrode, (b) 11464_3, Fe bottom electrode. Red triangles indicate a typical height and half period of the variation. Note different scales on the height of (a) and (b).

in Chapter 7. A drop of 0.1 M copper sulphate 0.1 M sulphuric acid solution was placed on the film with a pipette (Figure 7.15). A sprung-loaded touch-down tip placed on the bare film provided the anode. A copper needle cathode was lowered into the drop of electrolyte. A Keithley 487 was used to apply a voltage of -300 mV for thirty seconds and to measure the current. The Keithley 487 was controlled via a LabVIEWTM computer programme, written by Dr G. Burnell. The chip was removed, rinsed gently in distilled water and then dried in air. Digital images of the area which had been covered by the drop were recorded with a JEOL 820 scanning electron microscope. Copper features were clearly visible due to their high conductance compared to the insulating barrier. The number of copper features per image was estimated using the UTHSCSA ImageToolTM graphics package. The number of features represents the number of pinholes and weak-points in that region.

The number of copper features per unit area was $1.35 \times 10^{10} \text{ m}^{-2}$ for a film with cobalt bottom electrode (11464_2), and was $4.56 \times 10^9 \text{ m}^{-2}$ for an iron bottom electrode (11464_3). The number of weak-links and pinholes per unit area increases when the iron bottom electrode is replaced by cobalt. This is in accordance with the decrease in magnetic tunnel junction TMR from 3% to 0.2%, at 77 K. However, in zero magnetic field at 77 K, the resistance of equivalent devices 11336_2_1d (Fe) and 11363_1_1g (Co) was extremely similar ($\approx 32.3 \Omega$). The distribution of pinholes and weak-links over the junction area is random. It is likely that no significant barrier defect is present in the $6 \times 6 \mu\text{m}$ area of device 11363_1_1g (Co). The decrease in TMR for working devices

caused by replacing the iron bottom electrode with cobalt is not likely to be caused by an increase in weak-link and pinhole density. The increase in defect density in the barrier may be reflected in the yield of working devices. Six working magnetic tunnel junctions were present on 11336_2 (Fe) compared to only three on 11363_1_1 (Co).

6.3.1.1.2 Magnetic coupling

Orange peel coupling increases with roughness, as shown by Equations (6.6) and (6.7). The amplitude, h , and period, λ , of roughness at the interface were estimated from the sections shown in Figure 6.16. The red triangles indicate the measurements taken. For the cobalt lower electrode, values of $h = 1.7$ nm and $\lambda = 79$ nm were estimated. Those for iron lower electrode were $h = 0.32$ nm and $\lambda = 12$ nm. Such values are extremely difficult to estimate from Figure 6.16, since the real section is not a regular sinusoidal variation. As a result, values of orange peel coupling estimated from Equations (6.6) and (6.7) are subject to large error. The saturation magnetisations per unit volume were estimated from VSM data and scaled to the junction area. Iron was considered the pinned electrode due to its higher coercive field (≈ 145 Oe compared to ≈ 20 Oe). Layer thickness was taken from Table 6.1. Coupling fields, $H_{CP} \approx 55$ Oe and ≈ 0.7 Oe, were estimated for cobalt and iron lower electrodes respectively. As expected, H_{CP} predicted by Néel's model for orange peel coupling is much larger for cobalt than iron lower electrodes. The values of the coercivity indicate that considerable independent switching should still occur. However, the application of this model is not as simple as suggested above. The thickness variation of the barrier is likely to be considerable due to such a large roughness. Coupling occurs through regions of the barrier thinner than that estimated from the deposition rate, further pinning the layers together. These results indicate that magnetic coupling between layers with cobalt lower and iron top electrode is much higher than that for films in which the ferromagnets are interchanged. This may explain the low TMR of devices from the deposition run 11363.

The strong orange peel coupling predicted between ferromagnetic electrodes when the lower ferromagnet is cobalt (145 Oe) may explain the failure of this study's Nb/Co/Al₂O₃/Al/Co/Nb devices to exhibit a TMR. SIF devices with cobalt lower and top electrode exhibited good FOM (Section 6.3.1). The different environment and deposition procedure of the top and bottom electrode yields layers with slightly different coercivity.

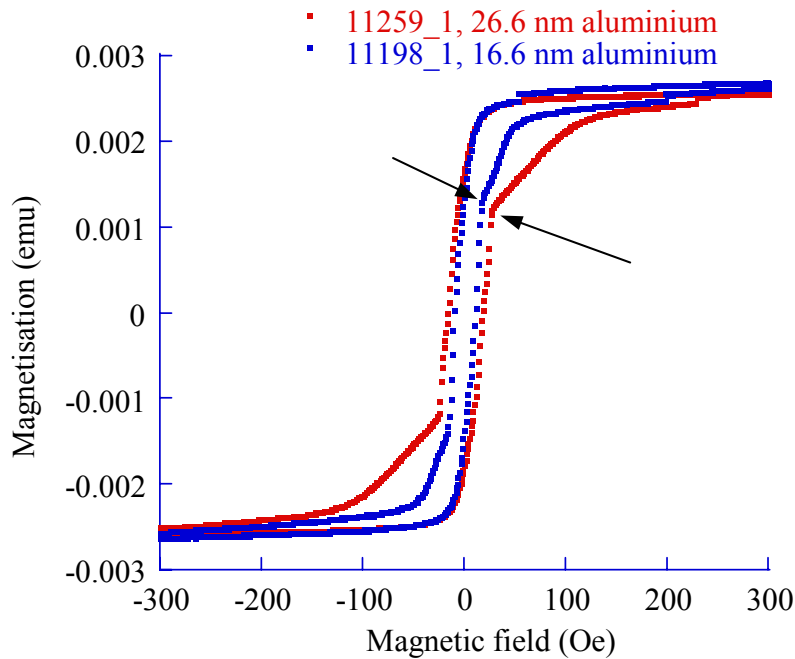


Figure 6.17: Hysteresis curves for the films 11198_1 (16.6 nm Al) and 11259_1 (26.6 nm Al). Arrows indicate positions at which it appears that the cobalt has completely aligned to the magnetic field.

It was hoped to produce devices with a sharp peak in TMR at low fields. However, the predicted orange peel coupling and additional magnetic coupling through thin regions of barrier appear to exceed the small coercivity difference. The cobalt electrodes behave as if they are ‘locked together’ with no independent switching and no TMR.

6.3.1.2 Effect of thick aluminium

The decrease in TMR obtained by depositing a thick layer of aluminium was discussed in Section 6.1.7.1.2. Non-magnetic material between a ferromagnetic electrode and the barrier has been found to decrease the effective polarisation of the electrode. From Equation (6.1), reduced polarisation lowers the TMR. This effect is evident in devices on the chip 11336_3_1, which displayed negligible TMR at 77 K. Aluminium thickness for these films was 10 nm which is four times that for 11336_2.

6.3.1.2.1 Effect of aluminium thickness on magnetic coupling

Figure 6.17 shows the effect on hysteresis curves of increasing the spacer thickness from 16.6 nm to 26.6 nm for Nb/Co/Al/Al₂O₃/Al/CoFe/Nb multilayers (11198_1 and 11259_1). Arrows indicate inflections where, for a totally decoupled film, magnetic

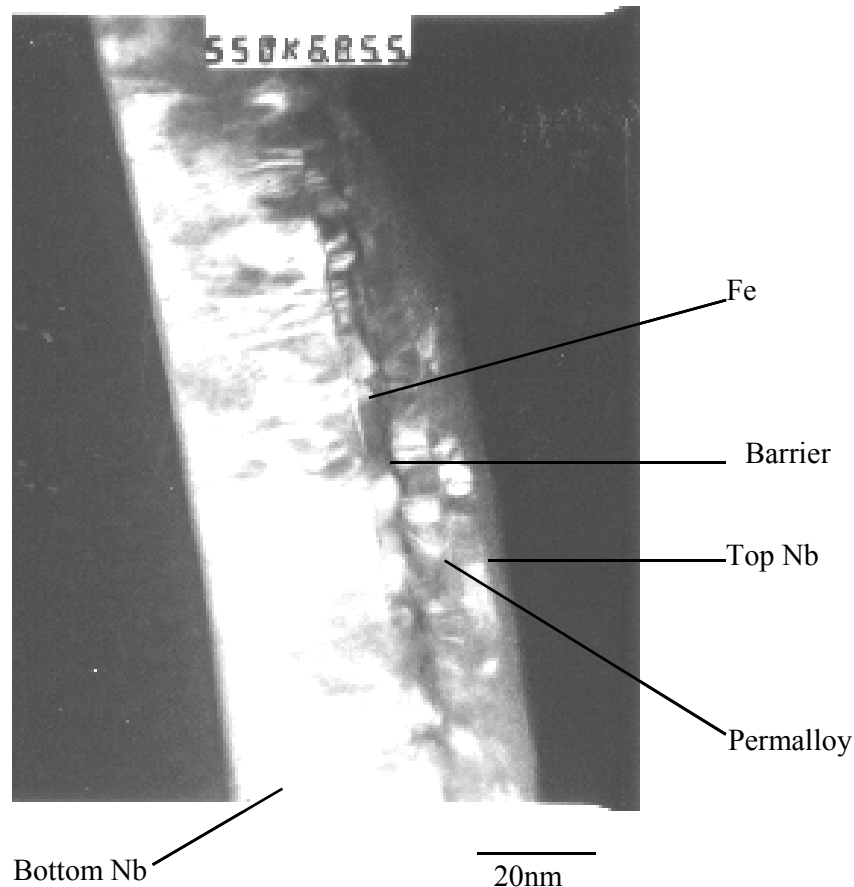


Figure 6.18: TEM image of film 9716_3. Crystalline grains of niobium, permalloy and iron are visible.

switching of the lower coercivity film would be complete and the field would not be high enough to switch the magnetisation of the second layer. Magnetic coupling clearly decreases as aluminium thickness increases. The layers behave more like independent magnetic films. However, the aluminium thickness for both films is too high to allow fabrication of working magnetic tunnel junctions.

6.3.2 Device and TEM characterisation

Structural properties of films were investigated using transmission electron microscopy (TEM), in collaboration with Dr Stephen Lloyd of the High Resolution TEM group in the Materials Science Department at the University of Cambridge. Details of the deposition of the films studied (from 9716_3) are shown in Table 6.1. Devices were fabricated and then tested using the variable temperature magnetoresistance apparatus (Section 3.4.2.5).

The magnetic properties of the as-deposited films were further investigated with the VSM.

The TEM image of 9716_3, shown in Figure 6.18, reveals the crystalline structure of the niobium contacts and ferromagnetic electrodes. Roughness of the oxide layer appears to be induced by the crystallographic growth of layers onto which it was deposited. As discussed above in Sections 6.1.7.2 and 6.3.1.1.2, such roughness encourages orange peel coupling and an inhomogeneous barrier with associated weak-links and pinholes.

High resolution TEM (Figure 6.19(a)) and oxygen mapping (Figure 6.19(b)) was used to investigate the barrier region in detail. The crystalline nature of the electrodes shown in Figure 6.19(a) is associated with the regular diffraction pattern observed. However, the barrier appears to be amorphous. This agrees with previous work, described in Section 6.1.7.1.4. The observed aluminium thickness is also greater than expected, ≈ 1.6 nm on the image, compared with a predicted 0.8 nm. A 26% increase of volume due to aluminium oxidation has been reported in Section 6.1.7.1.4 which is insufficient to explain the difference. The likely cause of this disparity is an increased aluminium deposition rate, due to either fluctuation in the power or calibration error with the profilometer. Variation in the barrier width was approximately 0.3 nm in the small sample area of Figure 6.19(a). Shadowing effects of deposition onto a rough substrate are may be responsible for the barrier thickness inhomogeneity.

Oxygen mapping took place with electron energy loss spectroscopy (EELS), which identifies the oxygen atoms within a film by observing the energy loss of incident electrons and characterising materials by their spectra. Energy loss depends on phonon excitations, electron transitions, plasmon excitation and absorption edges [Brandon 1999] In Figure 6.19(b) oxygen is depicted in white. The white line running through the middle of the sample is the barrier, however its edges are not well defined. Since such thin aluminium was used, oxidation may have occurred at the interface of the bottom electrode. As discussed in Sections 6.1.5 and 6.1.7.1.2, such magnetic oxides at the interface contribute to spin scattering and significantly decrease TMR. Diffusion of oxygen from the barrier into the aluminium capping layer, combined with damage during its deposition, may have caused the indistinct oxide definition at the upper barrier interface.

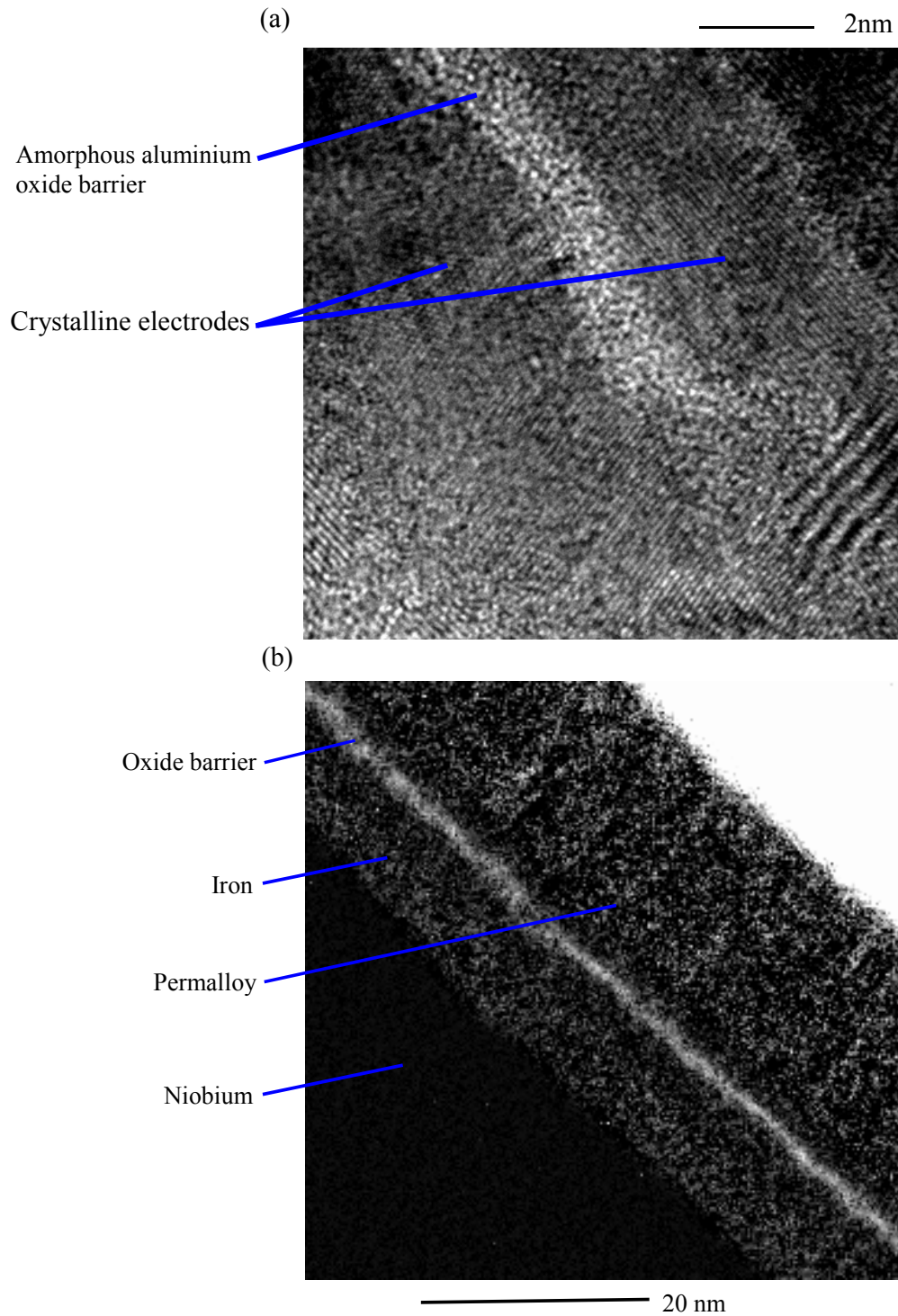


Figure 6.19: (a) High resolution TEM image of 9716_3, showing crystalline electrodes and amorphous barrier. Fringes in the bottom right corner are an artifact of preparing the film for TEM. (b) Oxygen map of 9716_3 indicating that the barrier interfaces are not abrupt.

Figure 6.20 shows resistance versus field at 77 K for 9716_3_1d. It also shows film behaviour measured with the VSM at room temperature. The TMR is small (0.2%),

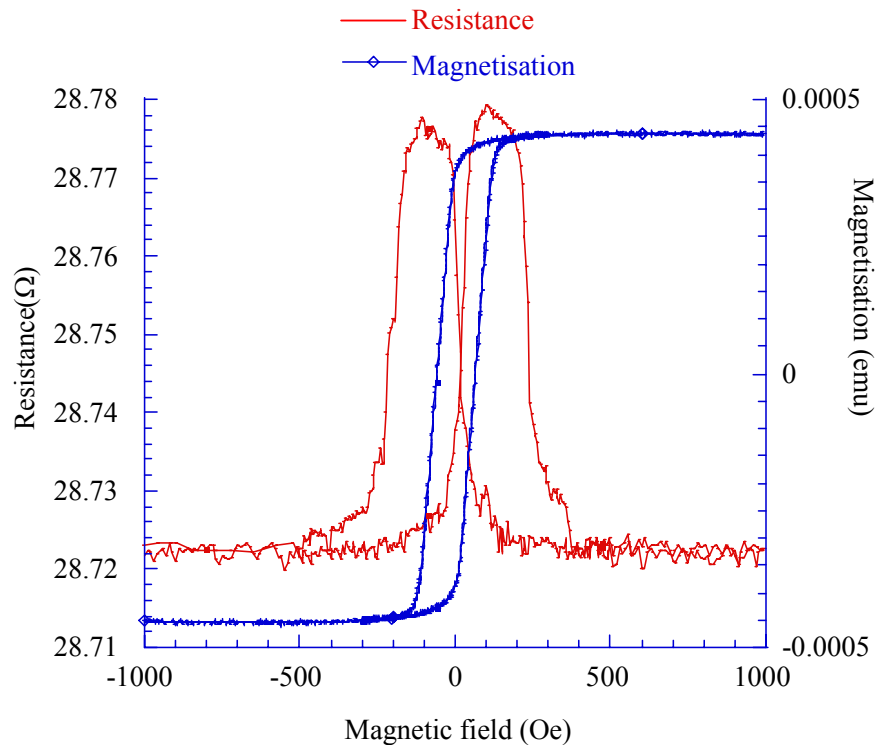


Figure 6.20: Resistance-field characteristic of 9716_3d and hysteresis loop for 9716_3.

however switching between high and low resistance states is abrupt. The low TMR is may result from spin scattering due to over oxidation of the barrier, as well as the reduction of polarisation caused by a non-magnetic aluminium layer above the barrier. No independent switching of the layers is visible in the hysteresis curve of 9716_3, shown in Figure 6.20. Strong magnetic coupling between the layers may reduce the TMR.

6.4 Conclusions

Magnetic tunnel junctions have been fabricated with TMR in the range 0.2-2.9% at 77 K. Tunnel junctions of the structure Nb/Fe/Al₂O₃/Al/Co/Nb exhibited TMR up to 2.9%, whereas interchanging the iron and cobalt layers to produce a cobalt bottom electrode led to a much smaller TMR of 0.3% at 77 K. As-deposited films were investigated with the AFM and VSM. Magnetic switching was not clearly visible on the hysteresis curves for the films. Roughness measurements between tunnel junction films indicated negligible

difference between the order of electrodes. However, measurements on films only fabricated to the barrier with the AFM indicated a low roughness for an iron bottom electrode (0.3 nm) and far higher roughness for a cobalt lower electrode (1.8 nm). Néel's model for orange peel coupling was applied to the films, using the AFM cross-section to estimate the height and period of roughness. Orange peel coupling was estimated to be 55 Oe for these films with a cobalt bottom electrode and only 0.7 Oe with an iron bottom electrode. Additional coupling is expected due to variation in the barrier thickness. Stronger coupling between the magnetic layers in tunnel junctions fabricated with a cobalt bottom electrode may impede independent switching of the layers and reduce TMR.

Copper decoration of pinholes and weak-links was performed by electrodeposition using films only deposited to the barrier. Copper feature density was more than doubled when the iron bottom electrode was replaced with cobalt. Insignificant differences in the resistance of working devices indicates that significant defects are not likely in these junction areas. The yield of working devices was lower from films with a cobalt bottom electrode than with iron. This may reflect the increase in barrier defect density.

Thick aluminium deposition led to a decrease in TMR at 77 K from 2.9% for 2.5 nm thick aluminium in 11336_2_1d to 0.2% for 10 nm thick aluminium in 11336_3_1f. This is attributed to a decrease in the effective polarisation of the ferromagnetic electrodes due to the excess non-magnetic layer at the interface. The effect of aluminium thickness on the shape of hysteresis loops was investigated for films with cobalt and CoFe electrodes. More pronounced step-features in magnetisation data were present after the aluminium thickness was increased from 16.6 nm to 26.6 nm. This supports the hypothesis that magnetic coupling is significant between the two ferromagnetic layers in tunnel junction films fabricated during this study.

TEM images of the film 9716_3 indicate crystalline electrodes and niobium contact layers. The aluminium layer appears to be amorphous as expected. However, an oxygen map of the film indicates that the barrier did not have well defined, sharp boundaries. The oxidation may have progressed through the thin aluminium into the lower electrode. Magnetic oxides at the interface have been shown to decrease the TMR from devices due to spin scattering [Zhang, 1997]. Additionally, damage due to aluminium deposition on

top of the barrier and diffusion from the oxide may have produced the poorly defined top surface of the barrier. Devices fabricated from these films had low TMR (0.2% at 77K), but rapid switching to and from the high and low resistance state. No visible independent switching of the magnetic layers was evident in the hysteresis curves of the corresponding film.

The technique of fabricating SIF tunnel junctions prior to magnetic tunnel junctions has proved useful in device development. SIF films deposited during the same run as magnetic tunnel junction films facilitated the checking of the deposition and fabrication route, which was extremely valuable. However, it has been found that working tunnel junctions with ferromagnetic electrodes do not necessarily produce a good TMR. The fabrication of superconducting tunnel junctions allows the identification of such problems as magnetic, rather than tunneling device effects.

Chapter 7:

Copper **decoration** of pinholes and weak-links

“Everything should be made as simple as possible, but not simpler.”

-Albert Einstein

Read head applications require low resistance magnetic tunnel junctions, so the insulating barrier must be thin. The requirement of low resistance magnetic tunnel junctions for read head applications suggests a thin insulating barrier should be produced. However, as discussed in Section 6.1.7.1.1, a thinner barrier increases the incidence of pinholes and weak-links. Although the distribution of these defects is random, raising their density per unit area decreases the yield of working devices. This yield must be high if the manufacture of magnetic tunnel junctions for read heads is to prove economically viable. Furthermore, a high incidence of pinholes in tunnel junctions makes analysis difficult and performance unpredictable. Weak-links consist of a thin barrier region, this is a lower resistance path and carries a great deal of current, forming hot-spots which break down prematurely. Device performance is affected by many different variables and barrier characteristics are difficult to identify. Improvements to existing techniques for studying barrier quality, independent of device performance, are needed.

The electrodeposition of copper onto pinholes and weak-links in the barrier is developed in this chapter as a viable analytical technique. Firstly, electrodeposition is discussed, with emphasis on practical aspects, followed by a review of the relevant literature. Initial results of basic plating experiments are presented. These include the variation of copper feature density with voltage and its relation to the E model of dielectric breakdown. Improvements to experimental apparatus and techniques developed over the course of this study are then discussed. Results for the variation of pinhole and weak-link density with roughness and aluminium thickness are presented, in addition to the relationship between copper feature density and current.

7.1 Introduction to electrodeposition

The concepts of electrochemistry required to understand the copper decoration of weak-links and pinholes are introduced below. A broader understanding of physical chemistry may be obtained from a standard text, such as Atkins [Atkins, 1994]. Electrodeposition, also termed electroplating or simply plating, is rarely discussed in detail. Specific texts tend to concentrate on industrial applications and recipes for metal deposition. Satisfactory treatment is found in Canning [Canning, 1978]. Firstly, electrochemical cells

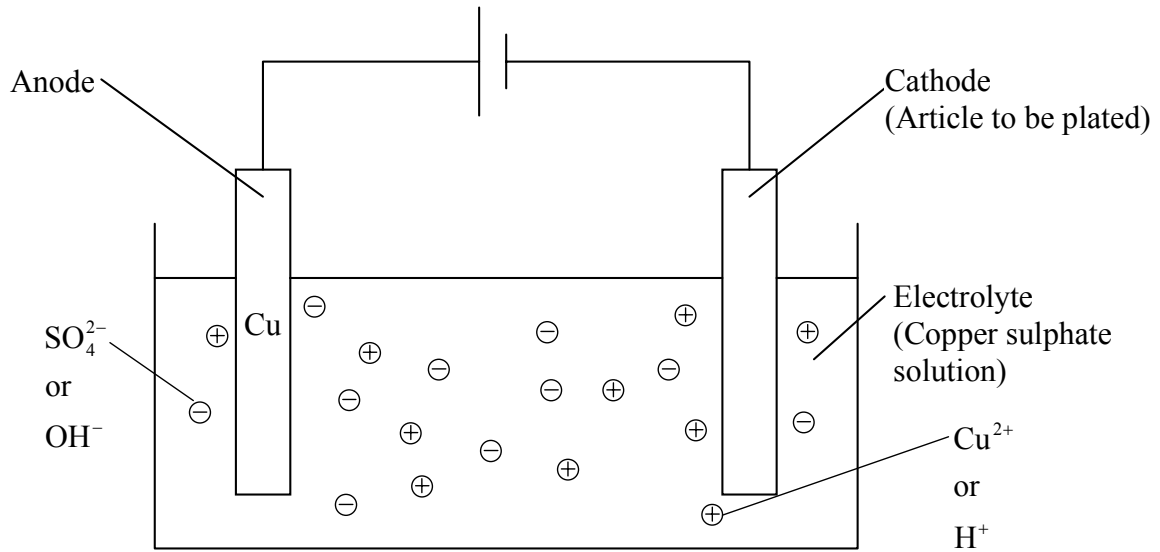


Figure 7.1: Simple electrodeposition apparatus for the deposition of copper.

and potentials are introduced below, followed by simple electrodeposition, then Faraday's laws and apparatus.

7.1.1 Electrochemical cells

An electrochemical cell consists of two electrodes dipped into electrolyte. The arrangement is termed a galvanic cell when used as a source of energy. When a reaction within the cell is driven by an external source of power, it is called an electrolytic cell. Figure 7.1 shows a simple electrolytic cell. Firstly, consider a copper electrode dipped into copper sulphate solution. An equilibrium forms between the copper ions in solution, electrons and copper in the anode:



When the electrode is first placed in solution, the tendency of copper either to dissociate from the electrode, or to form on it, causes an exchange of electrons and thus a potential exists. The equilibrium is partly determined by the chemical potentials of the copper ions in solution, $\mu_{\text{Cu}^{2+}}$, electrons from the metal electrode, μ_{e^-} and metal atoms μ_{Cu} . The free energies of the copper ions and electrons, but not the uncharged copper atoms, are affected by the electric potentials of the solution, ϕ_{S} , and metal, ϕ_{M} . At equilibrium the

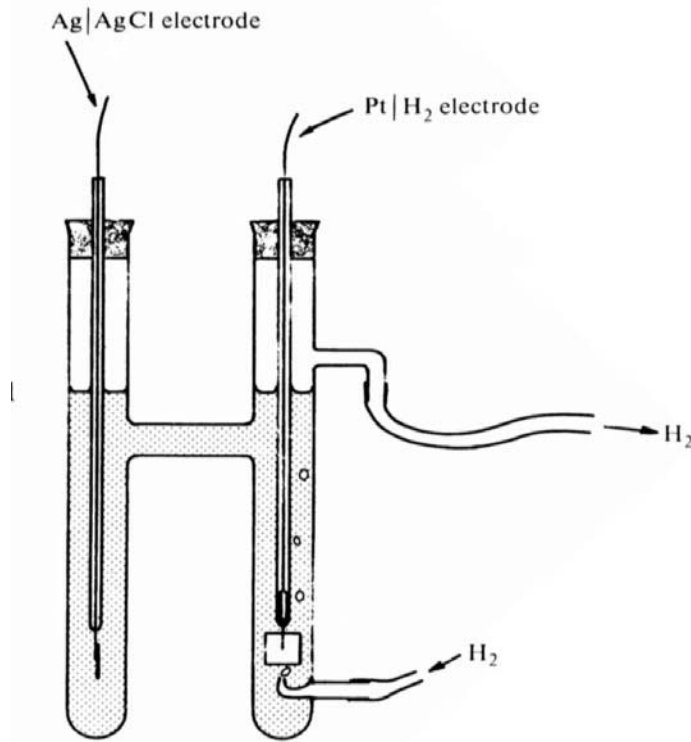


Figure 7.2: Harned cell used to measure standard potentials. Pictured measuring the standard potential of silver. [Matthews, 1985]

combination of the electric potential and chemical potential, the electrochemical potential, is the same for reactants and products:

$$\left[\mu_{\text{Cu}^{2+}} + 2F\phi_S \right] + 2 \left[\mu_{e^-} - F\phi_M \right] = \left[\mu_{\text{Cu}} \right]. \quad (7.2)$$

The factor $2F$ is introduced to convert electric potentials to free energies of the ions and electrons in the reduction of one mole of ions. F is the Faraday constant, the magnitude of the charge on one mole of electrons. The electrode potential difference, $\Delta\phi$, is given by Equation (7.3).

$$\Delta\phi = \phi_M - \phi_S = \frac{1}{2F} \left[\mu_{\text{Cu}^{2+}} + 2\mu_{e^-} - \mu_{\text{Cu}} \right]. \quad (7.3)$$

Equation (7.3) indicates that a potential difference forms on the introduction of a metal into a solution containing its ions. Furthermore, the magnitude of this potential depends on the specific metal used, the concentration of the solution and the temperature. The standard electrode potential is defined as the difference between the measured potential

and a standard hydrogen electrode in a 1 M solution of metal ions. The standard hydrogen electrode is arbitrarily assigned zero potential. Measurements are made with a Harned cell, as shown in Figure 7.2. Table 7.1 shows the electrochemical series, deduced by placing the elements in order of their standard electrode potentials. The electrochemical series provides an indication of the reducing power of elements. A metal high in the series may be used as an electrode and a placed into a solution containing ions of a metal lower in the series (e.g. zinc and copper, respectively). Some of the ions are displaced from the solution, forming metal (copper) deposit on the electrode (zinc) they are reduced (electrons are added). Metal (zinc) from the electrode therefore dissolves in the solution, becoming ionised. Potentials vary with solution concentration, and the relative reducing power of the metals in Table 7.1 may alter.

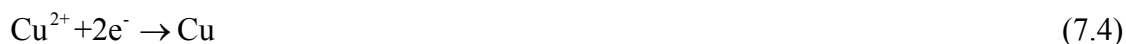
<i>Metal</i>	<i>Standard electrode potential (V) at 25°C.</i>
Zinc	-1.18
Chromium	-0.76
Iron (ferrous)	-0.44
Cobalt	-0.28
Nickel	-0.25
Tin (stannous)	-0.14
Copper	+0.34
Silver	+0.8
Gold	+1.5

Table 7.1: The electrochemical series.

7.1.2 Electrodeposition

Figure 7.1 shows simple apparatus for the electrodeposition of metals. The metal to be deposited is in solution, and also often used as the anode, the item to be electroplated is the cathode. The application of a potential encourages the migration of positive ions within the solution towards the cathode and negative ions towards the anode. Considering the specific case of a copper sulphate solution, both H^+ and Cu^{2+} ions are present and either hydrogen gas or copper metal may be produced at the cathode.

However, copper ions are deposited as copper metal at lower potential than hydrogen ions bind to form hydrogen gas. The main reaction at the cathode is:



As the applied potential is increased, the rate of copper deposition rises and eventually the co-production of hydrogen occurs. Most of the hydrogen is released as gas, but absorption into the metal leads to brittle copper. The anode reaction depends on the anode material.

7.1.2.1 Copper anode

At moderate potential, dissolution of the copper anode dominates the reaction, forming copper ions in solution. This reaction maintains the copper concentration in solution.



At higher potentials, reactions involving OH^{-} and SO_4^{2-} may occur, however the sulphate ion reaction is usually negligible. Oxygen is a by product of the hydroxyl ion reaction:



Assuming the electrodeposition occurs at low voltage, whilst the choice of copper anode maintains the overall copper concentration, localised copper ion depletion occurs at the cathode. The effect of ion motion on the solution, by migration, diffusion and convection is discussed in Section 7.1.2.3.

7.1.2.2 Inert anode

An inert anode dissolves extremely slowly in the electrolyte and is therefore sometimes termed an insoluble anode. Common materials for such anodes are graphite and platinum. The anodic reaction is represented by Equation (7.6). The hydroxyl ions required for this reaction are produced by the dissociation of water:



Therefore the by-product of these reactions is the increasing acidity of the solution. The plating current depends on the solution acidity and is therefore affected. Additionally, the concentration of copper ions in solution is depleted.

7.1.2.3 Ion transport

Three mechanisms for ion transport exist in the solution: migration; diffusion; and convection. Migration of ions due to the application of an electric potential is a slow process. Whilst migration is significant very close to the electrode, it is not sufficient to equalise the concentration of ions throughout the electrodeposition cell. Diffusion is a relatively slow process, strongly dependent on temperature, and does not regulate ion concentration throughout the solution. Convection, caused by agitation or heating is often used to equalise ion concentration in electrodeposition cells.

7.1.2.4 Faraday's laws

There is a simple relationship between the deposition rate and charge passed in the cell. Faraday investigated electrodeposition and proposed two laws:

1. The mass of product formed is directly proportional to the charge passed (current \times time); and
2. for a specific quantity of charge passed, the masses of products formed are proportional to their electrochemical equivalents (assuming an efficiency of 100%).

These laws are represented by Equation (7.8), where m is the mass of the deposit, M is the atomic or molecular weight, I is the current, F is Faraday's constant, z is the metal ion charge and t the elapsed time.

$$m = \frac{ItM}{zF} \quad (7.8)$$

The cathode efficiency is defined as the proportion of total current used to electrodeposit the desired metal. The production of hydrogen at the cathode is the principal source of efficiency loss. Electrodeposition has high efficiency when performed at low voltage.

7.1.2.5 Cell voltage

The voltage required to maintain finite plating current is termed the cell voltage, or liberation potential. The cell voltage, V_C , is therefore subjective, depending on apparatus sensitivity. On application of a small potential, a current flows and rapidly decreases to zero, due to a back EMF caused by solution polarisation. The cell voltage is given by:

$$V_C = E_{cell} + \text{total cathodic polarisation} + \text{total anodic polarisation} + IR, \quad (7.9)$$

where E_{cell} is the minimum voltage required to cause the electrode reactions to take place. The resistive contribution, IR , represents the normal Ohmic potential for the current, I , and electrolyte resistance, R . Polarisation at the anode and cathode has three contributions: the concentration; activation; and Ohmic overpotentials. The concentration overpotential represents the potential associated with the depletion of ions around the cathode and excess ions around the anode, discussed in Section 7.1.2.3. The energy required to move ions across the interface between the electrolyte and electrode, that is remove atoms from the anode and add atoms to the crystal structure of the cathode, is referred to as the activation overpotential. Other electrode reactions contribute, including the hydration and dehydration of ions. Activation overpotential is a complicated function of the electrodes, ions and complexes formed. The presence of ionically conducting films on the interfaces of the electrodes produces Ohmic overpotential. It is a function of the solution and films, such as oxides, which may be present at the interface.

The cell voltage is a highly complicated function of the electrodes and solution. It is extremely difficult to predict as it depends on the precise environment in the cell. Cell voltage is generally determined experimentally and is reduced by various additions to the solution. For example, sulphuric acid is often added to a copper sulphate solution.

7.1.3 Electrodeposition apparatus

Figure 7.1 shows simple electrodeposition apparatus. However, due to the potential formed between a metal and solution of its ions (Section 7.1.1), uncertainty arises in the potential experienced within the cell. The potential of a cell is therefore measured relative to a reference electrode. The most commonly used reference is the standard

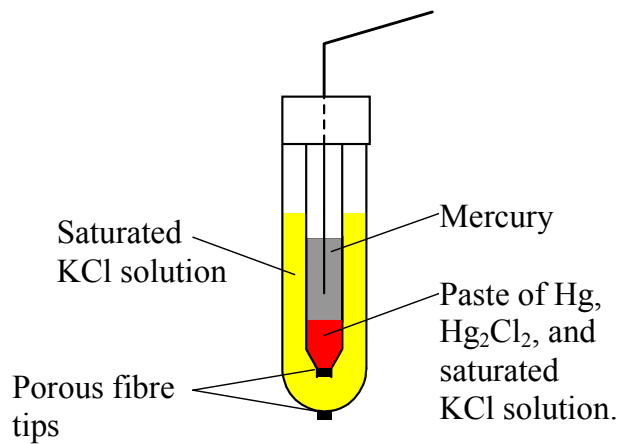


Figure 7.3: Standard calomel reference electrode.

calomel electrode. Calomel is mercurous chloride, Hg_2Cl_2 ; the electrode design is shown in Figure 7.3. The EMF of a calomel electrode is 0.244 V at 25°C.

Constant voltage relative to the standard calomel electrode is achieved using a potentiostat. The reference electrode is dipped into a salt solution, and linked to the deposition vessel via a salt bridge providing a complete electrical circuit. Wenking potentiostats are regularly used for laboratory electrodeposition due to their excellent stability and ease of operation. The Wenking potentiostat provides a voltage source as well as current monitoring over a wide range of scales. It may be computer interfaced and used in conjunction with Equation (7.8) to estimate the mass of deposited metal.

7.2 Previous work

7.2.1 Copper decoration of pinholes

As discussed in Section 6.1.7.1, barrier quality is critical to device performance. Schad *et al.* proposed the identification of pinhole and weak-link density (number per unit area) in tunnel barriers by electrodeposition [Schad, 2000]. This uses the obvious property of pinholes, of increased conduction compared to the barrier. Weak-links may undergo dielectric breakdown in the applied electric field, forming conducting shorts. By electrodeposition at low voltage, copper only forms on pinholes and weak-links below some critical barrier thickness. These authors observed cauliflower shaped structures on the barrier by scanning electron microscopy (SEM). These features were identified by

energy dispersive X-ray spectroscopy (EDX or EDS) as copper. The electron beam of an SEM is used to excite the atoms just below the surface of the sample. Electrons in these atoms return to the ground state, emitting characteristic X-rays associated with their energy levels. These X-rays are measured in EDX and their frequencies matched to the known peaks of elements.

Schad *et al.* prepared samples by radio frequency (RF) diode sputtering 12.5 nm NiFeCo followed by 1.2 nm aluminium on a 4 inch silicon wafer, covered with 200 nm silicon nitride. Oxidation occurred by sputtering aluminium in an atmosphere containing some oxygen (unspecified pressure). Identical conditions were used to fabricate magnetic tunnel junctions with high tunneling magnetoresistance (TMR) [Tondra, 1998]. Prior to electrodeposition, the samples were washed thoroughly in acetone and dried in a nitrogen stream. If the samples are not contaminated after deposition such cleaning with acetone should not be required. Polymeric paint was used to define 1 cm^2 , although no use was later made of recorded plating currents. Electrodeposition was performed using a three-electrode electrochemical cell, calomel reference electrode and potentiostat. The calomel electrode was at a potential of 242 mV compared to the standard hydrogen electrode; all voltages are quoted relative to the calomel electrode. A platinum anode and electrolyte of 0.1 M CuSO_4 and 0.1 M sulphuric acid completed the circuit. Electrodeposition took place at room temperature, an initial voltage of -0.5 V was applied for 10 seconds and then reduced to -0.3 V for 300 seconds. No hydrogen was released at the cathode.

A sample was immersed in the solution without metal electrodeposition to investigate the effect of the solution on the film surface. AFM roughness measurements, small-angle X-ray diffraction (SA XRD) and X-ray photoemission spectroscopy (XPS) were used to indicate structural change. XPS is particularly sensitive to chemical changes occurring at the surface, with a depth resolution close to atomic dimensions [Brandon, 1999]. XPS measures the characteristic energies of secondary electrons emitted from a surface following electronic excitation with X-rays. The solution used had no significant effect on the film quality, whereas a high concentration of sulphuric acid deteriorated the surface.

Schad *et al.* identified copper features of diameter $\approx 200 \text{ nm}$ after 10 seconds at -0.5 V . Following full deposition the diameter had increased to $\approx 4 \text{ }\mu\text{m}$ and the number per unit

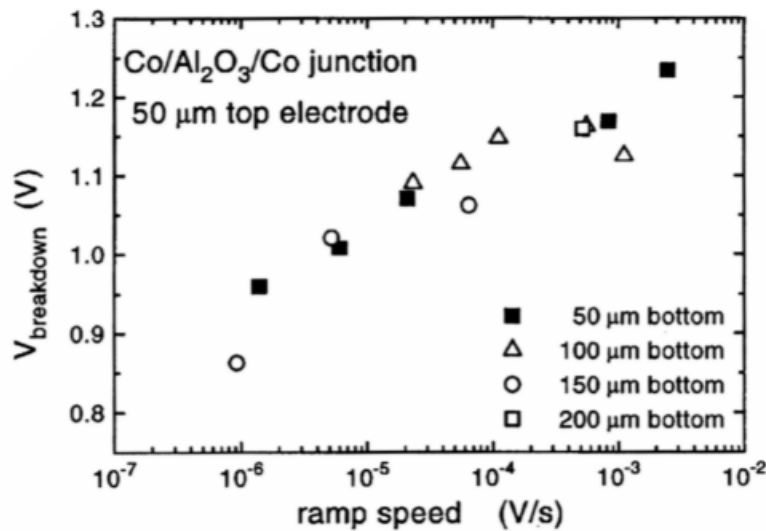


Figure 7.4: The effect of voltage ramp speed on dielectric breakdown voltage [Oepts, 1999]

area was $\approx 2500 \text{ mm}^2$. They did not investigate the cross-section of the copper features. Feature size is dependent on the current distribution, caused by electrolyte concentration and plating current, in addition to pinhole size and density. Dielectric breakdown in Al_2O_3 generally occurs in field strengths exceeding 10^9 Vm^{-1} [Oepts, 1998]. Using this value, Schad *et al.* calculated that the initial -0.5 V potential lead to the dielectric breakdown of all areas of barrier thickness less than 0.5 nm . No copper features were observed on omission of the initial -0.5 V electrodeposition voltage. They suggested that the lack of copper deposition at -0.3 V indicates that no intrinsic pinholes were present.

7.2.2 Dielectric breakdown

The dielectric breakdown process of weak-links in the Al_2O_3 barrier is fundamental to the copper decoration process. The dielectric breakdown of SiO_2 in capacitors has been widely studied, however no clear single mechanism is responsible for breakdown over the full range of voltage and thickness. Oepts *et al.* analysed the dielectric breakdown of magnetic tunnel junctions, relating their results to the models of breakdown for SiO_2 [Oepts, 1999]. Figure 7.4 shows the effect of voltage ramp speed on dielectric breakdown. Dielectric breakdown was observed with thin liquid crystal films deposited on the junction [Oepts, 1998] and almost always occurred at a single point in each device. The junctions were prepared by shadow mask deposition. The authors noted a significant

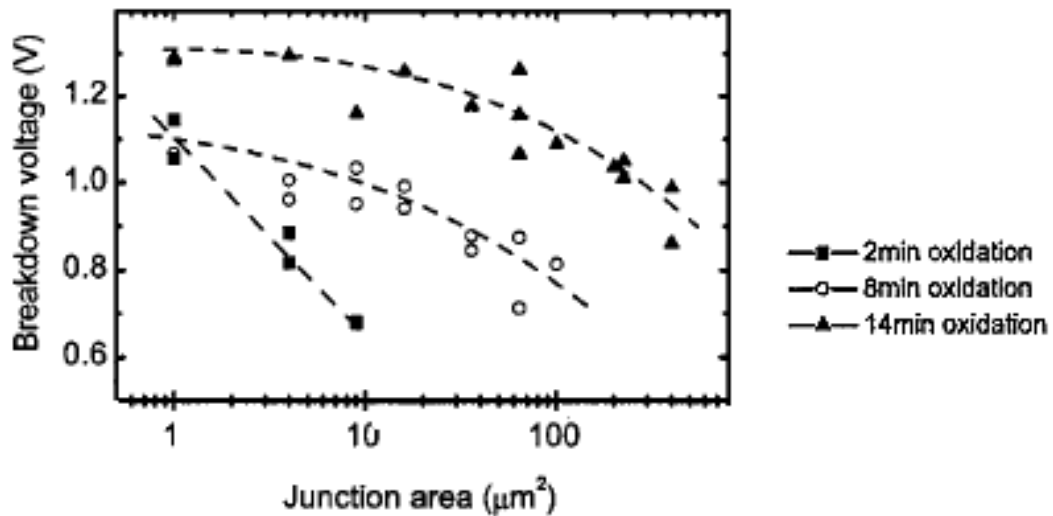


Figure 7.5: The effect of junction area on dielectric breakdown voltage. Lines are fits to E model. Adapted from [Shimazawa, 2000]

decrease in barrier quality and thickness for a band of width $10 \mu\text{m}$ around the edge of each junction. Breakdown occurred in this region for $\sim 50\%$ of devices. Due to this edge effect, no relationship was observed between the area of the junctions and breakdown voltage. Figure 7.5 shows the results of Shimazawa *et al.*, who investigated the effect of junction area on dielectric breakdown voltage [Shimazawa, 2000]. Defects leading to dielectric breakdown are randomly distributed within a barrier. Increasing junction area should decrease the breakdown voltage, due to an increase in the likelihood of encountering a significant barrier defect. They therefore suggest that smaller junctions facilitate better study of the intrinsic behaviour of Al_2O_3 . Figure 7.5 also shows reasonable fits to the data by the E model (Section 7.2.2.3).

Three models are commonly discussed for the dielectric breakdown of SiO_2 , the Q_{bd} model, anode hole injection model and E model. The key problem to interpreting the relationship between such models and breakdown in thin Al_2O_3 , is that most studies have taken place on thick SiO_2 . Direct tunneling is not the main transport mechanism in thick barriers, instead multistage Fowler-Nordheim tunneling occurs, with inelastic scattering of tunneling electrons by the conduction band of the dielectric [Wolf, 1985]. The treatment of the models of dielectric breakdown in this section follows that of Oepts *et al.* [Oepts, 1999]

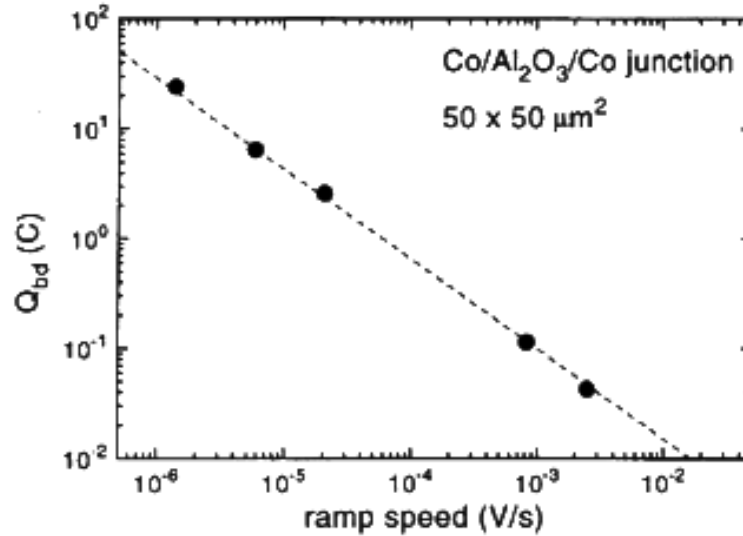


Figure 7.6: The effect of voltage ramp speed on total charge passed at breakdown for thin aluminium oxide insulator. Decrease in Q_{bd} as ramp speed increases implies that Q_{bd} model does not apply. [Oepts, 1999]

7.2.2.1 Q_{bd} model

The Q_{bd} model applies when electrons have sufficient energy to damage the oxide layer locally, termed wearing. The fundamental concept of this model is that breakdown occurs after the passage of a certain amount of charge, Q_{bd} . It predicts breakdown at a total charge independent of the ramp speed. Figure 7.6 shows the effect of ramp speed on Q_{bd} , measured by Oepts *et al.*, breakdown charge is not constant [Oepts, 1999]. The Q_{bd} model does not describe the dielectric breakdown in these magnetic tunnel junctions.

7.2.2.2 Anode hole injection model

The anode hole injection model leads to the $1/E$ model. This model assumes that incident electrons at the anode excite deep valence band electrons to a state above the Fermi level, creating a hole in the anode that may tunnel into the oxide. This hole may lead to an electron trap in the oxide, with high local current density, increasing the likelihood of breakdown. In the Fowler-Nordheim tunneling regime, Equation (7.10) representing the break down probability density, $p(E)$, has been derived [Schuegraf, 1994].

$$p(E) = CJ(E)E^2 \exp\left(\frac{-D}{E}\right) \quad (7.10)$$

Where C is a constant, $J(E)$ the current density and D a parameter independent of the electric field, E . Whilst this model adequately fits the data of Oepts *et al.*, it is unlikely to describe breakdown in magnetic tunnel junctions as tunneling is not in the Fowler-Nordheim regime for thin aluminium oxide barriers

7.2.2.3 E model

The E model, or thermochemical model, of dielectric breakdown concerns the distortion of atomic bonds in the oxide. A quantitative thermodynamic model for breakdown has been developed for SiO₂ [McPherson, 1998]. Silicon is normally surrounded by a tetrahedron of oxygen atoms. However, in the presence of an external field or growth defect, distortion of the bonds may occur. Above a critical distortion angle an Si-Si bond can form, which is believed to be a precursor to breakdown. Dielectric breakdown occurs when this Si-Si bond, or a number of them, breaks. McPherson and Mogul derived Equation (7.11).

$$\tau(E) = a \exp\left(\frac{\Delta H}{k_B T}\right) \exp(-\gamma E), \quad (7.11)$$

where $\tau(E)$ is the average time to breakdown, a is a constant, γ is the field acceleration factor, T is the temperature, k_B is the Boltzmann constant and ΔH is the enthalpy of breaking the Si-Si bond. The E model fits the data presented by Oepts *et al.*; they found a value of γ approximately twice that of SiO₂. They suggest that the larger γ results from three factors. Firstly, the electric susceptibility of Al₂O₃ is larger (≈ 7) than SiO₂ (≈ 2.9), leading to higher polarisation and local field and in turn larger γ . Secondly, Al₂O₃ bonds are more ionic than those of SiO₂. This may lead to a higher ionic charge of aluminium, compared to silicon, and therefore greater dipole moment and larger γ . Finally, the structure of amorphous Al₂O₃ is more complex than SiO₂ and local octahedral symmetry has been observed [Van Beek, 1984]. Tetrahedral coordination is common in amorphous aluminium oxide; migration of aluminium could occur via the octahedral vacancies. Additionally, the lack of threshold voltage required by this model supports the low voltages at which breakdown occurred in the junctions. Oepts *et al.* conclude that dielectric breakdown in their junctions is likely to conform to the E model.

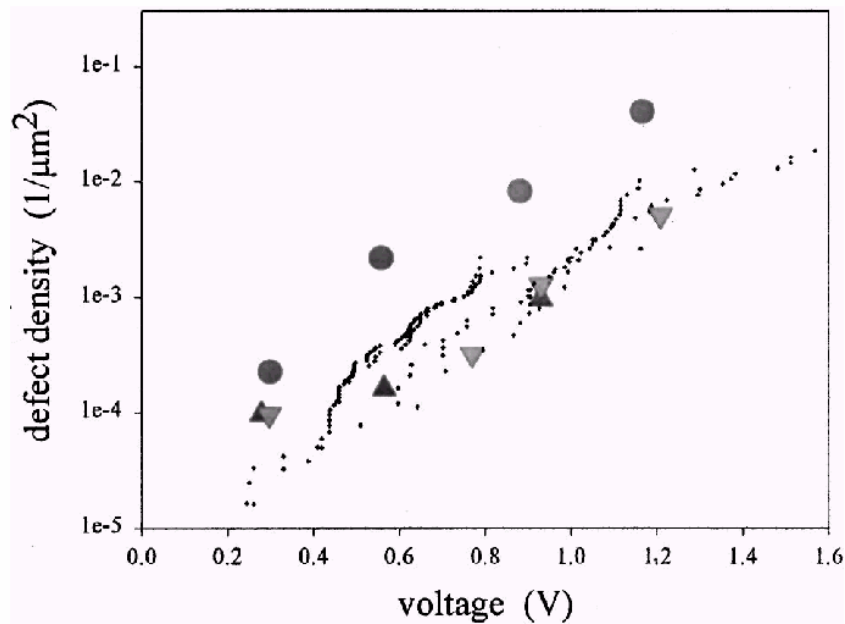


Figure 7.7: The relationship between defect density and voltage derived from electrodeposition experiments, where the circles represent data from complete oxidation of the aluminium and the triangles incomplete oxidation. Also shown are dots to indicate calculated defect density from the dielectric breakdown in tunnel junctions. [Allen, 2001]

7.2.2.4 Dielectric breakdown and copper decoration

Allen *et al.* (including Schad) presented results from the dielectric breakdown in magnetic tunnel junctions in addition to the decoration of pinholes and weak-links with copper [Allen, 2001]. Tunnel junctions were subjected to a current ramp speed of $0.4 \mu\text{A}\mu\text{m}^{-2}\text{s}^{-1}$ and their breakdown voltage noted. The defect density was determined by calculating the breakdown probability in an applied voltage and fitting to a Poisson distribution. The copper feature density was determined for films only grown to the barrier and subsequently electroplated at a range of voltages for 10 seconds (Figure 7.7). They claim that the good correlation indicates the worth of copper electrodeposition as a ‘reliable tool for indicating insulator defect density in the early stages of tunnel junction preparation’. However, Figure 7.4 shows that the breakdown voltage depends on voltage ramp speed. Assuming that similar behaviour occurs for a current ramp, the calculated defect density depends on the rate of current increase. Electrodeposition did not take place with a controlled ramp rate and the authors do not justify their choice of ramp speed for the investigation of magnetic tunnel junction breakdown. Whilst their data indicates good correlation for the current ramp speed of $0.4 \mu\text{A}\mu\text{m}^{-2}\text{s}^{-1}$, it may be a fortuitous choice.

7.3 Experimental technique

The experimental methods for the decoration of pinholes and weak-links by copper deposition used in initial investigations are described in this section. Section 7.5, describes the development of new experimental apparatus and techniques for the determination of defect density of thin insulators.

7.3.1 Deposition of thin films

Thin films of aluminium on tantalum were deposited onto four inch diameter oxidised silicon substrates, by Seagate Technology, Springtown. The metals were DC magnetron sputter deposited at high vacuum. Oxidation of the aluminium took place in flowing oxygen at a pressure of 0.3 Pa for one hour. This was the largest pressure possible in the system. The insulator was formed in two of the films by oxidation in air, rather than *in situ*. Aluminium of 3 nm thickness was used throughout. Table 7.2 shows the tantalum thickness and oxidation method of films corresponding to data presented below. These films were fabricated to investigate the effect of lower electrode roughness on pinhole density. Roughness is expected to increase as layer thickness rises. A series of films with varying aluminium thickness were also deposited and measured, but the density of copper features produced was extremely low. It was not possible to collect sufficient data for statistical significance. This is discussed in Section 7.4.5. Results of the study of aluminium thickness on weak-link and pinhole density in films provided by Seagate Technology are not presented. The films were broken into 8×15 mm chips and dust was removed with compressed air prior to electrodeposition.

7.3.2 Electrodeposition

Electrodeposition took place using a three electrode system, with a standard calomel reference electrode. A Wenking potentiostat was used as the electrodeposition source, current was monitored using the appropriate scale on the potentiostat and a Keithley 197 meter. A copper anode was used to reduce the cell voltage and to ensure that the solution did not become copper deficient. Figure 7.8 shows the apparatus. The calomel electrode was placed in a 0.1 M sulphuric acid solution, minimising its contamination by salts. The reference and electrodeposition vessels were connected via a bridge containing 0.1 M

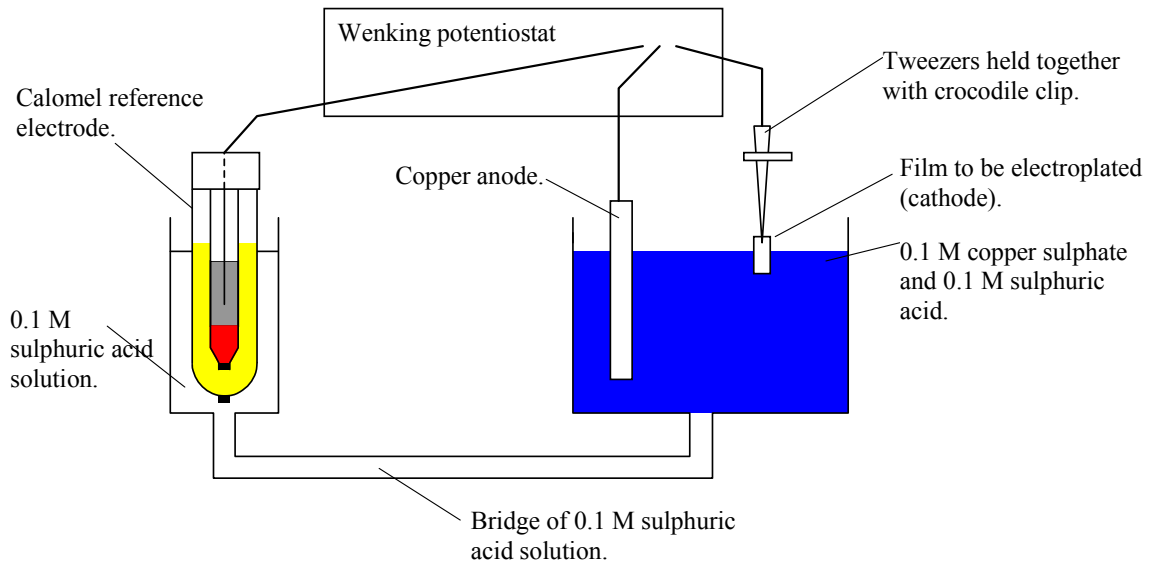


Figure 7.8: Apparatus used for electrodeposition.

sulphuric acid. The electrodeposition vessel contained a solution of 0.1 M copper sulphate and 0.1 M sulphuric acid. Good metallic contact with the film was made by clamping it firmly between sharp, straight tweezers with a crocodile clip. The thin aluminium oxide on the wafers was easily damaged, producing good contact to the tantalum bottom electrode. Plating generally took place at -500 mV for 10 seconds, followed by five minutes at -300 mV. Investigation into the effect of voltage on defect density was undertaken by electrodeposition onto samples with 250 nm tantalum thickness. The specified voltage was applied for 10 seconds, followed by growth at -300 mV for five minutes. Following electrodeposition, the samples were carefully removed and gently rinsed in distilled water, then dried in air. Vigorous rinsing or drying using a compressed air line removed a large number of copper features.

<i>Tantalum thickness (nm)</i>	<i>Oxidation method</i>
10	In system
10	In air
70	In system
70	In air
100	In system
130	In system
200	In system
250	In system

Table 7.2: Tantalum thickness and oxidation technique for films deposited by Seagate Technology and presented below.

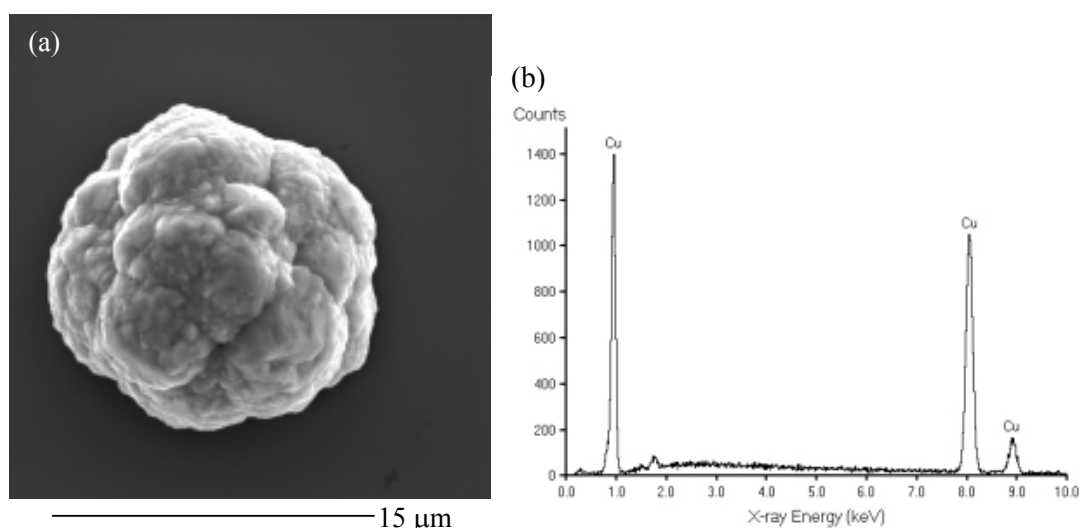


Figure 7.9: (a) Copper feature formed by electrodeposition. (b) EDX on the same feature.

7.3.3 Analysis of electrodeposited films

Following electrodeposition, analysis took place using an SEM. Initial results were observed with a high resolution JEOL 5800 SEM. This system allowed feature identification using EDX. Determination of the chemical composition of features provided proof that copper deposition occurred. Such features were easily distinguishable by eye. Later results were taken with a JEOL 700 SEM, due to its speed of operation and ample resolution for the identification of copper features. Digital images were stored and the number of copper features counted. Due to the low number of copper features per unit area, a large number of films were measured to improve statistical significance.

Further identification took place in a focussed ion beam system, allowing canting of the sample relative to normal to the film. The ion beam was also used to ion mill features, providing a view of their interior.

7.4 Results of initial experimental investigations

7.4.1 Feature identification

Figure 7.9(a) shows an SEM image of a copper feature deposited by electroplating as described in Section 7.3.2. The feature was identified as copper using EDX, as shown by Figure 7.9(b). The shape and internal structure of copper features was further

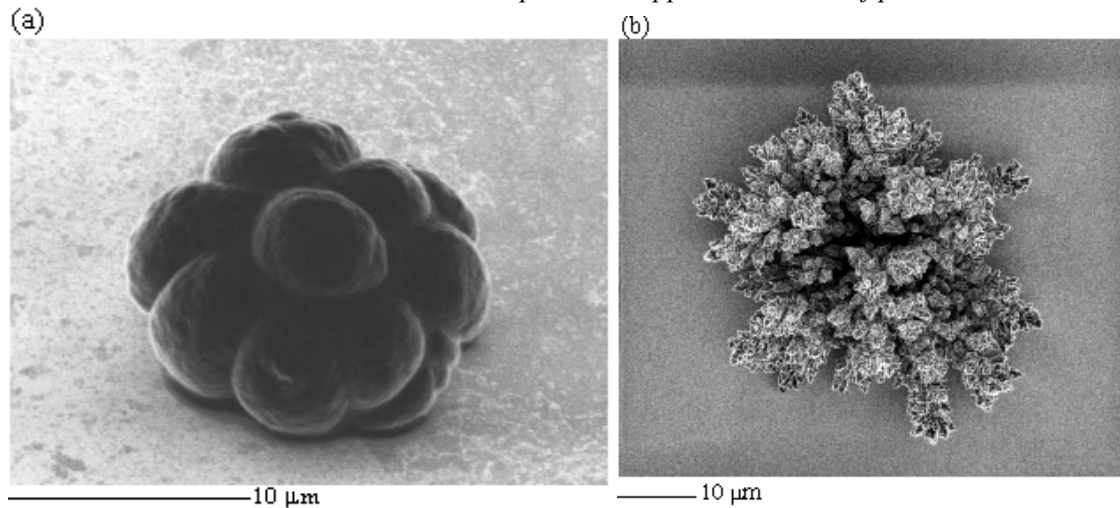


Figure 7.10: (a) Copper feature at 45° to the normal, grown at -500 mV 10 secs and -300 mV 5 mins. (b) Dendritic copper feature formed by increasing plating voltage to -500 mV throughout.

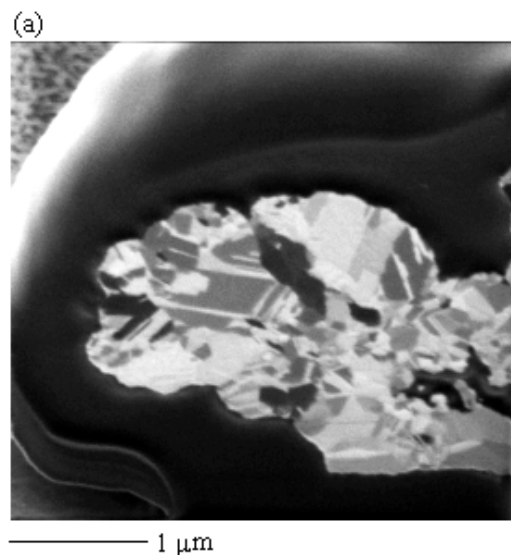


Figure 7.11: FIB cut cross-section of copper feature shown in Figure 7.10(a). Crystallographic grains are clear

investigated using a focussed ion beam (FIB). Figure 7.10(a) shows a copper feature at an angle to the film normal. It has a cauliflower-like shape. The effect of more rapid deposition was studied, using a voltage of -500 mV for the entire electrodeposition. Figure 7.10(b) shows the copper dendrites formed during rapid deposition. Growth occurs preferentially along certain orientations, which may be the result of the crystal structure or current distribution. Figure 7.11 shows the cross-section of a copper feature, milled using the focussed ion beam. A regular, crystalline granular structure is visible inside the ‘cauliflower’. A poorly conducting outer layer is present due to a combination of copper oxidation, gallium ion implantation during FIB imaging and chemical residues.

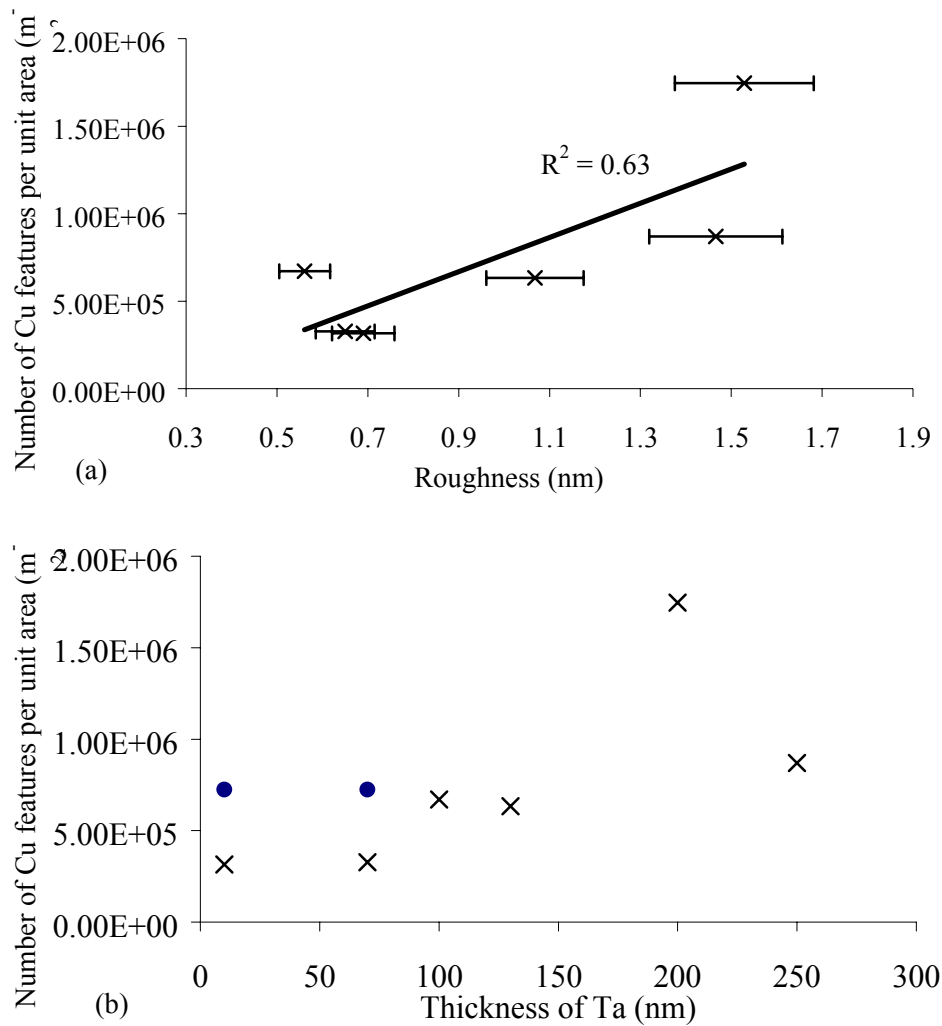


Figure 7.12: Dependence of the copper feature density on (a) roughness and (b) tantalum thickness circles are data for wafers oxidised in air.

7.4.2 Effect of roughness

Figure 7.12(a) and (b) show the variation of pinhole density with the roughness and thickness of the tantalum underlayer, respectively. Pinhole density appears to increase with both underlayer roughness and thickness. The points have been fitted by a linear regression to provide a guide to the eye and also to permit statistical analysis. Two assumptions of linear regression are significant to the data, that the trend is actually linear and also that there is no error in the values of roughness. A theoretical model of the system will not predict a linear trend, since a residual number of pinholes and weak-links should exist for very smooth films. However, the trend may be fitted to a straight line

over the region of interest. The R^2 value shown on the graph represents the percentage of the data variation for which the fitted regression may be responsible; 63% is a poor fit. A student t-test was used to investigate the hypothesis that the true linear regression best fit line to the data has gradient greater than zero. The calculated t value of 13.8 is much higher than the $t_{99,9}$ value of 5.9, representing 99.9% certainty that the gradient is greater than zero. It is highly likely that copper feature density increases with roughness.

Two factors significantly affect interpretation of the results. These are measurements of the roughness and statistical significance of the number of copper features counted. Measurements of roughness were made using the AFM, as discussed in Section 3.4.1.2. This technique does not generally provide high accuracy, reflected in the error bars displayed. It is also important to consider the distance over which height variation occurs for roughness measurements. Consider the profile of a simplified layer as the superposition of two oscillations, of small amplitude (<5 nm) relative to the period. Height variation is pictured as a long period (>1 μm) height variation and a short period (<100 nm) variation. The long period oscillation has shallow gradient and is unlikely to cause significant shadowing or discontinuity in subsequent depositions. However, short range variation has a much steeper gradient, causing the inhomogeneous deposition of aluminium and weak-links in the insulator. Roughness was calculated within a 1 μm box for the Ta/Al multilayers, excluding most long period height variation. The roughness of Ta/Al was also considered identical to that for the tantalum underlayer, since the difference in aluminium thickness should be small compared to the tantalum roughness. It was not possible to determine the roughness accurately with X-ray analysis, as fits to the data produced a wide range of possible values.

A large number of events must be observed to assign significance to the results since dielectric breakdown occurs randomly (Section 7.2.2.3). As discussed in Section 7.4.5, the key problems encountered were the time required to identify features with the SEM and the low defect density of the wafers supplied by Seagate Technology. Figure 7.12 represents the collation of data for a large number of chips for each thickness of tantalum. However, the number of observed copper features was still low (from 14 to 123 in total). Takatsuji and Arai also observed an increase in pinhole density with surface roughness [Takatsuji, 2000]. They deposited films onto glass substrates. Pinholes were counted using optical microscopy, illuminating the films from behind to indicate holes in the film.

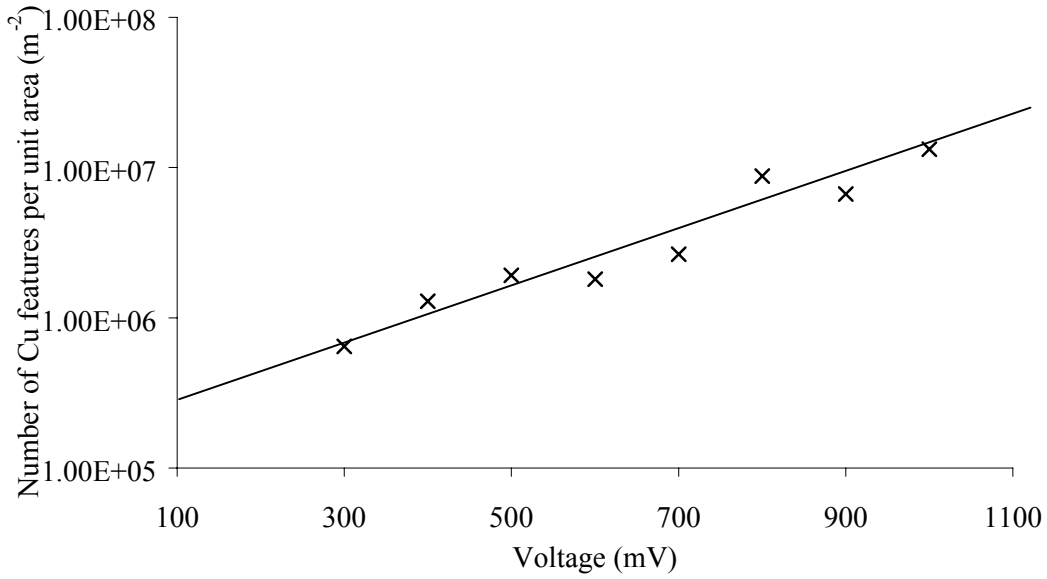


Figure 7.13: The dependence of copper feature density on electrodeposition voltage.

7.4.3 The effect of voltage

Figure 7.13 shows the effect of voltage on the number of copper features per unit area. The increase in the density of copper features with plating voltage exhibits a good fit to an exponential trend. The E model predicts such a relationship, where Equation (7.11) indicates that the time to dielectric breakdown is proportional to $\exp(-E)$. E is the electric field. The relationship between voltage and the number of breakdown events may be derived from the work of McPherson and Mogul, who deduced Equation (7.12) on the basis of the E model [McPherson, 1998].

$$\frac{dN}{dt} = -kN(t), \quad (7.12)$$

where $\frac{dN}{dt}$ is the rate of thermochemical bond-breakage, $N(t)$ is the number of bonds at a time t and k is the reaction rate constant, given by:

$$k = v_0 \exp\left(-\frac{(\Delta H_0) - aE}{k_B T}\right), \quad (7.13)$$

where ν_0 is a characteristic collision frequency, ΔH_0 is the enthalpy of activation of Al-Al bond breakage, T is the temperature, k_B the Boltzmann constant and a is the effective dipole moment. Integrating to find the number of broken bonds at time t :

$$N = -\nu_0 \exp\left(-\frac{(\Delta H_0) - aE}{k_B T}\right) \int_0^t N(t) dt. \quad (7.14)$$

Since it is assumed that $N(t)$ is independent of voltage and if it is further assumed that the number of broken bonds is directly proportional to the density of breakdown events:

$$\text{Number of pinholes} \propto \exp(E) \quad (7.15)$$

The data shows good fit to the E model prediction of the density of copper features, represented by Equation (7.15).

7.4.4 The effect of oxidation technique

Figure 7.12(b) shows that the copper features density for wafers oxidised in air was higher than that for wafers oxidised in the system. It is surprising that such a large difference in the weak-link and pinhole density resulted from such similar oxidation techniques. This difference is possibly caused by the absorption of contaminant molecules onto the surface of the aluminium in air, hindering oxidation. Likely candidates to prevent the full oxidation of aluminium in air include airborne grease and dirt particles. These contaminants are present in much smaller quantities when aluminium is oxidised *in situ* with ‘pure’ oxygen.

7.4.5 Problems with the technique

The application of the electrodeposition of copper onto pinholes and weak-links is limited by the time taken to analyse film quality and the equipment required. Attempts were made to relate the deposition current to the number of copper features recorded in a known area. A 5×5 mm area was defined on chips with photoresist using standard lithography techniques (Section 3.2). Photoresist was removed from one end to allow electrical contact. Details of this technique are given below (Section 7.5.2). Current was monitored on the Keithley 197 during electrodeposition. No relationship was determined

between the number of copper features present within the defined area and the current. Close inspection revealed the deposition of copper around the edges of the samples.

The low pinhole and weak-link density of wafers provided by Seagate Technology was also prohibitive, due the low number of copper features observed. It was difficult and extremely time consuming to collect sufficient data for statistical significance. SEM analysis took a particularly long time.

7.5 New experimental technique

The time taken and equipment required to perform the decoration of pinholes and weak-links in the manner described above (Section 7.3.2) is prohibitive to the development of this technique as a standard tool to investigate barrier quality. There is a need for a simple method of determining pinhole and weak-link density, requiring apparatus generally available within a device fabrication and testing laboratory. The technique suggested below uses a computer controlled voltage source and current meter to electrodeposit copper. The relationship between the current and number of copper features per unit area was investigated as a convenient and quick analysis tool. Films were deposited, with a higher pinhole and weak-link density than previously. Details of the depositions and lithography techniques are listed below.

7.5.1 Film deposition

Films were deposited onto oxidised silicon substrates of size 6×11 mm, using the Mk VII sputtering system described in Section 3.2. Substrate preparation and film deposition technique are described in Sections 3.1 and 3.2. The deposition details and estimated layer thickness for films presented in this chapter are listed in Table 7.3. Particular care was taken over handling films, since the thin oxide barrier was easily damaged.

Material	Process	11286 (1/2/3/4/5)	11317 (1/2/3)	11328 (1/2)	11352 (1/2/3/4/5)
Niobium	Passes, speed	2 and 15, 2×	2 and 15, 2×	2 and 15, 2×	2 and 15, 2×
	Pressure (Pa)	0.3 and 0.69	0.3 and 0.69	0.3 and 0.69	0.3 and 0.69
	Expected thickness (nm)	19.4	19.4	19.4	19.4
Cobalt	Time (s)	104	-	-	-
	Pressure (Pa)	1	-	-	-
	Expected thickness (nm)	11.7	-	-	-
Aluminium	Passes, speed	6, 4×/2×/1×/0.25×/0.5×	24, 1×	24, 1×	6, 4×/2×/1.33×/1×/0.5×
	Pressure (Pa)	0.7	0.3/0.5/1	3/2	0.7
	Expected thickness (nm)	4.9/10/19.9/79.7/39.8	39.8	39.8	4.9/10//14.9/19.9/39.8
Oxidation	Pressure (Pa)	1000	1000	1000	1000

Table 7.3: Deposition conditions for films presented in this study. Chapter 3 provides greater detail and explanation of techniques.

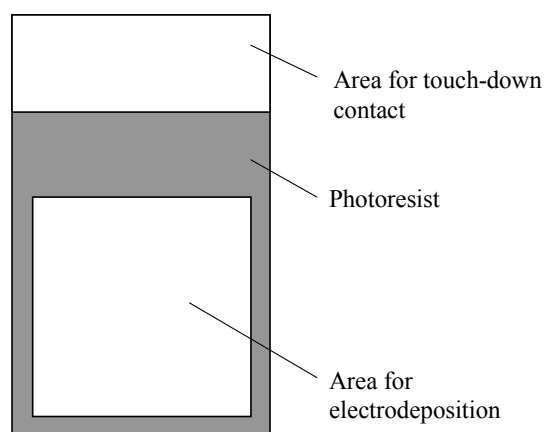


Figure 7.14: Lithography pattern.

7.5.2 Lithography and film preparation

Square regions of area 3×3 mm were defined using lithography to the pattern shown in Figure 7.14. Preparation of the chips prior to lithography is discussed in Section 7.5.2.1. AZ1529 photoresist was spun onto the substrates at 5000 rpm. Excess resist was removed from the underside of chips with a class 100 cleanroom wipe. The chips were then baked at 100°C for 1 minute. The Canon projection printer was used in conjunction with the CAM 31 maskset to define the area, aligned as shown in Figure 7.14. An exposure time of 40 seconds was used. Projection printing was used to allow the edge bead of photoresist, formed during spinning, to remain in place. The chips were then developed in 80% developer solution and rinsed in distilled water. The contact area for the sprung loaded cathode contact was cleared of resist by wiping with a cotton bud soaked in acetone. Care was taken throughout lithography not to scratch the samples.

7.5.2.1 Film preparation

Generally, dirt deposits are removed from samples by airbrushing with acetone prior to lithography. However, there is no obvious reason to clean a film which has not been handled or left uncovered prior to lithography. In this situation very little dirt should be present on the surface, dust is easily removed with an airgun.

The effect of damage caused to films by photolithography processes was investigated by comparing the density of observed copper features for differently prepared samples. Films from the deposition 11352 were patterned either without cleaning or with the chip

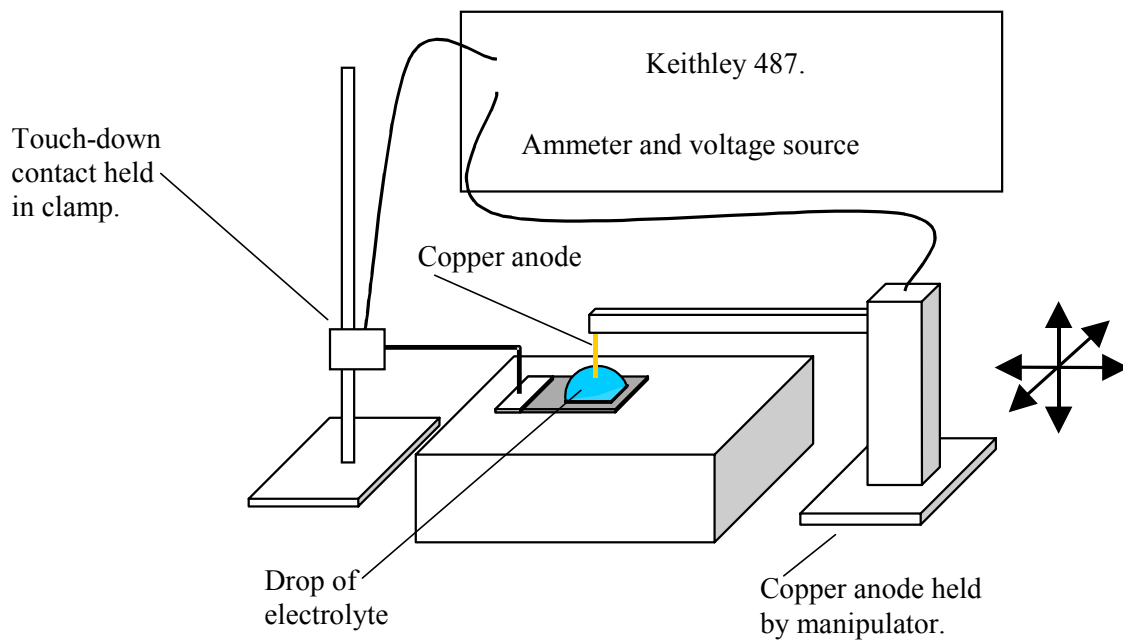


Figure 7.15: New apparatus for the electrodeposition of copper.

cleaned by airbrushing in acetone. Electrodeposition of the patterned films, in addition to unpatterned films, took place at -500 mV, as described in Section 7.5.3, below. Copper features were identified by SEM analysis. Negligible difference in the number of copper features per unit area was noted between as-deposited films and those with defined areas, but not cleaned with acetone. However, the average pinhole and weak-link density increased from $6.7 \times 10^8 \text{ m}^{-2}$ to $1.58 \times 10^9 \text{ m}^{-2}$ when samples were cleaned by airbrushing with acetone. The fragile Al_2O_3 insulating layer is damaged by airbrushing with acetone; it was not undertaken during lithography.

7.5.3 Apparatus and electrodeposition technique

Figure 7.15 is a schematic of the apparatus used for the electrodeposition of copper to identify pinholes and weak-links in insulating films. A Keithley 487 was used as both an ammeter and low noise voltage source. Current measurements were possible between 10 fA and 2.5 mA, with voltage steps of 10 mV. Shielded wire was used for all connections to reduce the effect of noise. A sprung-loaded tip provided the cathode contact to the chip. A copper needle was used as the anode, which was clamped into a manipulator. This allowed accurate alignment and lowering into the electrolyte. The film surface was not touched with the copper anode. A solution of 0.1 M copper sulphate and

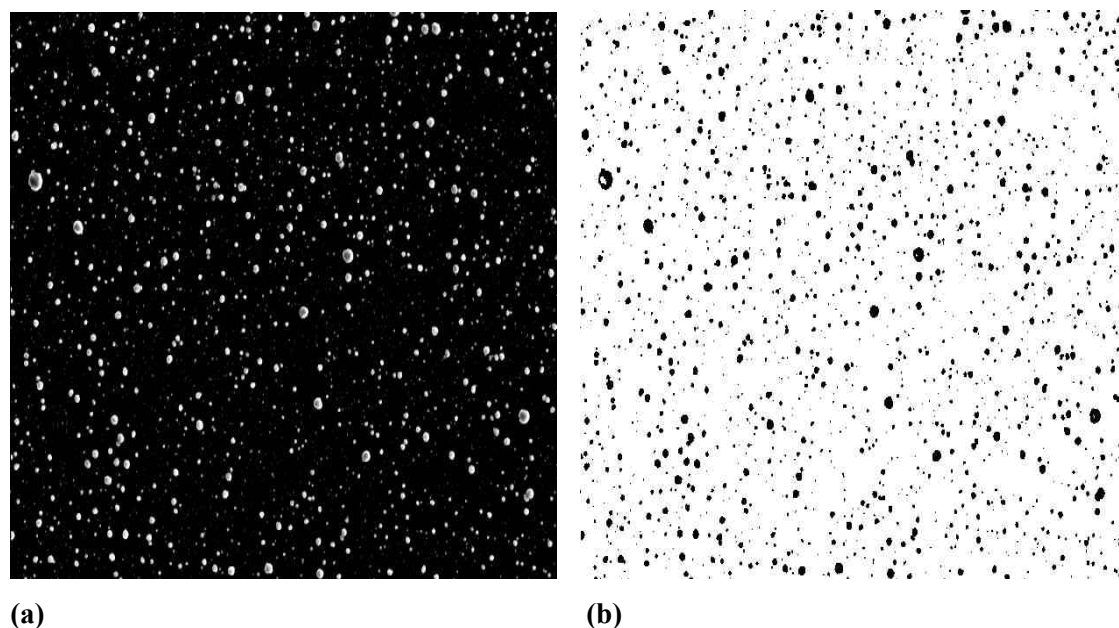


Figure 7.16: (a) Digital SEM image of plated area (b) threshold of the same image.

0.1 M sulphuric acid was used as the electrolyte, which was dropped onto the chip with a pipette. Care was taken to ensure that the defined area, but not beyond, was fully covered with electrolyte. Surface tension at the film-photoresist edge confined the solution well. The Keithley 487 was controlled via a LabVIEWTM computer programme written by Dr G. Burnell. The programme provided an on-screen graphical display of current versus time. It was used to control the applied voltage, current range and sampling rate. Current and time were recorded at the specified sampling rate.

Electrodeposition generally took place at constant voltage for 30 seconds. Different electrodeposition conditions are highlighted below where used. Following electrodeposition the samples were rinsed gently in a beaker of distilled water and dried in air.

7.5.4 Analysis of the films

The samples were imaged using the JEOL 700 SEM. A large number of copper features per unit area were observed. The UTHSCSA ImageToolTM image analysis programme was used to count the number of copper features. Successful processing required high contrast between the copper and the insulating film, as shown by Figure 7.16(a). This image was converted into a threshold plot, containing only two colours: black, representing features to be counted, and white background (Figure 7.16(b)). The

threshold limits were set by hand to allow visual interpretation of image reproduction. The programme was then used to count features in the image. Noise was excluded from the feature count by setting a minimum pixel size, which was set to 2 pixels in Sections 7.6.1 to 7.6.3. The effect of minimum pixel size on the observed trends is discussed in Section 7.6.3.1. Image analysis took approximately five minutes per picture. Up to 2000 copper features were measured on a single image, decreasing the time required to obtain statistical significance.

7.6 Results

The effect of aluminium roughness and thickness on the number of pinholes and weak-links per unit area has been investigated. The effect of bottom electrode material on copper feature density was studied using this technique and is presented in Section 6.3.1.1.1. The relationship between the electrodeposition current and copper feature density is discussed in Section 7.6.3.

7.6.1 Effect of roughness

The effect of roughness on pinhole and weak-link density was investigated using films provided by Seagate Technology, using the original electrodeposition apparatus (Section 7.4.2). Further investigation into the effect of roughness on the number of pinhole and weak-links per unit area was undertaken to obtain a clearer correlation. Film roughness was altered by varying the deposition pressure of niobium, as shown in Table 7.3 (depositions 11317 and 11328). Figure 7.17 shows the dependence of roughness on deposition pressure. Roughness values were measured in images of 1 μm square using the AFM (Section 7.4.2). The Thornton zone model of deposition is useful to explain the trends in roughness and is illustrated by Figure 3.4 [Thornton, 1989]. At low pressure and normal system temperature, deposition is expected to occur in Zone T. This is the transition zone, consisting of closely packed fibrous grains. The voids between grains caused by self-shadowing are largely overcome by adatom diffusion. As pressure rises the structure increasingly resembles that of Zone 1. Self-shadowing becomes more significant at higher pressure, producing larger voids between grains. Adatom mobility is not sufficient to fill the large gaps. As pressure rises, the surface

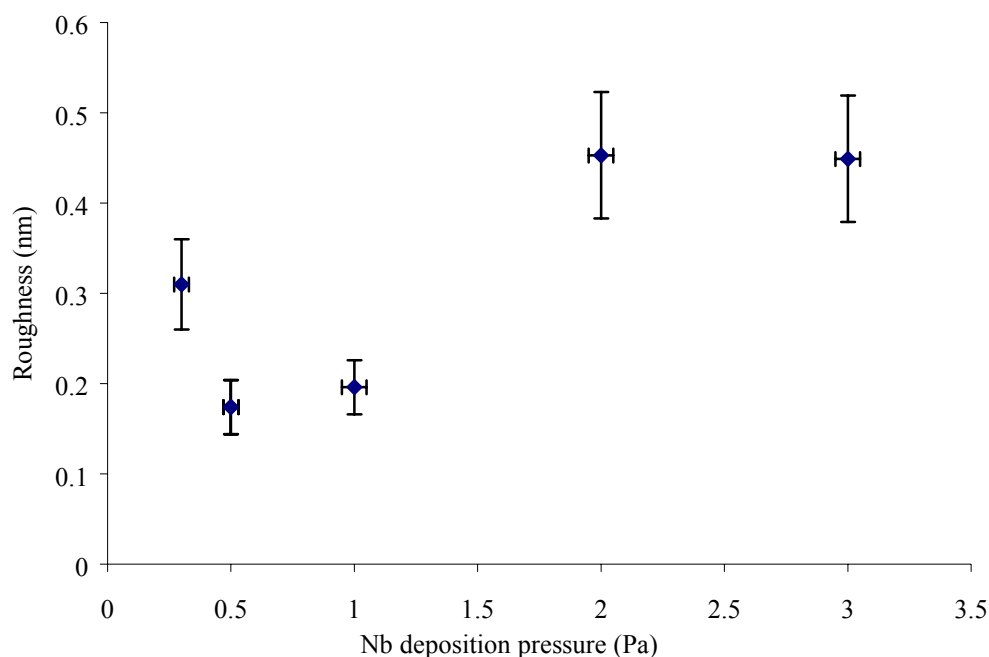


Figure 7.17: The effect of niobium deposition pressure on film roughness.

becomes increasingly rough. The Thornton zone model does not predict increased roughness at the lowest pressures. A number of different mechanisms may be responsible for this structural change. Compressive film stress at low pressure may be relieved by the formation of surface texture: whisker growth and extrusions from the surface are possible. Sputtered atoms encounter fewer scattering events at low pressure and therefore have high kinetic energy on impact with the film. This high energy input may promote diffusion and lead to island growth. Preferential resputtering of certain crystallographic directions is also possible, although this should be accompanied by a decrease in deposition rate, which was not observed [Chiu, 1999].

Figure 7.18 shows that as expected, pinhole and weak-link density increases with roughness. The correlation is better than that presented in Section 7.4.2, although it is not sufficient to derive an empirical relationship. A linear regression fit to the data is shown, with a respectable R^2 value of 0.89. The regression line is not a suggestion of the actual relationship between roughness and the number of pinholes and weak-links per unit area. The variation of plating current with roughness is shown in Figure 7.19. The standard deviations of current and roughness measurements were used to estimate error bars. The linear regression fit to the data shown is reasonable, with an R^2 value of 0.86. This line is primarily intended as a guide to the eye and is not a suggestion of the actual relationship

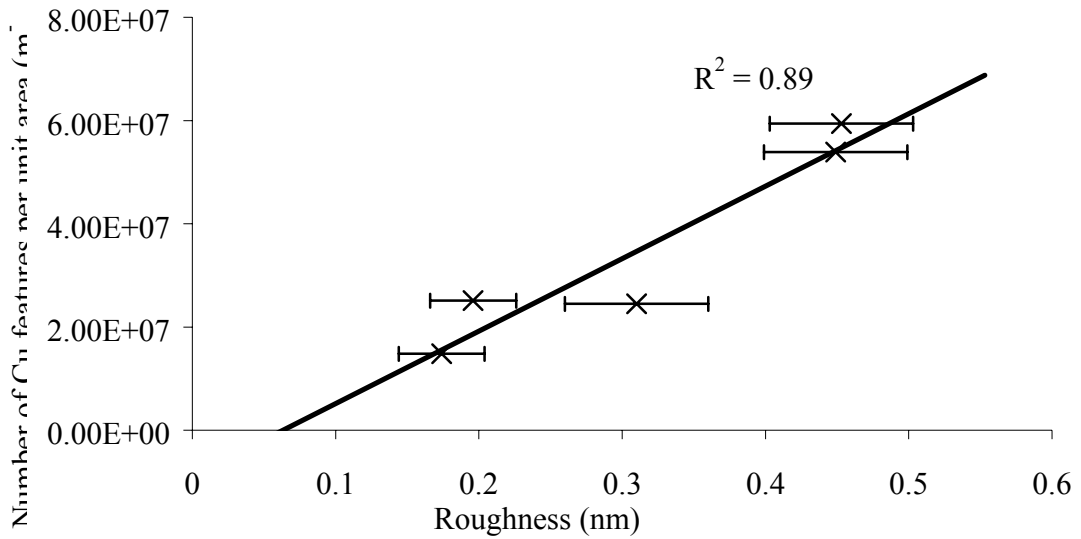


Figure 7.18: The effect of film roughness on pinhole and weak-link density.

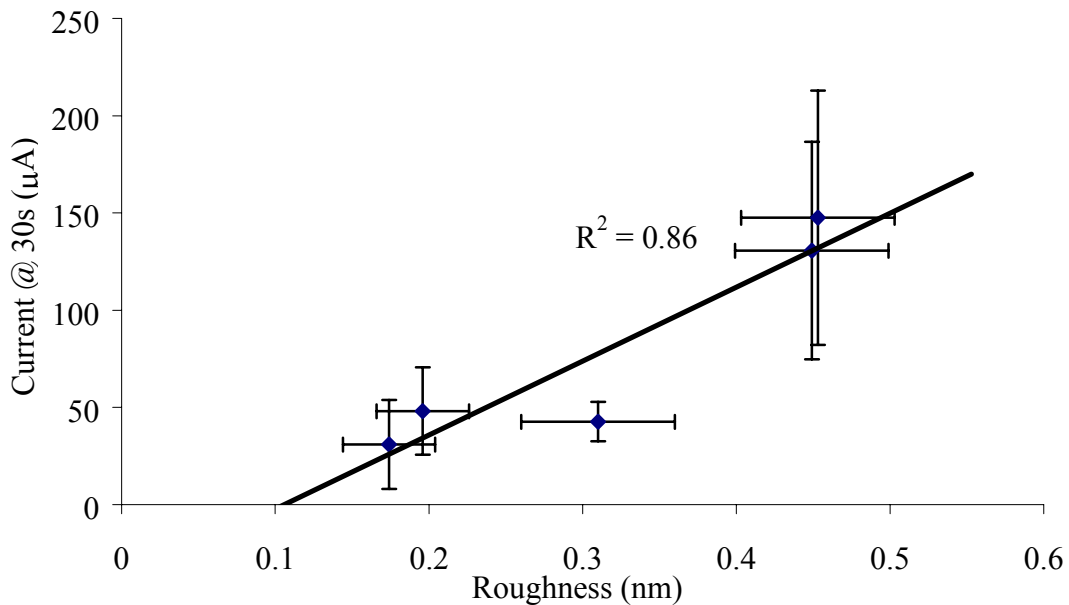


Figure 7.19: The effect of roughness on deposition current.

between current and roughness. The current after electrodeposition for 20 seconds clearly increases with roughness, supporting the use of the current to indicate pinhole density. The dependence of current on pinhole density is discussed in Section 7.6.3.

7.6.2 The effect of aluminium thickness on pinhole density

Figure 7.20 shows that the number of pinholes and weak-links per unit area decreases as aluminium thickness increases. Electrodeposition took place for 20 seconds at -300 mV using films from 11286 (Table 7.3). The model of Rabson *et al.*, discussed in

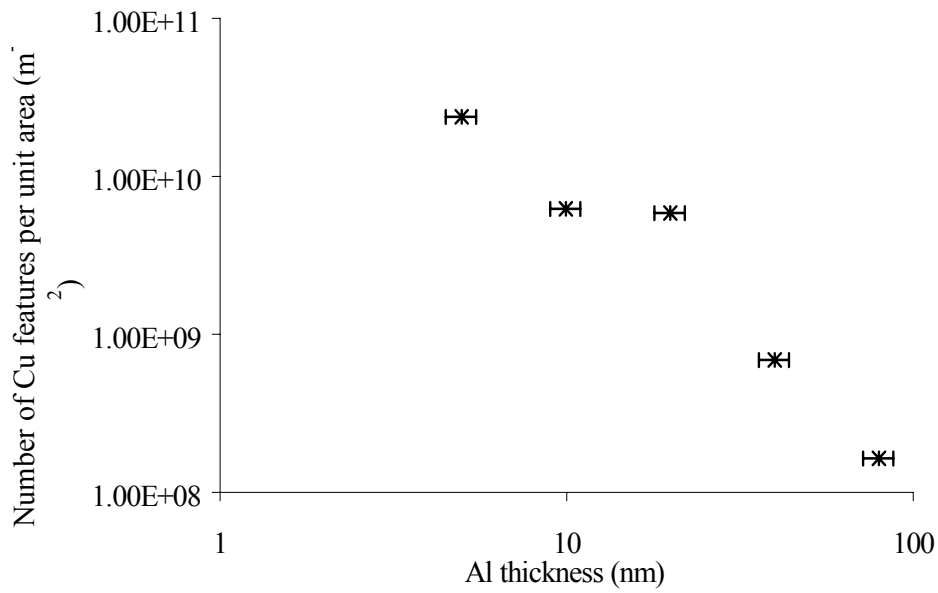


Figure 7.20: Decrease of pinhole and weak-link density as the aluminium thickness increases.

Section 4.1.2.1, may be applied to this situation. They pictured barrier growth as the random deposition of regular blocks of insulator onto a two dimensional grid. The height of deposited material was modelled with a Poisson distribution. Rabson *et al.* predicted that two regimes exist for the probability of any given grid point containing no insulator, $p(0)$:

$$p(0) \propto \begin{cases} \exp(-\mu) & \text{small thickness,} \\ \frac{1}{\mu} & \text{large thickness,} \end{cases} \quad (7.16)$$

where μ is the average film height in monolayers. $\mu \propto t$, where t is the aluminium thickness. Figure 7.21(a) shows the natural log of the number of copper features against aluminium thickness. A good correlation is observed with high R^2 value of 0.93. The R^2 value represents the proportion of the data variation that may be accounted for by the fitted regression. Figure 7.21(b) shows a plot of copper feature density against $1/(\text{aluminium thickness})$. The trend is also adequately fitted by a straight line, with a high R^2 value of 0.95. It is not possible to distinguish between the two regimes of the pinhole dependence on insulator thickness. During electrodeposition, dielectric breakdown occurs for oxide thickness of less than 0.3 nm. This thickness was estimated by assuming dielectric breakdown in Al_2O_3 occurs for electric fields in excess of 10^9 Vm^{-1} , given the

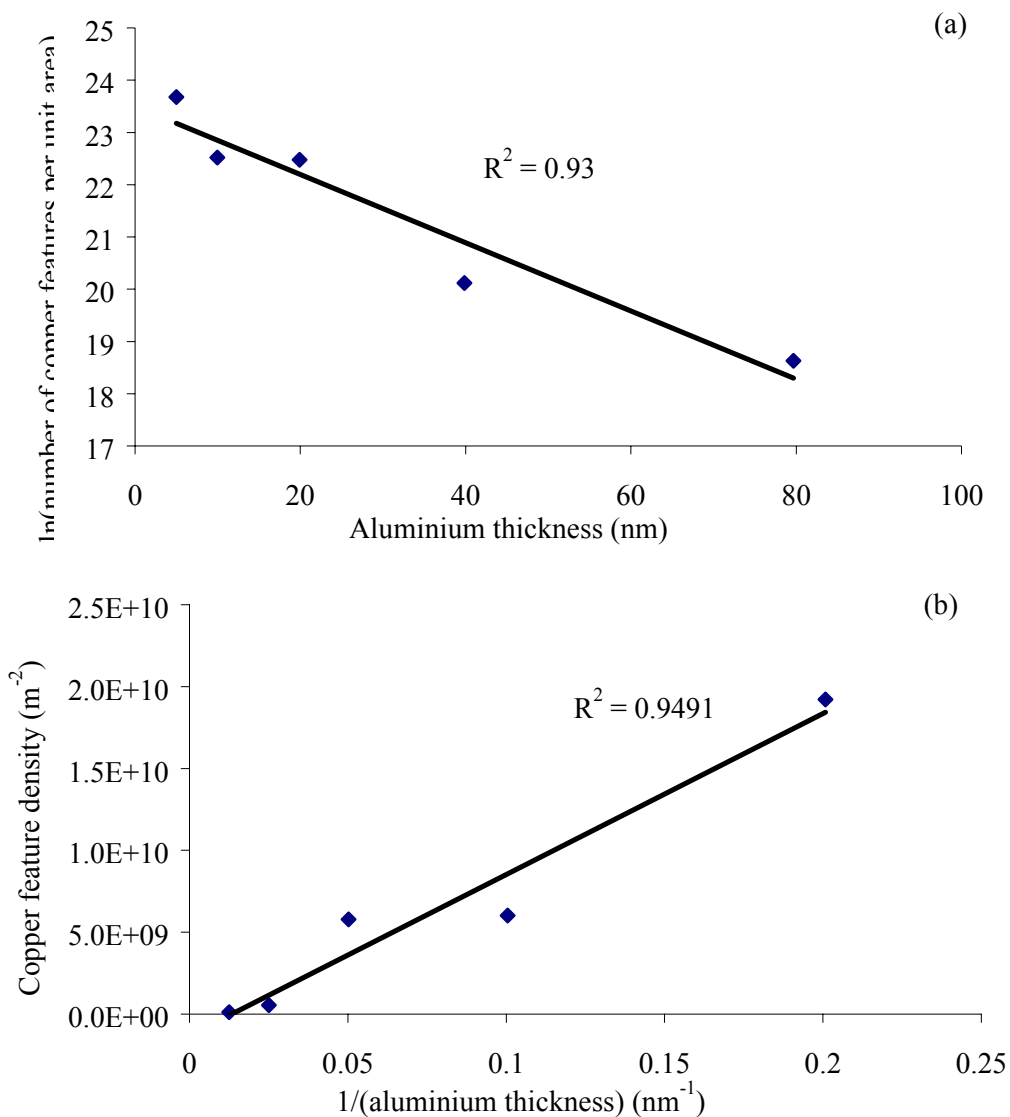


Figure 7.21: (a) Trend of $\ln(\text{number of Cu features per unit area})$ with aluminium thickness and (b) number of copper features per unit area against $1/(\text{aluminium thickness})$

applied voltage was -0.3 V (Section 7.2.1) [Oepts, 1998]. Therefore copper features represent regions in the barrier with thickness of less than 0.3 nm (weak-links) rather than the intrinsic pinholes. It is reasonable to assume that incidence of weak-links follows the same distribution as that of pinholes.

7.6.3 The relationship between current and pinhole density

Figure 7.22 shows the linear relationship between electrodeposition current and the number of copper features per unit area. This relationship is expected from a simple

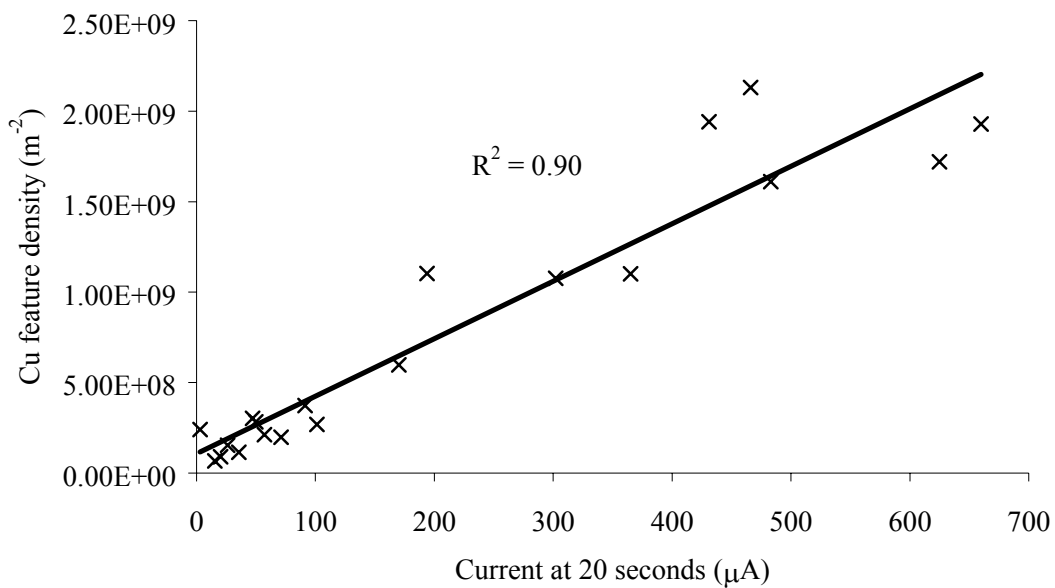


Figure 7.22: The relationship between copper feature density and electrodeposition current at 20 seconds. Fit to a linear trend is good.

interpretation of Faraday's laws (Section 7.1.2.4), that the rate of deposition is directly proportional to the current. Current is therefore also directly proportional to the area onto which deposition occurs. When the size of copper features is negligible, this suggests that current is directly proportional to the total area of pinholes and weak-links on the film. For the large sample sizes of this study, it is reasonable to assume that the number of weak-links and pinholes is directly proportional to their total area on a film. However, current distribution and copper feature size affect electrodeposition current. The non-linearity of the current distribution becomes significant as deposition rate increases. Following a fixed deposition time, the copper features formed on films with a large number of pinholes and weak-links per unit area were much smaller size those when few features were present. The surface area of copper 'cauliflowers' encourages high current. This surface area effect could be mistaken for a high pinhole and weak-link density. It was found that as plating time rose, the relationship between the number of copper features per unit area and current deviated from a linear trend. The effect of feature size on plating current was minimised by recording current at short deposition time. Measurements shown in Figure 7.22 were taken at 20 seconds, to allow initial transients to settle.

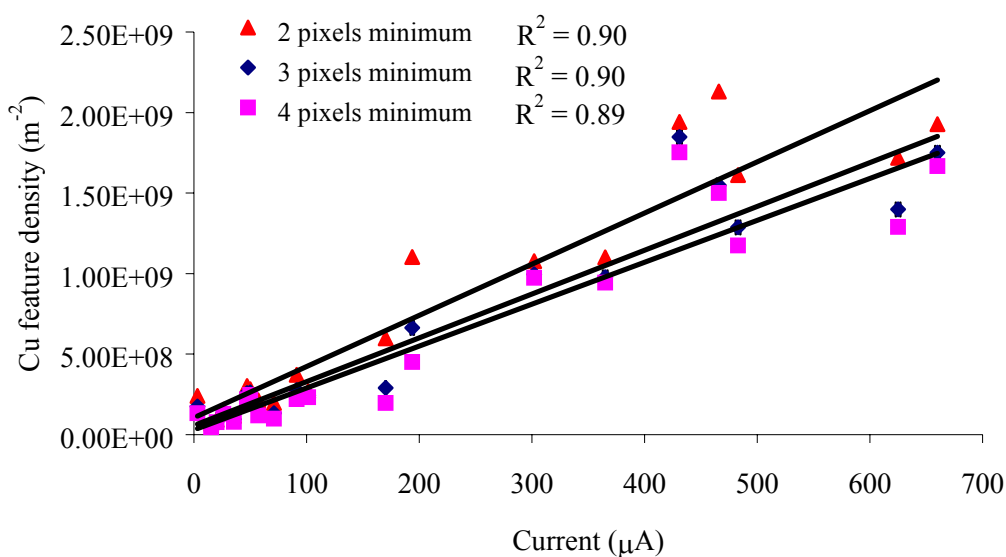


Figure 7.23: variation of copper feature density and current as the minimum pixel recognition size of the image analysis software is increased from 2 to 4. Good correlation to a linear regression is obtained for all three sizes.

The strong correlation between plating current and pinhole density shown in Figure 7.22 proves the concept of this technique. Scatter in the data is likely to result from two main causes. Firstly, SEM measurements did not sample the whole film surface, but current measurements do utilise the entire film area. A large number of images were taken across each area measured, but the sampled images will deviate slightly from the true population. Secondly, the copper ‘cauliflowers’ were extremely fragile and it is likely that some were removed during rinsing. Care was taken when handling the films, but it is inevitable that some scatter in the data will result from the loss of copper.

7.6.3.1 The effect of minimum pixel size on data analysis

The ImageTool™ analysis software was chosen specifically because it allowed the exclusion of features below a minimum pixel size during counting. Figure 7.23 shows the effect of the minimum pixel size on the relationship between electrodeposition current and pinhole density. The number of features counted when including all pixel sizes was strongly affected by image threshold values and a great deal of noise was measured. Therefore, measurements of features of size one pixel and above are not included on the graph. The R^2 value for a linear regression fitted to each set of data is shown on the graph. Minimum pixel sizes of 2, 3 and 4 all correlate well to a straight line, with R^2 of

≈0.90. Minimum pixel size of two was used in Sections 7.6.1 to 7.6.3, to include all data including small copper features.

7.7 Conclusions

Copper has been successfully electrodeposited to identify weak-links and pinholes in thin aluminium oxide. Copper features were identified on SEM images and using EDX, as bright, highly conducting regions. The focussed ion beam was used to image copper features at an angle to the film normal, revealing that they are ‘cauliflower shaped’ at low electrodeposition voltage, but become dendritic at higher voltage. Copper ‘cauliflowers’ were milled with the FIB, revealing crystalline grains in the cross-section.

A new technique has been developed to estimate the density of pinholes and weak-links in a barrier by measuring the electrodeposition current at short deposition time. A linear trend was discovered between the number of copper features and the current at 20 seconds. This method dramatically reduces the time required to measure barrier defect density thus making the technique highly practical. The apparatus is more simple than that generally used for electrodeposition; in particular, it does not use a reference electrode. This electrodeposition technique may be performed using equipment available within a normal magnetic tunnel junction device fabrication or measurement laboratory.

The number of copper features per unit area rose as electrodeposition voltage increased. The data fitted an exponential trend well. It has been shown that the E model of dielectric breakdown leads to an exponential increase in breakdown events at a fixed time in the barrier as voltage rises. This data provides evidence that the E model applies to the breakdown of aluminium oxide thin films.

Pinhole and weak-link density increased with film roughness. It was not possible to infer an empirical relationship due to the large scatter of data. This scatter in the recorded data is likely to result from measurement errors, particularly in the roughness. The amount of pinhole and weak-link formation in aluminium deposited on a rough electrode will depend on the amplitude and length scale over which profile changes occur. Steep gradients in the film profile are likely to cause significant shadowing and encourage pinhole and weak-link formation.

The number of pinholes and weak-links per unit area decreased as the thickness of the aluminium layer increased. The drop in the density of copper features recorded can be adequately fitted to either a $1/t$ or $\exp(-t)$ dependence, where t is the aluminium thickness. This supports the simple two dimensional model of insulator growth by the deposition of regular blocks, as suggested by Rabson *et al.* [Rabson, 2001]. However, it was not possible to differentiate between a $1/t$ (thick film) and $\exp(-t)$ (thin film) dependence. Other models may also fit the data.

This new technique for the identification of pinholes and weak-links by electrodeposition of copper may be applicable to a wide range of fields. Thin film insulator defects are particularly significant in capacitors, tunnel junctions and hard disk shield-to-wiring insulation. The final two applications are experiencing increasingly stringent insulator requirements as read head size decreases, forcing the insulator thickness to be reduced. The technique has already been used to aid the development of magnetic tunnel junctions in Section 6.3.1.1.1.

Chapter 8:

Conclusions

The truth is rarely pure, and never simple.

- Oscar Wilde.

8.1 Device fabrication

Superconductor-insulator-superconductor (SIS), superconductor-insulator-ferromagnet (SIF) and magnetic tunnel junctions (MTJs) have been successfully fabricated. SIS and SIF devices were found to be an extremely useful aid to the optimisation of film deposition and processing. The current-voltage characteristics of such devices are easily interpreted to indicate problems in the fabrication process, also making them useful for fault-finding in processing procedures.

The reliability of characteristics commonly used to identify tunneling as the principal cause of conductance were investigated using SIS devices. Measurements were made at 4.2 K and in their normal state, where they behave as normal metal-insulator-normal metal (NIN) tunnel junctions. As suggested by Rowell, it was established that the only reliable characteristic to indicate a working device was the observation of an energy gap in its superconducting state [Rowell, 1969]. This highlights the value of fabricating SIS and SIF devices prior to magnetic tunnel junctions, in order to develop deposition and processing techniques. Working tunnel junctions were found to satisfy certain criteria in their normal state. Absence of any of the criteria listed below indicates a poor device. However, meeting of all criteria does not necessarily indicate a working device. Firstly, the resistance of devices should be approximately inversely proportional to the junction area. The resistance-area product of devices should be comparable with previous working tunnel junctions produced on the fabrication route. Junction resistance must increase as temperature decreases; a drop in resistance indicates the presence of a conducting short. The conduction should increase, according to Stratton's theory, as a function of temperature squared [Stratton, 1962]. The conductance of the device must increase parabolically with bias voltage, according to Simmons' theory [Simmons, 1963(a)].

The figure-of-merit (FOM) of SIS and SIF junctions is a good measure of device leakage, permitting the determination of barrier problems and redeposition during ion milling. The relationship between the FOM of SIS junctions and NIN tunneling characteristics was not an accurate indicator of device quality. The correlation between FOM and both

the ratio of the resistance at 10 K to that at 300 K, $R(10K)/R(300K)$, and the resistance-area product, RA, was not clear. However, FOM appeared to increase as both RA and $R(10K)/R(300K)$ rose, although a significant scatter of points was evident. The simple model of leakage, as a resistor in parallel to the tunnel junction, did not fit the data well. No correlation was found between FOM and the barrier height and thickness derived by fitting conductance curves of NIN junctions to Simmons' theory.

Magnetic tunnel junction and SIF films were deposited during the same run, enabling the deposition integrity to be checked. The SIF devices produced were of a reasonable quality at 4.2 K. However, working SIF devices did not necessarily indicate that the magnetic tunnel junctions would display a significant tunneling magnetoresistance (TMR). Devices with cobalt lower and iron upper ferromagnetic electrodes were of poor quality, displaying a TMR of just 0.3% at 77 K, but inverting the deposition order of these electrodes produced a TMR of 2.9% at 77 K. Replacing cobalt with iron significantly reduced barrier roughness as a result of lower electrode profile. Increased roughness raises both magnetic coupling between the layers and pinhole and weak-link density. Hysteresis curves of working magnetic tunnel junction films displayed no clear indication of magnetic switching, indicating strong coupling between the ferromagnetic electrodes. Increasing barrier thickness reduced magnetic coupling, but significantly decreased TMR by reducing the effective polarisation of the ferromagnetic electrodes.

Transmission electron microscope images of MTJ films were used to identify the crystalline electrodes and amorphous barrier. The oxygen map indicated poor definition of the oxide at barrier interfaces. The lack of well-defined boundaries may indicate over oxidation, forming a magnetic oxide at the top of the electrode and therefore encouraging spin scattering. Oxygen may also have diffused into the aluminium capping layer or have been dispersed by damage due to deposition above the barrier. MTJ devices produced from these films had a low TMR of 0.2% at 77 K.

8.2 Copper decoration of pinholes

Weak-links and pinholes in thin aluminium oxide have been successfully identified by the electrodeposition of copper. Scanning electron microscopy and energy dispersive X-ray

spectroscopy were used to identify copper features. A focussed ion beam (FIB) was used to image copper features at an angle to the film normal, revealing their ‘cauliflower’ shape at low plating voltage. The shape became dendritic at higher deposition voltage. Copper ‘cauliflowers’ were milled with the FIB, to reveal the cross-section exhibiting crystalline grains.

The time taken to measure the defect levels of barriers was dramatically reduced by the development of an electrodeposition technique using simple apparatus available within a normal fabrication or measurement laboratory. The number of copper features increased linearly with electrodeposition current after 20 seconds, providing a rapid analysis tool to identify weak-links and pinholes in the barrier. This technique may be suitable for identifying insulator defects in a range of applications, including capacitors, read head insulation and tunnel junctions.

The number of copper features per unit area rose as electrodeposition voltage was increased. The data fitted an exponential trend well, as predicted by the E model of dielectric breakdown. Pinhole and weak-link density increased as film roughness rose. The density of copper features decreased as the thickness, t , of the aluminium layer increased. The decrease in the number of weak-links and pinholes per unit area was adequately described by both a $1/t$ and an $\exp(-t)$ dependence. The simple two-dimensional model of insulator growth by the deposition of regular blocks, suggested by Rabson *et al.* may describe these films [Rabson, 2001]. It was not possible to distinguish between the regimes of film growth.

8.3 High frequency testing of read heads

A network analyser was used to investigate the high frequency response of read heads at wafer level. Previously, full-build was required to measure read heads, producing read-back data from hard disks. Tests at wafer level enable the rapid investigation of changes to the reader geometry on the system frequency response. Furthermore, this technique allows the step-by-step build and testing read and write head structures, isolating the effect of parameters on the response. However, one-port network analyser measurements were subject to significant error and are not suitable for the investigation of dielectrics.

The -3dB frequency, or roll-off frequency, is the point at which the signal attenuation becomes -3dB and is a convenient measure of the limit of read-back. Wafers were fabricated to first half gap (bottom shield, insulators, sensor and wiring). The shield, insulator and wiring layer form a capacitor. The simple model of a capacitor and resistor in parallel satisfactorily represented a low roll-off frequency read head. A more complex model was required to account for the extra capacitance and system inductance of the read head and network analyser calibration errors. Two-port network analyser measurements are necessary for more accurate analysis of the system, since they allow the determination of more parameters and reduce calibration error.

Roll-off frequency decreases with increasing sensor resistance, for high resistance readers the -3dB frequency is inversely proportional to their resistance, R . Corresponding trends were observed in roll-off frequency with sensor length, CD , ($\propto R$) and sensor width ($\propto 1/R$). This highlights the requirement of low resistance magnetic tunnel junctions for read head sensors. Raising read head temperature increases sensor resistance and decreases roll-off frequency. Roll-off frequency increases as stray capacitance decreases. For large overlap area between shields and wiring, the -3dB point is inversely proportional to overlap area and modelled capacitance.

High frequency data transfer requires read heads with a low resistance sensor and minimal shield size. Creating a thin break in the shield between the sides of the wiring layer may increase roll-off frequency by decreasing the conductance of the parallel transport path. High frequency testing of read heads with a network analyser has significant potential as an analysis tool.

Publications

Cliff Elwell, P. Scullion, R. Lamberton, M. Blamire and A. Johnston (TBA). “High frequency testing of read heads at wafer level”. To be submitted to IEEE Transactions on Magnetics. Currently with Seagate Technology for approval.

Posters:

Cliff Elwell, Gavin Burnell and Mark Blamire (2000). “The development of magnetic tunnel junction fabrication techniques using superconducting tunnel junctions”. Presented at CMMP 2001.

C.A. Elwell, S.J Lloyd, P.K.Wong and M.G. Blamire (1999). “The development of magnetic tunnel junctions”. Presented at Seagate Technology UK Research Students Workshop.

Bibliography

- Akerman, J.J., J.M. Slaughter, R.W. Dave and I.K. Schuller (2001). "Tunneling criteria for magnetic-insulator-magnetic structures." *Applied Physics Letters* **79**: 3104-3106.
- Allen, D., R. Schad, G. Zangari, I. Zana, M. Tondra, D. Wang and D. Reed (2001). "Comparison of defect density measurements in magnetic tunnel junctions." *Journal of Applied Physics* **89**: 6662-6664.
- Atkins, P.W. (1994). "Physical Chemistry." Oxford University Press.
- Bai, H.L. and E.Y. Jiang (2001). "Magnetic tunnel junctions (MTJs)." *Chinese Science Bulletin* **46**: 709-716.
- Bardeen, J., L.N. Cooper and J.R. Schrieffer (1957). "Microscopic Theory of Superconductivity." *Physical Review* **108**: 1175.
- Blamire, M.G. (1993). "Anodization Spectroscopy." *Concise Encyclopedia of Materials Characterization*. Editors: R. E. Cahn and E. Lifshin. Oxford, Pergamon: 14-16.
- Blamire, M.G., R. E. Somekh, Z.H. Barber, G.W. Morris and J.E. Evetts (1988). "Microstructure effects on electronic properties of Nb/Al₂O₃/Nb tunnel junctions." *Journal of Applied Physics* **64**: 6396.
- Bloch, F. (1932). *Z. Physik* **74**: 295.
- Boeve, H., J. De Boeck and G. Borghs (2001). "Low-resistance magnetic tunnel junctions by in situ natural oxidation." *Journal of Applied Physics* **89**: 482-487.
- Brandon, D. and W. D. Kaplan (1999). "Microstructural Characterization of Materials." Wiley pp324.
- Bratkovsky, A. M. (1998). "Assisted tunneling in ferromagnetic junctions and half-metallic oxides." *Applied Physics Letters* **72**: 2334-2336.
- Brinkmann, W.F., R.C. Dynes and J.M. Rowell (1970). *J. Appl. Phys.* **41**: 1915.

Bruckl, H., J. Schmalhorst, G. Reiss, G. Gieres and J. Wecker (2001). "Evolution of barrier asymmetry in magnetic tunnel junctions." *Applied Physics Letters* **78**: 1113-1115.

Canning (1978). "Canning Handbook on Electroplating." Canning. pp271-291.

Cardoso, S., P.P. Freitas, C. de Jesus, P. Wei and J.C. Soares (2000). "Spin-tunnel-junction thermal stability and interface interdiffusion above 300°C." *Applied Physics Letters* **76**: 610-612.

Chiu, K. F., M. G. Blamire and Z. H. Barber (1999). "Microstructure modification of silver films deposited by ionized magnetron sputter deposition." *Journal of Vacuum Science & Technology A-Vacuum Surfaces and Films* **17**: 2891-2895.

Clark, T. E., F. B. Mancoff, S. X. Wang, B. M. Clemens and R. Sinclair (1999). "Study of DC plasma oxidized Al₂O₃ barriers in spin dependent tunneling junctions using high resolution transmission electron microscopy." *IEEE Transactions on Magnetics* **35**: 2922-2924.

Comstock, R. L. (1999). "Introduction to magnetism and magnetic recording." Wiley pp111.

Davis, A.H., J.M. MacLaren and P.LeClair (2001). "Inherent temperature effects in magnetic tunnel junctions." *Journal of Applied Physics* **89**: 7567-7569.

Dunin-Borkowski, R.E., M.R. McCartney, D.J. Smith, S. Gider, B.U. Runge and S.S.P. Parkin (1999). "Microstructural and micromagnetic characterization of thin film magnetic tunnel junctions." *Journal of Applied Physics* **85**: 4815-4817.

Gallagher, W.J., S.S.P. Parkin, Y. Lu, X.P. Bian, A. Marley, K.P. Roche, R.A. Altman, S.A. Rishton, C. Jahnes, T.M. Shaw and G. Xiao (1997). "Microstructured magnetic tunnel junctions." *Journal Of Applied Physics* **81**: 3741-3746.

Garcia, N. (2000). "Conducting ballistic magnetoresistance and tunneling magnetoresistance: Pinholes and tunnel barriers." *Applied Physics Letters* **77**: 1351-1353.

Gider, S., B.U. Runge, A.C. Marley and S.S.P. Parkin (1998). "The magnetic stability of spin-dependent tunneling devices." *Science* **281**: 797-799.

Gillies, M.F., A.E.T. Kuiper, J.B.A. van Zon and J.M. Sturm (2001). "Magnetic tunnel junctions with tantalum oxide barriers displaying a magnetoresistance ratio of up to 10% at room temperature." *Applied Physics Letters* **78**: 3496-3498.

Golubov, A. A. and M. Y. Kupriyanov (1988). "Theoretical Investigation of Josephson Tunnel-Junctions With Spatially Inhomogeneous Superconducting Electrodes." *Journal of Low Temperature Physics* **70**: 83-130.

Goodchild, M.S., Z.H. Barber and M.G. Blamire (1996). "Conductance and Leakage In Superconducting Tunnel-Junctions." *Journal Of Vacuum Science & Technology A-Vacuum Surfaces and Films* **14**: 2427-2432.

Gurvitch, M., M.A. Washington, H.A. Huggins and J.M. Rowell (1983). "Preparation and properties of Nb Josephson Junctions with thin Al layers." *IEEE Trans. Magn.* **19**: 791.

Guth, M., V. Da Costa, G. Schmerber, A. Dinia and H.A.M. van den Berg (2001). "Tunnel magnetoresistance in magnetic tunnel junctions with ZnS barrier." *Journal of Applied Physics* **89**: 6748-6750.

Hagler, T., R. Kinder and G. Bayreuther (2001). "Temperature dependence of tunnel magnetoresistance." *Journal of Applied Physics* **89**: 7570-7572.

Hodges, L., H. Ehrenreich and N. Lang (1966). "Interpolation Scheme for Band Structure of Noble and Transition Metals: Ferromagnetism and Neutron Diffraction in Ni." *Phys.Rev.* **152**: 505.

HP (1999). "HP Network Analyser Basics." Hewlett Packard literature.

IBM (2002). "HDD Technology." IBM online

<http://www.almaden.ibm.com/sst/images/HDD%20Technology.pdf>

Jansen, R. and J.S. Moodera (1998). "Influence of barrier impurities on the magnetoresistance in ferromagnetic tunnel junctions." *Journal of Applied Physics* **83**: 6682-6684.

- Jiles, D. (1998). "Introduction to Magnetism and Magnetic Materials." Chapman and Hall.
- Jonsson-Akerman, B.J, R. Escudero, C. Leighton, S. Kim, I.K. Schuller and D.A. Rabson (2000). "Reliability of normal-state current-voltage characteristics as an indicator of tunnel-junction barrier quality." *Applied Physics Letters* **77**: 1870-1872.
- Josephson (1962). "Possible new effects in superconductive tunneling." *Physics Letters* **1**: 251-253.
- Jullière, M. (1975). "Tunneling between ferromagnetic films". *Physics Letters A* **54**: 225.
- Jury, J.C. and S.X. Wang (2002). "Extending the bandwidth of magnetic tunnel junction sensors by a buffer amplifier." *IEEE Transactions on Magnetics* **38**: 295-297.
- Kittel, C. (1996). "Introduction to Solid State Physics." Wiley.
- Kools, J.C.S. (1996). "Exchange-biased spin-valves for magnetic storage." *IEEE Transactions on Magnetics* **32**: 3165-3184.
- Kroger, H., L.N. Smith and D.W. Jillie (1981). "Selective niobium anodization process for fabricating Josephson junctions." *Appl Phys Lett* **39**: 280.
- Landau, I.D. and E.M. Lifschitz (1935). *Physik Z. Sowjetunion* **8**: 153.
- LeClair, P., H.J.M. Swagten, J.T. Kohlhepp and W.J.M. de Jonge (2000). "Tunnel conductance as a probe of spin polarization decay in Cu dusted Co/Al₂O₃/Co tunnel junctions." *Applied Physics Letters* **76**: 3783-3785.
- Lehnert, T., D. Billon, C. Grassi and K.H. Gundlach (1992). *J. Appl. Phys.* **72**: 3165-3168.
- Lennert, T., C. Grassl, K.H. Gundlach and J. Blondel (1991). "Nb-AloxideNb junctions for 3mm SIS receivers." *Supercond. Sci. Technol.* **4**: 419-422.
- London, F. and H. London (1935). "The electromagnetic equations of the superconductors." *Proceedings of the Royal Society* **A149**: 71.

- Lu, Y., X.W. Li, G. Xiao, R.A. Altman, W.J. Gallagher, A. Marley, K. Roche and S. Parkin (1998). "Bias voltage and temperature dependence of magnetotunneling effect." *Journal Of Applied Physics* **83**: 6515-6517.
- Maeda, M., E. Yamamoto, S. Ohfuji and M. Itsumi (1999). *J. Vac. Sci. Technol. B* **17**: 201-204.
- Mallinson, J.C. (1996). "Magneto-resistive heads: fundamentals and applications." London, Academic Press.
- Matthews, G.P. (1985). "Experimental Physical Chemistry." Oxford Science Publications: 140.
- McPherson, J.W. and H.C. Mogul (1998). "Underlying physics of the thermochemical E model in describing low-field time-dependent dielectric breakdown in SiO₂ thin films." *Journal of Applied Physics* **84**: 1513-1523.
- Meissner, W. and R. Ochsenfeld (1933). *Naturwissenschaften* **21**: 787.
- Meservey, R. and P.M. Tedrow (1994). "Spin-Polarized Electron-Tunneling." *Physics Reports-Review Section of Physics Letters* **238**: 173-243.
- Miyazaki, T. and N. Tezuka (1995). "Giant Magnetic Tunneling Effect in Fe/Al₂O₃/Fe Junction." *Journal of Magnetism and Magnetic Materials* **139**: L231-L234.
- Miyazaki, T., T. Yaoi and S. Ishio (1991). "Large Magnetoresistance Effect In 82ni-Fe/Al-Al₂O₃/Co Magnetic Tunneling Junction." *Journal of Magnetism and Magnetic Materials* **98**: L7-L9.
- Molla, J., A. Ibarra and E.R. Hodgson (1995). "In-Beam Dielectric-Properties of Alumina." *Journal of Nuclear Materials* **219**: 182-189.
- Moodera, J.S., E.F. Gallagher, K. Robinson and J. Nowak (1997). "Optimum tunnel barrier in ferromagnetic-insulator-ferromagnetic tunneling structures." *Applied Physics Letters* **70**: 3050-3052.

Moodera, J.S. and L.R. Kinder (1996(a)). "Ferromagnetic-insulator-ferromagnetic tunneling: Spin-dependent tunneling and large magnetoresistance in trilayer junctions." *Journal of Applied Physics* **79**: 4724-4729.

Moodera, J.S., L.R. Kinder, T.M. Wong and R. Meservey (1995). "Large magnetoresistance at room-temperature in ferromagnetic thin film tunnel junctions." *Physical Review Letters* **74**: 3273-3276.

Moodera, J.S., J. Nassar and G. Mathon (1999). "Spin-tunneling in ferromagnetic junctions." *Annual Review of Materials Science* **29**: 381-432.

Moodera, J.S., J. Nowak and R.J.M. Van de Veerdonk (1998). "Interface magnetism and spin wave scattering in ferromagnet-insulator-ferromagnet tunnel junctions." *Physical Review Letters* **80**: 2941-2944.

Moodera, J.S., M.E. Taylor and R. Meservey (1989). "Exchange-Induced Spin Polarization of Conduction Electrons in Paramagnetic Metals." *Physical Review B* **40**: 11980-11982.

Neel, L. (1962). *Comptes Rendus* **255**: 1676-1681.

Nogues, J. and I.K. Schuller (1999). "Exchange bias." *Journal of Magnetism and Magnetic Materials* **192**: 203-232.

Oepts, W., H.J. Verhagen, R. Coehoorn and W.J.M. deJonge (1999). "Analysis of breakdown in ferromagnetic tunnel junctions." *Journal of Applied Physics* **86**: 3863-3872.

Oepts, W., H.J. Verhagen, W.J.M. deJonge and R. Coehoorn (1998). "Dielectric breakdown of ferromagnetic tunnel junctions." *Applied Physics Letters* **73**: 2363-2365.

Onnes (1911). *Leiden Communications* **124c**.

Park, B. and T. D. Lee (2001). "A study on tunneling magnetoresistance in magnetic tunnel junctions oxidized by ozone." *Journal of Magnetism and Magnetic Materials* **226**: 926-929.

Parkin, S.S.P., K.S. Moon, K.E. Pettit, D.J. Smith, R.E. Dunin-Borkowski and M.R. McCartney (1999). "Magnetic tunnel junctions thermally stable to above 300°C." *Applied Physics Letters* **75**: 543-545.

Pedersen, R.J. and F.L. Vernon (1967). *Appl Phys Lett* **10**: 29.

Pierce, D. T. and H. C. Siegmann (1974). *Phys. Rev. B* **9**: 4035-4038.

Platt, C.L., B. Dieny and A.E. Berkowitz (1997). "Spin polarized tunneling in reactively sputtered tunnel junctions." *Journal of Applied Physics* **81**: 5523-5525.

Portier, X., A.K. Petford-Long, J.H. Nickel, T.C. Anthony and J.A. Brug (2001). "Microstructural studies of top and bottom magnetic tunnel junctions." *Applied Physics Letters* **79**: 57-59.

Powell, J.L. and B. Crasemann (1968). "Quantum Mechanics." Addison-Wesley.

Rabson, D.A., B.J. Jonsson-Akerman, A.H. Romero, R. Escudero, C. Leighton, S. Kim and I.K. Schuller (2001). "Pinholes may mimic tunneling." *Journal of Applied Physics* **89**: 2786-2790.

Rowell, J.M. (1969). "Tunneling Phenomena in Solids." Plenum (Editors E. Burnstein and S. Lunqvist).

Rudiger, U., R. Calarco, U. May, K. Samm, J. Hauch, H. Kittur, M. Sperlich and G. Guntherodt (2001). "Temperature dependent resistance of magnetic tunnel junctions as a quality proof of the barrier." *Journal of Applied Physics* **89**: 7573-7575.

Schad, R., D. Allen, G. Zangari, I. Zana, D. Yang, M. Tondra and D.X. Wang (2000). "Pinhole analysis in magnetic tunnel junctions." *Applied Physics Letters* **76**: 607-609.

Schuegraf, K.F. and C.M. Hu (1994). "Metal-Oxide-Semiconductor Field-Effect-Transistor Substrate Current During Fowler-Nordheim Tunneling Stress and Silicon Dioxide Reliability." *Journal of Applied Physics* **76**: 3695-3700.

Shang, C.H., J. Nowak, R. Jansen and J.S. Moodera (1998). "Temperature dependence of magnetoresistance and surface magnetization in ferromagnetic tunnel junctions." *Physical Review B-Condensed Matter* **58**: R2917-R2920.

Shimazawa, K., N. Kasahara, J.J. Sun, S. Araki, H. Morita and M. Matsuzaki (2000). "Electrical breakdown of the magnetic tunneling junction with an AlO_x barrier formed by radical oxidation." *Journal of Applied Physics* **87**: 5194-5196.

Shimazawa, K., J.J. Sun, N. Kasahara, K. Sato, T. Kagami, S. Saruki, O. Redon, Y. Fujita, T. Umehara, J. Syoji, S. Araki and M. Matsuzaki (2001). "Frequency response of common lead and shield type magnetic tunneling junction head." *IEEE Transactions on Magnetics* **37**: 1684-1686.

Shull, C.G. and H.A. Mook (1966). *Phys. Rev. Lett.* **16**: 184-186.

Simmons, J.G. (1963(a)). "Generalized formula for the electric tunnel effect between similar electrodes separated by a thin insulating film." *J. Appl. Phys.* **34**: 1793.

Simmons, J.G. (1963(b)). "Generalized J-V characteristic for the electric tunnel effect." *J. Appl. Phys.* **34**: 2581.

Simmons, J.G. and G.J. Unterkofer (1963(c)). "Potential barrier shape determination in tunnel junctions." *J. Appl. Phys.* **34**: 1828.

Slater, J.C. (1936). *Phys. Rev.* **49**: 537.

Slonczewski, J.C. (1989). "Conductance and exchange coupling of two ferromagnets separated by a tunneling barrier." *Physical Review B-Condensed Matter* **39**: 6995.

Sommerfeld, A. and H. Bethe (1933). "Handbuch der Physik." Springer-Verlag **24**.

Soulen, R.J., J.M. Byers, M.S. Osofsky, B. Nadgorny, T. Ambrose, S.F. Cheng, P.R. Broussard, C.T. Tanaka, J. Nowak, J.S. Moodera, A. Barry and J.M.D. Coey (1998). "Measuring the spin polarization of a metal with a superconducting point contact." *Science* **282**: 85-88.

Sousa, R.C., J.J. Sun, V. Soares, P.P. Freitas, A. Kling, M.F. daSilva and J.C. Soares (1999). "Temperature dependence and annealing effects on spin dependent tunnel junctions." *Journal of Applied Physics* **85**: 5258-5260.

Stearns, M. (1977). "Simple explanation of tunneling spin-polarisation of Fe, Co, Ni and its alloys." *Journal of magnetism and magnetic materials* **5**: 167-171.

Stoner, E. C. (1933). *Phil. Mag.* **15**: 1080.

Stratton, R. (1962). *J. Phys Chem. Solids* **23**: 1177.

Takatsuji, H. and T. Arai (2000). "Pinholes in Al thin films: their effects on TFT characteristics and a taguchi method analysis of their origins." *Vacuum* **59**: 606-613.

Thompson, D.A. and J.S. Best (2000). "The future of magnetic storage technology." *IBM J. Res. Develop.* **44**: 311-322.

Thompson, L.F., C.G. Willson and M.J. Bowden (1994). "Introduction to microlithography." *ACS Professional Reference Book*.

Thornton, A.J. (1974). *J. Vac. Sci. Tech. A* **4**: 666.

Tinkham, M. (1996). "Introduction to Superconductivity". Singapore, McGraw-Hill Book Co.

Tondra, M., J.M. Daughton, D.X. Wang, R.S. Beech, A.Fink and J.A. Taylor (1998). "Picotesla field sensor design using spin-dependent tunneling devices." *Journal of Applied Physics* **83**: 6688-6690.

Vanbeek, H.J. and E.J. Mittemeijer (1984). "Amorphous and crystalline oxides on aluminum." *Thin Solid Films* **122**: 131-151.

Van de Veerdonk, R. J. M., J. Nowak, R. Meservey, J.S. Moodera and W.J.M. deJonge (1997). "Current distribution effects in magnetoresistive tunnel junctions." *Applied Physics Letters* **71**: 2839-2841.

Wang, J.G., S. Cardoso, P.P. Freitas, P. Wei, N.P. Barradas and J.C. Soares (2001). "Tunnel junctions with AlN barriers and FeTaN electrodes." *Journal of Applied Physics* **89**: 6868-6870.

Weiss, P. (1907). *J. Phy.* **6**: 661.

Wolf, E. L. (1985). "Principles of Electron Tunneling Spectroscopy." Oxford Scientific Publications.

Wong, P.K., J.E. Evetts and M.G. Blamire (1998). "High conductance magnetoresistive tunnel junctions with multiply oxidized barrier." *Journal of Applied Physics* **83**: 6697-6699.

Zhang, X.D., B.Z. Li, S. Gang and F.C. Pu (1998). "Spin-polarized resonant tunneling and quantum-size effect in ferromagnetic tunnel junctions with double barriers subjected to an electric field." *Physics Letters A* **245**: 133-138.

Zhang, X.D., B.Z. Li and F.C. Pu (1997). "Theory of spin-polarized tunneling between ferromagnetic films." *Physics Letters A* **236**: 356-359.